Technische Universität München
TUM School of Computation, Information and Technology

Metriplectic relaxation for calculating equilibria: theory and structure-preserving discretization

Camilla Bressan

Vollständiger Abdruck der von der TUM School of Computation, Information and Technology der Technischen Universität München zur Erlangung einer
Doktorin der Naturwissenschaften (Dr. rer. nat.)
genehmigten Dissertation.

Vorsitz: Prof. Dr. Johannes Zimmer

Prüfer*innen der Dissertation:

1. Prof. Dr. Eric Sonnendrücker
2. Prof. Dr. Masaru Furukawa
3. Prof. Dr. Cesare Tronci

Die Dissertation wurde am 09.09.2022 bei der Technischen Universität München eingereicht und durch die TUM School of Computation, Information and Technology am 01.02.2023 angenommen.

Metriplectic relaxation for calculating equilibria: theory and structure-preserving discretization

Author: Camilla Bressan
Supervisor: Prof. Dr. Eric Sonnendrücker
Advisors: Dr. Michael Kraus and Dr. Omar Maj

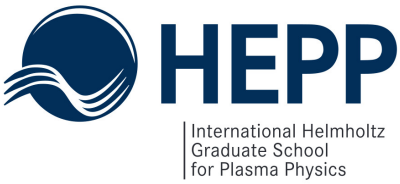

Max Planck Institute for Plasma Physics
Division of Numerical Methods in Plasma Physics
2022

To my family and friends

Contents

Acknowledgements

I would first like to thank Prof. Dr. Eric Sonnendrücker for giving me the opportunity to conduct this research. Further opportunities I would like to thank for have not been strictly limited to academic activities, such as attending relevant conferences and workshops. In fact, I could join the CEMRACS program, visit my advisor Dr. Michael Kraus at the Waseda University in Tokyo and also attend a Data Science program in London that ultimately was crucial for the type of career I later decided to pursue. These experiences exposed me to a wider scientific community, contributed to my professional and personal development, and finally allowed me to start my career after the years spent at the Institute.

This work could have not been possible without the daily advice of my two advisors, Dr. Michael Kraus and Dr. Omar Maj. I will be forever grateful for the numerous scientific discussions, the guidelines, the dedication and the time spent in trying to solve the problems and challenges I faced. They have been the best teachers I ever had and the best advisors I could wish for. My work in my current role is valued thanks to what I learnt from them during these years. Thanks both for your patience and extraordinary dedication, and for taking the time to explain difficult concepts and answer all my questions. Thanks Michael for teaching me a rigorous research approach, for your sharp observations and your attention to the details. In particular, thanks for making my visit to the Waseda University possible, despite many difficulties, because it has been one of the most enriching experiences of the past years. Thanks Omar for being always available, no matter how late or which day of the week it is, for making the work of your students always a priority, and for being patient and generous in sharing knowledge and advice. I never learnt so much by simply listening. Thanks especially for supervising my work after I left the Institute, reviewing my writing multiple times and making sure that I could meet all the deadlines. Without your support, completing this work would have not been possible.

I will never forget the brilliant, fast-pacing and inspiring conversations of Prof. Dr. Philip J. Morrison. Not only his previous works represent the foundation for the current project, but during his frequent visits to the NMPP division and through numerous discussions he steered the research direction multiple times. Thank you also for taking the time to carefully read and review this work.

Thanks to Prof. Dr. Masaru Furukawa, for inviting Michael and me to Tottori University and the interesting discussions that followed that visit.

A special thanks is for Dr. Cesar Allande Alvarez, who at the time worked as a researcher at the Max Planck Computing and Data Facility (MPCDF). He took on the responsibility for the installation of the `FEniCS` library on the extension clusters DRACO and COBRA of the High Performance Computing (HPC) system of MPCDF. Without his pivotal support, the three-dimensional numerical experiments here presented would have not been possible. I would also like to thank other researchers of the MPCDF team who gave their support in understanding performance issues of the same library.

I had my first lessons of serious Software Engineering from Dr. Jalal Lakhlili and Dr. Yaman Güçlü, who were both kind in sharing their knowledge during numerous discussions.

Thanks to Dr. Mariarosa Mazza for investigating a better preconditioner. I am sure there will be the opportunity to explore some of those ideas in future works.

I would also like to thank Dr. Masaru Furukawa and Dr. Cesare Tronci for agreeing to participate in the examining committee.

The NMPP division has always been a thrilling and stimulating environment: thanks to all the researchers who happened to be there during those years and shared some of their experience with me.

The numerical experiments presented in this work have been performed on the extension clusters DRACO and COBRA of the HPC system of MPCDF.

This work has been carried out within the framework of the EUROfusion Consortium and has received funding from the Euratom research and training programme 2014-2018 under grant agreement No 633053. The views and opinions expressed herein do not necessarily

reflect those of the European Commission.

List of Figures

List of Tables

Abstract

We use the theory of metriplectic dynamical systems to construct relaxation methods for the computation of solutions of ill-posed equilibrium problems. We propose two classes of methods, inspired by the Landau collision operator: the collision- and diffusion-like operators. These ideas are illustrated by means of numerical experiments. The physical models considered are Euler's equations in vorticity form, the Grad-Shafranov equation, and force-free MHD equilibria.

Zusammenfassung

Wir verwenden die Theorie metriplektischer dynamischer Systeme, um Relaxationsmethoden zur Berechnung von Lösungen schlecht gestellter Gleichgewichtsprobleme zu konstruieren. Wir schlagen zwei Methodenklassen vor, die vom Landau-Kollisionsoperator inspiriert sind: die kollisions- und die diffusionsähnlichen Operatoren. Diese Ideen werden anhand numerischer Experimente veranschaulicht. Die betrachteten physikalischen Modelle sind die Euler-Gleichungen in Vortizitätsform, die Grad-Shafranov-Gleichung und kräftefreie MHD-Gleichgewichte.

Chapter 1

Introduction

Here we introduce the problem considered in this work, we summarize the main contributions and the outline of the thesis, in Section 1.1, 1.2 and 1.3, respectively.

1.1 Problem statement

Certain physical systems have a multiplicity of equilibrium points, so that the equilibrium conditions for such systems lead to ill-posed problems. Further constraints are needed to select a unique solution, and imposing them is usually not trivial. This is a common problem but it becomes particularly challenging in fusion applications, where the exact computation of general three-dimensional magnetohydrodynamics (MHD) equilibria is of fundamental importance. Despite the many approaches considered in the literature [2, 3, 4, 5, 6, 7, 8, 9, 10, 11, 12, 13, 14], no fully satisfactory solution has been found.

In this work we use the framework of metriplectic dynamics to construct a relaxation method for the computation of solutions of ill-posed equilibrium problems. Metriplectic structures have been proposed by Morrison [15, 16], and later developed by the same author in [17, 18]. We will briefly review metriplectic dynamics and related results in Chapter 2.

We demonstrate the proposed method with the computation of equilibria for Euler's equations, the Grad-Shafranov equation and force-free MHD equilibria.

1.2 Main contributions

Metriplectic dynamical systems are dissipative systems with an evolution equation that can be written as the sum of a conservative Hamiltonian part and a dissipative part, which is described by another algebraic structure: metric brackets.

In this work, we propose two new classes of metric brackets that are used to construct general relaxation methods for the solution of equilibrium problems. We will refer to the first class of metric bracket as collision-like brackets. This is a further generalisation of the brackets proposed by Morrison [15, 17], for the collision operators of Landau [19] and Lenard and Balescu [20, 21]. The second class of metric brackets, which is referred to as diffusion-like brackets, is introduced as an attempt to mitigate the computational cost of collision-like brackets.

The relaxation methods obtained from the metric brackets have been studied by means of three physical test cases: Euler's equations and the Grad-Shafranov equation in two dimensions, and force-free MHD equilibria in three dimensions. For the latter, we find that the classical magnetic relaxation method [22, 13, 23], which can be traced back to the work of Chodura and Schlüter [12], is recovered as a simple special case of diffusion-like brackets.

The second contribution is the development of a structure preserving discretization of the relaxation method with the diffusion-like operator for force-free fields in the framework

of finite element exterior calculus. The numerical scheme is inspired by the work of Hu *et. al.* [24], but its application in the present work appears to be a novel contribution.

Another major contribution is the development of a code for the implementation of these classes of brackets and their application to our physical examples, the `PyMCO` code (Python code for Metric Collision Operators). It is written in Python and its main dependency is the finite element library `FEniCS` [25, 26] (version `2019.1.0`). All test cases have been run with `PyMCO`. Its modularity allows us to easily integrate new physical models and classes of metric operators.

1.3 Outline

In the following, we present an overview of the content of this thesis.

In Chapter 2 we review all the background material on which this work is based. We discuss the considered equilibrium problems in Section 2.1: Euler's equations in vorticity form, the Grad-Shafranov equation, and force-free magnetic fields. The corresponding variational principle formulation is presented in Section 2.2, while the general framework of metriplectic dynamics is reviewed in Section 2.3.

A first relaxation method built with a metric bracket obtained from the scalar product of Lie brackets [27] is presented in Chapter 3. We recall the general theoretical formulation in Section 3.1 and the application to one of the test cases considered in Section 3.2, i.e. Euler's equations. In 3.3 we discuss the structure preserving discretization of the bracket and we conclude in 3.4 with the numerical results. However, the relaxed state depends on the initial and boundary conditions and in general the method does not relax the initial condition to a minimum entropy state.

In Chapter 4 we propose two new classes of metric brackets, the collision-like and diffusion-like bracket, cf. Section 1.2. The original bracket [15, 17], from which they are inspired, is presented in Section 4.1. We discuss the collision-like bracket and how to specialize it to construct the relaxation methods for our physical examples in Section 4.2. Likewise the diffusion-like bracket and its applications can be found in Section 4.3.

In Chapter 5, we discuss the discretization of the equations of motion of the relaxation methods with the collision- and diffusion-like operators for the physical examples of Section 2.1. After introducing some necessary notation in Section 5.1, we present the discretization of the relaxation method with the collision-like bracket for Euler's equations and the Grad-Shafranov equation in Section 5.2 and 5.3 respectively. We discuss in particular the numerical scheme, its properties, computational aspects, and implementation details. In 5.4 and 5.5 we repeat the same for the relaxation methods with the diffusion-like bracket for both Euler's and Grad-Shafranov equations.

In Chapter 6 we present selected numerical experiments (run with the `PyMCO` code) for the cases of Euler's and Grad-Shafranov equations with both the collision- and diffusion-like bracket. We study in particular the relaxation mechanism in different scenarios, varying the entropy function, the initial conditions and the domain mapping. The results of these test cases are in accordance with the properties of the numerical schemes presented in Chapter 5. For the collision-like bracket, the relaxed state of the initial condition is a minimum entropy state. The diffusion-like bracket on the other hand does not completely relax the initial condition to a minimum entropy state, at least in the considered cases. However, such cases are rather special, as we shall see in Chapter 2 and 4.

The novel structure preserving discretization of the magnetic relaxation method for force-free fields is presented in Chapter 7. We discuss the numerical scheme, which is adapted from the one by Hu and co-authors [24], and the relevant numerical properties in Section 7.3. We add computational and implementation remarks in Section 7.4 and 7.5, respectively.

We present a numerical test case for force-free fields with the diffusion-like operator in Chapter 8. The evolution in time of the quantities of interest appears to be in accordance with the properties of the numerical scheme proven in Chapter 7.

In Appendix A we discuss the common setup used to run the experiments for the case of Euler's and Grad-Shafranov equations, and the diagnostics used to analyze the results. We recall some well known results on the eigenvalue problem for the Laplacian in Appendix B.

Chapter 2

Examples of equilibrium problems and metriplectic systems

In this chapter, we first introduce the equilibrium problems we considered in this work in Section 2.1. In Section 2.2 and 2.3 we introduce respectively a variational principle formulation of such problems, and metriplectic dynamics, which is the framework we will use in order to construct relaxation methods for their solution.

2.1 Physical models

The physical models considered for this work are fluid and magnetohydrodynamics problems with relevant plasma physics applications. In particular, we selected the reduced Euler's equations in vorticity form in two dimensions, the Grad-Shafranov equation, and force-free fields. We discuss them in Section 2.1.1, 2.1.2 and 2.1.3, respectively.

2.1.1 Reduced Euler's equations in two-dimensions

Let A be a domain (i.e. an open, non empty, connected set) in $\mathbb{R}^d$, $d = 3$, filled with a fluid. The velocity of a fluid element at time $t \in I \subseteq \mathbb{R}$ and position $x = (x_1, x_2, x_3) \in A$ is described by a vector field $u : I \times A \to \mathbb{R}^d$, which is referred to as the fluid velocity.

If viscosity can be neglected, the fluid is called ideal. In addition, if the flow of the vector field u preserves the volume of a fluid element [28, 29], the fluid is incompressible and, by the Reynold's transport theorem [28], the fluid velocity is divergence free, i.e. $\nabla \cdot u = 0$. The mass density of an incompressible fluid is taken to be constant.

The evolution of the vector field u for an ideal, incompressible fluid without external forces is governed by Euler's equations [28]

$$\frac{\partial u}{\partial t} + (u \cdot \nabla)u = -\nabla p, \qquad \nabla \cdot u = 0, \tag{2.1}$$

where the pressure (per unit mass) $p : I \times A \to \mathbb{R}$ can be viewed as a Lagrange multiplier for the incompressibility constraint. Equation (2.1) is usually complemented with initial and boundary conditions (if ∂A is not empty) for u, thus leading to an initial/boundary value problem [28].

We can write a formally equivalent formulation of Euler's equations in which the pressure gradient does not appear explicitly. With this aim we define the vorticity field, $\xi : I \times A \to \mathbb{R}^d$,

$$\xi = \nabla \times u, \tag{2.2}$$

and take the curl of equation (2.1). The pressure gradient is cancelled because of the identity $\nabla \times \nabla f = 0$, which holds for any scalar function f. One also has the identities

$$(u \cdot \nabla)u = \frac{1}{2}\nabla|u|^2 - u \times \xi, \qquad -\nabla \times (u \times \xi) = (u \cdot \nabla)\xi - (\xi \cdot \nabla)u,$$

where, in the latter, the incompressibility constraint $\nabla \cdot u = 0$ has been accounted for. The right hand side of the second identity is the bilinear operation

$$[v,w] = v \cdot \nabla w - w \cdot \nabla v, \tag{2.3}$$

which defines a Lie-algebra structure on the space of smooth vector fields over the domain A [29]. Physically $[v,w]$ describes the advection of w by the flow of v.

In terms of the Lie brackets 2.3, the vorticity form of Euler's equations for an ideal, incompressible fluid without external forces reads [30]

$$\begin{aligned} \frac{\partial \xi}{\partial t} + [u,\xi] &= 0, \\ \nabla \times u &= \xi, \\ \nabla \cdot u &= 0, \end{aligned} \tag{2.4}$$

completed with boundary conditions for ξ and u, and an initial condition for ξ.

Let D be a domain in $\mathbb{R}^2$. With $A = D \times \mathbb{R}$, we can restrict ourselves to two-dimensional flows,

$$u = (u_1, u_2, 0), \qquad \text{with} \quad u_i = u_i(x_1, x_2), \quad i = 1,2.$$

Then the vorticity from equation (2.2) has one component, that is

$$\xi = (0,0,\omega), \quad \omega = \partial_1 u_2 - \partial_2 u_1, \quad \text{with} \quad \partial_i = \partial / \partial_{x_i}.$$

In view of the incompressibility condition, $\partial_1 u_1 = -\partial_2 u_2$, and if D is simply connected there exists a scalar function $\phi = \phi(t,x_1,x_2)$ such that

$$u_1 = \partial_2 \phi, \qquad u_2 = -\partial_1 \phi.$$

We refer to ϕ as the streaming function.

The scalar vorticity can also be written in terms of ϕ,

$$\omega = \partial_1 u_2 - \partial_2 u_1 = -\partial_1^2 \phi - \partial_2^2 \phi = -\Delta \phi, \tag{2.5}$$

where $\Delta = \partial_1^2 + \partial_2^2$ is the two-dimensional Laplacian. With appropriate boundary conditions for ϕ, equation (2.5) is a Poisson equation which determines ϕ given the vorticity ω.

The evolution equations for the vorticity ω for a two-dimensional incompressible flow are then [18]

$$\begin{aligned} \frac{\partial \omega}{\partial t} + [\omega, \phi] &= 0, \\ -\Delta \phi &= \omega, \end{aligned} \tag{2.6}$$

to be complemented with boundary conditions for ω and ϕ, and an initial condition for ω. The bilinear antisymmetric operator

$$[\chi, \phi] = u \cdot \nabla \chi = (\nabla \chi \times \nabla \phi) \cdot e_3 = \partial_1 \chi \partial_2 \phi - \partial_1 \phi \partial_2 \chi, \tag{2.7}$$

defines a Lie-algebra structure on the space of smooth scalar functions. Physically it describes the advection of a scalar field $\chi = \chi(t,x_1,x_2)$ by the flow of u. Here e_3 is the unit vector in the x_3-direction.

Equilibrium points of equation (2.6) are all time-independent vorticity functions $\omega : D \to \mathbb{R}$ such that

$$[\omega, \phi] = 0, \qquad -\Delta\phi = \omega. \tag{2.8}$$

Even after specifying boundary conditions (when ∂D is non-empty), equations (2.8) have multiple solutions. In order to see this, one can start form the observation that, in the two-dimensional domain D, the map $(x_1, x_2) \mapsto (\omega(x_1, x_2), \phi(x_1, x_2))$ can be regarded as a change of variables with Jacobian determinant [28]

$$[\omega, \phi] = \det \begin{bmatrix} \partial_1\omega & \partial_2\omega \\ \partial_1\phi & \partial_2\phi \end{bmatrix}. \tag{2.9}$$

Therefore the equilibrium condition,

$$[\omega, \phi] = 0, \tag{2.10}$$

is satisfied if and only if ω and ϕ are functionally dependent, which implies there exists a function f such that

$$\omega = f(\phi). \tag{2.11}$$

Upon substituting equation (2.11) into the Poisson equation (2.5) we find a semi-linear elliptic problem for ϕ,

$$-\Delta\phi = f(\phi).$$

On a bounded domain D, we choose homogeneous Dirichlet boundary conditions, leading to the problem

$$\begin{aligned} -\Delta\phi = f(\phi), &\qquad \text{in } D, \\ \phi_{|\partial D} = 0, &\qquad \text{on } \partial D, \end{aligned} \tag{2.12}$$

and let $f \in C^\infty(\mathbb{R})$ for simplicity. This problem is well known [31, Chapter 14, Section 1]. A sufficient condition for the existence of a unique solution in $C^\infty(\overline{D})$ is

$$f'(s) \leq 0, \qquad s \in \mathbb{R}. \tag{2.13}$$

For every choice of $f \in C^\infty(\mathbb{R})$ satisfying condition (2.13) we have a unique equilibrium point

$$\omega = f(\phi),$$

where $\phi \in C^\infty(\overline{D})$ is the unique solution of the semi-linear elliptic problem (2.12).

However, different choices of f may lead to the same equilibrium. For instances,

$$f(0) = 0 \quad \Longrightarrow \quad \phi = 0 \text{ is the solution of (2.12).}$$

Therefore all $f \in C^\infty(\mathbb{R})$, $f'(s) \leq 0$, $f(0) = 0$, yield the same trivial equilibrium.

On the other hand, when f does not satisfy (2.13), the solution may still exist. For instance, when $f(\phi) = a\phi$ for $a \in \mathbb{R}$, we have the unique solution $\phi = 0$ for $a \leq 0$ (since (2.13) is satisfied), while for $a > 0$ ($f'(s) > 0$), problem (2.12) reduces to

$$\begin{aligned} -\Delta\phi = a\phi, &\qquad \text{in } D, \\ \phi_{|\partial D} = 0, &\qquad \text{on } \partial D. \end{aligned}$$

If $\sigma(-\Delta, D) \subset \mathbb{R}^+$ is the spectrum of the operator $-\Delta$ on the bounded domain D with Dirichlet boundary conditions, we have that when $a \notin \sigma(-\Delta, D)$ the only solution is $\phi = 0$, while for $a \in \sigma(-\Delta, D)$, we have a linear space of solutions with dimension given by the multiplicity of the eigenvalue $\lambda = a$.

This example suggests the following reformulation of the problem (2.12):

Find a pair (λ, ϕ), with $\lambda \in \mathbb{R}$, such that

$$\begin{aligned} -\Delta\phi &= \lambda f(\phi), && \text{in } D, \\ \phi_{|\partial D} &= 0, && \text{on } \partial D, \\ \omega &= \lambda f(\phi), && \text{in } D. \end{aligned} \tag{2.14}$$

This is informally referred to as a non-linear eigenvalue problem. Any smooth solution of (2.14) satisfies the equilibrium conditions (2.8).

Among the many solutions of (2.14), for physical reasons, one favors those that minimize the energy of the system,

$$W(\omega) = \frac{1}{2}\|\nabla\phi\|_{L^2}^2 = \lambda \int_D \phi f(\phi) dx \geq 0.$$

For instance, if $f(\phi) = \phi$, then $\lambda > 0$, and the minimum energy eigenvalue is the smallest eigenvalue of $-\Delta$ on the considered domain.

In summary:

- equilibrium conditions (2.8) admit a large family of solutions;
- if a vorticity profile $\omega = f(\phi)$ is prescribed as an additional constraint to (2.8), then we have a unique solution when $f'(s) \leq 0$, but if $f'(s) > 0$ the solution may or may not exist;
- we can relax the problem as in (2.14), which again has multiple solutions.

In this work we propose a method that allows us to compute a solution of (2.8) satisfying $\omega = \lambda f(\phi)$, with minimal energy without directly solving the nonlinear eigenvalue problem (2.14).

Efficient iterative methods to find the minimum-energy solution of (2.14) exist, e.g. [1, pp. 22-23, equations (2.111) and (2.112)]. We study this problem only as a testbed for our method. The proposed method has the advantage that it can be applied to more complicated equilibrium problems on three-dimensional domains, for which a reformulation like equation (2.14) is in general not available.

2.1.2 The Grad-Shafranov equation

Let A be a domain in $\mathbb{R}^3$. Let $B : A \to \mathbb{R}^3$ be the magnetic field, $J : A \to \mathbb{R}^3$ the current density, and $p : A \to \mathbb{R}$ the pressure of the plasma.

The ideal MHD equilibrium equations read [32] (in c.g.s. units)

$$J \times B = c\nabla p, \tag{2.15a}$$

$$\nabla \times B = \frac{4\pi}{c} J, \tag{2.15b}$$

$$\nabla \cdot B = 0. \tag{2.15c}$$

For the specific case of a toroidally symmetric domain, equations (2.15) can be reduced to a nonlinear elliptic eigenvalue problem of the same structure as (2.14).

By toroidally symmetric domain, we mean that $A \subset \mathbb{R}^3$ is the image of the map

$$x = (x_1, x_2, x_3) = (R\cos\varphi, -R\sin\varphi, z),$$

where $(R, z, \varphi) \in D \times [0, 2\pi)$ for $(R, z) \in D \subset \mathbb{R}^2$ such that $\overline{D} \subset \mathbb{R}^+ \times \mathbb{R}$, that is, $R > 0$ in $\overline{D}$.

The domain D is referred to as poloidal domain and (R, z) are the poloidal coordinates.

An axisymmetric solution of (2.15) is a solution in a toroidally symmetric domain A such that all quantities are independent of the toroidal angle φ. Axisymmetric solutions are described by the Grad-Shafranov equation in the two-dimensional, poloidal domain D.

First, we introduce a flux function for the magnetic field B. Since the magnetic field is by construction divergence-free and φ is an ignorable coordinate, we can introduce the

scalar function $\psi = \psi(R,z)$ to represent the poloidal components of the magnetic field B_p, such that

$$B_p = \frac{\nabla\psi}{R} \times e_\varphi, \tag{2.16}$$

where e_φ is the unit vector in the toroidal direction, that is, $e_\varphi = R\nabla\varphi$. In this section, $\nabla = (\partial_1, \partial_2, \partial_3)$, $\partial_j = \partial/\partial x_j$, always denotes the three-dimensional gradient; e.g. $\nabla\psi = \partial_R\psi\nabla R + \partial_z\psi\nabla z$. We refer to the scalar function ψ as the magnetic flux function.

We also introduce the toroidal component of the magnetic field B_φ. This term usually represents the principal contribution to the magnetic field in magnetically confined plasmas. Thus the magnetic field B is

$$B = \frac{B_\varphi}{R} e_\varphi + \frac{\nabla\psi}{R} \times e_\varphi. \tag{2.17}$$

Upon inserting the definition (2.17) in the Ampere's law (2.15b), we find that the magnetic current density is [32]

$$\begin{aligned} \frac{4\pi}{c} J &= \frac{4\pi}{c} J_\varphi e_\varphi + \frac{1}{R}\nabla B_\varphi \times e_\varphi, \\ \frac{4\pi}{c} J_\varphi &= -\frac{1}{R}\Delta^*\psi, \end{aligned} \tag{2.18}$$

where J_φ is the toroidal current and the operator Δ^* is the Grad-Shafranov operator,

$$\Delta^* = R\frac{\partial}{\partial R}\Big(\frac{1}{R}\frac{\partial}{\partial R}\Big) + \frac{\partial^2}{\partial z^2}. \tag{2.19}$$

This form of the current density is readily obtained upon noting that

$$\nabla\psi \times \nabla\varphi = -\partial_R\Big(\frac{1}{R}\partial_R\psi\Big)e_\varphi - \frac{1}{R}\partial_z^2\psi e_\varphi.$$

The last part of the derivation is carried out by analysing the components of the equilibrium equation (2.15a). Multiplying from the left equation (2.15a) by B and J, respectively, and using (2.17) for the magnetic field and (2.18) for the current density yields [32]

$$\begin{aligned} B \cdot \nabla p = 0 &\implies e_\varphi \cdot \Big(\frac{\nabla\psi}{R} \times \nabla p\Big) = 0, \\ J \cdot \nabla p = 0 &\implies e_\varphi \cdot \Big(\nabla B_\varphi \times \nabla p\Big) = 0. \end{aligned}$$

These equations imply that both the pressure p and the toroidal component of the magnetic field B_φ are functions of ψ: there are $P : \mathbb{R} \to \mathbb{R}$ and $F : \mathbb{R} \to \mathbb{R}$ such that

$$p = P(\psi), \qquad B_\varphi = F(\psi).$$

The pressure profile P and the function F are arbitrary smooth functions and additional constraints need to be specified in order to determine them. Finally, (2.15a) reduces to [32]

$$-\Delta^*\psi = 4\pi R^2 \frac{dP(\psi)}{d\psi} + \frac{1}{2}\frac{dF^2(\psi)}{d\psi}, \tag{2.20}$$

which is a second order, nonlinear elliptic partial differential equation describing general axisymmetric toroidal equilibria. It is referred to as the Grad-Shafranov equation [32]. The functions $P(\psi)$ and $F(\psi)$ are arbitrary functions which need to be determined.

We observe that equation (2.20) is formally analogous to (2.14) if we replace the Laplace operator by Δ^*, the stream function ϕ with the flux function ψ, and if we allow the function f to depend on x explicitly. The same considerations apply.

Equation (2.20) can also be relaxed to a non-linear eigenvalue problem

$$\begin{aligned} -\Delta^* \psi = \lambda \Big(4\pi R^2 \frac{dP(\psi)}{d\psi} + \frac{1}{2} \frac{dF^2(\psi)}{d\psi} \Big), \qquad & \text{in } D, \\ \psi_{|\partial\psi} = 0, \qquad & \text{on } \partial D, \\ B_\varphi = F(\psi), \qquad p = P(\psi), \qquad & \text{in } D, \end{aligned} \tag{2.21}$$

Other reformulations of the Grad-Shafranov equation with different constraints are possible [33, 34, 1, and references therein].

As in the case of Euler's equilibria of Section 2.1.1, efficient algorithms for the minimum-energy solution of the Grad-Shafranov eigenvalue problem (2.21) exist [1]. We use this problem as a physically relevant test bed for the relaxation methods developed in this thesis.

2.1.3 Force-free fields

Let $D \subseteq \mathbb{R}^3$ be a domain. In the case of constant pressure, the ideal MHD equilibrium equations (2.15) reduce to

$$(\nabla \times B) \times B = 0, \qquad \nabla \cdot B = 0. \tag{2.22}$$

Solutions of equation (2.22) are referred to as force-free MHD equilibria, since the pressure gradient and the Lorentz force are both zero. Equivalently, equation (2.22) can be written as

$$\begin{aligned} \nabla \times B &= \mu B, \\ B \cdot \nabla \mu &= 0, \\ \nabla \cdot B &= 0. \end{aligned} \tag{2.23}$$

The function μ in general depends on position $x \in D$, i.e. $\mu = \mu(x)$. Solutions of equation (2.23) are referred to as nonlinear Beltrami fields.

If the function $\mu(x)$ is equal to a constant λ, then equation (2.23) reduces to

$$\begin{aligned} \nabla \times B &= \lambda B, \qquad \lambda \in \mathbb{R}, \\ \nabla \cdot B &= 0, \end{aligned} \tag{2.24}$$

and defines divergence-free eigenvectors of the curl operator with suitable boundary conditions. These solutions are referred to as linear Beltrami fields [35] or Woltjer-Taylor relaxed states [36, 37, 38].

For the computation of linear Beltrami fields we can use analytical methods leveraging the fact that the solutions are eigenvectors of the curl operator [39, 40], or variable separation [41]. Linear and nonlinear Beltrami analytical fields can also be constructed with a local representation theorem [42]. For the computation of linear Beltrami fields, we cite the recent boundary integral solver [43, 44]. The solutions of linear Beltrami equations (2.24) is a basic step in the algorithm of the SPEC code [6]. The method of Chodura and Schlüter [12], with zero pressure gradient, appears to have received some attention for space-plasma applications [45, 22]. The classical iterative method by Grad and Rubin [46] has been recently put into a rigorous mathematical framework by Amari *et. al.* [47], that also provides references to results on existence of solutions of (2.23).

In this work, we show that the magnetic relaxation method of Chodura and Schlüter can be recovered as a special case of the proposed class of relaxation methods. Then we derive and test a structure-preserving numerical scheme for the Chodura and Schlüter method, which is the simplest method in the proposed class of methods.

2.2 The variational principle

We introduced in Section 2.1 a collection of equilibrium problems for physical models which are representative of the class of fluid and magnetohydrodynamics systems.

Particular solutions of the equilibrium problems introduced in Section 2.1 can in fact be described as extrema of an entropy functional on a constrained manifold defined by constant energy. Here, we review the general formulation of such variational principles.

Let $D \subset \mathbb{R}^n$ be a domain and let $u : D \to \mathbb{R}^N$ be a field in a space V of functions on the domain D. We shall always assume $V \subseteq L^2(D,\mu)^N$, where μ is a measure of the form $d\mu(x) = m(x)dx$, $m \in C^\infty(\overline{D})$, $m > 0$, and thus μ is absolutely continuous with respect to the Lebesgue measure. If the function $F : V \to \mathbb{R}$ is differentiable at $u \in V$, we can define its functional derivative. Let $\langle \cdot\,,\,\cdot \rangle : W \times V \to \mathbb{R}$ be a non-degenerate pairing [29, pp. 103, Supplement 2.4C] of V with another space of functions W. Then the functional derivative $\delta F(u)/\delta u$ of F at u is the unique element of W, if it exists, such that

$$DF(u)v = \left\langle \frac{\delta F(u)}{\delta u}, v \right\rangle, \qquad \forall\, v \in V,$$

where DF is the Frechet derivative. Unless stated otherwise, we use $W = L^2(D,\mu)^N$ and the pairing is the standard product in $L^2(D,\mu)$ with the given measure μ on D.

We denote respectively by $H = H(u)$ and $S = S(u)$ the energy and entropy functionals of the system. The relevant variational problem is:

Find all $u_e \in V$ such that

$$S(u_e) = \min\{S(u) : u \in V,\, H(u) = H_0\}. \tag{2.25}$$

Upon using the method of Lagrange multipliers, we obtain a necessary condition for (2.25). If u_e satisfies equation (2.25) and functional derivatives of H and S exist, then there is a constant $\lambda \in \mathbb{R}$ such that

$$\frac{\delta S(u_e)}{\delta u} - \lambda \frac{\delta H(u_e)}{\delta u} = 0, \quad H(u_e) = H_0. \tag{2.26}$$

In the following, the variational principle (2.25) is specialized to the physical examples of Section 2.1. Among the solutions of the ill-posed equilibrium problems presented in Section 2.1, the variational principle (2.25) selects a smaller set of equilibrium points. In some cases, the selected equilibrium is unique.

In this work, we are concerned with dynamical systems that are irreversible, that is, they have a preferred direction of time, while conserving a Hamiltonian H. The irreversibility is characterised by a functional S being dissipated along the orbits of the system. Then S can be though of as a Lyapunov function for the dynamics. The direction of time is chosen to be such that S decreases. Following the mathematician convention, we refer to S as entropy. The physicist entropy can be identified with $-S$ and increases monotonically. The conservation of H and the irreversibility with the monotonic behavior of S can be considered the equivalent of the first and second law of thermodynamics, respectively.

2.2.1 Reduced Euler's equations in two-dimensions

Let us study the equilibrium solutions of the 2D ideal incompressible Euler's equations in vorticity form via the variational principle. This example was already discussed by Arnold [48, 49, 50].

Let $u = \omega$ and the energy functional is the fluid kinetic energy per unit mass

$$H(\omega) = \frac{1}{2}\int_D |\nabla\phi|^2\, dx = \frac{1}{2}\int_D \omega\phi\, dx, \qquad -\Delta\phi = \omega, \tag{2.27}$$

where the second identity in the first equation holds because of the Poisson equation, after integrating by parts and provided that the boundary terms do not contribute, e.g. with homogeneous Dirichlet boundary conditions.

We restrict the entropy functional to be of the form

$$S(\omega) = \int_D s(\omega)\, dx, \tag{2.28}$$

where we choose $s = s(\omega)$ as a sufficiently smooth function such that its derivative $\omega \mapsto s'_\omega(\omega)$ is monotonic, i.e., s'_ω has an inverse $(s'_\omega)^{-1}$ on its range. A formulation that allows us to relax this hypothesis on s is currently under investigation.

We compute the functional derivatives of both H and S with respect to the product in $L^2(D)$ so that

$$\frac{\delta H}{\delta \omega} = \phi, \qquad \frac{\delta S}{\delta \omega} = s'_\omega(\omega).$$

Equation (2.26) becomes

$$s'_\omega(\omega) = \lambda\phi,$$

which can be solved for ω explicitly, i.e. if $\lambda\phi$ belongs to the range of s'_ω,

$$\omega = (s'_\omega)^{-1}(\lambda\phi). \tag{2.29}$$

With

$$f = (s'_\omega)^{-1}, \tag{2.30}$$

equations (2.29)-(2.30) with the Poisson equation (2.5) yield

$$-\Delta\phi = f(\lambda\phi). \tag{2.31}$$

Equation (2.31) is a necessary condition for constrained entropy minima and we can see all solutions of (2.31) satisfy the equilibrium condition (2.8) of Section 2.1.1. Among such solutions, those that have minimum entropy (under the assumption that S is bounded from below) satisfy the variational principle (2.25). The variational principle thus restricts the set of possible solutions.

Let us illustrate this by means of specific examples of entropy. If we choose as entropy the enstrophy of the fluid, that is

$$S(\omega) = \frac{1}{2}\int_D \omega^2\, dx, \tag{2.32}$$

following [51], the necessary condition (2.29) reads

$$\omega = \lambda\phi, \tag{2.33}$$

which corresponds to the function f in equation (2.11) being linear. Using the Poisson equation (2.5), equation (2.31) becomes

$$-\Delta\phi = \lambda\phi, \tag{2.34}$$

which is a the eigenvalue problem for the Laplace operator, cf. Appendix B.

The equilibria are the eigenvector-eigenvalue pairs $(\alpha_i\phi_i, \lambda_i)$, where $\alpha_i \in \mathbb{R}\backslash\{0\}$ is a suitable normalization constant, and the index $i \in \mathbb{N}$ labels the solutions. If each ϕ_i can be normalized such that $||\phi_i||_{L^2} = 1$, then the energy constraint amounts to

$$H(\omega) = \frac{\alpha_i}{2}\int_D \omega_i\phi_i dx = \frac{1}{2}\lambda_i\alpha_i^2||\phi_i||_{L^2}^2 = H_0, \qquad \omega_i = \lambda_i\alpha_i\phi_i, \tag{2.35}$$

which allows us to derive an expression for α_i^2,

$$\alpha_i^2 = \frac{2H_0}{\lambda_i}. \tag{2.36}$$

With equation (2.36) we can write the quadratic entropy (2.32) evaluated on the set of solutions satisfying the variational principle, that is,

$$S(\omega) = \frac{1}{2}\lambda_i^2 \alpha_i^2 ||\phi_i||_{L^2}^2 = H_0 \lambda_i, \qquad \omega_i = \lambda_i \alpha_i \phi_i,$$

which is bounded from below because, for the Laplace operator, $\lambda_i > 0$. Thus we see that the solutions of the variational principle in equation (2.25) are the eigenfunctions corresponding to the minimum eigenvalue. Because the sign of α_i is not defined by equation (2.36) and the lowest eigenvalue is usually non-degenerate, the variational principle identifies two possible solutions.

Another choice for S consists in

$$S(\omega) = \int_D \omega \log \omega \, dx, \qquad \omega > 0. \tag{2.37}$$

Then the necessary condition (2.26) reads

$$\omega = C \exp(\lambda \phi), \tag{2.38}$$

where $C = 1/e$. The arbitrary function f in equation (2.11) is exponential. Combining equation (2.38) with the Poisson equation (2.5), we have

$$-\Delta \phi = C \exp(\lambda \phi), \tag{2.39}$$

which is the well known Liouville-Bratu-Gelfand equation [52, 53, 54].

2.2.2 The Grad-Shafranov equation

The standard variational formulation of the Grad-Shafranov equation is written in terms of a Lagrangian density [55, 56], which is not in the form (2.25). With the aim of finding a variational principle in the form of equation (2.25), we introduce the dynamical variable

$$u = \frac{4\pi}{c} R J_\varphi, \tag{2.40}$$

where c is the speed of light in vacuum in c.g.s. units, R is the radial coordinate and J_φ the toroidal current. Then from equation (2.18) we see that with this definition, u is related to the flux function ψ by the linear elliptic operator Δ^*,

$$-\Delta^* \psi = u, \tag{2.41}$$

to be complemented with suitable boundary conditions. Notice that equation (2.41) is analogous to the Poisson equation (2.5) for Euler's equations.

We define the energy of the system as

$$H(u) = \frac{1}{2}\int_D |\nabla \psi|^2 \, R^{-1} dR dz = \frac{1}{2}\int_D u \, \psi \, R^{-1} dR dz, \tag{2.42}$$

where the last equality holds because of equation (2.41), after integrating by parts and provided that boundary terms are zero. In equation (2.42) we introduced the following measure on D,

$$d\mu = R^{-1} dR dz, \tag{2.43}$$

and $R > 0$ in $\overline{D}$, cf. Section 2.1.2.

We restrict the entropy functional to be of the form

$$S(u) = \int_D s(R,u) \, R^{-1} dR dz. \tag{2.44}$$

As in Section 2.2.1, we require s to be smooth and such that $u \mapsto s'_u(R,u)$ is monotonic.

With these choices for the energy and entropy functional, we have

$$\frac{\delta H}{\delta u} = \psi, \qquad \frac{\delta S}{\delta u} = \frac{\partial s(R,u)}{\partial u} = s'_u(R,u),$$

where the functional derivatives are defined with respect to the standard product in $L^2(D,\mu)$ with $d\mu = R^{-1}dRdz$. We note that in general the functional derivative of the entropy may depend on the radial coordinate R.

The necessary condition in equation (2.26) reads

$$s'_u(R,u) = \lambda\,\psi, \tag{2.45}$$

which can be solved for u explicitly if s'_u is monotonic, i.e., if $\lambda\,\psi$ belongs to the range of $s'_u(R,\ \cdot\ )$,

$$u = \big(s'_u(R,\ \cdot\ )\big)^{-1}(\lambda\,\psi). \tag{2.46}$$

We compare equation (2.46) and (2.21) with (2.41) to find again a relation between the function f and the choice of the entropy functional s,

$$f = \big(s'_u(R,\ \cdot\ )\big)^{-1}. \tag{2.47}$$

Equations (2.46)-(2.47) and (2.41) yield

$$-\Delta^\star\psi = f(R,\lambda\,\psi). \tag{2.48}$$

Solution of (2.48) define axisymmetric MHD equilibria with toroidal current given by (2.40) with (2.46). We note that this does not fully determine the profiles P and F of Section 2.2.2.

Among all these equilibria, the variational principle (2.25) selects those with minimal entropy. The choice of the entropy function is used to prescribe the right-hand side of the Grad-Shafranov equation.

Let us illustrate an example of entropy. We choose

$$S(u) = \frac{1}{2}\int_D \frac{u^2}{\mathrm{C}R^2+\mathrm{D}}\,R^{-1}dRdz. \tag{2.49}$$

where C and D are positive constants. Equation (2.26) reads

$$\frac{u}{(\mathrm{C}R^2+\mathrm{D})} = \lambda\,\psi. \tag{2.50}$$

Combining equation (2.50) with (2.41) we have

$$-\Delta^*\psi = \lambda\,(\mathrm{C}R^2+\mathrm{D})\,\psi, \tag{2.51}$$

which is a weighted linear eigenvalue problem. Solutions of equation (2.51) have been obtained by Herrnegger and Maschke [57, 58].

2.2.3 Force-free fields

The variational principle for linear Beltrami fields is already in the form of equation (2.25) [35, 36]. With $u = B$, we choose as "energy" the magnetic helicity,

$$H(B) = \frac{1}{2}\int_D B\cdot A\,dx, \tag{2.52}$$

where $A = A(x)$ is the magnetic vector potential defined as the solution of

$$\nabla\times A = B, \qquad \nabla\cdot A = 0.$$

The entropy functional is

$$S(B) = \frac{1}{2}\int_D |B|^2 \, dx, \tag{2.53}$$

which is proportional to the magnetic energy of the system,

$$W(B) = \frac{1}{8\pi}\|B\|^2_{L^2}.$$

We can compute the functional derivatives with the L^2 pairing,

$$\frac{\delta H}{\delta B} = A, \qquad \frac{\delta S}{\delta B} = B.$$

The necessary condition (2.26) reads

$$B = \lambda A, \quad \text{with } H(B) = H_0,\ \nabla \times A = B,\ \nabla \cdot A = 0, \tag{2.54}$$

and suitable boundary conditions. The solutions in equation (2.54) also satisfy the eigenvalue problem of the curl operator, i.e.

$$\nabla \times A = \lambda A, \quad \nabla \cdot A = 0, \tag{2.55}$$

to be complemented with suitable boundary conditions.

Formally, if we take the curl of equation (2.55), given that λ is a constant, we see that $B = \nabla \times A$ is necessarily a linear Beltrami field.

2.3 Hamiltonian and metriplectic systems

We use the framework of metriplectic dynamics to construct an artificial dynamical system that relaxes a given initial condition to an equilibrium of the considered physical system.

In Section 2.3.1 we briefly recall a few concepts about Hamiltonian dynamics, while in Section 2.3.2 we discuss metriplectic dynamics. Finally, in Section 2.3.3 we present an overview of related works. However, an exhaustive review of these topics is beyond the scope of this Section.

As before, we will not attempt to give a completely rigorous mathematical treatment of the material presented. In fact, to the best of the author's knowledge, for infinite dimensional systems, a mathematically rigorous Hamiltonian formulation is known in a few cases only [59, 60]. Some of the difficulties involved are well described by Kolev [61] for the specific case of hydrodynamics.

2.3.1 Hamiltonian dynamics

A variety of systems can be cast in Hamiltonian form. This not only ensures the possibility to write the governing equations of different physical systems using the same formalism, which is an appealing property by itself, but also possesses practical applications. For instance, symmetries of the Hamiltonian function are directly linked to conservation laws of corresponding dynamical quantities. For computations, the equation of motion can then be discretized preserving, if possible, the Hamiltonian structure, which is usually beneficial for stability and long-time accuracy. Another advantage is the fact that the Hamiltonian structure is intrinsic, that is, it does not depend on the choice of a coordinate system.

The literature regarding Hamiltonian systems is vast. Notable reviews which present Hamiltonian systems with applications to fluid dynamics are the ones by Salmon [62, 63] and Morrison [18].

Here we consider dynamical systems defined on a linear space V, that is, an evolution equation describing the motion of $u(t) \in V$ for $t \in I \subseteq \mathbb{R}$, I being a time interval. In our

application, V is a space of functions on a domain $D \subseteq \mathbb{R}^n$, and the evolution equation amounts to a system of partial differential equations. It is common to denote both the trajectory $u = u(t) \in V$ and a generic point $u \in V$ by the same letter u. This slight abuse of notation simplifies the presentation without too much loss of clarity, and it will be adopted throughout this thesis, unless otherwise specified.

A dynamical system on V is Hamiltonian if the evolution equation is equivalent to

$$\frac{dF(u)}{dt} = \{F,H\}(u), \qquad \forall\, F = F(u), \tag{2.56}$$

where $H : V \to \mathbb{R}$ is a function over V, referred to as the Hamiltonian function, and $\{\,\cdot\,,\,\cdot\,\}$ is a Poisson bracket, that is, a bilinear form over an algebra of functions, including the Hamiltonian H, with the following properties:

(i) it is anti-symmetric;

(ii) it satisfies the Jacobi identity,

$$\{F,\{G,H\}\} + \{H,\{F,G\}\} + \{G,\{H,F\}\} = 0, \qquad \forall\, F,G,H;$$

(iii) it satisfies the Leibniz identity,

$$\{FG,H\} = \{F,H\}G + F\{G,H\}, \qquad \forall\, F,G,H.$$

Conservation of the Hamiltonian is naturally built-in in the anti-symmetry of the Poisson bracket. In fact, anti-symmetry implies that $\{F,F\} = 0$ for all F, and thus

$$\frac{dH}{dt} = \{H,H\} = 0,$$

which follows from (2.56) with $F = H$.

2.3.2 Metriplectic dynamics

The original idea of adding dissipation to a Hamiltonian system by means of an algebraic structure (i.e., a bracket) goes back to the early works of Morrison at the beginning of the eighties [15, 16], with contribution from Kaufman [64, 65]. A later publication from Grmela [66] considered a specific formalism for the Boltzmann equation without the symmetry properties (discussed below) of metriplectic dynamics. It is thanks to the seminal contribution of Morrison [17, 18] that the method reaches its full maturity.

Many physical models have been shown to have a metriplectic structure. For example, the finite-dimensional free rigid body with a suitable chosen torque is a metriplectic system, as described in [18] and Materassi and Morrison [67]. Among infinite-dimensional examples, we recall that the metriplectic brackets for fluid systems with viscosity and thermal production were already introduced by Morrison [16] and later they were introduced also for n-fluid models with chemical reactions by Eldred and Gay-Balmaz [68], for elasticity by Edwards and Besis [69], for resistive MHD by Materassi and Tassi in [70], and for fully extended MHD with a variety of dissipative processes by Coquinot and Morrison [71]. We also mention that the Lindblad equation for open quantum systems is a metriplectic system, as first discussed by Mittnenzweig and Mielke in [72]. Collisional kinetic models can be naturally written as metriplectic systems, among which we recall the metriplectic structure of the Vlasov-Poisson equations with a collision term introduced by Morrison in the seminal work [15, 17].

With the same notation of Section 2.3.1, a dynamical system is metriplectic if the equation of motion can equivalently be written as

$$\frac{dF(u)}{dt} = \big\{F,H\big\}(u) + \big(F,S\big)(u), \qquad \forall\, F = F(u), \tag{2.57}$$

where H is the Hamiltonian function, and S the entropy function. The bracket $\{\,\cdot\,,\,\cdot\,\}$ is a Poisson bracket introduced in Section 2.3.1, while the bracket $(\,\cdot\,,\,\cdot\,)$ is a bilinear form over the considered algebra of functionals, including both H and S, with the properties:

(i) it is symmetric;
(ii) it has a semi-definite sign. We adopt the convention that $(\,\cdot\,,\,\cdot\,)$ is negative semi-definite.

We require the following compatibility conditions, i.e.

$$\{F,S\} = 0, \qquad (F,H) = 0, \qquad \forall\, F = F(u). \tag{2.58}$$

The anti-symmetry and symmetry of the Poisson and symmetric bracket respectively, together with equation (2.58), naturally imply

$$\frac{dH}{dt} = 0, \qquad \frac{dS}{dt} \leq 0, \tag{2.59}$$

that is, the entropy functional is dissipated at constant Hamiltonian. If the entropy is bounded from below, then the system is expected to relax toward an equilibrium state u_e defined by

$$\{F,H\}(u_e) + (F,S)(u_e) = 0, \qquad \forall\, F = F(u), \qquad \text{and } H(u_e) = H_0, \tag{2.60}$$

where H_0 is the initial value of the Hamiltonian. In the following, we discuss the relation between the relaxed states defined by equation (2.60) and those defined by the variational principle (2.25).

If we require the symmetric bracket to satisfy also the Leibniz identity, in addition to being symmetric and with a semi-definite sign, then we can write it in terms of the functional derivatives of its arguments. In this work, we will refer to this type of symmetric bracket as metric bracket. Because by definition also the Poisson bracket satisfies the Leibniz identity, we can write both brackets as

$$\begin{aligned} \{A,B\} &= \int_D \frac{\delta A}{\delta u}(x) J(u) \frac{\delta B}{\delta u}(x)\, d\mu(x), \\ (A,B) &= -\int_D \frac{\delta A}{\delta u}(x) K(u) \frac{\delta B}{\delta u}(x)\, d\mu(x), \end{aligned} \tag{2.61}$$

where the functional derivatives are evaluated at the dynamical variable u and computed with respect to the L^2 product with a given measure μ on the domain D. The operators $J(u)$ and $K(u)$ are respectively an anti-symmetric and a symmetric operator, with $K(u)$ being positive semi-definite.

We write the strong form of the evolution equation (2.57) as

$$\frac{\partial u}{\partial t} = J(u)\frac{\delta H}{\delta u} - K(u)\frac{\delta S}{\delta u}. \tag{2.62}$$

We observe that if $u_e \in V$ is a solution of the variational principle (2.25), then it is also an equilibrium point of (2.57) or equivalently (2.62). Upon evaluating equation (2.62) at $u = u_e$ such that equation (2.26) holds, if $\lambda \neq 0$, we have

$$\left[J(u)\frac{\delta H}{\delta u} - K(u)\frac{\delta S}{\delta u}\right]\Big|_{u_e} = \frac{1}{\lambda} J(u)\frac{\delta S}{\delta u} - \lambda K(u)\frac{\delta H}{\delta u} = 0, \qquad \lambda \neq 0,$$

which follows after using the necessary condition (2.26) and the compatibility condition, cf. equation (2.58), which is equivalent to

$$J(u)\frac{\delta S}{\delta u} = 0, \qquad K(u)\frac{\delta H}{\delta u} = 0.$$

However, in general there may exist equilibrium points of (2.57) or (2.62) that are not constrained minima of the entropy. In fact,

$$J(u)\frac{\delta H}{\delta u} - K(u)\frac{\delta S}{\delta u} = 0,$$

does not necessarily imply the condition (2.26).

If the solution of the metriplectic system (2.57) is such that

$$\lim_{t\to\infty} u(t) = u_e, \qquad H(u_e) = H_0,$$

where u_e is a solution of the variational principle, then we say that u has completely relaxed.

Whether complete relaxation is important or not depends on the application. We shall see that for the cases of Euler's equations in two-dimensions, and the Grad-Shafranov equation complete relaxation is desirable since the profiles are encoded in the entropy function. On the other hand, for nonlinear Beltrami fields complete relaxation is not desirable since the solutions of the corresponding variational principle are only linear Beltrami fields.

In this work we will focus on the metric part of equation (2.57) only. Thus equation (2.57) becomes

$$\frac{dF(u)}{dt} = \big(F,S\big)(u), \qquad \forall\, F = F(u), \tag{2.63}$$

with the compatibility condition

$$(F,H) = 0, \qquad \forall\, F = F(u). \tag{2.64}$$

Both equations (2.59) remain valid. Then solutions of (2.26) with both $\lambda \neq 0$ and $\lambda = 0$, are equilibrium points of (2.63).

Equations (2.64) and (2.59) clarify the link with thermodynamics that we introduced in Section 2.2. Upon interpreting the functional S as the entropy, the first equation shows that by construction the metric bracket has a strong formulation of the first law of thermodynamics. Equation (2.59) instead corresponds to the second law of thermodynamics, up to a conventional sign introduced by the choice of the negative semi-definite convention for the metric bracket. We refer to [71] for further details.

For a metric bracket to satisfy (2.64), the functional derivative of the Hamiltonian, $\delta H/\delta u$, must belong to the null space of the operator K defined in equation (2.61). Therefore a metric bracket has a built-in degeneracy, which, in some way, depends on the Hamiltonian H. In [15], Morrison proposed brackets of the form

$$(F,G) = (F,G;H), \tag{2.65}$$

where the dependence on H is made explicit. For any sufficiently regular function H, $(\,\cdot\,,\,\cdot\,;H)$ is a metric bracket satisfying (2.64). In the original formulation [15] the dependence on H was taken to be linear. Later [17] brackets with a quadratic dependence on H have been introduced.

Currently, one can identify two paradigmatic ways to build the necessary degeneracy into the bracket. In the first way one uses projectors [15, 17], while in the second way the metric bracket is constructed from a scalar product and a Lie bracket [17, 73, 27]. We discuss these two paradigms for the cases of a scalar and a vector field.

Let $u : D \to \mathbb{R}$ be a scalar field, $H = H(u)$ a Hamiltonian with sufficiently regular functional derivative $h = \delta H(u)/\delta u$, and $J = J(x)$ a Poisson tensor, that is an anti-symmetric matrix-valued function of $x \in D$ such that the bilinear form on $C^\infty(D)$ given by

$$[f,g] \coloneqq \nabla f \cdot J \nabla g, \tag{2.66}$$

satisfy the Jacobi identity [18]. Then we can introduce the linear operator on $\mathbb{R}^n$ defined by

$$Q_h^\perp = |\nabla h|^2 I - \nabla h \otimes \nabla h, \tag{2.67}$$

which is proportional to the projector onto the plane perpendicular to ∇h. We can see that $Q_h^\perp$ is quadratic in $h = \delta H/\delta u$, and that ∇h belongs to its null space, since

$$Q_h^\perp \nabla h = |\nabla h|^2 \nabla h - \nabla h(\nabla h \cdot \nabla h) = 0. \tag{2.68}$$

The first paradigm of brackets can then be constructed by

$$(F,G;H) = -\int_D \nabla\frac{\delta F}{\delta u} \cdot Q^{\perp}_{\delta H/\delta u}\nabla\frac{\delta G}{\delta u}\,dx, \tag{2.69}$$

which gives a symmetric, negative semi-definite bracket, that satisfies $(F,H;H) = 0 \quad \forall\, F$ due to the perpendicular projection. The bracket in equation (2.69) is quadratic in H.

The second paradigm of brackets can be constructed as a scalar product of two Lie brackets, assuming that the considered Lie algebra is endowed with a scalar product [27]. For the case of the scalar field under consideration, let the Lie bracket be the one defined in (2.66) and let the scalar product be the standard L^2 product. Then we can define the metric bracket [27]

$$(F,G;H) = \int_D \Big[\frac{\delta F}{\delta u},\frac{\delta H}{\delta u}\Big]\Big[\frac{\delta H}{\delta u},\frac{\delta G}{\delta u}\Big]\,dx, \tag{2.70}$$

where $[\,\cdot\,,\,\cdot\,]$ is defined in equation (2.66). Equation (2.70) also defines a symmetric, negative semi-definite bracket, such that $(F,H;H) = 0 \quad \forall\, F$.

In general, equation (2.70) can also be written as

$$(F,G;H) = -\int_D \nabla\frac{\delta F}{\delta u} \cdot Q^{\parallel}_{\delta H/\delta u}\nabla\frac{\delta G}{\delta u}\,dx, \tag{2.71}$$

with

$$Q^{\parallel}_h = X_h \otimes X_h, \tag{2.72}$$

where X_h is the Hamiltonian vector field generated by h, i.e.

$$X_h = J\nabla h.$$

The operator $Q^{\parallel}_h$ is proportional to the projector onto the line $\mathbb{R}X_h$, parallel to the field X_h.

However, we observe that for $n = 2$, equation (2.70) defines the same bracket as equation (2.69). Equation (2.67) can in fact be expanded as

$$Q^{\perp}_h = \begin{pmatrix} \partial_2^2 h & -\partial_2 h\partial_1 h \\ -\partial_2 h\partial_1 h & \partial_1^2 h \end{pmatrix}, \qquad (n=2), \tag{2.73}$$

where $\nabla = (\partial_1,\partial_2)$. Let f and g denote $\delta F/\delta u$ and $\delta G/\delta u$, respectively. Equation (2.69) with (2.73) for $n = 2$ then reads

$$\begin{aligned}(F,G;H) &= -\int_D \big(\partial_1 f\partial_2^2 h\partial_1 g - \partial_1 f\partial_1 h\partial_2 h\partial_2 g - \partial_2 f\partial_1 h\partial_2 h\partial_1 g + \partial_2 f\partial_1^2 h\partial_2 g\big)\,dx \\ &= -\int_D \big(\partial_1 f\partial_2 h - \partial_2 f\partial_1 h\big)\big(\partial_1 h\partial_2 g - \partial_2 h\partial_1 g\big)\,dx,\end{aligned} \tag{2.74}$$

which corresponds to equation (2.70) with the canonical tensor

$$J = J_c = \begin{pmatrix} 0 & 1 \\ -1 & 0 \end{pmatrix}.$$

One should observe, however, that the specific case of a scalar field in two-dimensions is particularly simple since if $D(x) = (D_{ij}(x))$ is a symmetric, positive semi-definite matrix, such that $D(x)\nabla h(x) = 0$ for all $x \in D$, we have the spectral decomposition

$$D(x) = \sum_{i=1,2} \lambda_i(x) e_i(x) e_i(x)^T, \quad \text{pointwise in } x,$$

with eigenvalue-eigenvectors pairs (λ_i, e_i), and

$$e_i(x)^T D(x)\nabla h(x) = \lambda_i(x) e_i(x) \cdot \nabla h(x) = 0, \quad i = 1,2.$$

One of the two eigenvalues must be zero, and the other one must be positive, lest $D = 0$. Let $\lambda_1 = 0$, and $\lambda_2 > 0$, then $e_2 \cdot \nabla h = 0$, which for $n = 2$ implies $\nabla h \propto e_1$. We deduce

$$D(x) = \lambda_2 e_2 e_2^T = \lambda_2 (I - e_1 e_1^T)$$

or, if $\nabla h(x) \neq 0$,

$$D(x) = \frac{\lambda_2(x)}{|\nabla h(x)|^2} \Big(|\nabla h(x)|^2 I - \nabla h(x) \otimes \nabla h(x) \Big),$$

which shows that in two dimensions the condition $D\nabla h = 0$ imposes $D \propto Q_h^\perp$ where $\nabla h \neq 0$. Therefore in two dimensions, modulo a multiplicative factor, there is only one class of metric brackets of the form

$$(F, G; H) = -\int_D \nabla \frac{\delta F}{\delta h} \cdot D \nabla \frac{\delta G}{\delta h} \, dx, \tag{2.75}$$

and they can be written either as the product of Lie brackets or in terms of the projector.

Brackets of the form (2.75) can also be defined in arbitrary dimensions $n \geq 2$, with both (2.69) and (2.70) being special cases of (2.75) obtained for

$$D = Q_h^\perp, \qquad \text{and } D = -J(\nabla h \otimes \nabla h)J = X_h \otimes X_h,$$

respectively. We see that $\dim\ker(X_h \otimes X_h) = n - 1$, while $\dim\ker Q_h^\perp = 1$, hence the two metric brackets can be equal only for $n = 2$. The general form of equation (2.75) will be introduced and discussed in Chapter 4.

Let us now consider $D \subseteq \mathbb{R}^3$ and a vector field $u : D \to \mathbb{R}^3$. Then if $H = H(u)$ is the Hamiltonian, and the derivative $h = \delta H / \delta u$ with respect to the standard L^2 product is a sufficiently regular vector field on $D \subseteq \mathbb{R}^3$, one can consider, for instance, the linear operator

$$\mathrm{Q}_h^\perp = |\nabla \times h|^2 I - (\nabla \times h) \otimes (\nabla \times h), \tag{2.76}$$

so that $\nabla \times h$ belongs to the null space of $\mathrm{Q}_h^\perp$. This operator yields the metric bracket

$$(F, G; H) = -\int_D \Big(\nabla \times \frac{\delta F}{\delta u} \Big) \cdot \mathrm{Q}^\perp_{\delta H / \delta u} \Big(\nabla \times \frac{\delta G}{\delta u} \Big) \, dx, \tag{2.77}$$

which is a symmetric, negative semi-definite bracket, such that $(F, H; H) = 0 \quad \forall F$.

On the other hand, the bilinear operation on vector fields ξ, $\eta : D \to \mathbb{R}^3$ defined by [27]

$$[\xi, \eta] = (\nabla \times \xi) \times (\nabla \times \eta),$$

is antisymmetric and satisfies the Jacobi identity (which follows from the vector-calculus identity $a \times (b \times c) + b \times (c \times a) + c \times (a \times b) = 0$) and thus it is a Lie bracket. Using this Lie bracket with the standard product in $L^2(D, \mathbb{R}^3)$ yields [27, eq. 1.10, pp.9]

$$(F, G; H) = -\int_D \Big[\frac{\delta F}{\delta u}, \frac{\delta H}{\delta u} \Big] \cdot \Big[\frac{\delta G}{\delta u}, \frac{\delta H}{\delta u} \Big] \, dx. \tag{2.78}$$

As for the scalar case, in two-dimensions, by applying well-known vector calculus identities we can show that (2.78) is equivalent to (2.77). In fact, upon using the vector identity $d^T(a^T c I - a c^T) b = (a \times b) \cdot (c \times d)$, which holds for any vector a, b, c, and $d \in \mathbb{R}^3$, we write equation (2.77) with (2.76) as

$$\begin{aligned} (F, G; H) &= -\int_D \Big(\nabla \times \frac{\delta F}{\delta u} \Big) \cdot \Big[\Big| \nabla \times \frac{\delta H}{\delta u} \Big|^2 I - \Big(\nabla \times \frac{\delta H}{\delta u} \Big) \otimes \Big(\nabla \times \frac{\delta H}{\delta u} \Big) \Big] \Big(\nabla \times \frac{\delta G}{\delta u} \Big) \, dx \\ &= -\int_D \Big[\Big(\nabla \times \frac{\delta H}{\delta u} \Big) \times \Big(\nabla \times \frac{\delta F}{\delta u} \Big) \Big] \cdot \Big[\Big(\nabla \times \frac{\delta H}{\delta u} \Big) \times \Big(\nabla \times \frac{\delta G}{\delta u} \Big) \Big] \, dx, \end{aligned} \tag{2.79}$$

which is equivalent to (2.78).

As the examples of a scalar field in two dimensions and of a vector field in three dimensions show, these constructions of metric brackets can in special cases give the same result. In general, however, they are different. The metric brackets for collision operators in kinetic theory of plasmas [17] are examples in which the degeneracy is built-in by a projection. For collision operators, however, the projector is used in a very specific way which is not a special case of (2.75).

In Chapter 3, we shall consider the bracket (2.70). We shall show a numerical example, obtained with a structure-preserving scheme in the framework of mixed finite elements. We shall see that the system relaxes to a valid equilibrium state, but such a relaxed state is not a constrained entropy minimum, that is, the relaxation is not complete in the sense defined above.

In Chapter 4, we propose metric brackets based on the paradigm that involves projection in the same way as for collision operators. Numerical experiments show that these brackets are more efficient in relaxing the state of the system completely toward a constrained entropy minimum.

In an attempt to reduce the computational cost of this class of brackets we also introduce a reduced version of brackets which for a scalar field takes the form of (2.75). In two dimensions this reduces to the case studied in Chapter 3 and therefore adds nothing to the theory of metric brackets, yet the numerical schemes used in the two cases are different and the comparative study is quite insightful. As a special case of this reduced form of the brackets we also obtain equation (2.77) or equivalently (2.78). This bracket is proposed as a way to obtain force-free MHD equilibria with non-trivial magnetic field-line topology. The evolution equation generated by these brackets with magnetic energy as entropy and magnetic helicity as Hamiltonian amounts to the well-known equation of magnetic relaxation [22, 13, 23] which is recovered here as a special case. In Chapter 7 a structure-preserving scheme is proposed for this magnetic-relaxation bracket.

2.3.3 Related work

After the seminal work of Morrison [15, 17, 18], alternative approaches to dissipative dynamics have been studied.

The framework GENERIC (General Equations for Non-Equilibrium Reversible-Irreversible Coupling) stems in particular from the work of Grmela [66] on the Boltzmann equation that lacked the symmetry of the dissipative metric bracket. The method was developed over the past decades and applied to a number of thermomechanical models and solid mechanics. This framework became the same as metriplectic dynamics when the symmetry condition was later adopted. The main references can be found in the works of Grmela and Oettinger [74], Mielke [75, and references therein]. An extensive review about GENERIC has been published by Oettinger [76].

Simulated annealing (SA) is a different dissipation mechanism, alternative to metriplectic dynamics, constructed from the Poisson bracket alone. The evolution equation of simulated annealing reads

$$\frac{\partial u}{\partial t} = J(u)\frac{\delta H}{\delta u} - J(u)K(u)J(u)\frac{\delta H}{\delta u}, \tag{2.80}$$

in strong form. In this framework, the system dissipates the Hamiltonian while preserving all the other invariants. It was originally proposed by Brockett [77] and Vallis, Carnevale and Young [78, 79], with following work by Bloch *et al.* [80, 81] and Shepherd [82]. The original symmetric bracket, used for numerical experiments conducted by Vallis, Carnevale and Young [78, 79], did not have the operator K, which was introduced in Flierl and Morrison [83]. These authors showed that K can provide both smoothing and the imposition of constraints by Dirac's method. Additional related work includes Holm, Putkaradze, Tronci [84] and Brody, Ellis and Holm [85]. With the operator K the method was applied to a number of models in plasma physics: notable examples are from Chikasue and Furukawa [86, 87] for Euler's equations and low-beta reduced MHD (R-MHD). More recently, Furukawa

and Morrison [88] applied the method of simulated annealing for the calculation of 3D equilibrium of ideal, low-beta R-MHD in cylindrical geometry, while in another paper of the same authors and Watanabe and Ichiguchi [89], the method is applied for high-beta reduced MHD equilibria in toroidal geometry.

Finally, Bloch, Morrison and Ratiu [90] present a general class of metriplectic flows arising from antisymmetric triple brackets, as a generalization of the Nambu bracket [91].

Chapter 3

Relaxation via metric double brackets

In this chapter we study numerically an example of evolution with metric brackets constructed as a product of Lie brackets [17, 73, 27]. Particularly, we aim at understanding the potential of these brackets as a relaxation method for the computation of equilibria of a selected physical system, as discussed in Section 2.3. The relaxed state obtained by this method will be compared to the solution of the variational principle (2.25).

We briefly recall the general theory of such metric brackets in Section 3.1 and we discuss its application to Euler's equations in vorticity form in Section 3.2. The structure-preserving discretization is presented in Section 3.3. Finally, the numerical result of a test case is illustrated in Section 3.4. This test case shows that, in general, the final relaxed state is not in accordance with the solution of the variational principle, cf. equation (2.25), yet it is a different equilibrium of the considered physical system.

3.1 Metric double brackets

A metric bracket that depends quadratically on the gradient of the Hamiltonian, designed as a projection to conserve energy for any entropy, was first given in the context of metriplectic dynamics in [17] and subsequently in [73]. An infinite-dimensional quadratic metric bracket, suitable for vortex dynamics, was given by Gay-Balmaz and Holm in [27]. In the context of their work, this bracket is referred to as quadratic Lie-Poisson bracket. However, to avoid confusion with different structures, we will use in this work the name of metric double brackets, which signifies that we regard this structure as a metric counterpart of the double bracket used in the simulated-annealing method [83, 86, 87, 88, 89], cf. Section 2.3.3. We recall that the double bracket used in simulated annealing is not a metric bracket.

Let the dynamical variable take values in a space of scalar fields $u : D \to \mathbb{R}$ on a domain $D \subseteq \mathbb{R}^n$. The metric double bracket is a symmetric bilinear form on the space of functionals of u given, for any two functionals $F = F(u)$ and $G = G(u)$, by

$$(F,G) = \int_D \left[\frac{\delta F}{\delta u}, \frac{\delta H}{\delta u}\right]\left[\frac{\delta H}{\delta u}, \frac{\delta G}{\delta u}\right] dx, \tag{3.1}$$

where $[\,\cdot\,,\,\cdot\,]$ is the canonical Lie bracket introduced in equation (2.7) and H is the Hamiltonian functional. The Lie bracket of the finite dimensional case introduced in [17] is that for $SO(3)$. One should note that $(\,\cdot\,,\,\cdot\,)$ depends quadratically on the fixed Hamiltonian H, as discussed in Section 2.3.2.

The metric double bracket of equation (3.1) is indeed a metric bracket according to the definition of Section 2.3, i.e.

(i) it is symmetric, i.e. $(F,G) = (G,F)$;

(ii) it preserves the Hamiltonian H, i.e.

$$(H,G) = 0 \qquad \forall\, G = G(u);$$

(iii) it is negative semi-definite, i.e.

$$(F,F) \leq 0 \qquad \forall\, F = F(u).$$

Upon integrating equation (3.1) by parts we formally obtain

$$(F,G) = \int_D \frac{\delta F}{\delta u}\Big[\frac{\delta H}{\delta u}, \Big[\frac{\delta H}{\delta u}, \frac{\delta G}{\delta u}\Big]\Big] dx, \tag{3.2}$$

where we assume that, when D is bounded, the boundary conditions are such that the boundary terms coming from the integration by parts are zero.

With a given choice of an entropy functional $S = S(u)$, the bracket (3.1) generates the equation of motion for $u = u(t) = u(t,x)$,

$$\frac{dF}{dt} = (F,S), \qquad \forall\, F = F(u). \tag{3.3}$$

The strong form of the evolution equation follows from equation (3.2) and reads

$$\frac{\partial u}{\partial t} = \Big[\frac{\delta H}{\delta u}, \Big[\frac{\delta H}{\delta u}, \frac{\delta S}{\delta u}\Big]\Big], \tag{3.4}$$

to be complemented with suitable boundary and initial conditions for u. We note that equation (3.4) has the same structure as the Lindblad equation for open quantum systems [72], and reduces to the Fokker-Planck equation on phase-space when the functional derivative of H with respect to u is linear and $[\,\cdot\,,\,\cdot\,]$ is the canonical Lie bracket of equation (2.7).

The form of (3.4) justifies the name "metric double bracket".

3.2 Application to the Euler's equation

We use the metric double bracket of equation (3.1) to construct general relaxation methods for the calculation of the equilibria of Euler's equations in vorticity form.

For equilibria of Euler's equations, the dynamical variable is identified with the scalar vorticity, $u = \omega$, and it is related to its scalar potential ϕ via the Poisson equation (2.5). The Hamiltonian functional is given in equation (2.27); its functional derivative with respect to the dynamical variable ω reads

$$\frac{\delta H}{\delta \omega} = \phi. \tag{3.5}$$

We assume that the entropy functional can be written in the form (2.28), and therefore its functional derivative with respect to ω is

$$\frac{\delta S(\omega)}{\delta \omega} = \frac{ds(\omega)}{d\omega} = s'_\omega(\omega). \tag{3.6}$$

Upon using equation (3.5) and (3.6) we can write the metric double bracket in equation (3.1) with $G = S$, the entropy functional, as

$$(F,S) = \int_D \Big[\frac{\delta F}{\delta \omega}, \phi\Big]\Big[\phi, s'_\omega(\omega)\Big] dx. \tag{3.7}$$

Likewise we can insert equation (3.5) and (3.6) in (3.4) to write the evolution equation for ω in the strong form as

$$\frac{\partial \omega}{\partial t} = \big[\phi, [\phi, s'_\omega(\omega)]\big], \qquad \text{with } -\Delta\phi = \omega, \tag{3.8}$$

to be complemented with suitable boundary conditions for ω and ϕ, and an initial condition for ω.

As an example, we choose enstrophy as the entropy functional, i.e.

$$S(\omega) = \frac{1}{2}\int_D \omega^2 \, dx,$$

then $s'(\omega) = \omega$. Equation (3.8) becomes

$$\frac{\partial \omega}{\partial t} = \big[\phi, [\phi, \omega]\big], \qquad \text{with } -\Delta\phi = \omega, \tag{3.9}$$

to be complemented with boundary and initial conditions.

3.3 Discretization

We discuss the discretization of the equation of motion arising from the application of the metric double bracket to Euler's equations.

The full problem (including boundary conditions) is defined in Section 3.3.1. The necessary notation and the numerical scheme are discussed in Sections 3.3.2 and 3.3.3, respectively. We discuss the computational aspects and implementation issues in Section 3.3.5 and 3.3.6.

3.3.1 Formulation of the continuous problem

The equation of motion generated by the metric bracket in equation (3.1) is already in a weak form. Then we can write the evolution equation (3.3) explicitly in the weak form upon choosing F in equation (3.7) as

$$F(\omega) = \int_D \omega\alpha \, dx,$$

where $\alpha = \alpha(x)$ is a test function. The evolution equation, cf. equation (3.3) with (3.7), reads

$$\Big(\frac{\partial \omega}{\partial t}, \alpha\Big) = ([\alpha, \phi], [\phi, \omega]), \qquad \forall\, \alpha = \alpha(x), \tag{3.10a}$$

$$(\nabla\phi, \gamma) = (\tilde{u}, \gamma), \qquad \forall\, \gamma = \gamma(x), \tag{3.10b}$$

$$-(\nabla \cdot \tilde{u}, \eta) = (\omega, \eta), \qquad \forall\, \eta = \eta(x), \tag{3.10c}$$

$$\omega_{|\partial D} = 0, \qquad \phi_{|\partial D} = 0, \qquad \text{on } \partial D, \tag{3.10d}$$

where we introduced the flux $\tilde{u} = \nabla\phi$ to write the Poisson equation in a mixed formulation [92].

3.3.2 Notation

Let $\Omega \subset \mathbb{R}^2$ be a polygonal domain and let $\partial\Omega$ denote its boundary. We discretize the domain Ω via finite elements with a shape regular and uniform triangulation denoted by $\mathbb{T}_h$.

With grad $= \nabla$ and div $= \nabla\cdot$ viewed as unbounded operators from $L^2(\Omega) \to L^2(\Omega)^3$, and $L^2(\Omega)^3 \to L^2(\Omega)$, respectively, we define the linear sub-spaces

$$H(\text{grad}, \Omega) := \{v \in L^2(\Omega) : \nabla v \in L^2(\Omega)^3\} \subset L^2(\Omega),$$
$$H(\text{div}, \Omega) := \{w \in L^2(\Omega)^3 : \nabla \cdot w \in L^2(\Omega)\} \subset L^2(\Omega)^3.$$

These are the domains of the respective operators, and are Banach spaces with respect to the graph norm of the operator.

The operations, defined for $v \in C^\infty(\overline{\Omega})$, $w \in C^\infty(\overline{\Omega}, \mathbb{R}^3)$,

$$t_{\text{grad}} v = v_{|\partial\Omega}, \qquad t_{\text{div}} w = w \cdot n_{|\partial\Omega},$$

where n is the unit outward normal to $\partial\Omega$, can be extended to continuous linear operators on $H(\text{grad},\Omega)$ and $H(\text{div},\Omega)$, respectively. Then,

$$\begin{aligned} H_0(\text{grad},\Omega) &:= \{v \in H(\text{grad},\Omega) : t_{\text{grad}} v = 0\}, \\ H_0(\text{div},\Omega) &:= \{w \in H(\text{div},\Omega) : t_{\text{div}} w = 0\}. \end{aligned} \tag{3.11}$$

We introduce the following conforming finite element spaces,

$$\begin{aligned} V_h^0 &= \{v \in H_0(\text{grad},\Omega) := H_0^1(\Omega) : v_{|T} \in P_q(T) \ \forall\, T \in \mathbb{T}_h\}, \\ V_h^1 &= \{v \in H_0(\text{div},\Omega) : v_{|T} \in RT_q(T) \ \forall\, T \in \mathbb{T}_h\}, \\ V_h^2 &= \{v \in L^2(\Omega) : v_{|T} \in P_{q-1}(T) \ \forall\, T \in \mathbb{T}_h; v_{|(T\cap\partial\Omega)} = 0\}, \end{aligned} \tag{3.12}$$

where $P_q(T)$, $RT_q(T)$, $P_{q-1}(T)$ are the spaces of Lagrange [93], Raviart-Thomas [94] and discontinuous Lagrange [95, and references therein] polynomials of degree q on a finite element cell $T \in \mathbb{T}_h$. The parameter $h > 0$ in equation (3.12) represents the size of an element in $\mathbb{T}_h$.

Let us denote by v_h^n the numerical approximation of a variable $v \in \{\omega, \phi\}$ at time t_n, $v_h^n \approx v(t_n)$, where $0 = t_0 < t_1 < \ldots t_N$ are discrete points in time and $n = 0, 1, \ldots, N$. Then we define the sequence

$$v_h = (v_h^n)_n,$$

as the discrete numerical approximation of the variable v.

We also introduce a compact notation for the discrete time derivative,

$$\delta v_h^{n+1} = \frac{1}{\Delta t_n}(v_h^{n+1} - v_h^n), \qquad \Delta t_n = t_{n+1} - t_n. \tag{3.13}$$

In the following we use the Crank-Nicolson method for the discretization in time, for which we need to evaluate the variables at the mid-point. Therefore we introduce the additional notation,

$$v_h^{n+1/2} = \frac{1}{2}(v_h^{n+1} + v_h^n). \tag{3.14}$$

3.3.3 Numerical scheme

We look for an approximation of the solution of the system (3.10), such that ω_h^n, $\phi_h^n \in V_h^0$.

To discretize the mixed formulation of the Poisson equation (3.10b)-(3.10c) we introduce the discrete flux $\tilde{u}_h$ and vorticity $\tilde{U}_h$ evaluated at the time step n as

$$\left(\tilde{u}_h^n, \tilde{U}_h^n\right) \in V_h^1 \times V_h^2. \tag{3.15}$$

Because we discretize the strong form of equation (3.10a) we also need an additional auxiliary variable

$$\tilde{\phi}_h^{n+1} \in V_h^0, \tag{3.16}$$

which represents the projection of the Lie bracket onto the space V_h^0. For this purpose we introduce the L^2-orthogonal projectors $\mathbb{P}_i : [L^2(\Omega)]^2 \to V_h^i$ defined by

$$(\mathbb{P}_i u, v_h) = (u, v_h) \qquad \forall\, v_h \in V_h^i, \ i = 0, 1. \tag{3.17}$$

Therefore we define $\tilde{\phi}_h^{n+1}$ in equation (3.16) with (3.17) as

$$\tilde{\phi}_h^{n+1} = \mathbb{P}_0[\phi_h^{n+1/2}, \omega_h^{n+1/2}].$$

Given a discrete initial condition $\omega_h^0 \in V_h^0$, the numerical approximation of the solution at any subsequent point in time is obtained by solving the problem:

Find $(\omega_h^{n+1},\, \phi_h^{n+1},\, \tilde{\phi}_h^{n+1},\, \tilde{u}_h^{n+1},\, \tilde{U}_h^{n+1}) \in (V_h^0)^3 \times V_h^1 \times V_h^2$ such that:

$$(\delta\omega_h^{n+1}, \alpha_h) - \big([\phi_h^{n+1/2}, \tilde{\phi}_h^{n+1}], \alpha_h\big) = 0, \qquad \forall\, \alpha_h \in V_h^0, \tag{3.18a}$$

$$(\tilde{\phi}_h^{n+1}, \beta_h) - \big([\phi_h^{n+1/2}, \omega_h^{n+1/2}], \beta_h\big) = 0, \qquad \forall\, \beta_h \in V_h^0, \tag{3.18b}$$

$$(\nabla\phi_h^{n+1}, \gamma_h) - (\tilde{u}_h^{n+1}, \gamma_h) = 0, \qquad \forall\, \gamma_h \in V_h^1, \tag{3.18c}$$

$$-(\nabla\cdot\, \tilde{u}_h^{n+1}, \eta_h) - (\tilde{U}_h^{n+1}, \eta_h) = 0, \qquad \forall\, \eta_h \in V_h^2, \tag{3.18d}$$

$$(\tilde{U}_h^{n+1}, \chi_h) - (\omega_h^{n+1}, \chi_h) = 0, \qquad \forall\, \chi_h \in V_h^0, \tag{3.18e}$$

where we integrated equation (3.10a) by parts to obtain the strong form, setting the boundary terms to zero according to equation (3.10d).

The numerical scheme (3.18) can be also written with the definition of the L^2-orthogonal projectors, cf. equation (3.17), as

$$\delta\omega_h^{n+1} = \mathbb{P}_0\Big[\phi_h^{n+1/2}, \mathbb{P}_0\big[\phi_h^{n+1/2}, \omega_h^{n+1/2}\big]\Big], \tag{3.19a}$$

$$-\mathbb{P}_0\nabla\cdot\,(\mathbb{P}_1\nabla\phi_h^{n+1}) = \omega_h^{n+1}, \tag{3.19b}$$

where we use the fact that $\nabla\cdot\,\gamma_h \in V_h^2$ for all $\gamma_h \in V_h^1$, hence $\tilde{U}_h^{n+1} = \nabla\cdot\,\tilde{u}_h^{n+1} \in V_h^2$.

3.3.4 Properties of the numerical scheme

The numerical scheme (3.18) satisfies the properties of the metric double bracket discussed in Section 3.1.

Proposition 3.3.1 (Conservation of the discrete energy)**.** If $(\omega_h^{n+1},\, \phi_h^{n+1},\, \tilde{u}_h^{n+1},\, \tilde{U}_h^{n+1},\, \tilde{\phi}_h^{n+1}) \in (V_h^0)^3 \times V_h^1 \times V_h^2$ is a solution of system (3.18), then the discrete energy is preserved, i.e.

$$H(\omega_h^n) = \frac{1}{2}\|\mathbb{P}_1\nabla\phi_h^{n+1}\|^2 = \frac{1}{2}(\omega_h^n, \phi_h^n) = H(\omega_h^0), \qquad \forall\, n \geq 0.$$

Proof. Let us evaluate equation (3.18a) for $\alpha_h = \phi_h^{n+1/2}$. Upon accounting for equation (3.13) and (3.14), the term on the left hand side reads

$$\begin{aligned}(\delta\omega_h^{n+1}, \phi_n^{n+1/2}) &= \frac{1}{2\Delta t_n}\big(\omega_h^{n+1} - \omega_h^n, \phi_h^{n+1} + \phi_h^n\big) \\ &= \frac{1}{2\,\Delta t_n}\Big[(\phi_h^{n+1},\, \omega_h^{n+1}) - (\phi_h^n,\, \omega_h^n) + (\phi_h^n,\, \omega_h^{n+1}) - (\phi_h^{n+1},\, \omega_h^n)\Big].\end{aligned} \tag{3.20}$$

The last two terms of equation (3.20) cancel each other. In fact, in view of (3.19), we have

$$\begin{aligned}(\omega_h^{n+1}, \phi_h^n) &= -\Big(\mathbb{P}_0\nabla\cdot\,\big(\mathbb{P}_1\nabla\phi_h^{n+1}\big), \phi_h^n\Big) \\ &= -\Big(\nabla\cdot\,\big(\mathbb{P}_1\nabla\phi_h^{n+1}\big), \phi_h^n\Big) \\ &= \big(\mathbb{P}_1\nabla\phi_h^{n+1}, \nabla\phi_h^n\big),\end{aligned}$$

where the first equality holds because $\mathbb{P}_0 v_h^n = v_h^n$ for $v_h^n \in V_h^0$ and the second equality after integrating by parts. The boundary terms are zero, cf. equation (3.12). Then we have that

$$(\omega_h^{n+1}, \phi_h^n) = \big(\mathbb{P}_1\nabla\phi_h^{n+1}, \mathbb{P}_1\nabla\phi_h^n\big),$$

which follows again from the fact that the L^2-orthogonal projector is idempotent.

With the same arguments, we can show that

$$(\omega_h^n, \phi_h^{n+1}) = \big(\mathbb{P}_1 \nabla \phi_h^n, \mathbb{P}_1 \nabla \phi_h^{n+1}\big).$$

Thus the first term of equation (3.18a) reduces to

$$\frac{1}{2\,\Delta t_n}\Big[(\phi_h^{n+1}, \omega_h^{n+1}) - (\phi_h^n, \omega_h^n)\Big] = \frac{1}{\Delta t_n}\big[H(\omega_h^{n+1}) - H(\omega_h^n)\big]. \tag{3.21}$$

Upon evaluating also the second term of equation (3.18a) for $\alpha_h = \phi_h^{n+1/2}$ we have:

$$\big([\phi_h^{n+1/2}, \tilde{\phi}_h^{n+1/2}], \phi_h^{n+1/2}\big) = \big([\phi_h^{n+1/2}, \phi_h^{n+1/2}], \tilde{\phi}_h^{n+1/2}\big) = 0,$$

after integrating by parts, and this is zero because the Lie bracket is anti-symmetric by definition and the boundary terms do not contribute because both ϕ_h and $\tilde{\phi}_h$ are in V_h^0.

Hence the numerical scheme in equation (3.18) preserves the discrete energy. □

Proposition 3.3.2 (Relaxation of the discrete quadratic entropy)**.** If $(\omega_h^{n+1},\ \phi_h^{n+1},\ \tilde{u}_h^{n+1},\ \tilde{U}_h^{n+1},\ \tilde{\phi}_h^{n+1}) \in (V_h^0)^3 \times V_h^1 \times V_h^2$ is a solution of the system (3.18) and the entropy functional is,

$$S(\omega) = \frac{1}{2}\int_\Omega \omega^2\, dx,$$

then

$$S(\omega_h^{n+1}) \leq S(\omega_h^n) \qquad \forall\, n \geq 0.$$

Proof. Let us evaluate equation (3.18a) for $\alpha_h = \omega_h^{n+1/2}$. The first term is

$$(\delta\omega_h^{n+1}, \omega_h^{n+1/2}) = \frac{1}{2\,\Delta t_n}\big(\omega_h^{n+1} - \omega_h^n, \omega_h^{n+1} + \omega_h^n\big) = \frac{1}{\Delta t_n}\big(S(\omega_h^{n+1}) - S(\omega_h^n)\big).$$

The second term of equation (3.18a) evaluated for $\alpha_h = \omega_h^{n+1/2}$ is

$$\begin{aligned}\big([\phi_h^{n+1/2}, \tilde{\phi}_h^{n+1}], \omega_h^{n+1/2}\big) &= \big([\omega_h^{n+1/2}, \phi_h^{n+1/2}], \tilde{\phi}_h^{n+1}\big)\\ &= \big(\mathbb{P}_0[\omega_h^{n+1/2}, \phi_h^{n+1/2}], \tilde{\phi}_h^{n+1}\big)\\ &= -\big(\mathbb{P}_0[\phi_h^{n+1/2}, \omega_h^{n+1/2}], \tilde{\phi}_h^{n+1}\big),\end{aligned}$$

where in the first identity we integrated by parts, while, in the second one, we used the idempotence of the projector $\mathbb{P}_0$. The boundary terms coming from the integration by parts do not contribute.

By choosing the test function β_h in equation (3.18b) as $\mathbb{P}_0[\phi_h^{n+1/2}, \omega_h^{n+1/2}]$, we finally have

$$\big([\phi_h^{n+1/2}, \tilde{\phi}_h^{n+1}], \omega_h^{n+1/2}\big) = -\|\mathbb{P}_0[\phi_h^{n+1/2}, \omega_h^{n+1/2}]\|^2 \leq 0.$$

Hence the numerical scheme in equation (3.18) dissipates a discrete quadratic entropy. □

We stress that for other choices of the entropy functional, this property is not guaranteed by the numerical scheme of equation (3.18).

3.3.5 Computational aspects

For the solution of the nonlinear system (3.18) we use the Newton method and LU decomposition with no preconditioner for the linear system at each Newton step. Additionally, we implemented a procedure to update the time step dynamically during the simulation, according to the number of Newton iterations per time step. Given a fixed relative increment f_{update} and a maximum allowed value for the time step $\Delta t_{\max}$, we either decrease or increase Δt_n by $f_{\text{update}} > 1$ if the number of iterations is above or below two thresholds, $N_{\max}$ and $N_{\min}$, respectively. This mechanism is summarized in Algorithm 1.

The entire time-stepping scheme is summarized in Algorithm 2.

Algorithm 1 Time step update

N_T, total number of time steps
N, number of iterations of the outer loop
$N_{\min}$, $N_{\max}$, minimum and maximum thresholds on the number of iterations
$f_{\text{update}} > 1$, multiplicative factor to update the time step
$\Delta t_{\max}$, maximum allowed value for the time step
while $n \leq N_T$ **do** ▷ Time stepping loop
  Solve the given nonlinear system with Newton method in N iterations
  if $N \leq N_{\min}$ and $\Delta t_n < \Delta t_{\max}$ **then**
    $\Delta t_n \leftarrow \Delta t_n \cdot f_{\text{update}}$
  else if $N > N_{\max}$ **then**
    $\Delta t_n \leftarrow \Delta t_n / f_{\text{update}}$
  end if
end while

Algorithm 2 Time stepping scheme

N_T total number of time steps
ω_h^n, $\phi_h^n \in (V_h^0)^2$, fields at the previous time step n
ω_h^{n+1}, ϕ_h^{n+1}, $\tilde{\phi}_h^{n+1}$, $\tilde{u}_h^{n+1}$, $\tilde{U}_h^{n+1}$, $\in (V_h^0)^3 \times V_h^1 \times V_h^2$, fields at the current time step $n+1$
Initialize $\omega_h^n = \omega_h^0$, at $n = 0$
while $n \leq N_T$ **do** ▷ Time stepping loop
  Solve system (3.18) for ω_h^{n+1}, ϕ_h^{n+1}, $\tilde{\phi}_h^{n+1}$, $\tilde{u}_h^{n+1}$, $\tilde{U}_h^{n+1} \in (V_h^0)^3 \times V_h^1 \times V_h^2$ with Newton and LU decomposition in N iterations
  Update $\omega_h^n \leftarrow \omega_h^{n+1}$
  Update $\phi_h^n \leftarrow \phi_h^{n+1}$
  Update $t \leftarrow t + \Delta t_n$
  Update Δt_n according to the number of Newton iterations, cf. Algorithm 1
end while

3.3.6 Implementation

For the implementation of the numerical scheme in equation in equation (3.18) we use the `FEniCS` finite element library [25, 26]. `FEniCS` provides the discretization of the domain Ω in a triangular mesh, the finite element spaces needed in finite element exterior calculus, and the interface with the numerical linear algebra library `PETSc` [96, 97, 98] and with the `MPI` library [99] for distributed computing.

The Newton method is automatically provided by `FEniCS`, while the LU method is provided by the `PETSc` library directly interfaced via `FEniCS`.

The finite elements spaces in `FEniCS` are denoted $\mathtt{P}_1$, $\mathtt{RT}_1$, $\mathtt{DG}_0$ for the linear Lagrange, linear Raviart-Thomas and Discontinuous Lagrange of oder zero. For visualization purposes, we always use linear Lagrange elements $\mathtt{P}_1$.

3.4 Numerical results

The results of a test case performed with the metric double bracket, cf. Section 3.2, is presented here. We evaluate the results of our experiment with the diagnostics discussed in Appendix A.1 and for reproducibility we adopt the notation of experiment tags described in Appendix A.2. The initial condition of this test case is presented in Appendix A.3.1.

3.4.1 Test case: euler-dlgr

The aim of this test case is to understand whether the metric double bracket relaxes the initial condition to a solution of the variational principle (2.25) according to the choice of the entropy functional.

In Table 3.1 we show the setup for this test case. We use the metric double bracket with a quadratic entropy functional and the initial condition is chosen as an anisotropic Gaussian in a rectangular domain. Also reported are the tolerances of the methods used to solve the nonlinear system (3.18) and the parameters of the procedure to update the time step, cf. Algorithm 1.

Variable	Value
Operator	metric double, equation (3.8)
Entropy	quadratic, $S(\omega) = \frac{1}{2}\int_\Omega \omega^2 dx$, equation (2.32)
Initial condition	Gaussian, equation (A.1), with $\sigma^2_{x_1} = 0.01$, $\sigma^2_{x_2} = 0.07$
Domain	rectangular $\Omega = [0,1]^2$
Boundary condition	Homogeneous Dirichlet
Resolution	64×64
Newton tolerance	atol $= 10^{-14}$, rtol $= 10^{-13}$
Δt_n update, cf. Algorithm 1	$N_{\min} = 3$, $N_{\max} = 6$, $\Delta t_{\max} = 1$, $f_{\text{update}} = 2$

Table 3.1: **Setup of the *euler-dlgr* test case.**

Runtime information for this test case is presented in Table 3.2. These figures are provided to give an hardware agnostic indication of the computational cost of the experiment.

In Figure 3.1 we see the evolution in time of energy and entropy. In (a) we have the relative energy error, while in (b) the entropy. Both figures are in accordance with the properties of the numerical scheme discussed in Section 3.3.4. The error in Figure 3.1(a) depends on the finite precision needed to solve the discrete equations with the Newton method. Entropy in particular is quickly dissipated at the beginning down to a level which is maintained for the rest of the simulation with little or no numerical dissipation.

The relaxed state at the end of the simulation is shown in Figure 3.2. From the color plot in (a) we see that the contours of the dynamical variables are parallel to each other,

Time steps	$\text{Newton}_{\text{avg}}$	$\text{Newton}_{\text{max}}$	dt_i	dt_f
319	1.67	3.0	0.01	1.28

Table 3.2: **Runtime information for the *euler-dlgr* test case.** From left to right, we report the total number of time steps and the average and maximum number of Newton iterations per time step. Also reported are the initial (dt_i) and final (dt_f) values of the time step, which is adapted automatically according to the number of Newton iterations per time step, as discussed in Section 3.3.5.

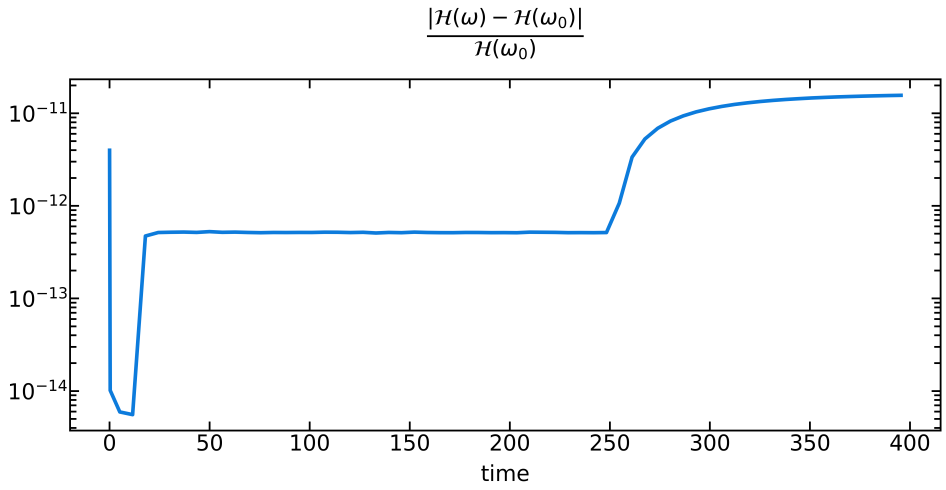

(a) Temporal evolution of the relative energy error.

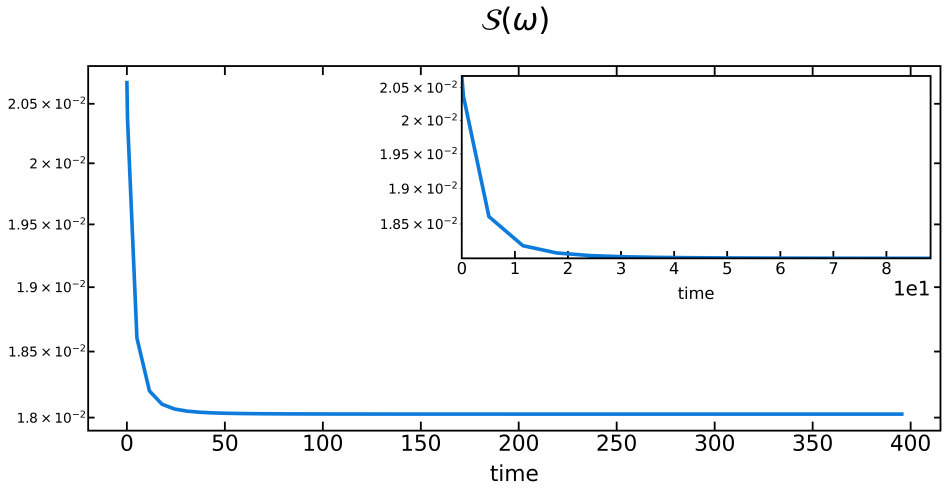

(b) Temporal evolution of the entropy.

Figure 3.1: **Evolution of the test case *euler-dlgr*.** In (a) we see the temporal evolution of the relative energy error (with respect to the initial value) in a semi-logarithmic scale. The error on the energy conservation saturates at 10^{-11}, which is to be attributed to the finite precision with which the equations are solved. In (b) the temporal evolution of the entropy is shown. The inset shows the evolution of the same quantity during the early phase of the experiment.

which suggests that an equilibrium state has been reached. The scatter plot in (b) shows that the functional relation of the relaxed state is different from the solution predicted by the variational principle in equation (2.25) for this choice of the entropy functional. In fact, we find that the relaxed state can be fitted by a cubic functional relation where we expected a linear one, cf. equation (2.33).

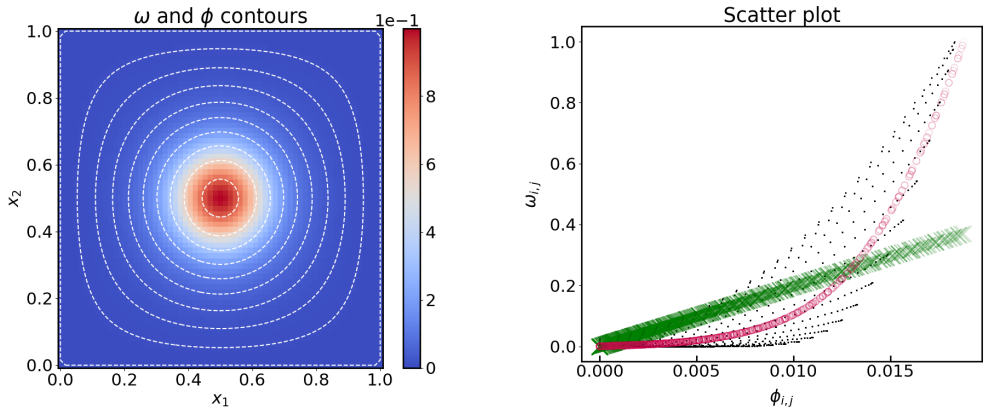

(a) Color plot. (b) Scatter plot.

Figure 3.2: **Relaxed state for the test case *euler-dlgr*.** In (a) we see the color plot of ω and contours of ϕ (in white dashed lines), at the end of the simulation. The colorbar shows the intensity of the vorticity field ω. In (b) we present a comparison between the functional relation of the two variables at the initial time (black dots) and at the final time (red circles), together with the expected relation for the solution of the variational principle (2.25) (green crosses). This type of diagnostic is referred to as scatter plot and it is discussed in detail in Appendix A.1. The discrete values of the variables are well distributed over the plane at the initial time. At equilibrium, the solution has collapsed into a distinguishable functional relation, marked by the red circles. This shows that the relaxed state is an equilibrium of Euler's equations, cf. equation (2.8). However, it is clear from the plot that this functional relation is not in accordance with the solution predicted by the variational principle of equation (2.25).

This test case illustrates that the metric double bracket does not relax the initial condition toward the solution predicted by the variational principle. The final relaxed state is an equilibrium of both the bracket and the considered physical system, but it is not in accordance with the prediction of the variational principle for a fully relaxed state. In fact, the final relaxed state depends on the choice of the initial and boundary conditions, as other test cases show. We note that this feature does not disqualify the relaxed state from being a valid physical equilibrium, but it restricts the number of applications the it can be used for. See also Section 8.5.

This behavior can be understood from equation (2.71) which gives the bracket in terms of the projection onto the direction of the Hamiltonian field X_h. In this case

$$X_h = \begin{pmatrix} 0 & 1 \\ -1 & 0 \end{pmatrix} \nabla\phi = (\partial_2\phi, -\partial_1\phi)$$

is tangent to the contours of ϕ. Hence the bracket tends to diffuse the scalar vorticity along the contours of the potential ϕ only, and little relaxation happens in the perpendicular direction. This qualitative argument can be made rigorous for the case of a fixed potential ϕ, which can be treated analytically.

Chapter 4

Relaxation via collision-like brackets

In this work we propose two distinct classes of metric brackets, with degeneracy built-in by a projection, cf. Section 2.3.2, for the construction of relaxation methods. The first one is a generalization of the Landau operator for Coulomb collisions in plasmas and for this reason we will refer to it as collision-like brackets. This bracket can be simplified to reduce the computational cost of solving the resulting integro-differential equations, leading to a different class of bracket. This is referred to as diffusion-like brackets, because of the similarities with the class of diffusion operators. To the best of the author's knowledge, using these metric brackets to construct relaxation methods appears to be a novel contribution.

In Section 4.1 we present the bracket proposed by Morrison [15, 17] as a generalization of the structure of the Landau collision operator. The two classes of operators proposed in this work are discussed respectively in Section 4.2 and 4.3.

4.1 The metric structure of the Landau operator

In the seminal work of Morrison [15, 17], a symmetric bracket is introduced as a generalization of the structure of the collision operators proposed by Landau [19], and Lenard and Balescu [20, 21].

Let $A \subseteq \mathbb{R}^d$ be a domain (an open, connected, and non empty set), and let $f : A \times \mathbb{R}^d \to \mathbb{R}^+$ be a phase space particle distribution function.

The Landau collision operator [19] reads

$$C(f) = \frac{\partial}{\partial v_i} \cdot \int_D Q_{ij}(v - v') \cdot \Big(f(r,v') \frac{\partial f(r,v)}{\partial v_j} - f(r,v) \frac{\partial f(r,v')}{\partial v'_j} \Big) \, dv', \tag{4.1}$$

where Q_{ij} is the tensor

$$Q_{ij}(\xi) = \frac{\kappa}{|\xi|} \Big(\frac{\delta_{ij} - \xi_i \xi_j}{|\xi|^2} \Big), \qquad \xi \in \mathbb{R}^d,$$

where the constant $\kappa > 0$ is related to the physical collision frequency. Here and throughout this Chapter we will make use of the standard convention for which repeated indices are summed.

The generic form of the negative semi-definite bracket which reproduces the Landau collision operator (4.1) is [15, 17]

$$(F,G) = -\int_D \int_D \Big(\frac{\partial}{\partial v_i} \frac{\delta F}{\delta f}(x) - \frac{\partial}{\partial v_i} \frac{\delta F}{\delta f}(x') \Big) T_{ij}(x,x') \Big(\frac{\partial}{\partial v_j} \frac{\delta G}{\delta f}(x) - \frac{\partial}{\partial v_j} \frac{\delta G}{\delta f}(x') \Big) \, dx' dx, \tag{4.2}$$

where $x = (r,v)$, $x' = (r',v')$, and $F = F(f)$ and $G = G(f)$ are functionals. Unless stated otherwise, the functional derivatives $\delta F/\delta f$ and $\delta G/\delta f$ in equation (4.2) are defined with respect to the L^2 product and evaluated at f. In equation (4.2) the matrix kernel T is [17]

$$T_{ij}(x,x') = \frac{1}{2}M\big(f(x)\big)\,M\big(f(x')\big)w_{ij}(x,x'), \tag{4.3}$$

where M is a positive function defined on an interval of the real line, and w is a $d\times d$ matrix-valued function, symmetric in both the indices, $w_{ij}(x,x') = w_{ji}(x,x')$, and in the arguments, $w_{ij}(x,x') = w_{ij}(x',x)$, and such that $(v_i - v_i')w_{ij}(x,x') = 0$. This, in particular, guarantees the conservation of the energy

$$H(f) = \int_{A\times\mathbb{R}^d} f(r,v)\Big[\frac{v^2}{2} + \phi(r)\Big]\,drdv,$$

with any potential ϕ.

The Landau operator in equation (4.1) is recovered if $M(f) = f$ and the kernel $w_{ij}(x,x')$ is chosen as [15, 17]

$$w_{ij}^{(L)} = \frac{\kappa}{|g|}\Big(\delta_{ij} - \frac{g_i g_j}{|g|^2}\Big)\delta(r-r'), \qquad \text{with } g_i = v_i - v_i', \tag{4.4}$$

where δ_{ij} is the Kronecker delta and $\delta(r-r')$ the Dirac delta. Formally, we allow w_{ij} to be a distribution over $(A\times\mathbb{R}^d)\times(A\times\mathbb{R}^d)$.

4.2 The collision-like bracket

We can further generalize equation (4.2). With reference to the notation of Section 2.3.1, let $D\subseteq\mathbb{R}^n$ be a domain with coordinates $x = (x_1,\dots,x_n)$. The dynamical variable takes values in a linear space V of functions

$$u : D\to\mathbb{R}^k, \qquad k\geq 1,$$

over the domain D. The bracket is defined in terms of

(i) a linear operator

$$L : V\to\tilde{V}, \tag{4.5}$$

where $\tilde{V}$ is another space of functions

$$\tilde{v} : D\to\mathbb{R}^l, \qquad l\geq 1;$$

(ii) a fixed Hamiltonian functional $H = H(u)$, with $\delta H/\delta u\in V$;

(iii) a matrix kernel $w = (w_{ij}(x,x'))_{i,j=1}^{l}$ such that

- it is symmetric as a matrix,

$$w_{ij}(x,x') = w_{ji}(x,x'); \tag{4.6}$$

- it is positive semi-definite,

$$w(x,x')\geq 0,\ \forall\,(x,x'); \tag{4.7}$$

- it is symmetric as a kernel,

$$w_{ij}(x,x') = w_{ij}(x',x),\ \forall\,(i,j); \tag{4.8}$$

- $g_i(x,x')w_{ij}(x,x') = 0$, where

$$g_i(x,x') = L_i\Big(\frac{\delta H}{\delta u}\Big)(x) - L_i\Big(\frac{\delta H}{\delta u}\Big)(x'); \tag{4.9}$$

(iv) a function $M : D \times \mathscr{O} \to \mathbb{R}^+$ with $\mathscr{O} \subseteq \mathbb{R}^k$.
(v) a positive measure μ on D. We always assume $d\mu(x) = m(x)dx$, with $m \in C^\infty(\overline{D})$, $m > 0$ in $\overline{D}$.

Because g defined in equation (4.9) is anti-symmetric, under the change of variable $(x,x') \to (x',x)$, only the symmetric part of the kernel contributes to the bracket, therefore we require w to be also symmetric in its arguments.

As before let

$$T_{ij}(x,x') = \frac{1}{2} M\big(u(x)\big)\, M\big(u(x')\big) w_{ij}(x,x').$$

Then, the generalized collision-like bracket is formally defined at a point $u \in V$ by

$$(F,G) = -\int_D \int_D \Big(L_i\Big(\frac{\delta F}{\delta u}\Big)(x) - L_i\Big(\frac{\delta F}{\delta u}\Big)(x')\Big) T_{ij}(x,x') \Big(L_j\Big(\frac{\delta G}{\delta u}\Big)(x) - L_j\Big(\frac{\delta G}{\delta u}\Big)(x')\Big)\, d\mu(x') d\mu(x), \quad (4.10)$$

for any two functionals $F = F(u)$, $G = G(u)$, for which the expression is well-defined. We shall not attempt to specify either V or the algebra of functionals precisely. Unless stated otherwise, the functional derivatives are evaluated at $u \in V$ and are computed by using as pairing [29, Supplement 2.4C] the product in $L^2(D,\mu)$, with the given measure μ on D. Here and in the following, repeated indices are summed.

The collision-like bracket (4.10) contains as a special case Morrison's metric bracket (4.2) for the Landau collision operator, which is obtained for

- $D = A \times \mathbb{R}^d$, $n = 2d$, $x = (r,v)$;
- $k = 1$, i.e. functions are scalar;
- $u(x) = f(r,v)$;
- $L = \nabla_v$, with $l = d$;
- $H(u) = H(f) = \int_{A\times\mathbb{R}^d} f(r,v)\big[\frac{v^2}{2} + \phi(r)\big]\, drdv$;
- $w = w^{(L)}$, cf. equation (4.4);
- $d\mu = drdv$.

4.2.1 Properties of the collision-like bracket

Let us verify that the bracket introduced in equation (4.10) satisfies the properties discussed in Section 2.3.2.

Proposition 4.2.1. The bracket defined in equation (4.10) satisfies, for any choice of the functionals F and G,

(i) $(F,G) = (G,F)$;
(ii) $(H,F) = 0$;
(iii) $(F,F) \le 0$.

Proof. For every (x,x'), the integrand in equation (4.10) is a symmetric, positive definite quadratic form. (i) Follows immediately from the symmetry of w as a matrix, cf. equation (4.6), and thus of T.

(ii) Holds because $g_i(x,x')w_{ij}(x,x') = 0$.

(iii) Follows from $w(x,x')$ being positive semi-definite, $M > 0$, and $\mu > 0$. □

We recall from equation (2.63), that a metric bracket generates the equation of motion for $u(t) \in V$,

$$\frac{dF}{dt} = (F,S) \qquad \forall\, F = F(u), \quad (4.11)$$

with S the given entropy functional. Then Proposition 4.2.1 implies

$$\frac{dH}{dt} = 0, \qquad \frac{dS}{dt} \le 0.$$

Thus the collision-like bracket dissipates entropy at constant Hamiltonian.

We considered two particular cases of the collision-like brackets, that essentially differ only in the choice of the linear operator L.

4.2.2 The div-grad collision-like bracket

For the specific case of a scalar field $u : D \to \mathbb{R}$, $k = 1$, let

$$L(u) = \nabla u. \tag{4.12}$$

With this choice, equations (4.10) and (4.9) become

$$(F,G) = -\int_D \int_D \left(\nabla \frac{\delta F}{\delta u}(x) - \nabla \frac{\delta F}{\delta u}(x')\right) \cdot T(x,x') \left(\nabla \frac{\delta G}{\delta u}(x) - \nabla \frac{\delta G}{\delta u}(x')\right) d\mu(x') d\mu(x), \tag{4.13a}$$

$$g(x,x') = \nabla \frac{\delta H}{\delta u}(x) - \nabla \frac{\delta H}{\delta u}(x'). \tag{4.13b}$$

As for the choice of the kernel, let

$$w(x,x') = |g(x,x')|^2 I - g(x,x') \otimes g(x,x'), \tag{4.14}$$

where I is the identity matrix. Therefore we construct the kernel from the projector onto the hyperplane perpendicular to $g(x,x')$, cf. Section 2.3.2. Then, the condition $g_i w_{ij} = 0$ is fulfilled. We shall restrict our choice of the entropy functional to

$$S = \int_D s(x,\, u)\, d\mu(x), \tag{4.15}$$

where we allow s to depend on x and u alone, and we require s to be a sufficiently smooth function such that $u \mapsto s'_u(x,\, u)$ is monotonically increasing for all $x \in D$.

Examples of equation (4.15) are

$$S = \int_D u\, dx, \quad S = \int_D u \log u\, dx, \qquad u > 0.$$

More generally, one could also consider functions depending on high-order derivatives, e.g. $s(x,u,Du,D^2u,\ldots,D^nu)$, but (4.15) is sufficient for the envisaged applications.

Following [17] we impose a compatibility condition on the choice of the function M, i.e.

$$M(x,\, u) \frac{\partial^2 s(x,\, u)}{\partial u^2} = M(x,\, u) s''_{uu}(x,\, u) = 1. \tag{4.16}$$

Since we required $s''_{uu} > 0$, then $M(x,u) = 1/s''_{uu}(x,u) > 0$. Equation (4.16) allows us to simplify equation (4.13a). In fact,

$$\begin{aligned} \nabla \frac{\delta S}{\delta u}(x) &= \frac{\partial^2 s}{\partial u^2}(x,\, u) \nabla u(x) + \frac{\partial^2 s}{\partial x \partial u}(x,\, u) \\ &= s''_{uu}(x,\, u) \nabla u(x) + s''_{xu}(x,\, u), \end{aligned} \tag{4.17}$$

which follows from equation (4.15) and the chain rule of calculus.

With the compatibility condition (4.16), and an entropy functional S of the form (4.15), equation (4.13a) becomes

$$\begin{aligned} (F,S) = -\frac{1}{2} \int_D \int_D \left(\nabla \frac{\delta F}{\delta u}(x) - \nabla \frac{\delta F}{\delta u}(x')\right) \cdot w(x,x') \\ \Big(M(x',u(x'))\big(\nabla u(x) + M(x,u(x))\; s''_{xu}(x,u(x))\big) - \\ M(x,u(x))\big(\nabla u(x') + M(x',u(x'))\; s''_{xu}(x',u(x'))\big)\Big)\, d\mu(x') d\mu(x). \end{aligned} \tag{4.18}$$

If we assume that the entropy density $s = s(x,u)$ does not depend on the coordinate x, then the second term on the right-hand side of equation (4.17) is zero and we can write the bracket in equation (4.18) as

$$(F,S) = -\frac{1}{2}\int_D\int_D \Big(\nabla\frac{\delta F}{\delta u}(x) - \nabla\frac{\delta F}{\delta u}(x')\Big)\cdot w(x,x') \Big(M(x',u(x'))\nabla u(x) - M\big(x,u(x)\big)\nabla u(x')\Big)\, d\mu(x')d\mu(x). \quad (4.19)$$

Formally we can integrate by parts in equation (4.18) to obtain

$$(F,S) = \int_D \frac{\delta F}{\delta u}\mathrm{div}_\mu\Big[\int_D w(x,x')\,\Big(M(x',u(x'))\big(\nabla u(x) + M(x,u)\, s''_{xu}(x,u)\big) - M(x,u)\big(\nabla u(x') + M(x',u(x'))\, s''_{xu}(x',u(x'))\big)\Big)d\mu(x')\Big]d\mu(x), \quad (4.20)$$

where, for any vector field $h = h(x)$,

$$\mathrm{div}_\mu h = \frac{1}{m}\nabla\cdot(mh) \quad (4.21)$$

is the divergence operator associated to the measure $d\mu(x) = m(x)dx$, and the boundary terms coming from the integration by parts are zero for a suitable choice of boundary conditions. From equation (4.20) we deduce the strong form of the evolution equation, i.e.

$$\frac{\partial u}{\partial t} = \mathrm{div}_\mu\Big[\mathbb{D}\big[\nabla u + M\big(x,\, u\big)s''_{xu}(x,\, u)\big] - \mathbb{F}M\big(x,\, u\big)\Big], \quad (4.22a)$$

$$\mathbb{D} = \int_D M\big(x',\, u(t,x')\big)w(x,x')\, d\mu(x'), \quad (4.22b)$$

$$\mathbb{F} = \int_D w(x,x')\big[\nabla u(t,x') + M\big(x',\, u(t,x')\big)s''_{xu}(x',\, u(t,x'))\big]\, d\mu(x'), \quad (4.22c)$$

to be complemented with suitable initial and boundary conditions for u. Equation (4.22) is an integro-differential equation of Fokker-Planck type with nonlinear diffusion and friction coefficients given by the integrals $\mathbb{D}$ and $\mathbb{F}$ in equation (4.22b) and (4.22c), respectively.

4.2.3 The curl-curl collision-like bracket

If u is a vector field on a domain $D \subseteq \mathbb{R}^3$ and the linear operator L is the curl operator, i.e.

$$L(u) = \nabla\times u, \quad (4.23)$$

with $u : D \to \mathbb{R}^3$ an arbitrary vector field, then equations (4.10) and (4.9) amount to

$$(F,G) = -\int_D\int_D \Big(\nabla\times\frac{\delta F}{\delta u}(x) - \nabla\times\frac{\delta F}{\delta u}(x')\Big)\cdot T(x,x')\Big(\nabla\times\frac{\delta G}{\delta u}(x) - \nabla\times\frac{\delta G}{\delta u}(x')\Big)\, dx'dx, \quad (4.24a)$$

$$g(x,x') = \nabla\times\frac{\delta H}{\delta u}(x) - \nabla\times\frac{\delta H}{\delta u}(x'), \quad (4.24b)$$

and we choose $d\mu(x) = dx$ in this case.

The kernel w is based on the perpendicular projection as in Section 4.2.2, that is,

$$w = |g(x,x')|^2 I - g(x,x')\otimes g(x,x').$$

Formally we integrate by parts in equation (4.24a) with $G = S$, the entropy functional, to obtain

$$(F,S) = -\int_D \frac{\delta F}{\delta u}(x)\nabla\times\Big[\int_D M\big(x,u(x)\big)M\big(x',u(x')\big)w(x,x') \Big(\nabla\times\frac{\delta S}{\delta u}(x) - \nabla\times\frac{\delta S}{\delta u}(x')\Big)dx'\Big]\, dx, \quad (4.25)$$

where the boundary terms are zero for suitable choices of the boundary conditions. From equation (4.25) the strong form of the evolution equation is

$$\frac{\partial u}{\partial t} = -\nabla \times \Big[M\big(x,\, u\big) \Big(\mathbb{D} \nabla \times \frac{\delta S}{\delta u} - \mathbb{F} \Big) \Big], \tag{4.26a}$$

$$\mathbb{D} = \int_D M\big(x',\, u(t,x')\big)\; w(x,x')\; dx', \tag{4.26b}$$

$$\mathbb{F} = \int_D M\big(x',\, u(t,x')\big) w(x,x') \nabla \times \frac{\delta S}{\delta u}(x')\; dx', \tag{4.26c}$$

with suitable initial and boundary conditions for u. Equation (4.26) is again an integro-differential equation with nonlinear diffusion and friction coefficients $\mathbb{D}$ and $\mathbb{F}$ in equation (4.26b) and (4.26c), respectively.

4.2.4 Applications of the collision-like operator

We apply the collision-like bracket to the construction of relaxation methods for Euler's equations in vorticity form, the Grad-Shafranov equilibria, and force-free fields of Section 2.1.1, 2.1.2 and 2.1.3, respectively.

4.2.4.1 Euler's equations in vorticity form

We consider the domain $D \subseteq \mathbb{R}^2$ and $x = (x_1, x_2)$ as the Cartesian coordinates. On D we choose the measure $d\mu(x) = dx$.

We recall that the Hamiltonian functional H for the two dimensional ideal incompressible Euler's equations is

$$H = \frac{1}{2} \int_D \omega \phi \; dx = \frac{1}{2} \int_D |\nabla \phi|^2 \; dx,$$

where $\omega = \omega(x)$ is the vorticity variable and $\phi = \phi(x)$ is the stream function that satisfies the Poisson equation $-\Delta \phi = \omega$.

The entropy functional is taken of the form

$$S(\omega) = \int_D s(\omega)\; dx,$$

where s is sufficiently smooth and such that $\omega \mapsto s'_\omega(\omega)$ is monotonically increasing.

The functional derivative of H is

$$\frac{\delta H}{\delta \omega} = \phi,$$

computed with respect to the standard L^2 pairing. Therefore, from equation (4.13b), the vector-valued function $g(x,x')$ amounts to

$$g(x,x') = \nabla \phi(x) - \nabla \phi(x'), \tag{4.27}$$

and equation (4.19) becomes

$$(F,S) = -\frac{1}{2} \int_D \int_D \Big(\nabla \frac{\delta F}{\delta \omega}(x) - \nabla \frac{\delta F}{\delta \omega}(x') \Big) \cdot w(x,x') \Big(M(\omega(x')) \nabla \omega(x) - M(\omega(x)) \nabla \omega(x') \Big)\; dx' dx, \tag{4.28}$$

where the function $M\big(\omega(x)\big)$ is determined by the compatibility condition in (4.16) and therefore by the choice of the entropy functional S. The selected general form of entropy does not depend explicitly on the coordinates and therefore the second term of equation (4.17) disappears.

Finally we write system (4.22) for the evolution of the vorticity variable in the strong form as

$$\begin{aligned} &\frac{\partial \omega}{\partial t} = \nabla \cdot [\mathbb{D}\nabla\omega - \mathbb{F}M(\omega)], \\ &\mathbb{D} = \int_D w(x,x')M\big(\omega(t,x')\big)dx', \qquad \mathbb{F} = \int_D w(x,x')\nabla\omega(t,x')dx', \end{aligned} \tag{4.29}$$

to be complemented with suitable initial and boundary conditions for ω as well as boundary conditions for ϕ. In the following we discuss two choices of the entropy functional S, which determine two distinct evolution equations. We will examine these two choices in numerical experiments, cf. Chapter 6.

As a first choice of entropy functional, we consider enstrophy

$$S = \frac{1}{2}\int_D \omega^2\, dx,$$

then $M(\omega) = 1$ and equation (4.29) becomes

$$\begin{aligned} &\frac{\partial \omega}{\partial t} = \nabla \cdot [\mathbb{D}\nabla\omega - \mathbb{F}], \\ &\mathbb{D} = \int_D w(x,x')dx', \qquad \mathbb{F} = \int_D w(x,x')\nabla\omega(t,x')dx'. \end{aligned} \tag{4.30}$$

If instead the entropy functional is chosen as

$$S = \int_D \omega\log\omega\, dx, \qquad \omega > 0,$$

then $M(\omega) = \omega$ and equation (4.29) reads

$$\begin{aligned} &\frac{\partial \omega}{\partial t} = \nabla \cdot [\mathbb{D}\nabla\omega - \mathbb{F}\omega], \\ &\mathbb{D} = \int_D w(x,x')\omega(t,x')dx', \qquad \mathbb{F} = \int_D w(x,x')\nabla\omega(t,x')dx'. \end{aligned} \tag{4.31}$$

4.2.4.2 Grad-Shafranov equation

Let us consider again a two dimensional domain $D \subset \mathbb{R}^2$ such that $\overline{D} \subset \mathbb{R}^+ \times \mathbb{R}$ and $x = (R,z)$ as the radial and axial coordinates of a cylindrical coordinate system (R,z,φ). On D, the measure is $d\mu(R,z) = R^{-1}dRdz$.

The dynamical variable u is defined as

$$u = (4\pi/c)Rj_\varphi, \tag{4.32}$$

where j_φ is the toroidal current density, R is the radial coordinate and c is the speed of light in vacuum (in c.g.s. units), cf. Section 2.2.2. The scalar potential of u is the flux function ψ and it can be defined by solving a linear elliptic problem with homogeneous Dirichlet boundary conditions,

$$-\Delta^*\psi = u, \qquad \psi_{|\partial D} = 0, \tag{4.33}$$

where $\Delta^* = R\partial_R(R^{-1}\partial_R) + \partial_z^2$ is the Grad-Shafranov operator.

The Hamiltonian for the case of the Grad-Shafranov equation reads

$$H = \frac{1}{2}\int_D |\nabla\psi|^2\, R^{-1}dRdz = \frac{1}{2}\int_D \psi\, u\, R^{-1}dRdz, \tag{4.34}$$

and $d\mu(R,z) = R^{-1}dRdz$ is the measure we consider on D. The entropy functional is instead of the form

$$S(u) = \int_D s(R,\, u)\, R^{-1}dRdz,$$

where again we assume that s is sufficiently smooth and such that $u \mapsto s'_u(R,\, u)$ is monotonically increasing.

The functional derivative of H is

$$\frac{\delta H}{\delta u} = \psi, \tag{4.35}$$

computed with respect to the pairing of the L^2 product with the measure $R^{-1}dRdz$. Then the vector-valued function $g(x,x')$ from equation (4.13b) amounts to

$$g(x,x') = \nabla\psi(x) - \nabla\psi(x'), \tag{4.36}$$

where, in this Section, $\nabla = (\partial_R, \partial_z)$. Equation (4.18) becomes

$$\begin{aligned}(F,S) = -\frac{1}{2}\int_D\int_D \Big(\nabla\frac{\delta F}{\delta u}(x) - \nabla\frac{\delta F}{\delta u}(x')\Big)\,\cdot\, w(x,x') \\ \Big(M(R',u(x'))\big(\nabla u(x) + M(R,u(x))\; s''_{Ru}(R,u(x))\nabla R\big) - \\ M(R,u(x))\big(\nabla u(x') + M(R',u(x'))\; s''_{Ru}(R',u(x'))\nabla R\big)\Big)\; d\mu(R',z')d\mu(R,z).\end{aligned} \tag{4.37}$$

where $M = M(R,\, u)$ is chosen according to the compatibility condition (4.16).

The evolution equation in the strong form follows from equation (4.22),

$$\begin{aligned}\frac{\partial u}{\partial t} &= \mathrm{div}_\mu\Big[\mathbb{D}\big[\nabla u + M(R,\, u)\; s''_{Ru}(R,\, u)\nabla R\big] - \mathbb{F}M(R,\, u)\Big], \\ \mathbb{D} &= \int_D M\big(R',u(t,x')\big)w(x,x')\; d\mu(R',z'), \\ \mathbb{F} &= \int_D w(x,x')\big[\nabla u(t,x') + M\big(R',u(t,x')\big)s''_{Ru}(R',\, u(t,x'))\nabla R\big]\; d\mu(R',z'),\end{aligned} \tag{4.38}$$

with suitable boundary and initial conditions. We select the entropy functional as appropriate to obtain specific solutions of the Grad-Shafranov equation. For the Herrnegger-Maschke solutions [57, 58] we choose

$$S(u) = \frac{1}{2}\int_D \frac{u^2}{\mathrm{C}R^2 + \mathrm{D}}\; R^{-1}dRdz, \tag{4.39}$$

where C and D are positive constants. We compute the partial derivative s''_{Ru} of the entropy density as

$$s''_{Ru}(R,\, u) = -\frac{2\mathrm{C}R}{(\mathrm{C}R^2 + \mathrm{D})^2}u, \tag{4.40}$$

while condition (4.16) gives

$$M(R,\, u) = 1/s''_{uu}(R,u) = \mathrm{C}R^2 + \mathrm{D}. \tag{4.41}$$

Then the equation of motion (4.38) becomes

$$\begin{aligned}\frac{\partial u}{\partial t} &= \mathrm{div}_\mu\,\cdot\,\Big[\mathbb{D}\Big(\nabla u - \frac{2\mathrm{C}R}{\mathrm{C}R^2 + \mathrm{D}}u\,\nabla R\Big) - \mathbb{F}(\mathrm{C}R^2 + \mathrm{D})\Big], \\ \mathbb{D} &= \int_D w(x,x')(\mathrm{C}R'^{\,2} + \mathrm{D})\; d\mu(R',z'), \\ \mathbb{F} &= \int_D w(x,x')\Big(\nabla u(t,x') - \frac{2\mathrm{C}R'}{\mathrm{C}R'^{\,2} + \mathrm{D}}u(t,x')\nabla R\Big)\; d\mu(R',z').\end{aligned} \tag{4.42}$$

4.2.4.3 Force-free fields

We consider a domain $D \subseteq \mathbb{R}^3$ and $x = (x_1, x_2, x_3)$ are the Cartesian coordinates in D, with the measure $d\mu(x) = dx$. We consider a vector field $u = B = B(x)$, $\nabla \cdot B = 0$, which physically has the meaning of a magnetic field.

The entropy and Hamiltonian are proportional to the magnetic energy and helicity, respectively,

$$S(B) = \frac{1}{2}\int_D |B|^2\, dx, \qquad H(B) = \frac{1}{2}\int_D B \cdot A\, dx, \tag{4.43}$$

where $A = A(x)$ is the vector potential associated to B, determined by the conditions

$$\nabla \times A = B, \qquad \nabla \cdot A = 0.$$

The functional derivative of H with respect to the dynamical variable B reads

$$\frac{\delta H}{\delta B} = A,$$

computed with the standard L^2 product on D as pairing. The vector-valued function $g(x,x')$ from equation (4.24b) is

$$g(x,x') = \nabla \times A(x) - \nabla \times A(x') = B(x) - B(x'). \tag{4.44}$$

The functional derivative with respect to the dynamical variable B is

$$\frac{\delta S}{\delta B} = B.$$

Thus we write the metric bracket from equation (4.24a) for an arbitrary functional $F = F(u)$ and the chosen entropy functional S as

$$(F,S) = -\frac{1}{2}\int_D\int_D \Big(\nabla \times \frac{\delta F}{\delta B}(x) - \nabla \times \frac{\delta F}{\delta B}(x')\Big) \cdot w(x,x') \Big(\nabla \times B(x) - \nabla \times B(x')\Big)\, dx'dx, \tag{4.45}$$

where $M = 1$, and $d\mu(x) = dx$. The evolution equation for B in the strong form follows from equation (4.26),

$$\begin{aligned} &\frac{\partial B}{\partial t} = -\nabla \times [\mathbb{D}\nabla \times B - \mathbb{F}], \\ &\mathbb{D} = \int_D w(x,x')dx', \qquad \mathbb{F} = \int_D w(x,x')\nabla \times B(t,x')dx', \end{aligned} \tag{4.46}$$

with suitable boundary and initial conditions for B. We observe that equation (4.46) completed with equation (4.44) for g, does not involve the vector potential A, which therefore does not need to be computed.

However, this integro-differential equation is computationally expensive. In order to reduce the computational cost, we introduce the diffusion-like bracket, cf. Section 4.3.

4.3 The diffusion-like bracket

With the same notation as in Section 4.2, the diffusion-like bracket is defined in terms of

(i) the linear operator $L : V \to \tilde{V}$, cf. equation (4.5);

(ii) a fixed Hamiltonian $H = H(u)$, with $\delta H/\delta u \in V$;

(iii) a matrix $\mathsf{D} = \big(\mathsf{D}_{ij}(x)\big)_{i,j}^{l}$ such that

- it is symmetric, positive semi-definite;
- $g_i\, \mathsf{D}_{ij} = 0$, where

$$g_i = L_i\Big(\frac{\delta H}{\delta u}\Big); \tag{4.47}$$

(iv) a positive measure μ on D, such that $d\mu(x) = m(x)dx$, with $m \in C^\infty(\overline{D})$, $m > 0$ in $\overline{D}$.

The diffusion-like bracket is defined by

$$(F,G) = -\int_D L_i\Big(\frac{\delta F}{\delta u}\Big)\mathsf{D}_{ij}\, L_j\Big(\frac{\delta G}{\delta u}\Big)d\mu, \tag{4.48}$$

for any two functionals $F = F(u)$ and $G = G(u)$ for which the expression is well defined. Unless stated otherwise, the functional derivatives are always evaluated at u and computed with respect to the product in $L^2(D,\mu)$. We will omit to write the dependence on the coordinates, when possible. Equation (4.48) generalizes equation (2.75) in Section 2.3.2.

4.3.1 Properties of the diffusion-like bracket

The diffusion-like bracket defined in equation (4.48) is a metric bracket according to the definition of Section 2.3.2.

Proposition 4.3.1. For any choice of the functionals F and G, the bracket in equation (4.48) satisfies:

(i) $(F,G) = (G,F)$;
(ii) $(H,G) = 0$;
(iii) $(F,F) \leq 0$.

Proof. The claims follow from the properties of D as in the proof of Proposition 4.2.1. Specifically the integrand in (4.48) is a positive semi-definite quadratic form.

□

As in Section 4.2.1, we observe that the bracket generates the equation of motion as in equation (4.11) and that Proposition 4.3.1 implies that the diffusion-like bracket dissipates entropy at constant Hamiltonian, i.e.

$$\frac{dH}{dt} = 0, \qquad \frac{dS}{dt} \leq 0.$$

4.3.2 The div-grad diffusion-like bracket

When u is a scalar field, $u : D \to \mathbb{R}$, and $L = \nabla$, equation (4.48) and (4.47) reduce to

$$(F,G) = -\int_D \nabla\frac{\delta F}{\delta u} \cdot \mathsf{D}\,\nabla\frac{\delta G}{\delta u}\, d\mu, \tag{4.49a}$$

$$g = \nabla\Big(\frac{\delta H}{\delta u}\Big). \tag{4.49b}$$

Here the matrix D is chosen as

$$\mathsf{D} = |g|^2 I - g \otimes g, \tag{4.50}$$

which involves the perpendicular projection discussed in Section 2.3.2. If the dimension of the domain is $\dim(D) = n > 2$, other possibilities may be considered. In fact, equation (4.49a) with $d\mu(x) = dx$ is the same bracket introduced in Section 2.3.2, cf. equation (2.75), where we discussed two possible choices of D, one being exactly (4.50) with g as (4.49b) and the other corresponding to the metric double brackets of Chapter 3. In two-dimensions ($n = 2$), equations (4.50) with (4.49b) are the only possibility, modulo a positive factor, as discussed in Section 2.3.2.

We can integrate by parts in equation (4.49a) with $G = S$, for a given entropy functional S, to write

$$(F,S) = \int_D \frac{\delta F}{\delta u}\mathrm{div}_\mu\Big[\mathsf{D}\,\nabla\frac{\delta S}{\delta u}\Big]\, d\mu, \tag{4.51}$$

where boundary terms are zero for suitable choices of the boundary conditions. Equation (4.51) leads to the evolution equation for the field $u(t) \in V$ in the strong form,

$$\frac{\partial u}{\partial t} = \mathrm{div}_\mu \Big[\mathsf{D}\, \nabla \frac{\delta S}{\delta u} \Big]. \tag{4.52}$$

We note that equation (4.52) is a differential equation, unlike the collision-like bracket of Section 4.2.2.

4.3.3 The curl-curl diffusion-like bracket

When u is a vector field over D with $d\mu(x) = dx$, $u : D \to \mathbb{R}^3$, $d = 3$, and $L = \nabla\times$, equation (4.48) and (4.47) read

$$(F,G) = -\int_D dx \left(\nabla \times \frac{\delta F}{\delta u} \right) \cdot \mathsf{D} \left(\nabla \times \frac{\delta G}{\delta u} \right) d\mu, \tag{4.53a}$$

$$g = \nabla \times \frac{\delta H}{\delta u}. \tag{4.53b}$$

The matrix D is chosen as in Section 4.3.2,

$$\mathsf{D} = |g|^2 I - g \otimes g. \tag{4.54}$$

Additionally, we observe that

$$\mathsf{D}h = -g \times (g \times h), \tag{4.55}$$

for all $h \in \mathbb{R}^n$. Equation (4.53a) with $G = S$, for a given entropy functional S, after integrating by parts becomes

$$(F,S) = -\int_D \frac{\delta F}{\delta u} \nabla \times \left[\mathsf{D} \left(\nabla \times \frac{\delta S}{\delta u} \right) \right] dx, \tag{4.56}$$

with suitable boundary conditions such that the boundary terms coming from the integration by parts vanish.

With equation (4.56), the evolution equation for the dynamical variable u in strong form becomes

$$\frac{\partial u}{\partial t} = -\nabla \times \left[\mathsf{D} \left(\nabla \times \frac{\delta S}{\delta u} \right) \right], \tag{4.57}$$

to be complemented with suitable boundary and initial conditions for u. We obtained again a differential rather than integral equation.

4.3.4 Applications of the diffusion-like bracket

As in Section 4.2.4, we apply the diffusion-like bracket to the construction of relaxation methods for the calculation of equilibria of the Euler's equations in vorticity form, Grad-Shafranov equilibria, and force-free fields, introduced in Section 2.1.1, 2.1.2 and 2.1.3, respectively.

4.3.4.1 Euler's equations in vorticity form

Let $D \subseteq \mathbb{R}^2$ be a two-dimensional domain with Cartesian coordinates $x = (x_1, x_2)$, and measure $d\mu(x) = dx$.

Given the Hamiltonian $H = \frac{1}{2} \int_D \omega\, \phi\, dx$, its functional derivative with respect to the vorticity variable is the stream function ϕ. Then, cf. equation (4.47),

$$g = \nabla \phi, \tag{4.58}$$

while the metric bracket in (4.49a) becomes

$$(F,G) = -\int_D \Big(\nabla \frac{\delta F}{\delta \omega} \Big) \cdot \mathsf{D} \left(\nabla \frac{\delta G}{\delta \omega} \right) dx, \tag{4.59}$$

where

$$\mathsf{D} = |\nabla\phi|^2 I - \nabla\phi \otimes \nabla\phi.$$

Modulo a positive factor, this is the only possible choice in two-dimensions ($n = 2$).

The equation of motion in the strong form (4.52) for the vorticity variable ω is

$$\frac{\partial \omega}{\partial t} = \nabla \cdot \Big[\mathsf{D}\,\nabla \frac{\delta S}{\delta \omega}\Big], \tag{4.60}$$

to be complemented with boundary and initial conditions for ω and boundary conditions for ϕ.

We consider two choices of the entropy functional. For $S = \frac{1}{2}\int_D \omega^2\, dx$, equation (4.60) becomes

$$\frac{\partial \omega}{\partial t} = \nabla \cdot \Big[\mathsf{D}\,\nabla\omega\Big]. \tag{4.61}$$

Instead for $S = \int_D \omega \log\omega\, dx$, we have

$$\frac{\partial \omega}{\partial t} = \nabla \cdot \Big[\frac{1}{\omega}\mathsf{D}\nabla\omega\Big], \qquad \omega > 0, \tag{4.62}$$

where we notice the presence of a singularity where $\omega = 0$.

We further observe that, for the choice of D of equation (4.50) with g as in (4.58), the diffusion-like bracket reduces to, as a particular case, to equation (3.1), cf. Section 2.3.2. This bracket is therefore the same tested in Chapter 3, and we already know a special case in which equation (4.60) does not completely relax the initial condition in the sense of Section 2.3.2.

4.3.4.2 The Grad-Shafranov equation

Let us consider a domain $D \subset \mathbb{R}^2$ such that $\overline{D} \subset \mathbb{R}^+ \times \mathbb{R}$ with the coordinates $x = (R,z)$, respectively the radial and axial coordinates of a cylindrical coordinate system (R,z,φ). On D, the measure is $d\mu(R,z) = R^{-1}dRdz$.

The Hamiltonian of the system and its functional derivative with respect to the dynamical variable u are as in equation (4.34) and (4.35) respectively. The vector-valued function g from equation (4.49b) reads

$$g = \nabla\psi, \qquad \nabla = (\partial_R, \partial_z). \tag{4.63}$$

The metric bracket is, cf. equation (4.49a)

$$(F,G) = -\int_D \Big(\nabla\frac{\delta F}{\delta u}\Big) \cdot \mathsf{D}\Big(\nabla\frac{\delta G}{\delta u}\Big)\, R^{-1}dRdz, \tag{4.64}$$

with the matrix D defined as in equation (4.50), and g in equation (4.63).

Finally, the equation of motion for the dynamical variable u in strong form (4.52) reads

$$\frac{\partial u}{\partial t} = \mathrm{div}_\mu\Big[\mathsf{D}(\nabla\psi)\nabla\frac{\delta S}{\delta u}\Big], \tag{4.65}$$

with suitable boundary and initial conditions for u and boundary conditions for ψ.

To obtain the solutions of Hernegger-Maschke [57, 58] we select the entropy functional as in equation (4.39). Then, the functional derivative of equation (4.39) with respect to u is,

$$\frac{\delta S}{\delta u} = \frac{u}{(\mathrm{C}R^2 + \mathrm{D})}, \tag{4.66}$$

computed with the pairing given by the L^2 product again with the measure $d\mu(R,z) = R^{-1}dR\,dz$, and

$$\begin{aligned} \frac{\partial}{\partial R}\frac{\delta S}{\delta u} &= \frac{1}{\mathrm{C}R^2 + \mathrm{D}}\frac{\partial u}{\partial R} - \frac{2R\mathrm{C}}{(\mathrm{C}R^2 + \mathrm{D})^2}u, \\ \frac{\partial}{\partial z}\frac{\delta S}{\delta u} &= \frac{1}{\mathrm{C}R^2 + \mathrm{D}}\frac{\partial u}{\partial z}. \end{aligned} \tag{4.67}$$

Substituting equations (4.67) into (4.65) leads to the equation of motion for this choice of entropy functional.

As in Section 4.3.4.1, we observe that the choice of D is essentially unique since the domain is two-dimensional, as discussed in Section 2.3.2.

4.3.4.3 Force-free fields

Let $D \subseteq \mathbb{R}^3$ be a three-dimensional domain with Cartesian coordinates $x = (x_1, x_2, x_3)$, and $d\mu(x) = dx$.

Entropy and Hamiltonian functions are defined in (4.43). The functional derivative of H is the vector potential A. The vector-valued function g in equation (4.53b) reads

$$g = \nabla \times A = B. \tag{4.68}$$

The functional derivative of S is B. Equation (4.53a) becomes

$$(F,S) = -\int_D \left(\nabla \times \frac{\delta F}{\delta B}\right) \cdot \mathsf{D}\,(\nabla \times B)\, dx, \tag{4.69}$$

where, cf. equation (4.54) and (4.68),

$$\mathsf{D} = |B|^2 I - B \otimes B.$$

The equation of motion in the strong form (4.57) for the dynamical variable B reads

$$\frac{\partial B}{\partial t} = -\nabla \times [\mathsf{D}\, \nabla \times B], \tag{4.70}$$

to be complemented with suitable boundary and initial conditions for B. We observe that, because of the particular choices for the entropy and energy functionals, this formulation does not explicitly involve the vector potential A.

Upon applying standard vector calculus identities, we can write equation (4.70) in a form that is computationally more advantageous. Using the identity (4.55), equation (4.70) reduces to

$$\frac{\partial B}{\partial t} = \nabla \times \Big(B \times \big(B \times (\nabla \times B)\big)\Big), \tag{4.71}$$

which is explicitly a magnetic diffusion equation with a tensorial effective resistivity.

We observe that equation (4.71) is equivalent to Lie-dragging of B by an effective velocity field V, i.e.

$$\partial_t B - \nabla \times (V \times B) = 0, \quad V = (\nabla \times B) \times B. \tag{4.72}$$

Equation (4.72) is the evolution equation in the relaxation method of Chodura and Schlüter [12] specialized to the Beltrami fields. This method is recovered here as a special case of the diffusion-like metric brackets. Moreover, by choosing the kernel as equation (4.54) with g as (4.68), equation (4.69) also reduces to the 3D extension of the metric double bracket [27, eq. 1.10, pp. 9], cf. equation (2.79) in Section 2.3.2.

Chapter 5

Discretization: div-grad brackets in two dimensions

In this Chapter we discuss the discretization of the equations of motion arising from the application of the collision and diffusion-like operators discussed in Section 4.2 and 4.3, respectively, for the cases of Euler's and Grad-Shafranov equilibria.

The common notation used in this Chapter is introduced in Section 5.1. The relaxation method with the collision-like bracket for Euler's and Grad-Shafranov equations are recalled in Section 5.2 and 5.3, respectively. Similarly we discuss the relaxation method with the diffusion-like bracket for the same physical examples in Section 5.4 and 5.5. Finally, remarks on the implementation can be found in Section 5.6.

5.1 Notation

Let $\Omega \subset \mathbb{R}^2$ be a polygonal domain and let $\partial\Omega$ denote its boundary, which is Lipschitz continuous. We discretize the domain Ω via finite elements with a shape regular and uniform triangulation denoted by $\mathbb{T}_h$.

The discrete solution of the considered system is an element of the H^1-conforming finite element space

$$V_h^0 = \{v \in H_0(\text{grad},\Omega) \coloneqq H_0^1(\Omega) : v_{|T} \in P_q(T) \ \forall\, T \in \mathbb{T}_h\}, \tag{5.1}$$

where $H_0(\text{grad},\Omega)$ is as in equation (3.11) and $P_q(T)$ is the space of Lagrange polynomials [93] of degree q on a finite element cell $T \in \mathbb{T}_h$. The parameter $h > 0$ in equation (5.1) represents the size of an element in $\mathbb{T}_h$.

We denote by $u_h^n \approx u(t_n)$ the numerical approximation of the variable u at time t_n, where $0 < t_0 < t_1, \cdots < t_N$ are discrete points in time, $n = 0, 1, \ldots, N$. Then we define the sequence

$$u_h = (u_h^n)_n, \qquad u_h^n \in V_h^0$$

as the discrete numerical approximation of the variable u.

We will also use a compact notation for the discrete time derivative,

$$\delta(u_h)^{n+1} = \frac{1}{\Delta t_n}(u_h^{n+1} - u_h^n), \qquad \Delta t_n = t_{n+1} - t_n. \tag{5.2}$$

In the following, we will always use the Crank-Nicolson method [100] for the discretization in time, which guarantees that quadratic invariants are preserved. For this reason we introduce the average

$$u_h^{n+1/2} = \frac{1}{2}(u_h^{n+1} + u_h^n). \tag{5.3}$$

5.2 Relaxation method with the collision-like bracket for Euler's equations

We recall here the problem from Section 4.3.4.1. The variables ω and ϕ are the vorticity and scalar potential, related through the Poisson equation (2.5) on a bounded domain $\Omega \subset \mathbb{R}^2$.

The entropy functional is of the form

$$S = \int_\Omega s(\omega)\, dx, \tag{5.4}$$

and the function $M(\omega)$ is determined by the compatibility condition defined in equation (4.16).

We derive a suitable weak form for the equation of motion directly from the brackets, cf. equation (4.11). We choose $F = F(\omega)$ as a linear functional, i.e.

$$F(\omega) = \int_\Omega \omega\alpha\, dx,$$

where $\alpha = \alpha(x)$ is a test function. Then equation (4.11) with (4.28), complemented with the Poisson equation and homogeneous Dirichlet boundary conditions reads

$$\big(\partial_t \omega, \alpha\big) = -(\mathbb{D}\nabla\omega - \mathbb{F}M(\omega), \nabla\alpha), \qquad \forall\, \alpha = \alpha(x), \tag{5.5a}$$

$$(\nabla\phi, \nabla\beta) = (\omega, \beta), \qquad \forall\, \beta = \beta(x), \tag{5.5b}$$

$$\omega_{|\partial\Omega} = 0, \qquad \phi_{|\partial\Omega} = 0, \qquad \text{on } \partial\Omega, \tag{5.5c}$$

$$\mathbb{D}(x) = \int_\Omega w(x,x') M\big(\omega(x')\big) dx', \qquad \text{in } \Omega, \tag{5.5d}$$

$$\mathbb{F}(x) = \int_\Omega w(x,x') \nabla\omega(x') dx', \qquad \text{in } \Omega, \tag{5.5e}$$

where in equation (5.5b) we integrated by parts the Poisson equation (2.5), setting the boundary terms to zero because of equation (5.5c). In equation (5.5d) and (5.5e) the diffusive and friction coefficients are defined with the kernel matrix $w(x,x')$ and $g(x,x')$ as in equation (4.14) and (4.27), respectively,

$$w(x,x') = |g(x,x')|^2 I_2 - g(x,x') \otimes g(x,x'),$$
$$g(x,x') = \nabla\phi(x) - \nabla\phi(x'),$$

where I_2 is the identity matrix on $\mathbb{R}^2$. The system (5.5) is to be complemented with initial conditions for ω.

5.2.1 The numerical scheme

We look for a numerical solution of the system (5.5) $(\omega_h^n, \phi_h^n) \in V_h^0 \times V_h^0$, $n \in \{0, \dots, N\}$, where V_h^0 is defined in equation (5.1).

Given a discrete initial condition $\omega_h^0 \in V_h^0$, the numerical approximation of the solution at any subsequent point in time is:

Find $(\omega_h^{n+1}, \phi_h^{n+1}) \in V_h^0 \times V_h^0$ such that

$$(\delta(\omega_h)^{n+1}, \alpha_h) + (\mathbb{D}^{n+1/2}\nabla\omega_h^{n+1/2} - \mathbb{F}^{n+1/2} M(\omega_h^{n+1/2}), \nabla\alpha_h) = 0, \qquad \forall\, \alpha_h \in V_h^0, \tag{5.6a}$$

$$(\nabla\phi_h^{n+1}, \nabla\beta_h) - (\omega_h^{n+1}, \beta_h) = 0, \qquad \forall\, \beta_h \in V_h^0, \tag{5.6b}$$

$$\mathbb{D}^{n+1/2}(x) = \int_\Omega w(x,x') M\big(\omega_h^{n+1/2}(x')\big) dx', \tag{5.6c}$$

$$\mathbb{F}^{n+1/2}(x) = \int_\Omega w(x,x') \nabla\omega_h^{n+1/2}(x') dx', \tag{5.6d}$$

$$w = |g|^2 I - g \otimes g, \qquad g(x,x') = \nabla\phi_h^{n+1/2}(x) - \nabla\phi_h^{n+1/2}(x'). \tag{5.6e}$$

5.2.2 Properties of the numerical scheme

We prove that the numerical scheme in equation (5.6) preserves the properties of the collision-like brackets discussed in Section 4.2.1.

Proposition 5.2.1 (Conservation of the discrete energy)**.** Let $(\omega_h^n,\ \phi_h^n) \in V_h^0 \times V_h^0$ be a solution of the system (5.6). Then the discrete energy is preserved, i.e.

$$H(\omega_h^n) = \frac{1}{2}||\nabla\phi_h^n||^2 = H(\omega_h^0) \quad \forall\, n \geq 0.$$

Proof. With $\alpha_h = \phi_h^{n+1/2}$, the first term in equation (5.6a) reads, cf. equations (5.2) and (5.3),

$$\begin{aligned}(\delta(\omega_h)^{n+1}, \phi_n^{n+1/2}) &= \frac{1}{2\Delta t_n}\big(\omega_h^{n+1} - \omega_h^n,\ \phi_h^{n+1} + \phi_h^n\big) \\ &= \frac{1}{2\,\Delta t_n}\Big[(\phi_h^{n+1},\ \omega_h^{n+1}) - (\phi_h^n,\ \omega_h^n) + (\phi_h^n,\ \omega_h^{n+1}) - (\phi_h^{n+1},\ \omega_h^n)\Big].\end{aligned} \tag{5.7}$$

The last two terms of equation (5.7) cancel each other. In fact, choosing β_h in equation (5.6b) as either ϕ_h^n or ϕ_h^{n+1}, we have

$$(\omega_h^{n+1}, \phi_h^n) = (\nabla\phi_h^{n+1}, \nabla\phi_h^n),$$

and,

$$(\omega_h^n, \phi_h^{n+1}) = (\nabla\phi_h^{n+1}, \nabla\phi_h^n).$$

Thus the first term of equation (5.6a) reduces to

$$\frac{1}{2\,\Delta t_n}\Big[(\phi_h^{n+1}, \omega_h^{n+1}) - (\phi_h^n, \omega_h^n)\Big] = \frac{1}{\Delta t_n}\big[H(\omega_h^{n+1}) - H(\omega_h^n)\big], \tag{5.8}$$

where the last identity follows again from choosing β_h in equation (5.6b) as ϕ_h^{n+1} or ϕ_h^n.

Let us now consider the second term in equation (5.6a) for $\alpha_h = \phi_h^{n+1/2}$. We have

$$(\mathbb{D}^{n+1/2}\nabla\omega_h^{n+1/2} - \mathbb{F}^{n+1/2}M\big(\omega_h^{n+1/2}\big), \nabla\phi_h^{n+1/2}) = -(H,S)(\omega_h^{n+1/2}) = 0, \tag{5.9}$$

where the identity follows directly from the properties of the collision-like bracket in Proposition 4.2.1(ii). □

Proposition 5.2.2 (Relaxation of the quadratic entropy)**.** Let $(\omega_h^n,\ \phi_h^n) \in V_h^0 \times V_h^0$ be a solution of (5.6). If the entropy functional is

$$S(\omega) = \frac{1}{2}\int_\Omega \omega^2\, dx,$$

then

$$S(\omega_h^{n+1}) \leq S(\omega_h^n) \qquad \forall\, n \geq 0.$$

Proof. Let us choose $\alpha_h = \omega_h^{n+1/2}$ in equation (5.6a), so that

$$(\delta(\omega_h)^{n+1}, \omega_h^{n+1/2}) = \frac{1}{2\,\Delta t_n}\big(\omega_h^{n+1} - \omega_h^n,\ \omega_h^{n+1} + \omega_h^n\big) = \frac{1}{\Delta t_n}\big(S(\omega_h^{n+1}) - S(\omega_h^n)\big). \tag{5.10}$$

The second term of equation (5.6a) with $\alpha_h = \omega_h^{n+1/2}$ amounts to

$$(\mathbb{D}^{n+1/2}\nabla\omega_h^{n+1/2} - \mathbb{F}^{n+1/2}M\big(\omega_h^{n+1/2}\big), \nabla\omega_h^{n+1/2}) = -(S,S)(\omega_h^{n+1/2}) \geq 0,$$

where the inequality follows directly from Proposition 4.2.1(iii), where we proved that the collision-like bracket is negative semi-definite by construction. □

5.2.3 Computational aspects

Equation (5.6) cannot be solved directly because it is a system of integro-differential equations. Various approaches are available in the literature for the Landau collision operator, as for example [101, 102, 103]. However, they cannot be easily implemented with the library chosen for the current implementation, cf. Section 5.6. In this work, we choose to solve the system by a Picard iteration scheme to compute the integral nonlinear diffusion and friction coefficients. At each Picard iteration, we are left the solution of a nonlinear advection-diffusion equation, which can be solved with the Newton method. We observe that the remaining non-linearity is due to the function M in equation (5.6a). We solve the linear system for each Newton step with the GMRES method [104] and no preconditioner.

Let us write the Picard iteration scheme. For clarity of notation, we shall denote the variables computed inside the Picard loop with a hat symbol and we shall use the index p for Picard iterations. The initial condition of the Picard loop is set to the value of the variable at the previous time step, i.e. $\hat{\omega}_h^p = \omega_h^n$ and $\hat{\phi}_h^p = \phi_h^n$ for $p = 0$.

With

$$\hat{u}_h^{n,p} = \frac{\hat{u}_h^p + u_h^n}{2},$$

the Picard iteration scheme reads:

- Compute $\hat{\mathbb{D}}^p$ and $\hat{\mathbb{F}}^p$, evaluated at $\hat{\omega}_h^{n,p}$, $\hat{\phi}_h^{n,p}$,

$$\begin{aligned} \hat{\mathbb{D}}^p(x) &= \int_\Omega w(x,x') M\big(\hat{\omega}_h^{n,p}(x')\big) dx', \\ \hat{\mathbb{F}}^p(x) &= \int_\Omega w(x,x') \nabla \hat{\omega}_h^{n,p}(x') dx', \\ w = |g|^2 I - g \otimes g, \qquad & g = \nabla \hat{\phi}_h^{n,p}(x) - \nabla \hat{\phi}_h^{n,p}(x'). \end{aligned} \tag{5.11}$$

- Solve for $(\hat{\omega}_h^{p+1}, \hat{\phi}_h^{p+1}) \in V_h^0 \times V_h^0$ with the Newton method

$$(\hat{\omega}_h^{p+1}, \alpha_h) + \Delta t_n (\hat{\mathbb{D}}^p \nabla \hat{\omega}_h^{n,p+1} - \hat{\mathbb{F}}^p M\big(\hat{\omega}_h^{n,p+1}\big), \nabla \alpha_h) = (\omega_h^n, \alpha_h), \qquad \forall\, \alpha_h \in V_h^0, \tag{5.12a}$$

$$(\nabla \hat{\phi}_h^{p+1}, \nabla \beta_h) - (\hat{\omega}_h^{p+1}, \beta_h) = 0, \qquad \forall\, \beta_h \in V_h^0, \tag{5.12b}$$

  where $\hat{\mathbb{D}}^p$ and $\hat{\mathbb{F}}^p$ are computed according to equation (5.11). Note the term $M\big(\hat{\omega}_h^{n,p+1}\big)$ that introduces the nonlinearity in equation (5.12), which depends on the choice of the entropy functional.

- Verify that the residual of the Picard iterations $\varepsilon^p = \max(\varepsilon_1^p, \varepsilon_2^p)$ is below a certain threshold. The residuals ε_1^p and ε_2^p are computed as

$$\begin{aligned} \varepsilon_1 &= \|\hat{\omega}_h^{p+1} - \hat{\omega}_h^p\|_\infty, \\ \varepsilon_2 &= \|\hat{\phi}_h^{p+1} - \hat{\phi}_h^p\|_\infty, \end{aligned} \tag{5.13}$$

  where $\|\cdot\|_\infty$ is the norm in L^∞, e.g.,

$$\|\hat{\omega}_h^{p+1} - \hat{\omega}_h^p\|_\infty = \sup |\hat{\omega}_h^{p+1}(x) - \hat{\omega}_h^p(x)|.$$

At the end of the Picard loop, automatically adjust the time step Δt_n according to the number of Picard iterations per time step. We choose a minimum and maximum thresholds for the number of iterations below and above which the time step is increased or decreased, respectively, by a constant relative increment. These values can be set for the single test case. The procedure for the update of Δt_n is summarized in Algorithm 1.

The solution $\hat{\omega}_h^{p+1}$, $\hat{\phi}_h^{p+1}$ solves the nonlinear system (5.6) within the tolerances. We summarize the time stepping scheme in Algorithm 3.

Algorithm 3 Time stepping scheme with Picard iterations

N_T, total number of time steps
N_p, number of Picard iterations
tol_{N_p}, maximum number of Picard iterations
ε_p, residual of Picard iterations, computed as equation (5.13)
tol_p, tolerance on the residual of Picard iterations
$(\omega_h^n,\, \phi_h^n) \in V_h^0 \times V_h^0$, fields at the time step n
$(\hat{\omega}_h^p,\, \hat{\phi}_h^p) \in V_h^0 \times V_h^0$, fields at the previous Picard iteration p
$(\hat{\omega}_h^{p+1},\, \hat{\phi}_h^{p+1}) \in V_h^0 \times V_h^0$, fields at the current Picard iteration $p+1$
Initialize $\omega_h^n = \omega_h^0$ at $n = 0$
Initialize $\phi_h^n = \phi_h^0$ at $n = 0$ solving equation (5.12b) for ϕ_h^0 given ω_h^0
while $n \leq N_T$ **do** ▷ Time stepping loop
  Initialize the Picard loop $\hat{\omega}_h^p = \omega_h^n$, $\hat{\phi}_h^p = \phi_h^n$ at $p = 0$
  while $\varepsilon_p \geq \text{tol}_p$ **and** $N_p \leq \text{tol}_{N_p}$ **do** ▷ Picard loop
    Compute coefficients $\hat{\mathbb{D}}^p$, $\hat{\mathbb{F}}^p$ from equation (5.11)
    Solve for $(\hat{\omega}_h^{p+1},\, \hat{\phi}_h^{p+1}) \in V_h^0 \times V_h^0$ the system (5.12) with Newton method
    Verify the exit condition for the Picard iterations, from equation (5.13)
    Update $\hat{\omega}_h^p \leftarrow \hat{\omega}_h^{p+1}$
    Update $\hat{\phi}_h^p \leftarrow \hat{\phi}_h^{p+1}$
    Update index of the Picard iteration $p \leftarrow p+1$
  end while
  Update $\omega_h^n \leftarrow \hat{\omega}_h^{p+1}$
  Update $\phi_h^n \leftarrow \hat{\phi}_h^{p+1}$
  Update the time step $t \leftarrow t + \Delta t$
  Update Δt according to the number of Newton iterations, cf. Algorithm 1
end while

This scheme can be further generalized to treat all the nonlinearities within the Picard loop. All the steps described above remain the same, except for equation (5.12) that becomes

$$\begin{aligned} (\hat{\omega}_h^{p+1}, \alpha_h) + \Delta t_n (\hat{\mathbb{D}}^p \nabla \hat{\omega}_h^{n,p+1} - \hat{\mathbb{F}}^p M(\hat{\omega}_h^{n,p}), \nabla \alpha_h) = (\omega_h^n, \alpha_h), \qquad & \forall\, \alpha_h \in V_h^0 \\ (\nabla \hat{\phi}_h^{p+1}, \nabla \beta_h) - (\hat{\omega}_h^{p+1}, \beta_h) = 0, \qquad & \forall\, \beta_h \in V_h^0, \end{aligned} \tag{5.14}$$

which is now a linear system which can be solved iteratively with the GMRES method [104] and no preconditioner.

5.3 Relaxation method with the collision-like bracket for the Grad-Shafranov equation

Let u and ψ be the dynamical variable defined as equation (4.32) and the flux function defined via the elliptic problem in equation (4.33) on a bounded domain $\Omega \subset \mathbb{R}^2$ such that $\overline{\Omega} \subset \mathbb{R}^+ \times \mathbb{R}$.

We assume that the entropy functional is of the form

$$S = \int_\Omega s(R,u)\, R^{-1} dR dz, \tag{5.15}$$

where s depends on both the coordinate and the dynamical variable. The entropy density s determines the function $M(R,u)$ by the compatibility condition (4.16).

Upon choosing a linear functional F, the equation of motion generated by the collision-like bracket applied to Grad-Shafranov with an entropy functional of type (5.15), cf. equation

(4.11) with (4.37), reads

$$\big(\partial_t u,\alpha\big)_\mu = -\Big(\big[\mathbb{D}(\nabla u + M(R,u)s''_{Ru}(R,u)\nabla R) - \mathbb{F}M(R,u)\big],\nabla\alpha\Big)_\mu, \qquad \forall\,\alpha=\alpha(x), \tag{5.16a}$$

$$(\nabla\psi,\nabla\beta)_\mu = (u,\beta)_\mu, \qquad \forall\,\beta=\beta(x), \tag{5.16b}$$

$$u_{|\partial\Omega}=0, \qquad \psi_{|\partial\Omega}=0, \qquad \text{on } \partial\Omega, \tag{5.16c}$$

$$\mathbb{D}(x) = \int_\Omega w(x,x')M\big(R',u(x')\big)\frac{dR'dz'}{R'}, \qquad \text{in } \Omega, \tag{5.16d}$$

$$\mathbb{F}(x) = \int_\Omega w(x,x')\Big[\nabla u(x') + M\big(R',u(x')\big)\; s''_{Ru}(R',u(x'))\nabla R\Big]\frac{dR'dz'}{R'}, \qquad \text{in } \Omega, \tag{5.16e}$$

where $x=(R,z)$, $x'=(R',z')$ and

$$s''_{Ru}(R,u) = \frac{\partial^2}{\partial R\partial u}s(R,u),$$

and $(\,\cdot\,,\,\cdot\,)_\mu$ is the standard scalar product in $L^2(D,\mu)$.

The kernel matrix $w(x,x')$ in equation (5.16d) and (5.16e) is defined in equation (4.14) together with (4.36),

$$w(x,x') = |g(x,x')|^2 - g(x,x')\otimes g(x,x'), \qquad g(x,x') = \nabla\psi(x) - \nabla\psi(x').$$

5.3.1 The numerical scheme

We look for a numerical solution of the system (5.16) in the discrete space V_h^0 of equation (5.1).

We assign the discrete initial condition as $u_h^0 \in V_h^0$. The numerical approximation of the solution at any subsequent point in time is:

Find $(u_h^{n+1},\ \psi_h^{n+1}) \in V_h^0 \times V_h^0$ such that

$$(\delta(u_h)^{n+1},\alpha_h)_\mu + \Delta t_n(\mathbb{D}^{n+1/2}\tilde{u}^{n+1/2} - \mathbb{F}^{n+1/2}M(R,u_h^{n+1/2}),\nabla\alpha_h)_\mu = 0,\ \forall\,\alpha_h\in V_h^0, \tag{5.17a}$$

$$(\nabla\psi_h^{n+1},\nabla\beta_h)_\mu - (u_h^{n+1},\beta_h)_\mu = 0,\ \forall\,\beta_h\in V_h^0, \tag{5.17b}$$

$$\tilde{u}^{n+1/2}(x) = \nabla u_h^{n+1/2}(x) + s''_{Ru}\big(R,u_h^{n+1/2}(x)\big)M\big(R,u_h^{n+1/2}(x)\big)\;\nabla R, \tag{5.17c}$$

$$\mathbb{D}^{n+1/2} = \int_\Omega w(x,x')M\big(R',u_h^{n+1/2}(x')\big)dx', \tag{5.17d}$$

$$\mathbb{F}^{n+1/2} = \int_\Omega w(x,x')\tilde{u}^{n+1/2}(x')dx', \tag{5.17e}$$

$$w = |g|^2 I - g\otimes g, \qquad g = \nabla\psi_h^{n+1/2}(x) - \nabla\psi_h^{n+1/2}(x'). \tag{5.17f}$$

We observe that the system (5.17) is essentially the same as (5.6). We can repeat the same arguments of Section 5.4.2 to prove the properties of this numerical scheme. The time stepping scheme is as in Section 5.2.3.

5.4 Relaxation method with the diffusion-like bracket for Euler's equations

The equation of motion (4.11) for a linear functional F with the diffusion-like brackets defined in equation (4.59), reads

$$\big(\partial_t\omega,\alpha\big) = -\Big(\mathsf{D}\nabla s'_\omega(\omega),\nabla\alpha\Big), \qquad \forall\,\alpha=\alpha(x), \tag{5.18a}$$

$$(\nabla\phi,\nabla\beta) = (\omega,\beta), \qquad \forall\,\beta=\beta(x), \tag{5.18b}$$

$$\omega_{|\partial\Omega}=0, \qquad \phi_{|\partial\Omega}=0, \qquad \text{on } \partial\Omega, \tag{5.18c}$$

$$\mathsf{D} = |\nabla\phi|^2 I_2 - \nabla\phi\otimes\nabla\phi, \qquad \text{in } \Omega, \tag{5.18d}$$

where we added the Poisson equation and homogeneous Dirichlet boundary conditions. In equation (5.18a),

$$s'_\omega = \frac{ds}{d\omega} = \frac{\delta S}{\delta \omega},$$

and the kernel D in equation (5.18d) is defined according to equation (4.50) with (4.58).

5.4.1 The numerical scheme

As already observed at the end of Section 4.3.4.1, equation (5.18) is equivalent to the one obtained using the metric double bracket, cf. equation (3.10). In Section 3.3.3 we introduced a numerical scheme for the metric-double-bracket formulation cf. equations (3.18) and (3.19). The mixed-finite-element discretization used in Chapter 3 is obtained directly from the strong form of the evolution equation, with L^2-orthogonal projectors applied to non-linear fluxes, cf. equation (3.19).

The diffusion-like form obtained as a simplification of the collision-like bracket, on the other hand, suggests a different discretization, based on the weak form of the evolution equation in the framework of the classical finite element method for parabolic problems.

Although the evolution equation at the continuous level is exactly the same, the comparison of the two discretization schemes is interesting. Here we develop the discretization of the diffusion-like formulation and prove its properties. Both schemes are structure preserving in the sense that all relevant properties of the bracket are preserved.

We look for a numerical solution of the system (5.18) in the discrete space V_h^0 in equation (5.1). The discrete initial condition is $\omega_h^0 \in V_h^0$.

The numerical approximation of the solution at any subsequent point in time is given by:

Find $(\omega_h^{n+1},\, \phi_h^{n+1}) \in V_h^0 \times V_h^0$ such that

$$(\delta(\omega_h)^{n+1}, \alpha_h) + (\mathsf{D}^{n+1/2}\nabla s'_\omega(\omega_h^{n+1/2}), \nabla\alpha_h) = 0, \qquad \forall\, \alpha_h \in V_h^0, \tag{5.19a}$$

$$(\nabla\phi_h^{n+1}, \nabla\beta_h) - (\omega_h^{n+1}, \beta_h) = 0, \qquad \forall\, \beta_h \in V_h^0. \tag{5.19b}$$

$$\mathsf{D}^{n+1/2} = |\nabla\phi_h^{n+1/2}|^2 I_2 - \nabla\phi_h^{n+1/2} \otimes \nabla\phi_h^{n+1/2}. \tag{5.19c}$$

Using the numerical scheme (5.19) instead of (3.18) to follow the evolution of relevant test cases will allow us to draw interesting comparisons, cf. Section 6.2.3.

5.4.2 Properties of the numerical scheme

In the following, we prove that the numerical scheme introduced in equation (5.19) satisfies the properties of the diffusion-like brackets discussed in Section 4.3.1.

Proposition 5.4.1 (Conservation of the discrete energy)**.** If $(\omega_h^n,\, \phi_h^n) \in V_h^0 \times V_h^0$ is a solution of the system (5.19), then

$$H(\omega_h^n) = \frac{1}{2}\int_\Omega |\nabla\phi_h^n|^2\, dx = H(\omega_h^0), \quad \forall\, n \geq 0.$$

Proof. In equation (5.19a) we can choose $\alpha_h = \phi_h^{n+1/2}$. As shown in the proof of Proposition 5.2.1,

$$(\delta(\omega_h)^{n+1}, \phi_n^{n+1/2}) = \frac{1}{\Delta t_n}\big(H(\omega_h^{n+1}) - H(\omega_h^n)\big),$$

while

$$(\mathsf{D}^{n+1/2}\nabla s'_\omega(\omega_h^{n+1/2}), \nabla\phi_h^{n+1/2}) = 0,$$

since $\mathsf{D}^{n+1/2}\nabla\phi_h^{n+1/2} = 0$. Hence

$$H(\omega_h^{n+1}) - H(\omega_h^n) = \Delta t_n(\delta(\omega_h)^{n+1}, \phi_n^{n+1/2}) = 0.$$

□

Proposition 5.4.2 (Relaxation of the discrete quadratic entropy)**.** If $(\omega_h^n,\, \phi_h^n) \in V_h^0 \times V_h^0$ is a solution of the system (5.19) with entropy functional of the form

$$S(\omega) = \frac{1}{2}\int_\Omega \omega^2\, dx,$$

then

$$S(\omega_h^{n+1}) \leq S(\omega_h^n), \qquad \forall\, n \geq 0.$$

Proof. We can choose $\alpha_h = \omega_h^{n+1/2}$ in equation (5.19a). The Crank-Nicolson scheme gives

$$(\delta(\omega_h)^{n+1}, \omega_h^{n+1/2}) = \frac{1}{\Delta t_n}\big(S(\omega_h^{n+1}) - S(\omega_h^n)\big),$$

and

$$(\mathsf{D}^{n+1/2}\nabla\omega_h^{n+1/2}, \nabla\omega_h^{n+1/2}) \geq 0,$$

since D is positive semi definite. □

We remark that for different choices of the entropy, this property is not guaranteed.

5.4.3 Computational aspects

We compute the solution of the nonlinear system (5.19) with the Newton method. The linear system for each Newton step is solved with the GMRES method [104] and no preconditioner. The time-stepping scheme is summarized in Algorithm 4.

Algorithm 4 Time stepping scheme

N_T, total number of time steps
$(\omega_h^n,\, \phi_h^n) \in V_h^0 \times V_h^0$, fields at the previous time step n
$(\omega_h^{n+1},\, \phi_h^{n+1}) \in V_h^0 \times V_h^0$, fields at the current time step $n+1$
Initialize $\omega_h^n = \omega_h^0$, at $n = 0$
Initialize $\phi_h^n = \phi_h^0$, at $n = 0$ solving equation (5.19b) for ϕ_h^0 given ω_h^0
while $n \leq N_T$ **do** ▷ Time stepping loop
  Solve system (5.19) for $(\omega_h^{n+1},\, \phi_h^{n+1}) \in V_h^0 \times V_h^0$ with Newton and GMRES method
  Update $\omega_h^n \leftarrow \omega_h^{n+1}$
  Update $\phi_h^n \leftarrow \phi_h^{n+1}$
  Update $t \leftarrow t + \Delta t$
  Update Δt according to the number of Newton iterations, cf. Algorithm 1
end while

5.5 Relaxation method with the diffusion-like bracket for the Grad-Shafranov equation

The equation of motion (4.11) for a functional F linear in u with the diffusion-like brackets defined in equation (4.64), reads

$$\big(\partial_t u, \alpha\big)_\mu = -\Big(\mathsf{D}^{n+1/2}\nabla s_u'(u), \nabla\alpha\Big)_\mu, \qquad \forall\, \alpha = \alpha(x), \tag{5.20a}$$

$$(\nabla\psi, \nabla\beta)_\mu = (u, \beta)_\mu, \qquad \forall\, \beta = \beta(x), \tag{5.20b}$$

$$u_{|\partial\Omega} = 0, \quad \psi_{|\partial\Omega} = 0, \qquad \text{on } \partial\Omega, \tag{5.20c}$$

$$\mathsf{D} = |\nabla\psi|^2 I_2 - \nabla\psi\otimes\nabla\psi, \qquad \text{in } \Omega, \tag{5.20d}$$

where

$$s'_u(u) = \frac{ds}{du} = \frac{\delta S}{\delta u},$$

and $(\,\cdot\,,\,\cdot\,)_\mu$ is the standard scalar product in $L^2(D,\mu)$.

5.5.1 The numerical scheme

The numerical solution of the system (5.20) is looked for in the discrete space V_h^0 of equation (5.1). After setting the discrete initial condition $u_h^0 \in V_h^0$, the numerical approximation of the solution at any subsequent point in time is given by:

Find $(u_h^{n+1},\, \psi_h^{n+1}) \in V_h^0 \times V_h^0$ such that

$$\begin{aligned}
(\delta(u_h)^{n+1}, \alpha_h)_\mu + (\mathsf{D}^{n+1/2}\nabla s'_u(u_h^{n+1/2}), \nabla\alpha_h)_\mu = 0, \qquad & \forall\, \alpha_h \in V_h^0, \\
(\nabla\psi_h^{n+1}, \nabla\beta_h)_\mu - (u_h^{n+1}, \beta_h)_\mu = 0, \qquad & \forall\, \beta_h \in V_h^0, \\
\mathsf{D}^{n+1/2} = |\nabla\psi_h^{n+1/2}|^2 I_2 - \nabla\psi_h^{n+1/2} \otimes \nabla\psi_h^{n+1/2}. &
\end{aligned} \tag{5.21}$$

The numerical scheme in equation (5.21) is essentially the same as the one for Euler's equations in vorticity form, cf. equation (5.19). The same arguments of Section 5.4.2 apply. The choice of the time stepping follows that of Section 5.4.3.

5.6 Implementation

For the implementation of the numerical schemes in equation (5.6), (5.17), (5.19) and (5.21), we developed a suite of modules collected in the `PyMCO` code (Python code for Metric Collision Operators). `PyMCO` heavily leverages the finite element library `FEniCS` [25, 26] (version `2019.1.0`), a computing platform for solving partial differential equations. `FEniCS` provides the discretization of the domain Ω in a triangular mesh, the finite element spaces needed in finite element exterior calculus and also the interface with the numerical linear algebra library `PETSc` [96, 97, 98] and with the `MPI` library [99] for distributed computing.

The Newton method is automatically provided by `FEniCS`, while the GMRES method is provided by the `PETSc` library directly interfaced via `FEniCS`.

Linear Lagrange elements are implemented via the `FEniCS` element $\mathtt{P}_1$.

We used methods from the `FEniCS` API throughout the code. However, the implementation of the integral collision-like operator is non standard. For this reason, we report its implementation for the case of Euler's equations in Section 5.6.1, while a few remarks on the implementation for the case of the Grad-Shafranov equation are discussed in Section 5.6.2.

5.6.1 Implementation of the collision-like operator for the Euler's equation

First, let us introduce some notation from `PyMCO` and `FEniCS`:

- `Ut`, `phit`: `TrialFunction`, i.e. the dynamical variable and corresponding scalar potential at the current point in time;
- `Un`, `phin`: `Function`, the dynamical variable and corresponding scalar potential at the previous point in time;
- `Uv`, `phiv`: `TestFunction`;
- `dx`: measure associated with the interior domain representing integration over finite element cells;
- `dt`: time step;
- `inner`: inner product operation between for example a multicomponent `Trial u` and `TestFunction v`, defined as `inner(u, v) = u_i v_i`, where repeated indices are summed;
- `assemble`: operation to assemble a `FEniCS` form and return the corresponding matrix;

- `grad`: gradient operation.

We implemented the collision-like operator in components.

As already discussed in Section 5.2.3, the time stepping scheme consists of computing first the nonlinear diffusion and friction coefficients. The diffusion coefficient reads, cf. equation (5.6c) and (5.6e),

$$\mathbb{D}^{n+1/2}(x) = \int_\Omega w(x,x') M\big(\omega_h^{n+1/2}(x')\big) dx',$$
$$w = |g|^2 I - g \otimes g, \qquad g(x,x') = \nabla\phi_h^{n+1/2}(x) - \nabla\phi_h^{n+1/2}(x')$$

We define the components of the gradient of the scalar potential ϕ evaluated at the midpoint,

```
gradphi0 = 0.5*(grad(phit)[0] + grad(phin)[0])
gradphi1 = 0.5*(grad(phit)[1] + grad(phin)[1]),
```

while the `M` function evaluated at the midpoint of ω depends on the choice of the entropy. For a quadratic entropy, `M = 1`, while for a logarithmic choice, `M = 0.5 * (Ut + Un)`.

Given the variables `gradphi0`, `gradphi1` and `M`, we assemble the following forms

```
int_M = assemble(M * dx)
int1_p1p1 = assemble(grad_phi1 * grad_phi1 * M * dx)
int2_p1 = assemble(grad_phi1 * M * dx)
int3_p0 = assemble(grad_phi0 * M * dx)
int4_p0p0 = assemble(grad_phi0 * grad_phi0 * M * dx)
int5_p1p0 = assemble(grad_phi0 * grad_phi1 * M * dx),
```

Finally, we can build the blocks of the matrix `D` as follows:

```
D_11 = (grad_phi1*grad_phi1*int_M + int1_p1p1 - 2.0*grad_phi1*int2_p1)
D_12 = D21 = (-grad_phi0*grad_phi1*int_M + grad_phi0*int2_p1 + int3_p0*
grad_phi1 - int5_p1p0)
D_22 = (grad_phi0*grad_phi0*int_M + int4_p0p0 - 2.0*grad_phi0*int3_p0).
```

For the definition of the friction term, cf. equation (5.6d) and (5.6e),

$$\mathbb{F}^{n+1/2}(x) = \int_\Omega w(x,x') \nabla\omega_h^{n+1/2}(x') dx',$$
$$w = |g|^2 I - g \otimes g, \qquad g(x,x') = \nabla\phi_h^{n+1/2}(x) - \nabla\phi_h^{n+1/2}(x'),$$

we need the components of the gradient of the scalar potential , and the components of the gradient of the dynamical variable ω, i.e.

```
grad_omega_0 = 0.5*(grad(U)[0] + grad(Un)[0])
grad_omega_1 = 0.5*(grad(U)[1] + grad(Un)[1])
```

With these definitions we can assemble the following forms over the domain:

```
int6_du0 = assemble(grad_omega_0 * dx)
int7_du1 = assemble(grad_omega_1 * dx)
int8_p1p1du0 = assemble(grad_phi1 * grad_phi1 * grad_omega_0 * dx)
int9_p1du0 = assemble(grad_phi1 * grad_omega_0 * dx)
int10_p0du1 = assemble(grad_phi0 * grad_omega_1 * dx)
int11_p0p1du1 = assemble(grad_phi0 * grad_phi1 * grad_omega_1 * dx)
int12_p0du0 = assemble(grad_phi0 * grad_omega_0 * dx)
int13_p0p1du0 = assemble(grad_phi0 * grad_phi1 * grad_omega_0 * dx)
int14_p0p0du1 = assemble(grad_phi0 * grad_phi0 * grad_omega_1 * dx)
int15_p1du1 = assemble(grad_phi1 * grad_omega_1 * dx),
```

Then the two components of the friction vector are:

```
F_1 = (grad_phi1*grad_phi1*int6_du0 + int8_p1p1du0 -
    2.0*grad_phi1*int9_p1du0 -
    grad_phi0*grad_phi1*int7_du1 + grad_phi0*int15_p1du1 +
    int10_p0du1*grad_phi1 - int11_p0p1du1)
F_2 = (- grad_phi0*grad_phi1*int6_du0 + grad_phi0*int9_p1du0 +
    int12_p0du0*grad_phi1 - int13_p0p1du0 +
    grad_phi0*grad_phi0*int7_du1 + int14_p0p0du1 -
    2.0*grad_phi0*int10_p0du1).
```

The coefficients of $\hat{\mathbb{D}}^p$ and $\hat{\mathbb{F}}^p$ are computed at each Picard step, as illustrated in Algorithm 3.

The weak formulation implemented in `FEniCS` is written in terms of the components of $\mathbb{D}$ and $\mathbb{F}$. The diffusion term is

```
A1 = (dt * inner(D_11 * grad_omega_0 + D_12 * grad_omega_1), Uv.dx(0)) * dx +
    (dt * inner(D_12 * grad_omega_0 + D_22 * grad_omega_1), Uv.dx(1)) * dx
```

while the friction term reads

```
A2 = dt * inner(F_1 * M, Uv.dx(0)) * dx + dt * inner(F_2 * M, Uv.dx(1)) * dx.
```

The final weak formulation in `FEniCS` is implemented as `WF = Mass + A1 - L - A2`, where `Mass` and `L` are the usual mass matrix and right hand side, `M = inner(Ut, Uv) * dx` and `L = inner(Un, Uv) * dx`.

5.6.2 Implementation of the collision-like operator for the Grad-Shafranov equation

When we apply the collision-like operator to the Grad-Shafranov equation, we need to account for the additional term coming from the explicit dependence of the entropy functional on the coordinate of the domain, cf. equation (5.17c). For this reason, when computing the friction vector, `grad_omega_0` and `grad_omega_1` are defined as

```
grad_omega_0 = (0.5*(grad(Ut)[0] + grad(Un)[0]) - 2.0*CC*R_coord*0.5*(Ut + Un)
 * 1.0/(CC*R2_coord + DD))
grad_omega_1 = 0.5 * (grad(Ut)[1] + grad(Un)[1]),
```

where `CC` and `DD` are positive constants determined by the choice of the entropy, while `R_coord` and `R2_coord` are coefficients used in the variational form and defined in `FEniCS` as `Expression`,

```
R_coord = Expression("x[0]", element=discrete_space.ufl_element())
R2_coord = Expression("x[0]*x[0]", element=discrete_space.ufl_element()),
```

where `discrete_space` refers to the choice of the finite element space.

The diffusion matrix and friction vector `D` and `F` are then constructed as in Section 5.6.1.

Chapter 6

Numerical Experiments: div-grad brackets in two dimensions

We present numerical experiments with the collision- and diffusion-like brackets introduced in Section 4.2 and 4.3, respectively. The experiments are performed for the two physical examples of Euler's equations in vorticity form and the Grad-Shafranov equation introduced in Section 2.1.1 and 2.1.2, respectively. First, the common computational aspects of the test cases are discussed in Section 6.1. In Appendix A.1 and A.2 we describe the diagnostics we used to interpret the results and the notation to refer to each test case, respectively. The results of the experiments for the two physical models are presented in Section 6.2 and 6.3.

6.1 Computational aspects

All the test cases for Euler's equations in vorticity form are run in a domain $\Omega = [0,1]^2$, discretized with a uniform grid of 64×64 nodes. The resulting square cells are further divided into triangles by the `FEniCS` library. For the test cases of the Grad-Shafranov equation, we will consider also unstructured triangular meshes, cf. Appendix A.4.

The setup of the GMRES, Newton and Picard methods used to solve the nonlinear and linear systems, cf. Section 5.2.1, 5.3.1, 5.4.1, and 5.5.1, is reported in Table 6.1. These parameters are the same for all cases in this chapter.

	`atol`	`rtol`	`N_max`
`GMRES`	10^{-15}	10^{-13}	1000
`Newton`	10^{-14}	10^{-13}	50
`Picard`	10^{-12}	-	100

Table 6.1: **Setup of the GMRES, Newton and Picard method.** The parameters `atol`, `rtol`, and `N_max` refer to the absolute and relative tolerance, and to the maximum number of iterations, respectively.

In most cases, the time step is updated according to the mechanism illustrated in Algorithm 1 of Section 5.2.3. As already discussed, the procedure requires setting:

- the maximum time step $\Delta t_{\max}$ allowed during the simulation;
- the constant update factor Δt_{update};
- the minimum and maximum number of iterations, $N_{\min}$ and $N_{\max}$, respectively, beyond which the time step is updated by Δt_{update}.

We will report the value of these parameters separately for each of the considered test cases.

6.2 Euler's equations in vorticity form

We recall in Section 6.2.1 the common setup of the test cases performed for this model. In Section A.3 we present the two initial conditions we have considered, and in Section 6.2.2 we list the experiments performed. The results are discussed in Section 6.2.3 to 6.2.8.

6.2.1 Experiment's setup

In this section we summarize the common setup of the simulations for the physical case of Euler's equations in vorticity form.

We shall consider the domain $\Omega = [0,1]^2$. The energy and entropy functional respectively read

$$H(\omega) = \frac{1}{2}\int_\Omega |\nabla\phi|^2 dx, \qquad S(\omega) = \int_\Omega s(\omega) dx, \tag{6.1}$$

where the choice of the integrand $s(\omega)$ will depend on the numerical experiment. We also recall that the vorticity ω and its scalar potential ϕ are related through the Poisson equation, i.e.

$$\omega = -\Delta\phi, \qquad \phi_{\partial\Omega} = 0. \tag{6.2}$$

The functional derivatives of the energy and entropy functional in equation (6.1) read

$$\frac{\delta H(\omega)}{\delta \omega} = \phi, \qquad \frac{\delta S(\omega)}{\delta u} = s'_\omega(\omega). \tag{6.3}$$

Using equation (6.3), we also recall that the variational principle for the Euler's equation in the vorticity form implies as a necessary condition, cf. equation (2.26),

$$s'(\omega) + \lambda\phi = 0, \qquad \lambda \in \mathbb{R}. \tag{6.4}$$

6.2.2 Selected experiments

In Table 6.2 we present the list of relevant experiments for Euler's equations in vorticity form.

Name	Operator	Entropy	Initial condition	Domain
euler-llgr	diffusion-like	quadratic	gaussian	rectangular
euler-ilgr	collision-like	quadratic	gaussian	rectangular
euler-ller	diffusion-like	quadratic	eigenfunction	rectangular
euler-iler	collision-like	quadratic	eigenfunction	rectangular
euler-lhgr	diffusion-like	logarithmic	gaussian	rectangular
euler-ihgr	collision-like	logarithmic	gaussian	rectangular

Table 6.2: **List of experiments performed for Euler's equations in vorticity form.** The experiment tag in the first column is constructed as described in Appendix A.2.

6.2.3 Test case I: *euler-llgr*

This test case represents the first demonstration of the diffusion-like operator discussed in Section 4.3. For this reason we choose a simple entropy functional and initial condition. We recall that, at the continuous level, this problem is exactly the same as the one considered in Chapter 3. The only difference is the numerical scheme, which here is obtained from the diffusion-like formulation. The main focus of this section is the comparison of the results obtained by the two different schemes.

In Table 6.3 we summarize the setup of this test case. We choose the diffusion-like version of the operator, a quadratic entropy functional, the centered anisotropic Gaussian discussed in Section A.3.1 and a rectangular domain $\Omega = [0,1]^2$. The spatial resolution was selected equal to 64×64. We also report the values of the tolerances of the Newton and GMRES method used to solve the nonlinear system, as well as the parameters for the procedure to update the time step, cf. Algorithm 1.

Variable	**Value**
Operator	diffusion-like, equation (4.61)
Entropy	quadratic, $S(\omega) = \frac{1}{2}\int_\Omega \omega^2 dx$, equation (2.32)
Initial condition	Gaussian, equation (A.1), with $\sigma_{x_1}^2 = 0.01$, $\sigma_{x_2}^2 = 0.07$
Domain	rectangular $\Omega = [0,1]^2$
Boundary condition	Homogeneous Dirichlet
Resolution	64×64
GMRES tolerance	atol $= 10^{-15}$, rtol $= 10^{-13}$
Newton tolerance	atol $= 10^{-14}$, rtol $= 10^{-13}$
Δt update, cf. Algorithm 1	$N_{\min} = 3$, $N_{\max} = 6$, $\Delta t_{\max} = 100$, $f_{\text{update}} = 5$

Table 6.3: **Setup of the *euler-llgr* test case.**

Let us start by presenting runtime information for this experiment in Table 6.4. The figures about the number of iterations aim to be an implementation and hardware-agnostic assessment of the computational time. We notice that the final time step is four orders of magnitude bigger than the one at the start of the simulation, because the time step is adapted according to the number of Newton iterations per time step, as discussed in Section 6.1. We allow the time step to grow as large as possible since we are only interested in the relaxed state and, for a quadratic entropy, the numerical scheme preserves the Hamiltonian and dissipates entropy for all $\Delta t_n > 0$.

Time steps	Newton	GMRES	dt_i	dt_f
10248	1.22	58.02	0.01	156.25

Table 6.4: **Runtime information for the *euler-llgr* test case.** From left to right, we report the total number of time steps, the average number of Newton iterations per time step, and the average number of GMRES iterations per Newton step. Also reported are the initial (dt_i) and final (dt_f) values of the time step, which is adapted automatically according to the number of Newton iterations per time step, as discussed in Section 6.1.

In Figure 6.1 we show the temporal evolution of the relative energy error (with respect to the initial value) and entropy. We see in (a) that the maximum error on energy conservation is 10^{-11}. The adopted numerical scheme, discussed in Section 5.4.1, is designed to preserve energy exactly. The error in Figure 6.1(a) can be attributed to the finite precision with which the discrete equations are solved via Newton and GMRES iterations. In (b) we see that entropy relaxes as the system goes toward an equilibrium, as expected from theory.

To ease the comparison with other test cases, we also report in Table 6.5 the values of the entropy evaluated at the beginning and at the final state.

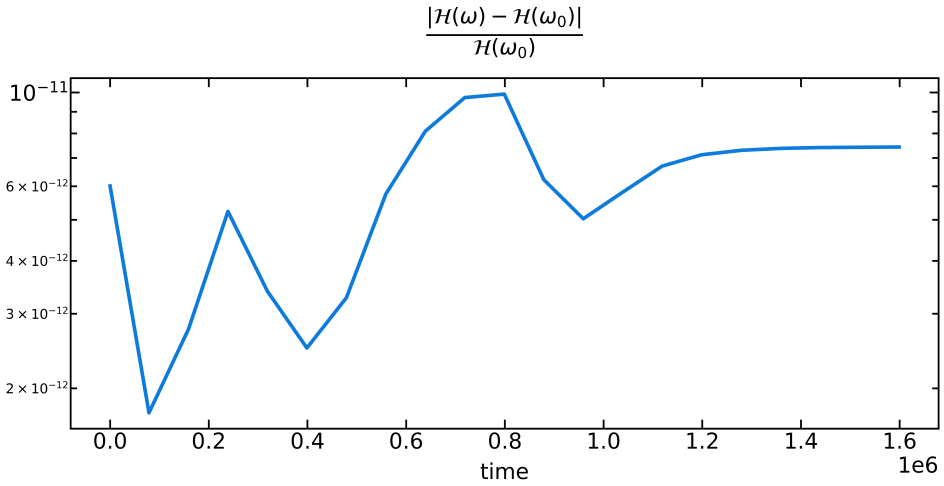

(a) Temporal evolution of the relative energy error.

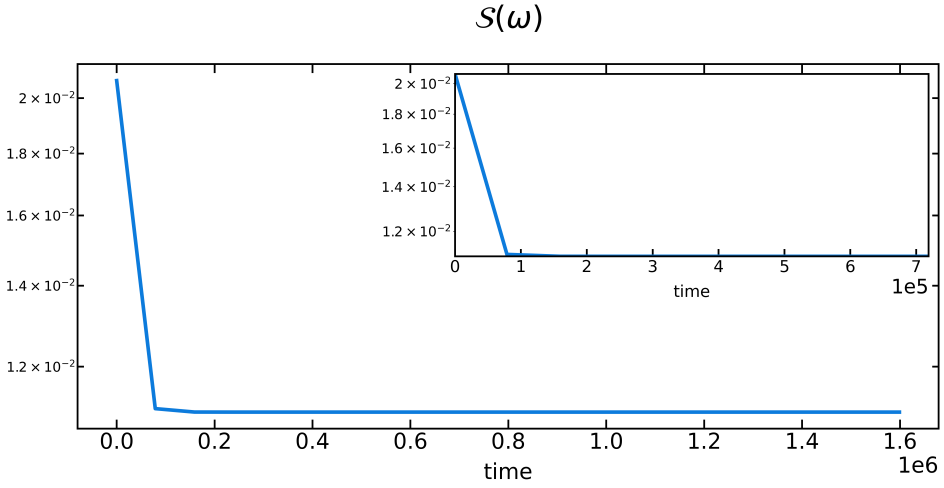

(b) Temporal evolution of the entropy.

Figure 6.1: **Evolution of the test case *euler-llgr*.** In (a) we see the temporal evolution of the relative energy error (with respect to the initial value) in a semi-logarithmic scale. The maximum error on the energy conservation is 10^{-11}, to be attributed to the finite precision with which the equations are solved. In (b) the temporal evolution of the entropy is shown. The inset shows the evolution of the same quantity during the early phase of the experiment.

$S(\omega_0)$	$S(\omega_e)$
0.02068	0.011007

Table 6.5: **Initial and final entropy values for *euler-llgr*.** The entropy is evaluated in ω_0 and ω_e, respectively the vorticity at the beginning and at the end of the simulation.

In Figure 6.2 we show two plots that characterize the final relaxed state. From the color plot in (a) we see that the contours of the vorticity and those of the associated potential are parallel to each other: this suggests that a final equilibrium state has been reached. From the scatter plot in (b) we can characterize the equilibrium state of the final condition. At $t = 0$, the data points are scattered in a certain region of the domain (in black), but, as the simulation advances in time, they collapse onto a linear functional relation, marked with red circles. They are perfectly overlapped by the green crosses, which represent the relation expected from the variational principle, cf. equation (6.4).

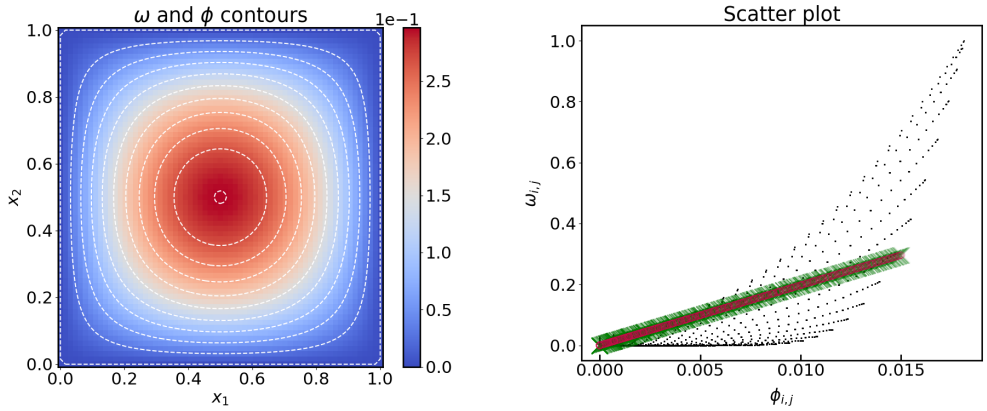

(a) Color plot. (b) Scatter plot.

Figure 6.2: **Relaxed state for the test case *euler-llgr*.** In (a) we see the color plot and contours (in white dashed lines) of the dynamical variables ω and ϕ respectively, at the end of the simulation. The colorbar shows the intensity of the vorticity field. In (b) we present a comparison between the functional relation of the two variables at the initial time (black dots) and at the final time (red circles), together with the prediction of the variational principle (green crosses). We see that the discrete values of the variables are well distributed over the plane at the initial time. At equilibrium, the data points have collapsed into a distinguishable linear functional relation, marked by the red circles. This can be compared with the expected relation from the variational principle, cf. equation (6.4) with the eigenvalue of equation (6.8), plot with green crosses. We can also fit the red data points of (b) to estimate the coefficient numerically, and compare them with the value predicted in theory, cf. Table 6.6.

We recall that for this particular choice of the entropy functional, equation (6.4) reduces to

$$\omega = \lambda \phi, \tag{6.5}$$

where λ is a real number. Using the Poisson relation (6.2) in Equation (6.5) we find the linear eigenevalue problem

$$-\Delta\phi = \lambda\phi \qquad \phi_{|\partial\Omega} = 0, \tag{6.6}$$

which has known analytical solutions, as briefly discussed in Appendix B, that is

$$\lambda_{n,m} = \pi^2(n^2 + m^2), \tag{6.7}$$

where n and m are two positive integer numbers.

In particular, cf. Section (2.2.1), the theoretical value for the eigenvalue λ is found in this case for $n = m = 1$, and gives

$$\lambda_{1,1} = 2\pi^2 = 19.7392. \tag{6.8}$$

We can use linear least squares to estimate the value of λ in equation (6.5) from the red data points of Figure 6.2(b), which represent the functional relation between ω and ϕ at the end of the simulation, and compare it with the value expected in theory, cf. equation (6.8).

a	**b**	$\|b-\lambda\|/\lambda$
-2.437402e-10	19.751101	0.000602

Table 6.6: **Results of the fit and comparison with the solution of the variational principle in equation** (6.4) **for the test case *euler-llgr*.** Values of the coefficients computed by fitting a linear functional relation to the red data points of Figure 6.2(b) and the relative error with respect to the eigenvalue $\lambda = \lambda_{1,1}$.

In Table 6.6 we show the estimate of the coefficients of the fitting function $f = a + b\,x$, together with the relative error with respect to the eigenvalue $\lambda_{1,1}$ of equation (6.8).

For this test case we see that the Gaussian initial condition evolves toward the equilibrium state of minimum entropy at constant energy. During the evolution, the operator preserves the energy and relaxes the entropy, as expected. The final relaxed state is the eigenfunction of the Laplacian corresponding to the smallest eigenvalue. This is somewhat surprising if one keeps in mind that the evolution equation, initial and boundary conditions are the same as those of the example in Chapter 3, for which we observed failure to find the constrained entropy minimum. The only difference between the test case of Chapter 3 and this one is of course the discretization.

To study the properties of the dynamics under this scheme, cf. Section 5.4.1, we tested it with Lagrange finite elements of order two. For this test, the quadratic Lagrange elements are implemented via the `FEniCS` element $\mathtt{P}_2$. We also fix the time step to 0.2 while disabling the mechanism to update the time step, cf. Algorithm 1, and we run the test case for 1000 time steps. All the other conditions of the test case, cf. Table 6.3, remain unchanged.

In Figure 6.3 we show the evolution of the relative energy error and entropy. We observe that the energy is preserved while entropy relaxed, similarly to Figure 6.1, as expected from theory.

We show in Figure 6.4 the final state of the test case, the color plot in (a) and the scatter plot in (b). We see that the relaxed state is an equilibrium of the operator, cf. Figure 6.3(b), but it is not in accordance with the solution of the variational principle. Compare this solution with both Figure 6.2, for the test case run with linear Lagrange finite elements, and Figure 3.2, run with the mixed formulation of the numerical scheme of Section 3.3.3. If we use the numerical scheme (5.19) with finite elements of higher order, we retrieve exactly the same solution as the one in Section 3.4 with mixed finite elements, as we expect from the fact that we are solving the same continuous problem.

We hypothesize that it is numerical diffusion, rather than intrinsic properties of the operator, to be responsible for the relaxation to the state of minimum entropy in Figure 6.2. On the contrary, the numerical scheme with mixed formulation, cf. Section 3.3.3, does not show numerical diffusion even when using finite elements of the lowest order.

To support this claim, we run again the test case with linear Lagrange finite elements with fixed time step equal to 0.2 for 1000 time steps and we compare the entropy evolution. The relative energy error evolution is comparable and shows in both cases that the energy is preserved, as expected from theory. The final state for both of these runs appears as in Figure 6.4.

We show the two plots of entropy evolution in Figure 6.5. The difference is that when using linear elements, the entropy does not appear to be relaxed after 1000 time steps. If we let the test case evolve for longer, we obtain again the state of minimum entropy of Figure 6.2. Numerical diffusion is accountable for this relaxation. We also ran the same test case with linear Lagrange elements with different time discretizations and double the spatial resolution, to qualitatively observe the impact of the numerical diffusion on the entropy evolution and the final solution. Upon reducing the time step and increasing the spatial resolution, we can reduce the effect of the numerical dissipation, similarly to using quadratic Lagrange elements. For a sufficiently large time step, i.e. $dt = 10$, we also observe numerical dissipation when using quadratic Lagrange finite elements. Note that numerical

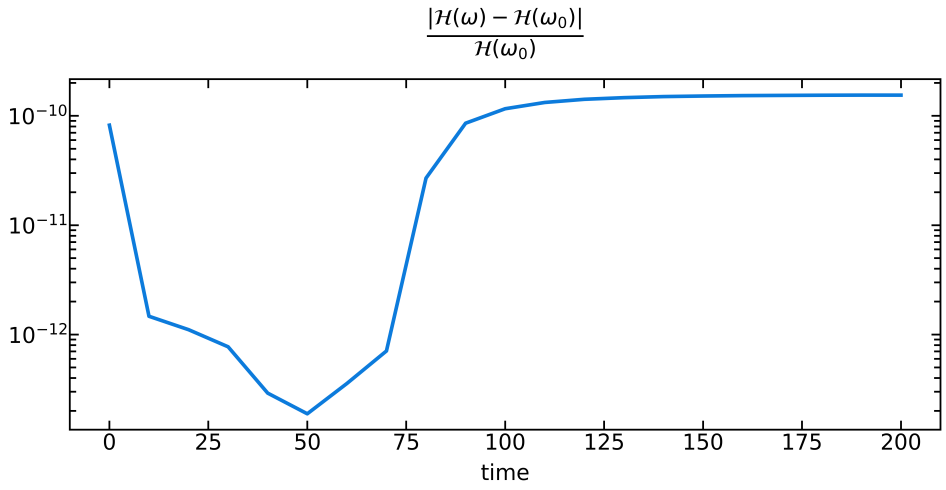

(a) Temporal evolution of the relative energy error.

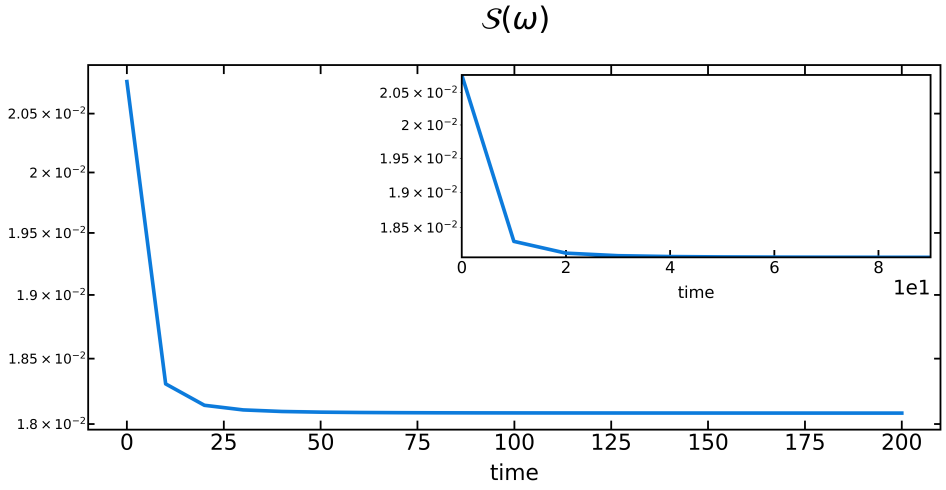

(b) Temporal evolution of the entropy.

Figure 6.3: **Evolution of the test case *euler-llgr* with quadratic Lagrange finite elements.** The same as in Figure 6.1, but for Lagrange finite elements of order 2.

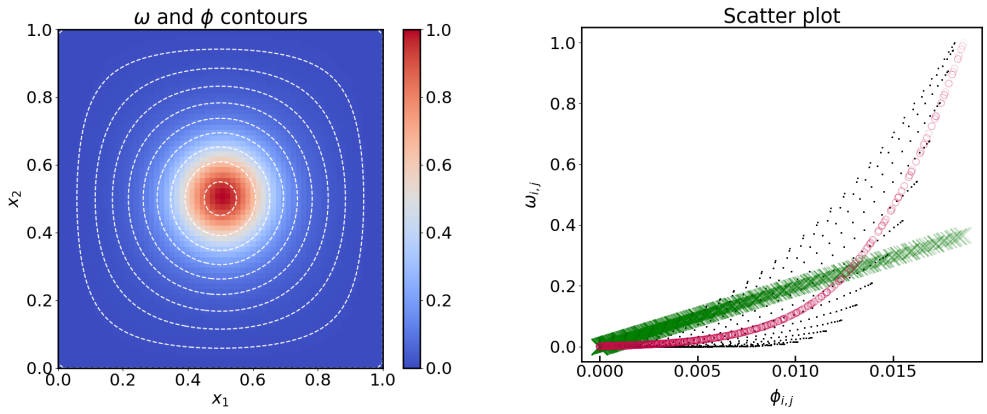

(a) Color plot. (b) Scatter plot.

Figure 6.4: **Relaxed state for the test case *euler-llgr* with finite element order equal to 2.** The same as in Figure 6.2, but with Lagrange finite elements of order 2. We note that the final solution, plot with the red circles, is not in accordance with the solution of the variational principle, cf. equation (6.4) with the eigenvalue from equation (6.8), which is plot with green crosses. This is because the higher finite elements order prevents numerical dissipation to relax the initial condition to the state of minimum entropy.

diffusion behaves in accordance with the properties of the numerical scheme, i.e. preserving the energy and dissipating the entropy until the state of minimum entropy, which happens to be in accordance with the solution of the variational principle.

We conclude that numerical dissipation, introduced by using the scheme of Section 5.4.1, and not the operator itself, is driving the relaxation to a solution of the variational principle. For the envisaged applications, relying on slow numerical diffusion to converge to the constrained entropy minimum, perhaps by means of large time steps, is not the robust and efficient strategy, which is the ultimate aim of this work. Moreover, we know that in a two-dimensional domain, the choice of the diffusion tensor D is essentially unique, and thus cannot be improved. However, the foregoing examples give us some insight on the very different behavior of the mixed finite-element scheme of Section 3.3.3 and the more traditional finite-element method of Section 5.4.1. Both schemes preserve the defining properties of the brackets, yet the mixed finite-element scheme seems to give a better approximation of the kernel of the metric operator too, since it can hold a local equilibrium even at low resolution. For problems on domains of dimension $n > 2$, the diffusion-like brackets constitute a rich class of metric operators as D can be defined in several non-equivalent ways, including the projector and the metric double bracket as special cases, cf. Section 2.3.2. This is, however, not useful for the physical problems at hand, that are inherently two-dimensional, and it has not been tested. From now on we focus on the comparison between the diffusion- and collision-like brackets both with the low-order finite element schemes of Chapter 5.

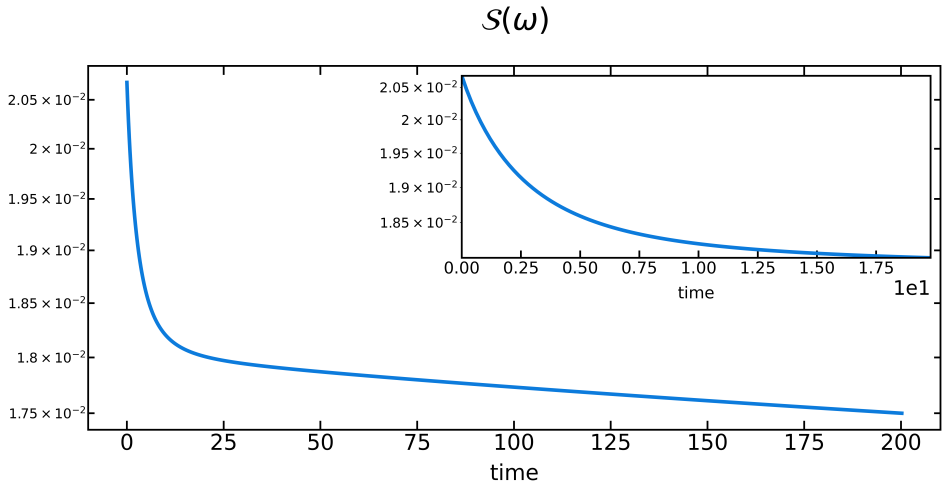

(a) Temporal evolution of the entropy.

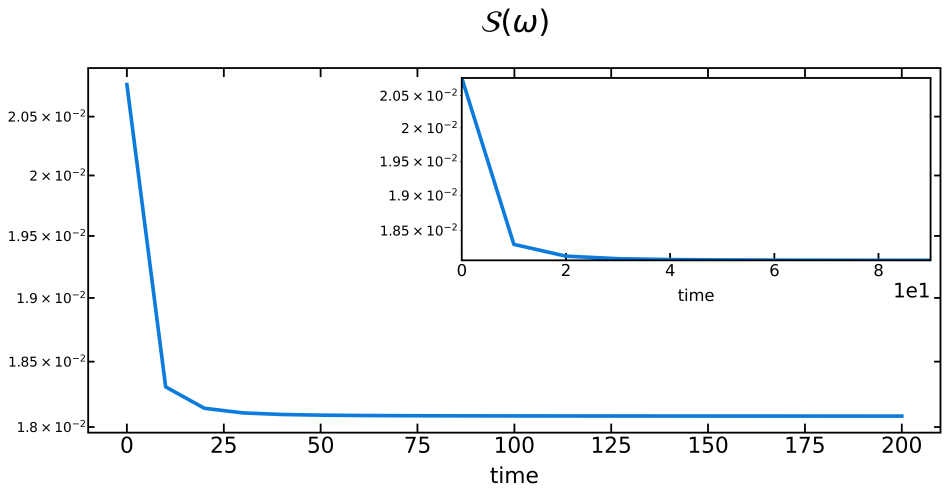

(b) Temporal evolution of the entropy.

Figure 6.5: **Entropy evolution of the test case *euler-llgr* run with linear (a) and quadratic (b) Lagrange elements.** Comparison of the entropy evolution of two test cases run under the same conditions, but for the order of the Lagrange elements. Notice that in (a) the entropy is still diffusing, while in (b) it appears to be completely relaxed.

6.2.4 Test case II: *euler-ilgr*

This test case can be regarded as the proof of concept of our method for the collision-like operator discussed in Section 4.2, similarly to the test case presented in Section 6.2.3 for the diffusion-like operator.

In Table 6.7 we summarize the setup for this test case. It is the same as the one presented in Section 6.2.3, but here we use the collision-like operator.

Variable	**Value**
Operator	collision-like, equation (4.30)
Entropy	quadratic, $S(\omega) = \frac{1}{2}\int_\Omega \omega^2 dx$, equation (2.32)
Initial condition	Gaussian, equation (A.1), with $\sigma_{x_1}^2 = 0.01$, $\sigma_{x_2}^2 = 0.07$
Domain	rectangular $\Omega = [0,1]^2$
Boundary condition	Homogeneous Dirichlet
Resolution	64×64
GMRES tolerance	atol $= 10^{-15}$, rtol $= 10^{-13}$
Newton tolerance	atol $= 10^{-14}$, rtol $= 10^{-13}$
Picard tolerance	tol $= 10^{-12}$
Δt update, cf. Algorithm 1	$N_{\min} = 3$, $N_{\max} = 6$, $\Delta t_{\max} = 10$, $f_{\text{update}} = 2$

Table 6.7: **Setup of the *euler-ilgr* test case.**

As before, we summarize runtime information in Table 6.8.

Time steps	Picard	Newton	GMRES	dt_i	dt_f
1034	2.88	1.0	44.21	0.01	10.24

Table 6.8: **Runtime information for the *euler-ilgr* test case.** From left to right, we report the total number of time steps, the average number of Picard iterations per time step, the average number of Newton iterations per Picard step, and the average number of GMRES iterations per Newton step. As discussed in Section 5.2.3, the nonlinearity and non-locality of the operator was treated with a double loop in Picard and Newton. We also report the initial (dt_i) and final (dt_f) values of the time step, which is adapted on the basis of the number of Picard iterations per time step as discussed in Section 6.1.

We notice that the final time step in Table 6.8 is three orders of magnitude larger than the value at the beginning of the simulation, while we observed an increase of four orders of magnitude in Table 6.4 for the test case *euler-llgr*. This is related to the different relaxation mechanism of the collision-like operator.

For this operator, the time stepping scheme, cf. Section 5.2.3, involves two nested iteration loops. The outer iteration is a Picard-type iteration which allows us to reduce the problem to a nonlinear advection-diffusion equation which is then solved with the Newton method.

For comparison, we ran the same test case with an implementation where the nonlinearity was treated with a Picard loop only, as discussed in Section 5.2.3. The setup of this test case is the same as Table 6.7. We report the runtime information for this test case in Table 6.9. Comparing Table 6.8 with 6.9 we observe that the computational cost of the two implementations is comparable.

Time steps	Picard	GMRES	dt_i	dt_f
1042	1.89	23.98	0.01	10.24

Table 6.9: **Runtime information for the *euler-ilgr* test case with a pure Picard loop.**

We can also compare Table 6.8 with the same Table 6.4 for the diffusion-like operator, to draw some conclusion about the computational cost of the two classes of operators. Despite apparently requiring more time steps for convergence, the diffusion-like operator is in fact cheaper because it does not involve the evaluation of the diffusion and friction coefficients at each Picard step, which is required for the collision-like operator and further increases the computational complexity.

In Figure 6.6 we show the temporal evolution of the relative energy error (a) and entropy (b). The behavior is similar to that of the diffusion-like operator in Section 6.2.3.

In Table 6.10 we report the values of the entropy evaluated at the beginning and at the end of the simulation.

$S(\omega_0)$	$S(\omega_e)$
0.02068	0.011007

Table 6.10: **Initial and final entropy values for the *euler-ilgr* test case.** The same as in Table 6.5, but for the collision-like operator.

It is interesting to compare the results of Table 6.10 with those of Table 6.5. The relative error between the two values of the entropy evaluated at the end of the simulation is 10^{-9}. This result supports the conclusion that the two operators relaxed to the same state at the end of the simulation.

In Figure 6.7 we present the final state: the solution is essentially the same as the one obtained in Section 6.2.3 for the diffusion-like operator, with the low-order elements, cf. Figure 6.2.

We can use linear least squares to fit the functional relation represented by the red data points of Figure 6.7(b), and compare these results with the analytical eigenvalues of the Laplace operator, as discussed for the *euler-llgr* test case in Section 6.2.3. The results are shown in Table 6.11.

a	**b**	$\|b-\lambda\|/\lambda$
8.510144e-11	19.751101	0.000602

Table 6.11: **Results of the fit and comparison with the solution of the variational principle in equation** (6.4) **for the test case *euler-ilgr*.** Same as Table 6.6, but for the case of the collision-like operator.

This test case shows that the collision-like operator behaves as predicted by theory. It preserves the energy while dissipating the entropy. It relaxes an initially centered anisotropic Gaussian to the final state predicted by the choice of the entropy functional and the variational principle.

In view of the discussion of Section 6.2.3, we ran this test case under the exact same conditions, cf. Table 6.7, but with quadratic Lagrange elements.

The runtime information for this test case is in Table 6.12. We note the larger number of both Picard iterations per time step and GMRES iterations per Newton step.

Time steps	Picard	Newton	GMRES	dt_i	dt_f
548	4.55	1.0	236	0.01	10.24

Table 6.12: **Runtime information for the *euler-ilgr* test case with quadratic Lagrange finite elements.** The same as in Table 6.8, but for quadratic Lagrange finite elements.

We show the evolution of the relative energy error and entropy in Figure 6.8(a) and 6.8(b), respectively. We can essentially repeat the same remarks of Figure 6.6.

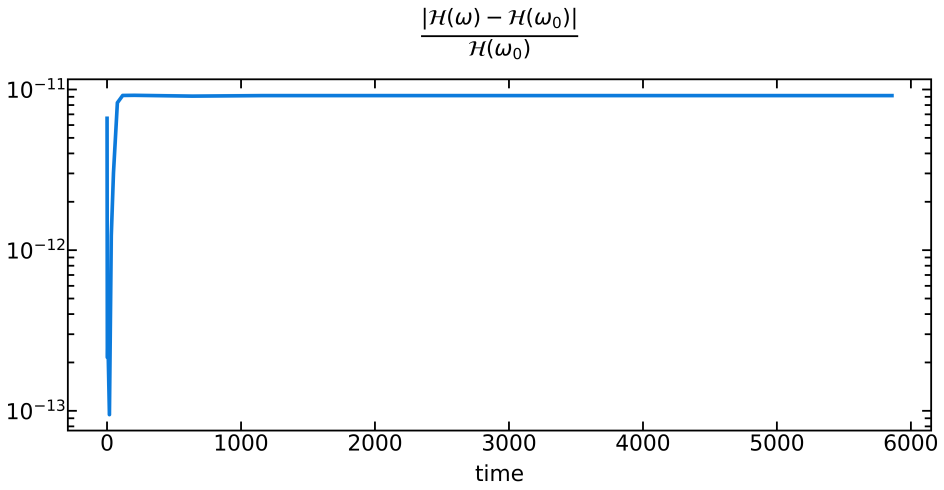

(a) Temporal evolution of the relative energy error.

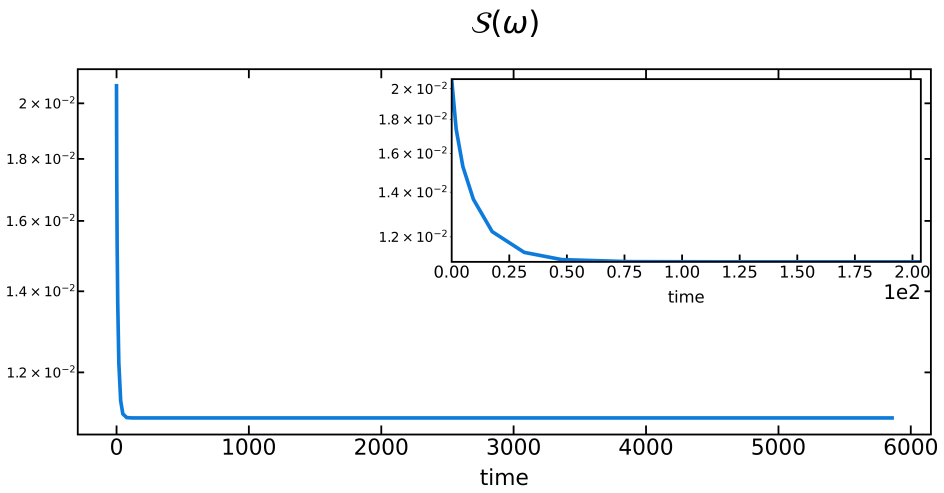

(b) Temporal evolution of the entropy.

Figure 6.6: **Evolution of the test case *euler-ilgr*.** The same as in Figure 6.1, but for the collision-like operator.

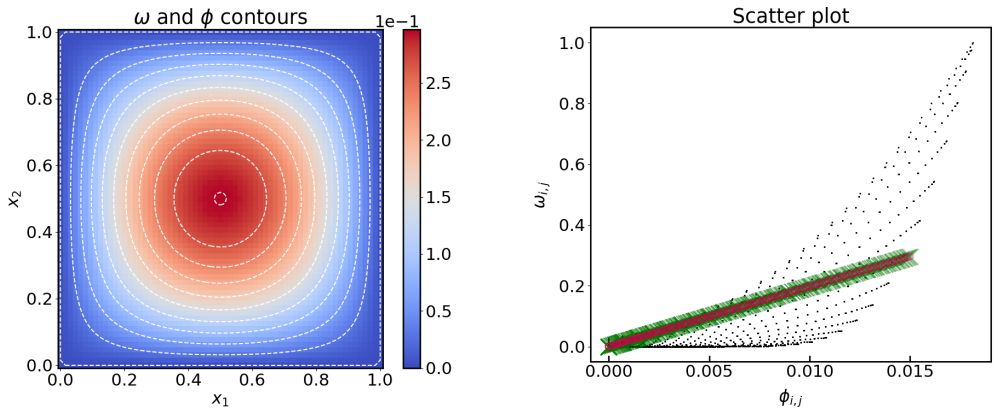

(a) Color plot. (b) Scatter plot.

Figure 6.7: **Relaxed state for the test case *euler-ilgr*.** The same as in Figure 6.2, but for the collision-like operator.

The relaxed state is presented in Figure 6.9: from both the color plot (a) and scatter plot (b) we see that the initial condition has relaxed to a solution in accordance with the variational principle.

For this test case, the results strongly suggest that the relaxation to the state of constrained minimum entropy, which corresponds to the solution of the variational principle, appears to be a feature of the collision-like operator, rather than being caused by numerical dissipation, as we observed for the diffusion-like operator.

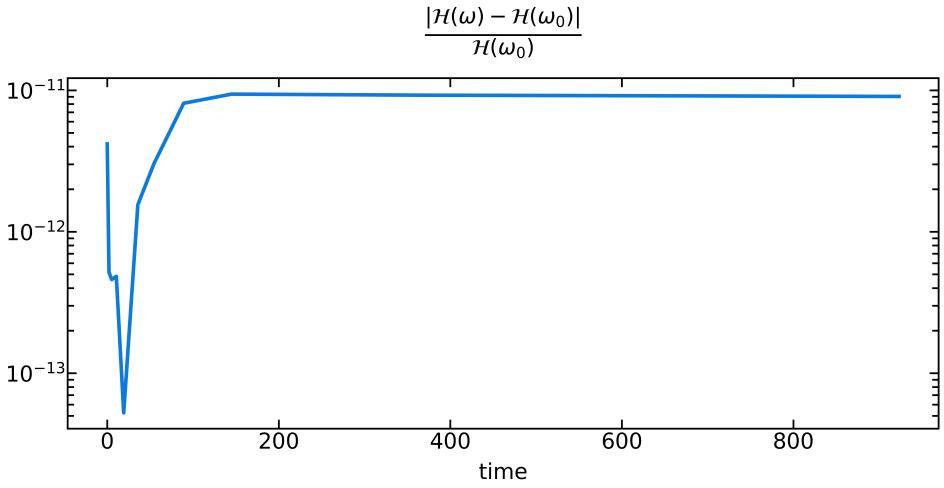

(a) Temporal evolution of the relative energy error.

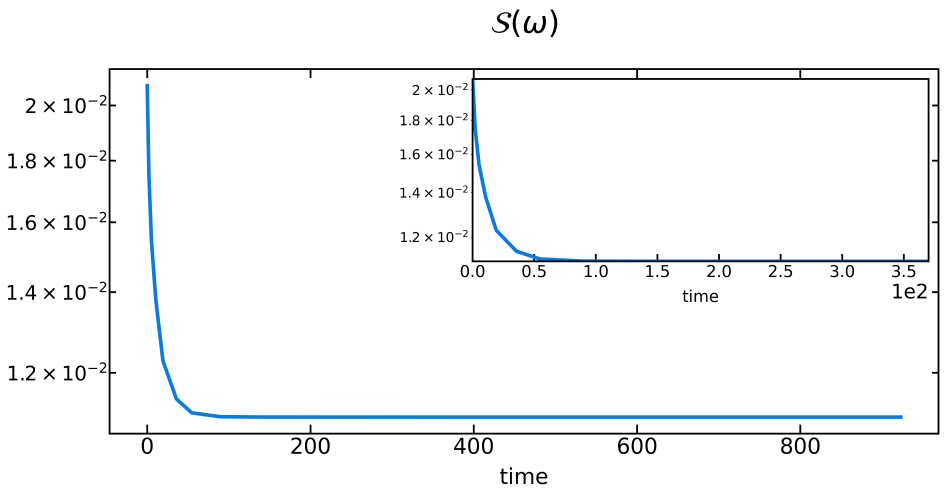

(b) Temporal evolution of the entropy.

Figure 6.8: **Evolution of the test case *euler-ilgr* with quadratic Lagrange finite elements.** The same as in Figure 6.6, but with Lagrange finite elements of order 2.

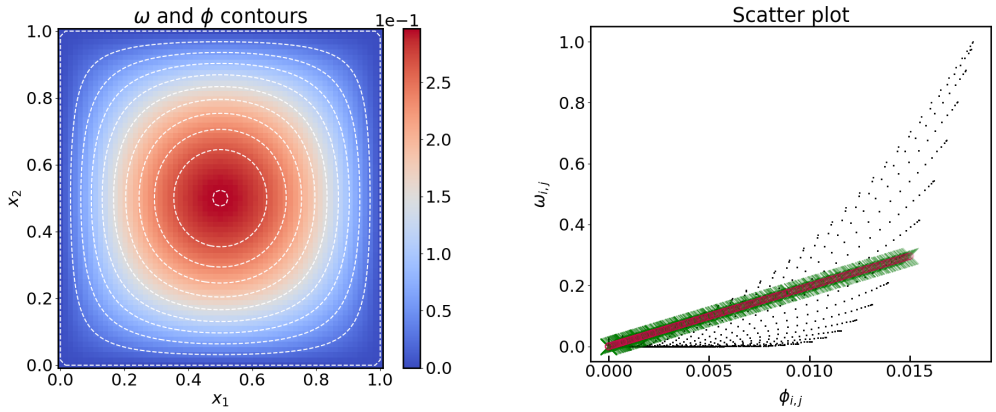

(a) Color plot. (b) Scatter plot.

Figure 6.9: **Relaxed state for the test case *euler-ilgr* with quadratic Lagrange finite elements.** The same as in Figure 6.7, but with Lagrange finite elements of order 2.

6.2.5 Test case III: *euler-ller*

In this test case we consider an initial condition which is constructed as a perturbation of an equilibrium of the metric operator, but far away from a solution of the variational principle in equation (6.4), that is far from a constrained entropy minimum. We ask ourselves whether the metric system relaxes to the close equilibrium point or it finds the constrained entropy minimum. In addition this test case allows us to understand the role of the conserved energy in the relaxation process.

In Table 6.13 we summarize the setup, which is the same as that of the test case *euler-llgr* except for the choice of the initial condition. Here we consider the perturbed eigenfunction of the Laplace operator with a Gaussian perturbation discussed in Section A.3.2. We run three test cases, one for each different value of the magnitude of the Gaussian perturbation, i.e. $A = 1.0$, $A = 0.1$ and $A = 0.01$.

Variable	**Value**
Operator	diffusion-like, equation (4.61)
Entropy	quadratic, $S(\omega) = \frac{1}{2}\int_\Omega \omega^2 dx$, equation (2.32)
Initial condition	Perturbed eigenfunction, equation (A.4)
Domain	Rectangular $\Omega = [0,1]^2$
Boundary condition	Homogeneous Dirichlet
Resolution	64×64
GMRES tolerance	atol $= 10^{-15}$, rtol $= 10^{-13}$
Newton tolerance	atol $= 10^{-14}$, rtol $= 10^{-13}$
Δt update, cf. Algorithm 1	$N_{\min} = 3$, $N_{\max} = 6$, $\Delta t_{\max} = 100$, $f_{\text{update}} = 2$

Table 6.13: **Setup of the test case *euler-ller*.** The magnitude of the perturbation in the initial condition is increased from $A = 0.01$, $A = 0.1$, upto $A = 1.0$. There is no difference in the setup of the three cases.

In Table 6.14 we report the runtime information for the three test cases with a different value of the Gaussian perturbation. We notice that the computational cost of the three test cases is comparable.

A	Time steps	Newton	GMRES	dt_i	dt_f
$A = 0.01$	7380	2.43	101.1	0.01	163.84
$A = 0.1$	7356	2.38	100.79	0.01	163.84
$A = 1.0$	7355	2.1	133.58	0.01	163.84

Table 6.14: **Runtime information for the *euler-ller* test case.** The same as in Table 6.4, but for the initial condition of the perturbed eigenfunction of the Laplace operator. Each row corresponds to a different choice of the value of the magnitude of the Gaussian perturbation.

In Figure 6.10 we show the temporal evolution of the relative energy error and entropy for the test case with Gaussian perturbation $A = 0.01$. The same remarks discussed in Section 6.2.3 apply here. We observe a similar behavior for the two test cases with $A = 0.1$ and $A = 1.0$, and therefore we omit the corresponding plots.

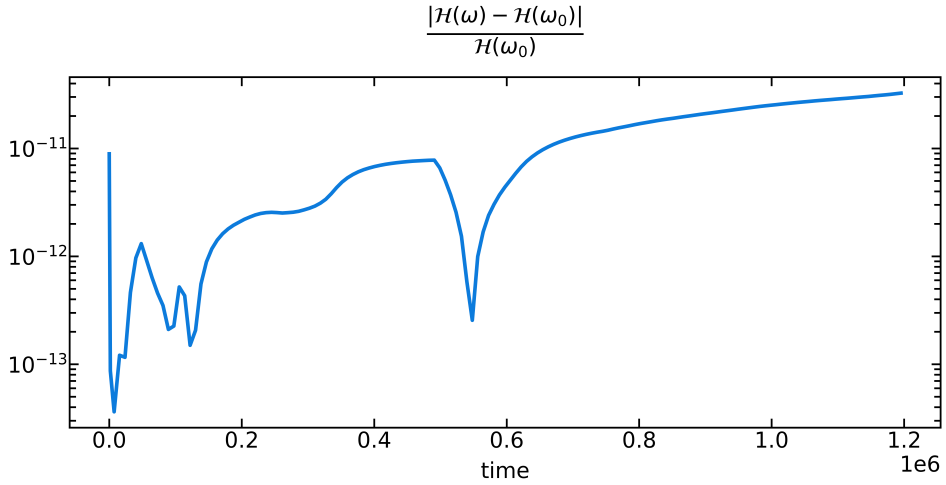

(a) Temporal evolution of the relative energy error.

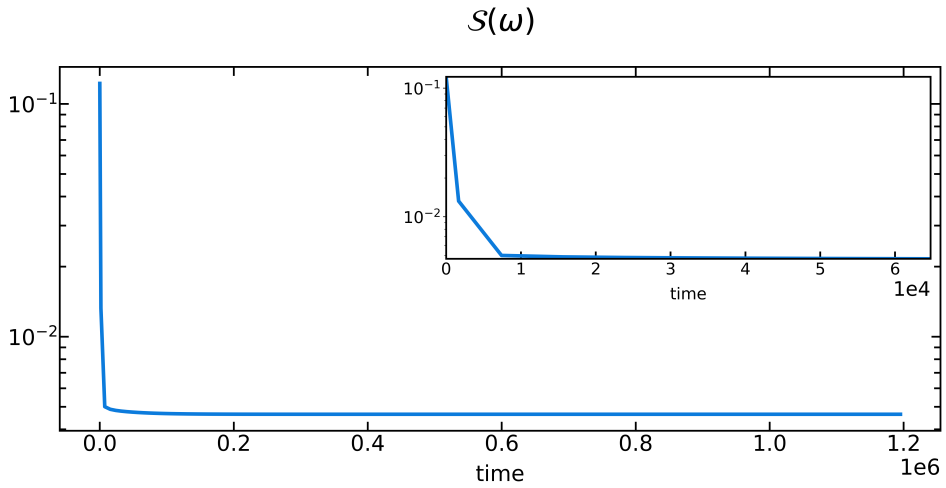

(b) Temporal evolution of the entropy.

Figure 6.10: **Evolution of the test case *euler-ller* with A = 0.01.** The same as in Figure 6.1, but for the initial condition discussed in Section A.3.2. Notice that in (b) the scale is semi-logarithmic.

In Figure 6.11 we see the final state for the test case with $A = 0.01$. In Figure 6.11(a), on the left-hand-side panel, we see the color plot of the dynamical variables. Qualitatively, the contours of the vorticity and its scalar potential are parallel to each other, thus suggesting that an equilibrium state has been reached, while on the right-hand-side panel, we show the absolute difference between the solution and the rescaled eigenfunction of the Laplace operator corresponding to the minimum eigenvalue, which is the theoretical constrained entropy minimum, as discussed in Section 6.2.1. We find good agreement. We observe some localized features that dominate the error. Such features are dissipated as the relaxation is continued.

In Figure 6.11(b) we show the scatter plot of the functional relation. The black data points corresponding to the initial condition are scattered over the domain, but relatively close to a straight line since the initial condition is close to an eigenvalue. At the end they reached a seemingly linear functional relation with different slope, represented by the red data points, that match the relation predicted by the variational principle, represented by the green crosses.

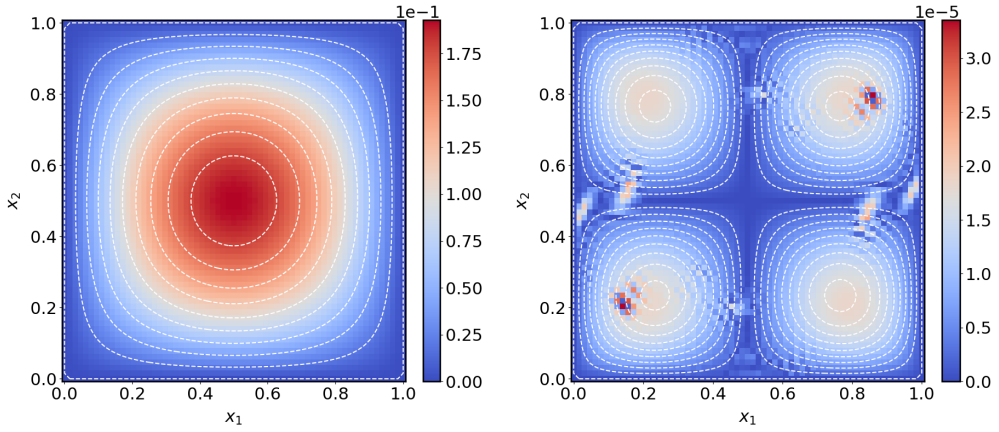

(a) Color plot and absolute difference with respect to the prediction of the variational principle.

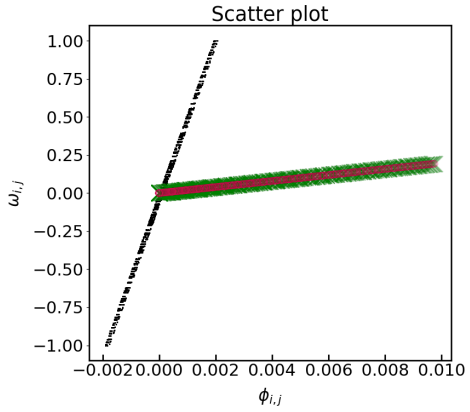

(b) Scatter plot.

Figure 6.11: **Relaxed state for the test case *euler-ller* with A = 0.01.** In (a) on the left, we show the color plot of ω and contours (in white dashed lines) of ϕ at the end of the simulation. On the right, we see the absolute difference between the solution and the rescaled fundamental eigenfunction of the Laplacian, the theoretical prediction from the variational principle (6.4). See the discussion in Section 2.2.1. The colorbar shows the intensity of the vorticity field. In (b) we show the scatter plot visualization of the functional relationship between ω and ϕ at the initial condition (black dots) and at the end of the simulation (red circles) compared with the prediction of the variational principle (green crosses). We see that, after relaxation, the discrete values of the variables have collapsed into a distinguishable linear functional relation, marked by the red circles. When compared with the functional relation predicted by the variational principle at equilibrium, cf. equation (6.4) with the theoretical prediction of the eigenvalue given by (6.8) (green crosses), we see that the two lines overlap. For a more quantitative estimate, we can compare the result of the fit of the red data points with the theoretical prediction, cf. Table 6.16.

In Figure 6.12 we show the relaxed state of the test case with $A = 0.1$. In Figure 6.12(a) we see the color plot and the absolute difference with respect to the theoretical prediction of the variational principle, as discussed in Section 2.2.1, while in (b) the scatter plot of the functional relation after relaxation. We observe a similar behavior as for the test case of Figure 6.11.

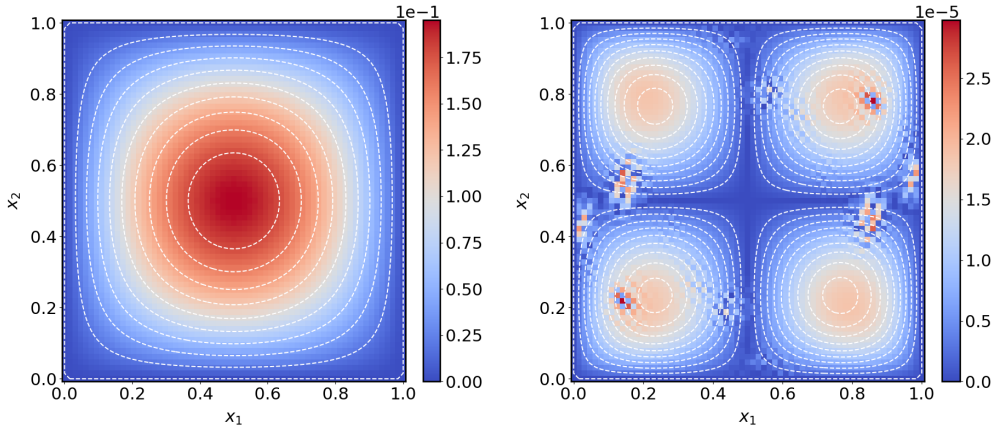

(a) Color plot and absolute difference with respect to the prediction of the variational principle.

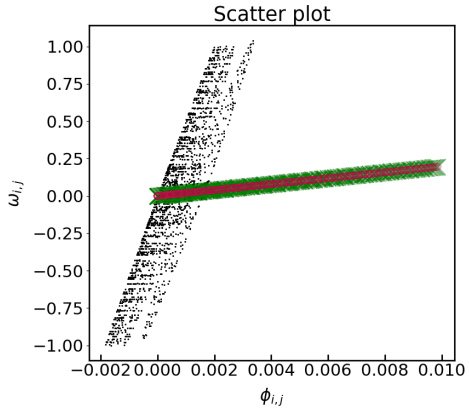

(b) Scatter plot.

Figure 6.12: **Relaxed state for the test case *euler-ller* with A = 0.1.** The same as in Figure 6.11, but for $A = 0.1$.

In Figure 6.13 we show the same results for the test case with $A = 1.0$: in (a) the color plot of the solution and in (b) the scatter plot. For all the three test cases, the relaxed state appears to be in agreement with the solution of the variational principle in equation (6.4).

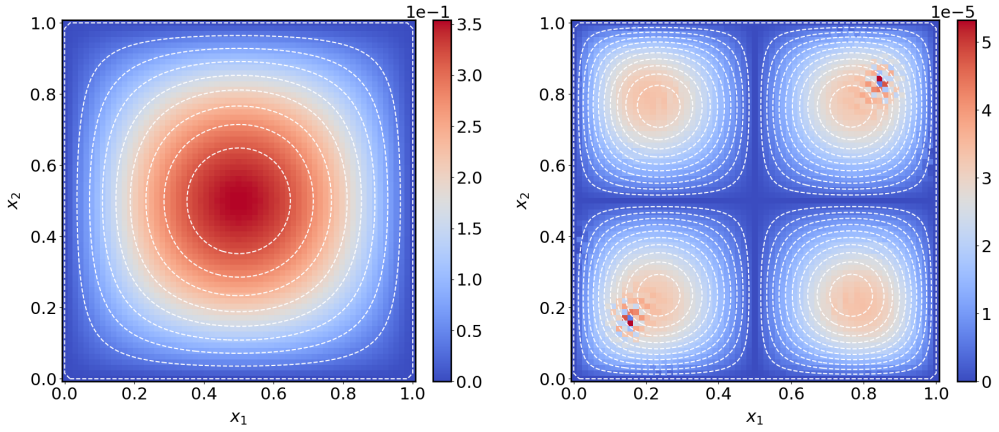

(a) Color plot and absolute difference with respect to the prediction of the variational principle.

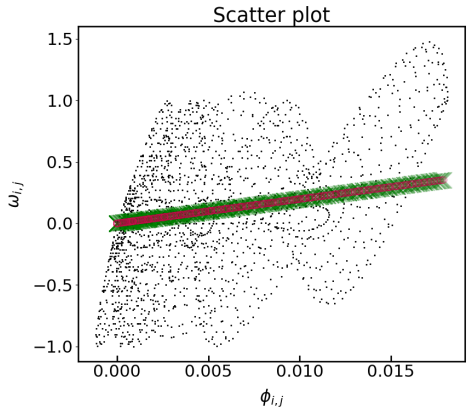

(b) Scatter plot.

Figure 6.13: **Relaxed state for the test case *euler-ller* with A = 1.0.** The same as in Figure 6.11, but for $A = 1.0$.

Let $f_{1,1}$ denote the eigenfunction of the Laplacian corresponding to the minimum eigenvalue on the domain Ω. See Appendix B for a summary of the eigenvalues and eigenfunctions of the Laplace operator.

We have shown in Section 2.2.1 that the relaxed state ω_e is proportional to an eigenfunction of the Laplacian operator, with proportionality constant determined by the energy of the initial condition. Specifically, with

$$\omega_e = f_{1,1}/\sqrt{\mathcal{N}}, \tag{6.9}$$

$\mathcal{N}$ being a normalization factor to be determined, the corresponding potential is $\phi_e = \omega_e/\lambda_{1,1} = f_{1,1}/(\lambda_{1,1}\sqrt{\mathcal{N}})$, and

$$H_0 = H(\omega_e) = \frac{1}{2}\int_\Omega \omega_e \phi_e \, dx = \frac{1}{\mathcal{N}}\Big(\frac{1}{2\lambda_{1,1}}\int_\Omega |f_{1,1}|^2 \, dx\Big),$$

where $H_0 = H(\omega_0)$ is the energy of the initial condition. The factor in parenthesis, on the other hand, amounts to the energy of $f_{1,1}$, defined by

$$H(f_{1,1}) = \frac{1}{2}\int_\Omega f_{1,1}\tilde{\phi}\, dx, \qquad -\Delta\tilde{\phi} = f_{1,1}, \qquad \tilde{\phi}_{|\partial\Omega} = 0,$$

where $\tilde{\phi}$ is the streaming potential associated to $f_{1,1}$ and it is given by $\tilde{\phi} = f_{1,1}/\lambda_{1,1}$. Therefore,

$$\mathscr{N} = \frac{H(f_{1,1})}{H_0}, \tag{6.10}$$

and this completely determines the relaxed vorticity ω_e.

In Table 6.15 we verify for each test case that equation (6.9), with a rescaling constant determined via (6.10), holds. The maximum difference between the relaxed solution and the solution of the variational principle is 10^{-5}, which is due to a residual relaxation error. If the simulation is continued, this error can be further reduced.

A	$\mathscr{H}_0$	$\mathscr{N}$	$S(\omega_0)$	$S(\omega_e)$	$(\|\|\omega_e - f_{1,1}/\sqrt{\mathscr{N}}\|\|_2)$
0.01	0.000235	26.898193	0.122424	0.004644	0.000009
0.1	.000241	26.281471	0.122627	0.004752	0.000009
1.0	0.000792	7.981245	0.143084	0.015649	0.000017

Table 6.15: **Comparison between the relaxed state for the *euler-ller* test case and the corresponding solution of the variational principle.** We report the energy of the initial condition and the rescaling factor $\mathscr{N}$ computed from Equation (6.10), the entropy of the initial and relaxed state and the L^2 norm between the solution and the solution predicted by the variational principle in equation (6.4).

To quantify the functional relation between the two dynamical variables, we can fit the linear function $f = ax + b$ to the red dots of Figure 6.11(b), 6.12(b) and 6.13(b). The estimated parameters of the fit can be compared against the lowest eigenvalue of the Laplace operator, as in Section 6.2.3 for the *euler-llgr* test case.

In Table 6.16 we report the values of the parameters a and b estimated with the fit for the three test cases and the relative error with respect to the lowest eigenvalue of the Laplace operator.

A	**a**	**b**	$\|b-\lambda\|/\lambda$
$A = 0.01$	-4.135301e-08	19.751108	0.000603
$A = 0.1$	-3.005136e-08	19.751106	0.000603
$A = 1.0$	1.497057e-09	19.751101	0.000602

Table 6.16: **Results of the fit and comparison with the solution of the variational principle in equation** (6.4) **for the *euler-ller* test case.** We report the values of the estimated parameters computed by fitting the experimental functional relation of Figure 6.11(b), 6.12(b) and 6.13(b), each corresponding to a different value of the Gaussian perturbation. In the third column, we report the relative error with respect to the lowest eigenvalue of the Laplace operator.

The relative error reported in Table 6.16 confirms that with this numerical scheme, the initial condition relaxes to the equilibrium state predicted by the variational principle in equation (6.4) for each value of the Gaussian perturbation.

We also ran a test case under the conditions of Table 6.13, but for the Gaussian perturbation $A = 0$. The initial condition is an exact equilibrium of the operator. However, the final state is the state of minimum entropy that we found for strictly positive values of the Gaussian perturbation, in accordance with the solution of the variational principle, and the evolution toward the constrained minimum follows Figure 6.10(b). On the one hand, one should recall that the exact eigenfunction cannot be represented in the finite-element space. Therefore the initial condition is projected onto the finite-element space and the result of the projection is not and exact equilibrium even when $A = 0$. On the other hand, we know from Section 6.2.3 that the finite-element scheme for the diffusion-like bracket (which in two dimensions is the same as the metric double bracket of Chapter 3) is affected by numerical diffusion that does not approximate well the null space of the evolution operator. The combination of these two effects is likely at the basis of the observed behavior.

This test case in particular illustrates the role of the energy conservation during the entropy relaxation process. For the chosen quadratic entropy, the variational principle of equation (6.4) characterizes a unique equilibrium state given by the eigenfunction of the Laplacian with lowest eigenvalue and with amplitude determined by the prescribed energy.

6.2.6 Test case IV: *euler-iler*

As discussed in Section 6.2.5 for the diffusion-like operator, we want to verify whether the collision-like operator relaxes to the closest equilibrium state or moves toward the solution of the variational principle of equation (6.4). We observe again the role of energy preservation during the dissipative dynamics. Finally, we discuss the differences with respect to the case of the diffusion-like operator presented in Section 6.2.5.

Table 6.17 is a summary of the setup for the test case. This is the same as the test case *euler-ller* of Section 6.2.5, but with the collision-like operator defined in equation (4.30).

Due to the computational cost of the collision-like operator, we choose only one value of the Gaussian perturbation A and we set it equal to $A = 0.01$.

Variable	**Value**
Operator	collision-like, equation (4.30)
Entropy	quadratic, $S(\omega) = \frac{1}{2}\int_\Omega \omega^2 dx$, equation (2.32)
Initial condition	Perturbed eigenfunction, equation (A.4)
Domain	rectangular $\Omega = [0,1]^2$
Boundary condition	Homogeneous Dirichlet
Resolution	64×64
GMRES tolerance	atol $= 10^{-15}$, rtol $= 10^{-13}$
Newton tolerance	atol $= 10^{-14}$, rtol $= 10^{-13}$
Picard tolerance	tol $= 10^{-12}$
Δt update, cf. Algorithm 1	$N_{\min} = 4$, $N_{\max} = 6$, $\Delta t_{\max} = 1$, $f_{\text{update}} = 2$

Table 6.17: **Setup for the *euler-iler* test case.** The value of A is fixed at $A = 0.01$.

In Table 6.18 we report runtime information. The computational cost of this test case from Table 6.18 appears to be less than the one estimated for the diffusion-like operator of Table 6.14. However, the computational complexity of each evaluation of the collision-like operator is significantly higher than that of the diffusion-like operator, as discussed in Section 6.1.

A	Time steps	Picard	Newton	GMRES	dt_i	dt_f
0.01	998	4.28	1.03	74.26	0.01	1.28

Table 6.18: **Runtime information for the *euler-iler* test case.** The same as in Table 6.8. The value of the Gaussian perturbation is also reported.

We show in Figure 6.14 the temporal evolution of the relative energy error and entropy. The maximum relative error on energy conservation is 10^{-11}, while entropy is dissipated as expected from theory.

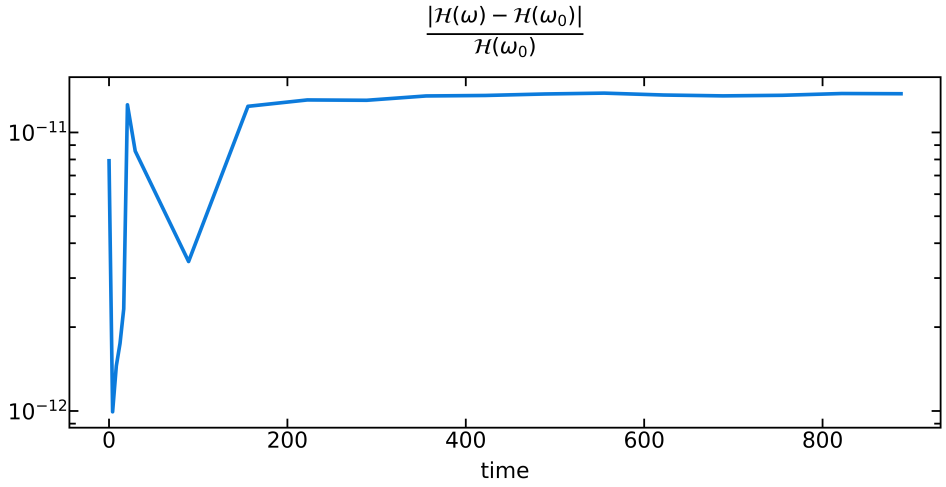

(a) Temporal evolution of the relative energy error.

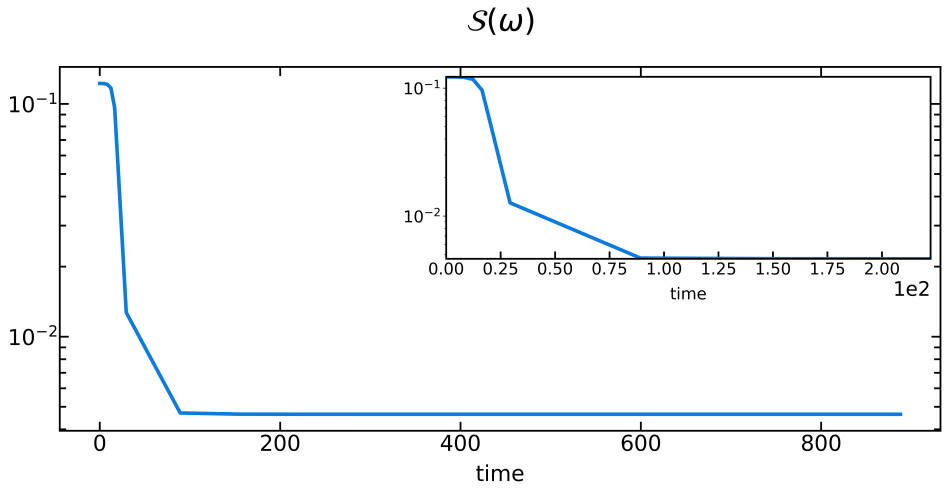

(b) Temporal evolution of the entropy.

Figure 6.14: **Evolution of the test case *euler-iler*.** The same as in Figure 6.1, but for the collision-like operator and with the initial condition discussed in Section A.3.2. The error on the energy conservation saturates at 10^{-11}. The scale in (b) is semi-logarithmic.

In Figure 6.15 we show the solution at the last point in time and the corresponding solution of the variational problem in equation (6.4). The contours of the vorticity and its scalar potential in Figure 6.15(a) on the left are parallel to each other, suggesting that a relaxed state has been reached. On the right-hand side of Figure 6.15(a), we compute the difference between the relaxed state and the solution of the variational principle of equation (6.4), computed as discussed in Section 6.2.5.

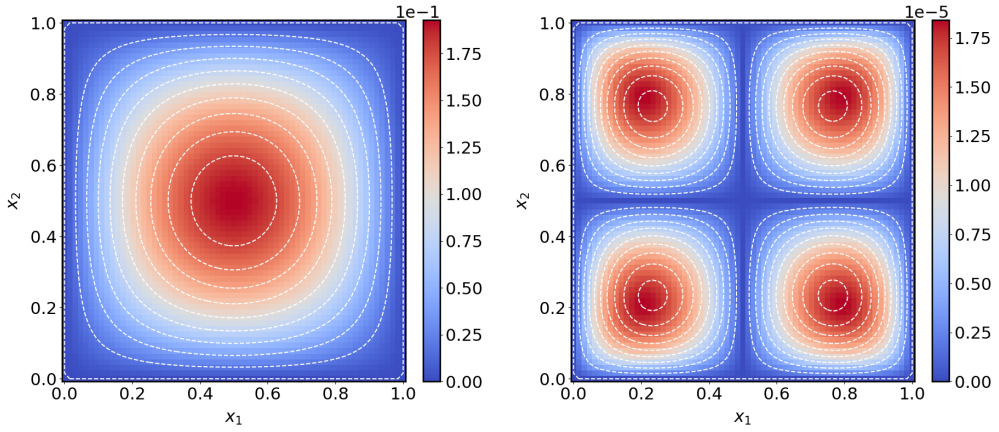

(a) Color plot and absolute difference with respect to the prediction of the variational principle.

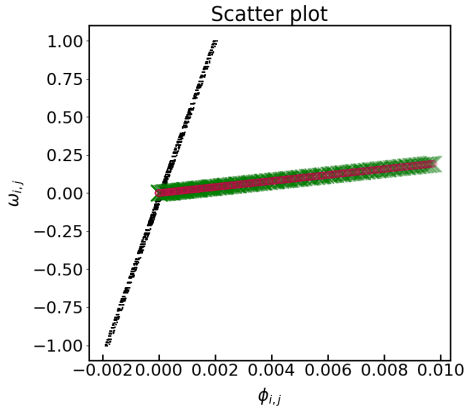

(b) Scatter plot.

Figure 6.15: **Relaxed state for the test case *euler-iler* with A = 0.01.** The same as in Figure 6.11, but for the case of the collision-like operator. One should notice that the difference between the relaxed state and the corresponding solution of the variational principle on the right of (a) does not show the localized features observed in Figure 6.11(a) for the diffusion-like operator.

It is interesting to compare Figure 6.15(a) with 6.11(a), which shows the solution relaxed with the diffusion-like operator. We conclude that the sharp features observed in Figure 6.11(a) are a characteristic of the diffusion-like operator.

In Figure 6.15(b) we show the scatter plot representing the functional relation between the dynamical variables at the initial (with black dots) and final (with red circles) time. The prediction of the variational principle is shown by green crosses.

In Table 6.19 we report the initial energy, the computed rescaling factor (6.10), the entropy of the solution at the initial and final time and the L^2 norm of the difference between the relaxed state and the solution of the variational principle of equation (6.4). We can compare this with the row corresponding to $A = 0.01$ in Table 6.15, to see that they are in fact the same values, up to numerical error.

In Table 6.20 we report the coefficients a and b estimated by fitting the red dots of Figure 6.15(b) with the linear function $f = ax + b$ and the relative error with respect to the lowest eigenvalue of the Laplacian, cf. Appendix B.

The results in Table 6.20 confirm that the system has relaxed to the eigenfunction of the Laplacian predicted by the variational principle.

Finally, in Figure 6.16 we show a comparison between an intermediate state of the dynamics of the test case *euler-ller* and *euler-iler*, both with $A = 0.01$. In Figure 6.16(a)

A	$\mathscr{H}_0$	$\mathscr{N}$	$S(\omega_0)$	$S(\omega_e)$	$(\|\|\omega_e - f_{1,1}/\sqrt{\mathscr{N}}\|\|_2)$
0.01	0.000235	26.898193	0.122424	0.004643	0.000009

Table 6.19: **Comparison between the relaxed state for the *euler-iler* test case and the corresponding solution of the variational principle.** Same as in Table 6.15, but for the case of the collision-like operator and $A = 0.01$.

a	**b**	$\|b-\lambda\|/\lambda$
-3.754632e-09	19.751101	0.000602

Table 6.20: **Results of the fit and comparison with the solution of the variational principle in equation** (6.4) **for the *euler-iler* test case.** We report the values of the coefficients computed by fitting the function $f = ax + b$ to the numerical values represented by the red dots of Figure 6.15(b). In the last column, we report the relative error with respect to the lowest eigenvalue of the Laplace operator.

and 6.16(b) we show the color plot. The intermediate states are selected having the same value of entropy, $S(\omega) = 0.01$. We can see from the plots how the time evolution with the two operators is different.

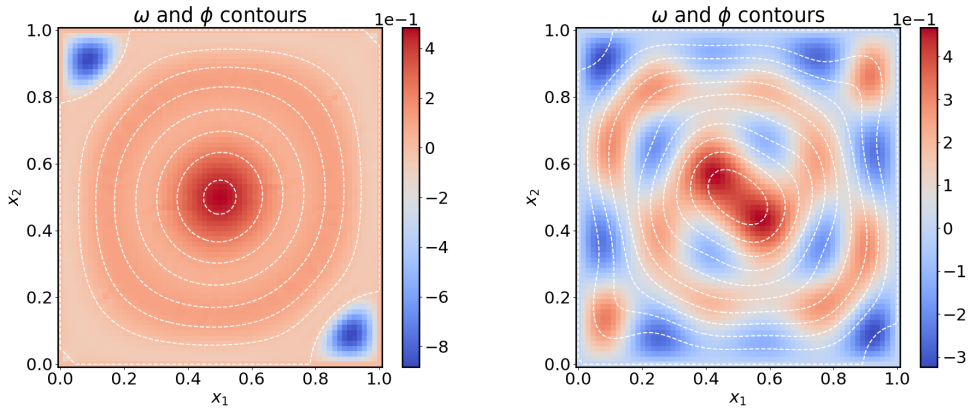

(a) (b)

Figure 6.16: **Intermediate state of the test case *euler-ller* (a) and *euler-iler* (b) with $A = 0.01$.** We show the color plot of the vorticity and the contours (in white dashed lines) of its scalar potential in (a) for the case of the diffusion-like operator and in (b) for the case of the collision-like operator. The colorbar shows the intensity of the vorticity field. The two states are selected so that they have the same entropy. These plots show how different is the dynamics produced by the two operators.

As in Section 6.2.5, we also ran a test case with the Gaussian perturbation $A = 0$. We observe a similar behavior: the operator relaxes the initial condition toward a solution that is compatible with the solution of the variational principle, cf. Figure 6.15. The entropy relaxation follows Figure 6.14(b). If we compare the entropy evolution of Figure 6.14(b) for the collision-like operator with the corresponding Figure 6.10(b) for the diffusion-like operator, we notice that the former shows an initially flat entropy evolution, while the latter starts dissipating since the beginning. The behavior of the collision-like operator seems consistent with what one would expect. Equation (4.28) with $M = 1$ implies that the bracket (F, S) evaluated at any ω such that $\omega = \lambda\phi$, $\lambda \in \mathbb{R}$, vanishes. Hence the initial condition with $A = 0$ is an exact equilibrium point of the collision-like metric operator. The discrete initial condition, however, is not an exact equilibrium of the discretized operator. This might explain the behavior for $A = 0$.

6.2.7 Test case V: *euler-lhgr*

This is the first test case for the diffusion-like operator for which we choose a trascendental function as entropy density. The aim of this test case is to understand the relaxation mechanism for this class of entropy functionals.

In Table 6.21 we show the setup of this test case. It is the same as that of Table 6.3, but for a logarithmic entropy functional. For the solution to be compatible with the necessary condition of the variational principle, cf. equation (6.4), one must have $\omega_{|\partial\Omega} = 1/e$ if $\phi_{|\partial\Omega} = 0$, hence we choose the offset $\mathsf{C} = 1/e$ of the Gaussian defined in equation (A.1), and non-homogeneous boundary conditions $\omega_{|\partial\Omega} = 1/e$.

Variable	Value
Operator	diffusion-like, equation (4.62)
Entropy	trascendental, $S(\omega) = \int_\Omega \omega \log(\omega)\, dx$, equation (2.37)
Initial condition	Gaussian, cf. (A.1), $A = 10$, $\mathsf{C} = e^{-1}$, $\sigma^2_{x_1} = 0.01$, $\sigma^2_{x_2} = 0.07$
Domain	rectangular $\Omega = [0,1]^2$
Boundary condition	non-homogeneous Dirichlet
Resolution	64×64
GMRES tolerance	atol $= 10^{-15}$, rtol $= 10^{-13}$
Newton tolerance	atol $= 10^{-14}$, rtol $= 10^{-13}$
Δt update, cf. Algorithm 1	$\Delta t_{\max} = 0.001$

Table 6.21: **Setup for the *euler-lhgr* test case.**

In Table 6.22 we provide runtime data of the test case. Because Proposition 5.4.2 does not hold for a logarithmic entropy, the discretization error is controlled by choosing a constant time step, $\Delta t_n = \Delta t = \Delta t_{\max}$, cf. Table 6.21. The numerical scheme still preserves the non-positive definiteness of the discretized brackets, but the time discretization introduces additional contributions to the entropy variation $S(\omega_h^{n+1}) - S(\omega_h^n)$ which do not have a definite sign and can become important when the brackets are zero, that is, near an equilibrium. We observe that entropy initially decreases while the solution approaches an equilibrium, reaches a minimum and then grows again. We attribute the entropy growth to the time discretization error and stop the simulation at the entropy minimum.

In this Section, we show the results of the test case at the entropy minimum.

Time steps	Newton	GMRES	dt_i	dt_f
151	2.19	58.87	0.001	0.001

Table 6.22: **Runtime information for the *euler-lhgr* test case.** The same as caption of Table 6.4, but for a logarithmic entropy functional, equation (2.37).

In Figure 6.17 we show the evolution in time of the relative energy error (with respect to the initial value) (a) and the entropy (b). The same remarks discussed in Section 6.2.3 apply here for the conservation of the energy.

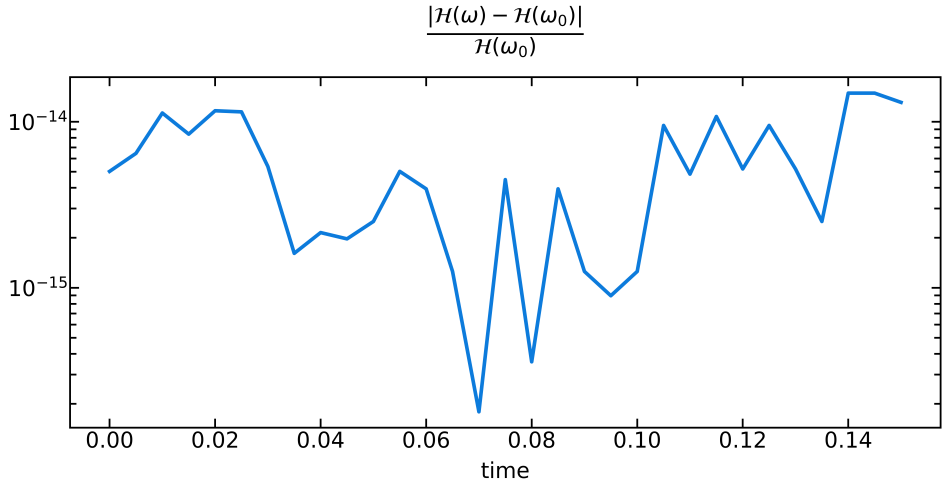

(a) Temporal evolution of the relative energy error.

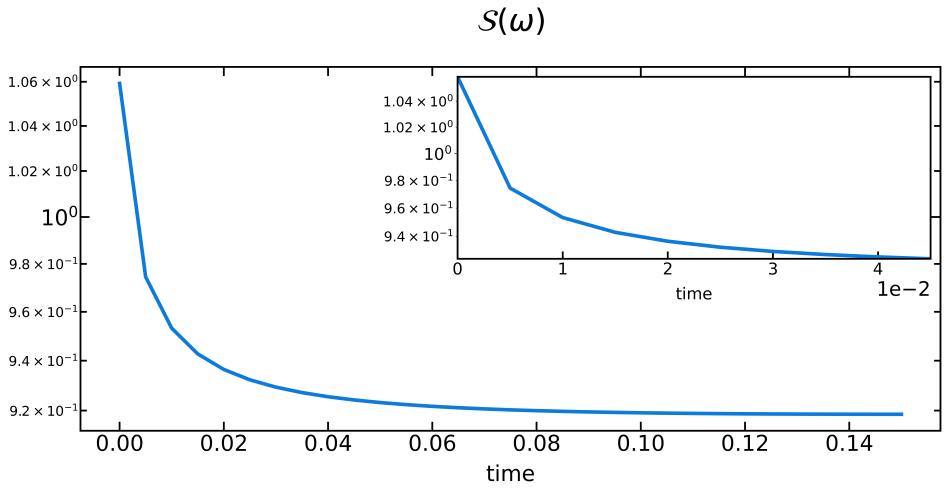

(b) Temporal evolution of the entropy.

Figure 6.17: **Evolution of the test case *euler-lhgr*.** The same as in Figure 6.1, but for the logarithmic entropy of equation (2.37).

In Figure 6.18 we show the state at the entropy minimum: in (a) we see the color plot and in (b) the scatter plot. Despite the fact that the contours of ω and ϕ in (a) seem to be parallel to each other, the scatter plot in (b) shows some correlation between ω and ϕ, but not a precise functional relation. The green crosses of Figure 6.18(b) are computed with the expected relation at entropy minimum, cf. equation (6.4),

$$\omega = \exp(\lambda\phi - 1), \tag{6.11}$$

and a theoretical estimation of the eigenvalue λ. In fact, equation (6.4) with $s'_\omega(\omega) = 1 + \log(\omega)$, after multiplying by ω and integrating over the domain, becomes

$$M(\omega) + S(\omega) = 2\lambda H(\omega),$$

where

$$M(\omega) = \int_\Omega \omega \, dx.$$

Therefore,

$$\lambda = \frac{S_f + M_f}{2H_0}, \tag{6.12}$$

where S_f and M_f are the entropy and the functional M evaluated at the last point in time, respectively, whereas H_0 is the conserved energy. Here, equation (6.12) yields $\lambda = 13.626$.

We conclude that the evolution with the diffusion-like operator and a trascendental entropy functional has not relaxed the initial condition to a constrained entropy minimum. We say that the diffusion-like operator has not completely relaxed the initial condition.

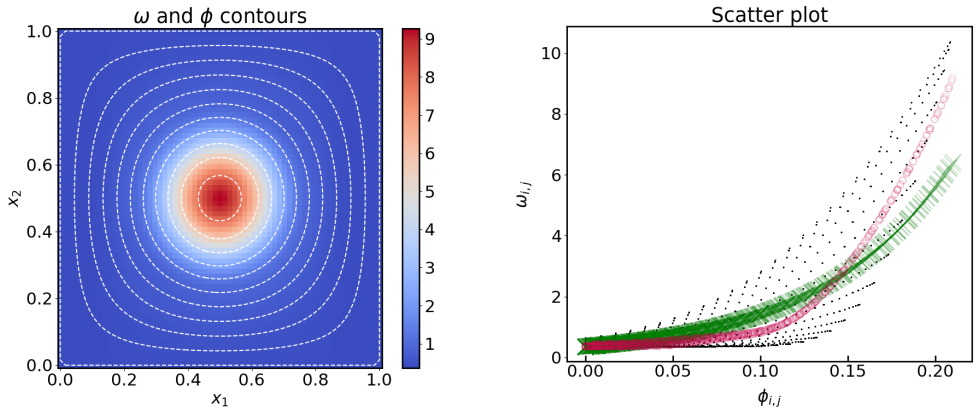

(a) Color plot. (b) Scatter plot.

Figure 6.18: **Relaxed state of the test case *euler-lhgr*.** In (a) we see the color plot of the vorticity variable and the contours of its scalar potential (in white dashed lines) at the final state of the simulation. The colorbar shows the intensity of the vorticity field. In (b) we plot (with the red dots) the functional relation between ω and ϕ at the final point in time of the simulation against the functional relation at the start (with the black dots). The green dots are plot with equation (6.11), with λ computed as in (6.12). We can see that they do not correspond to the values at the end of the simulation over the entire domain. The original relation has not collapsed onto the predicted functional relationship.

6.2.8 Test case VI: *euler-ihgr*

This test case illustrates how the collision-like operator works with a trascendental choice of the entropy density. It is interesting to compare the behavior of the diffusion- and collision-like operator under this choice.

In Table 6.23 we show the setup of this test case. It is the same of the test case *euler-lhgr* in Section 6.2.7, but for the collision-like operator.

Variable	Value
Operator	collision-like, equation (4.31)
Entropy	logarithmic, $S(\omega) = \int_\Omega \omega \ln \omega dx$, equation (2.37)
Initial condition	Gaussian, cf. (A.1), $A = 10$, $\mathsf{C} = e^{-1}$, $\sigma_{x_1}^2 = 0.01$, $\sigma_{x_2}^2 = 0.07$
Domain	rectangular $\Omega = [0,1]^2$
Boundary condition	non-homogeneous Dirichlet
Resolution	64×64
GMRES tolerance	atol $= 10^{-15}$, rtol $= 10^{-13}$
Newton tolerance	atol $= 10^{-14}$, rtol $= 10^{-13}$
Picard tolerance	tol $= 10^{-12}$
Δt update, cf. Algorithm 1	$\Delta t_{\max} = 0.001$

Table 6.23: **Setup for the *euler-ihgr* test case.**

In Table 6.24 we show runtime information for this test case. We can repeat the same remarks of Section 6.2.7. The test case is run with a fixed time step to avoid accumulation of discretization error and the results are taken at the entropy minimum.

Time steps	Picard	Newton	GMRES	dt_i	dt_f
1232	5.07	1.03	90.98	0.001	0.001

Table 6.24: **Runtime information for the *euler-ihgr* test case.** The same as in Table 6.8, but with a logarithmic entropy functional, equation (2.37).

In Figure 6.19 we show the evolution in time of energy and entropy. In (a) we see that the maximum error on energy conservation is 10^{-11}. The entropy in (b) is monotonically non increasing, in virtue of the choice of the small and constant time step, since Proposition 5.2.2 does not apply in this case.

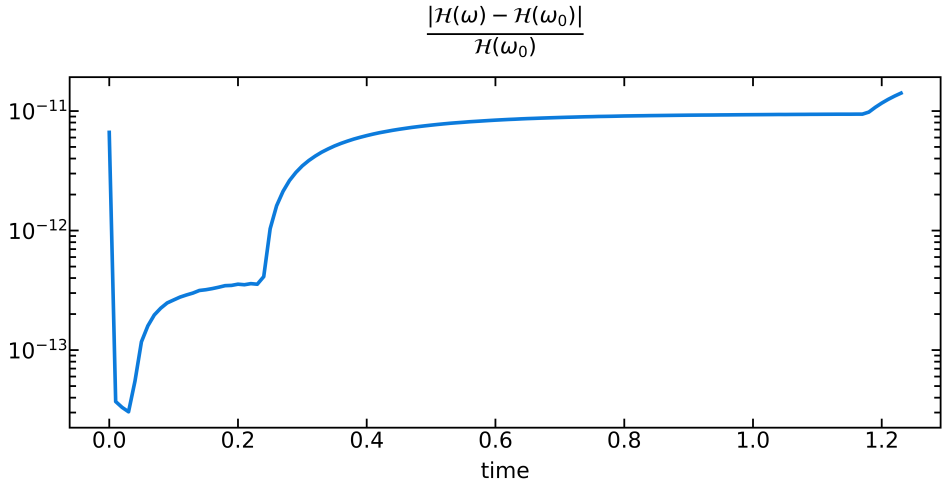

(a) Temporal evolution of the relative energy error.

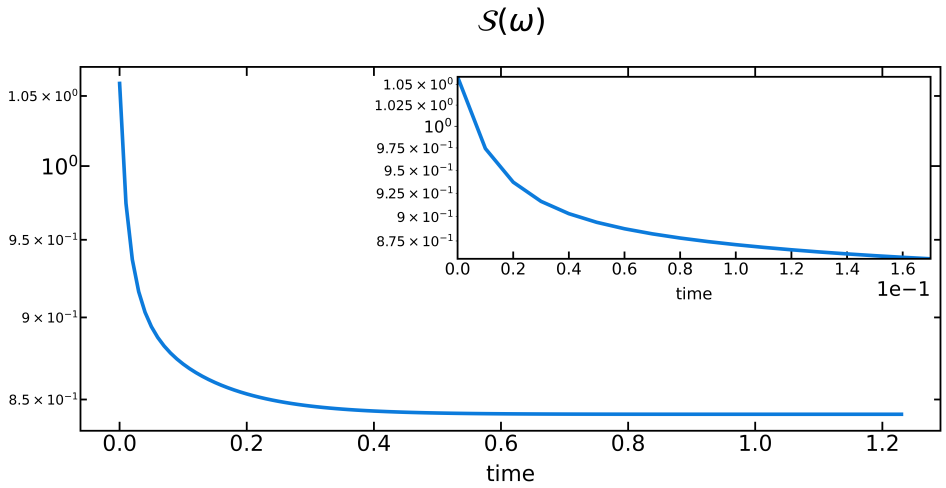

(b) Temporal evolution of the entropy.

Figure 6.19: **Evolution of the test case *euler-ihgr*.** The same as in Figure 6.1, but for the collision-like operator and for the logarithmic entropy of equation (2.37). In (a) the maximum error on energy conservation is 10^{-11}.

In Figure 6.20 we show the state at the entropy minimum. From the color plot in (a) we see that the contours of ω and ϕ are qualitatively parallel. In (b) the scatter plot shows that the initial state, the black data points, has collapsed onto a functional relation, represented by the red circles. These data points in turn overlap with the functional relation predicted by the variational principle, cf. equation (6.11), plot with the green crosses. We use equation (6.12) to estimate the eigenvalue, and we find $\lambda = 14.1869$.

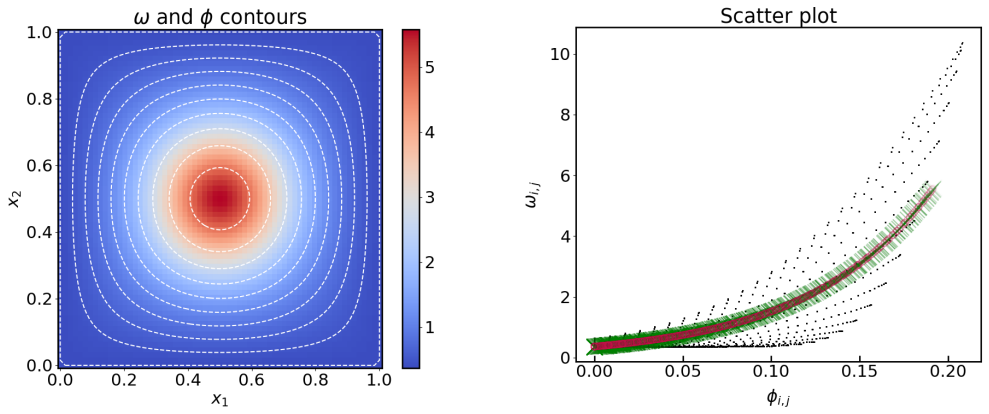

(a) Color plot. (b) Scatter plot.

Figure 6.20: **Equilibrium state of the test case *euler-ihgr*.** In Figure 6.20(a) we see the color plot of the vorticity variable and the contours of its scalar potential (in white dashed lines) at the final state of the simulation. The accompanying color bar shows the intensity of the vorticity field. In Figure 6.20(b) we plot (with the red dots) the functional relation between ω and ϕ at the state of minimum entropy against the functional relation at the beginning of the simulation (with the black dots). The green dots represent the functional relation predicted by the variational principle, i.e. an exponential relation between the vorticity and its scalar potential, with the eigenvalue estimated by equation (6.12). We can also fit the red dots of the final functional relation to numerically estimate the values of the coefficient, and compare them with the values predicted in theory, cf. equation (6.12), as shown in Table 6.25.

We can also compare the theoretically estimated eigenvalue with the result of a fit of the red data points of Figure 6.20(b), computed using non-linear least squares with fitting function $f = \exp(bx-1)$, b being the fit parameter. The value of the estimated coefficient is reported in Table 6.25, together with the comparison with the solution of equation (6.12).

b	$\|b-\lambda\|/\lambda$
14.1842	0.0002

Table 6.25: **Results of the fit and comparison with the solution of equation** (6.12) **for the *euler-ihgr* test case.** Values of the coefficients computed by fitting the the red circles of Figure 6.20(b) via the nonlinear function $f = \exp(b\,x-1)$.

Due to the different behavior of the diffusion- and collision-like operators, it is interesting to compare an intermediate state, which shows how the two operators generate very distinct dynamics. In Figure 6.21 we compare two intermediate states of the test case *euler-lhgr* (a) and *euler-ihgr* (b). For a meaningful comparison, the intermediate states are selected such that the entropy is the same, i.e. $S(\omega) = 0.936$.

We use the scatter plot diagnostics discussed in Appendix A.1 for this comparison. In both cases, the functional relation is shown with black dots representing the discrete values of ω and ϕ.

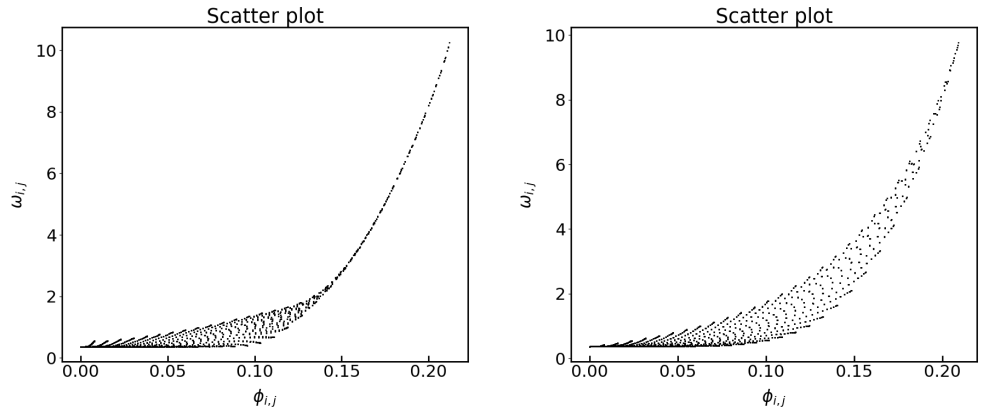

(a) (b)

Figure 6.21: **Intermediate state of the test case *euler-lhgr* (a) and *euler-ihgr* (b).** In (a) and (b) we show the scatter plot of two intermediate states of the dynamics evolved with the diffusion-like and collision-like operator, respectively. The states have been selected to have the same value of entropy. In both cases, we show the functional relation (with black dots) between the dynamical variables. As the system is still relaxing, we see that the black dots do not constitute a functional relation. We notice the qualitative different way in which the two systems are relaxing towards the final state.

The collision-like operator appears to be guiding the vorticity to the equilibrium state predicted by the variational principle. We stress again that this does not happen for the test case *euler-lhgr* discussed in Section 6.2.7, which is run under the same conditions except for the diffusion-like operator. In that case, we see that the final state does not exhibit a clear functional relation between the dynamical variables.

6.3 Grad-Shafranov equation

In this Section we discuss a few examples of applications of the relaxation methods described in Section 4.2 and 4.3 for the Grad-Shafranov equation. In Section 6.3.1 we recall the theoretical setup, while we refer again to Section 6.1 and Appendix A.1 for the computational aspects and the diagnostics used to analyze the numerical results. We present the initial conditions in Appendix A.4 and the list of the considered experiments in Section 6.3.2. From Section 6.3.3 to 6.3.6 we discuss the test cases.

6.3.1 Experiment's setup

In this Section we summarize the common setup for the Grad-Shafranov equation. With reference to the definition given in Section 2.1.2, we consider a toroidal domain $A \subset \mathbb{R}^3$ defined in cylindrical coordinates $x = (R\cos\varphi,\ -R\sin\varphi,\ z)$ with $\varphi \in [0, 2\pi]$ and (R,z) in a bounded domain Ω compactly included in $\mathbb{R}^+ \times \mathbb{R}$, that is, $\min R > 0$ on $\overline{\Omega}$.

All variables are functions of $(R,z) \in \Omega$ only. The dynamical variable u is defined as

$$u = (4\pi/c) R j_\varphi, \tag{6.13}$$

where j_φ is the φ-component of the current density and c is the speed of light in vacuum (using c.g.s. units). The scalar potential of u is the flux function ψ, which is determined by solving the following linear elliptic problem with homogeneous Dirichlet boundary conditions

$$-\Delta^\star \psi = u \qquad \psi_{\partial\Omega} = 0 \tag{6.14}$$

where $\Delta^\star = R\partial_R(R^{-1}\partial_R) + \partial_z^2$ is the Grad-Shafranov operator.

The energy and entropy functionals are given by

$$H(u) = \frac{1}{2}\int_\Omega u(R,z)\psi(R,z)\frac{dRdz}{R}, \qquad S(u) = \int_\Omega s(R,u(R,z))\frac{dRdz}{R}, \tag{6.15}$$

where the measure on Ω is $d\mu(R,z) = R^{-1}dRdz$, cf. equation (2.43). The choice of the integrand $s = s(R,u)$ will vary according to the experiment.

From equation (6.15) we can compute the functional derivatives with respect to the dynamical variable u,

$$\frac{\delta H}{\delta u} = \psi, \qquad \frac{\delta S}{\delta u} = s'_u(R,u), \tag{6.16}$$

where $s'_u(R,u) = \partial s(R,u)/\partial u$.

We also recall from equation (2.45) that the necessary condition for the variational principle in this case gives

$$s'(R,u) + \lambda\psi = 0. \tag{6.17}$$

For the following test cases we choose the entropy as

$$S(u) = \frac{1}{2}\int_\Omega \frac{u^2}{CR^2 + D} R^{-1} dRdz, \tag{6.18}$$

with $C = 0.6$ and $D = 0.2$. We will refer to this entropy as Herrnegger-Maschke entropy, since it leads to the solutions of Hernnegger-Maschke [57, 58].

6.3.2 Selected experiments

We present in Table 6.26 the list of experiments for Grad-Shafranov.

Name	**Operator**	**Entropy**	**Initial condition**	**Domain**
gs-lmgr	diffusion-like	Herrnegger-Maschke	gaussian	rectangular
gs-imgr	collision-like	Herrnegger-Maschke	gaussian	rectangular
gs-lmgc	diffusion-like	Herrnegger-Maschke	gaussian	czarny
gs-imgc	collision-like	Herrnegger-Maschke	gaussian	czarny

Table 6.26: **List of experiments for the Grad-Shafranov equation.** The same as in Table 6.2, but for the Grad-Shafranov equation.

6.3.3 Test case I: *gs-lmgr*

We consider first the Gaussian initial condition in a rectangular domain. This is similar to the test case discussed in Section 6.2.3 for the Euler's equations except for two aspects. The first is the non-trivial metric $R^{-1}\, dR\, dz$ leading to the variable-coefficient equation (2.20). The second is the non-trivial weight in the definition of the entropy functional in equation (6.18).

The setup is summarized in Table 6.27. Here, we consider the case of the diffusion-like operator and with the Herrnegger-Maschke entropy given in equation (6.18). The initial condition is an anisotropic Gaussian defined in a rectangular domain.

Variable	**Value**
Operator	diffusion-like, equation (4.65) with (4.67)
Entropy	Herrnegger-Maschke, $S(u) = \frac{1}{2}\int_\Omega \frac{u^2}{CR^2+D}\frac{dRdz}{R}$, equation (6.18)
Initial condition	Gaussian, equation (A.6), with $A = 0.1$, $\sigma_R^2 = 0.5$, $\sigma_z^2 = 3.2$
Domain	rectangular $\Omega = [1,7]\times[-9.5,9.5]$
Boundary condition	Homogeneous Dirichlet
Resolution	64×64
GMRES tolerance	atol $= 10^{-15}$, rtol $= 10^{-13}$
Newton tolerance	atol $= 10^{-14}$, rtol $= 10^{-13}$
Δt update, cf. Algorithm 1	$N_{\min} = 3$, $N_{\max} = 6$, $\Delta t_{\max} = 5000$, $f_{\text{update}} = 2$

Table 6.27: **Setup of the *gs-lmgr* test case.**

Table 6.28 reports the runtime information for this test case. Notice that convergence to the relaxed state is very slow.

Time steps	Newton	GMRES	dt_i	dt_f
133533	1.09	28.52	0.01	5242.88

Table 6.28: **Runtime information for the *gs-lmgr* test case.** From left to right, we show the total number of time steps, the average number of Newton iterations per time step and the average number of GMRES iterations per Newton step. Also reported are the initial (dt_i) and final (dt_f) values of the time step, which is adapted automatically according to the number of Newton iterations per time step, as discussed in Section 6.1.

In Figure 6.22, we show the evolution of the relative energy error (with respect to the initial value) (a) and of the entropy (b). Notice that the relative energy error saturates at 10^{-10} and that the entropy is dissipated as expected.

Figure 6.23 shows the relaxed state for this test case, with a color plot (a) and a scatter plot (b) of the variables. We plot the variable u rescaled by the factor $(CR^2 + D)$ because this is the quantity predicted to be in linear relation with the scalar potential ψ according to equation (6.19). Note from the the color plot (a) that the contours of the selected quantities appear parallel to each other. Also, we observe that the red circles in the scatter plot (b) coincide with the predicted functional relation, represented by the green crosses.

For this particular choice of the entropy functional, the necessary condition for the variational principle, cf. equation (6.4), reads

$$\frac{u}{(CR^2+D)} + \lambda\,\psi = 0, \tag{6.19}$$

where C and D are given after equation (6.18), and λ is a real number. Equation (6.14) leads to the generalized eigenvalue problem

$$-\Delta^*\psi = \lambda\,(CR^2+D)\,\psi, \tag{6.20}$$

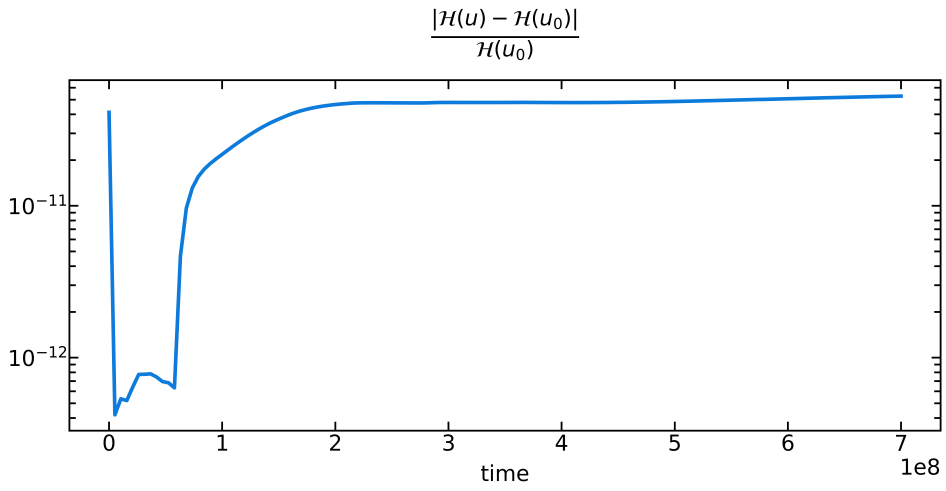

(a) Temporal evolution of the relative energy error.

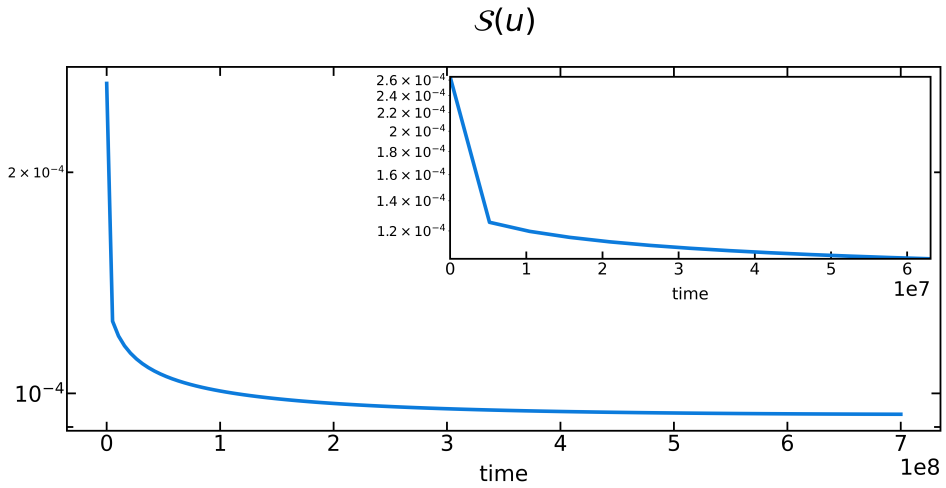

(b) Temporal evolution of the entropy.

Figure 6.22: **Evolution of the test case *gs-lmgr*.** In (a) we see the temporal evolution of the relative energy error (with respect to the initial value) in a semi-logarithmic scale. The maximum error on the energy conservation saturates at 10^{-10}, to be attributed to the finite precision with which the equations are solved. In (b) the temporal evolution of the entropy is shown. The inset shows the evolution of the same quantity during the early phase of the experiment. The visible jumps in (a) and the corners in (b) are due to restarts of the simulation with a larger time step.

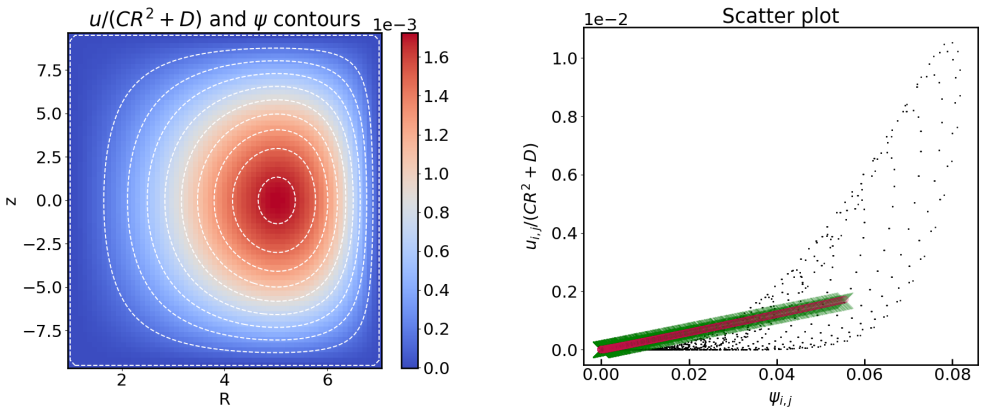

(a) Color plot. (b) Scatter plot.

Figure 6.23: **Relaxed state for the *gs-lmgr* test case.** In (a) we see the color plot of $u/(CR^2+D)$ and the contours of ψ (with white dashed lines) at the end of the simulation. The colorbar shows the intensity of $u/(CR^2+D)$. In (b) we see the scatter plot of $u/(CR^2+D)$ and ψ at different points in time. The black dots represent the functional relation at the beginning of the simulation while the red circles refer to the relaxed state. Green crosses markers represent the final functional relation predicted by the variational principle, cf. equation (6.17) with λ estimated by an iterative method [1, pp. 22-23, equations 2.111 and 2.112]. We see that the black dots, initially spread over the domain, have collapsed into a distinguishable functional relation, which overlaps with the prediction of the variational principle.

with $\Delta^* = R\partial_R(R^{-1}\partial_R) + \partial_z^2$. Equation (6.20) is solved numerically using for example the iterative method [1, pp. 22-23, equations 2.111 and 2.112].

We can use linear least squares via the function $f(x) = a + bx$ to fit the final functional relation of Figure 6.23(b), and compare the estimated value of the coefficients with the numerical approximation of the solution of equation (6.20) obtained by means of the iterative method. Direct solution of equation (6.20) yields the eigenvalue $\hat{\lambda}_0 = 0.030302$ in 60 iterations.

In Table 6.29 we report the values of the estimated coefficients of the fitted linear relation, and the error between the estimated and the directly computed eigenvalue.

a	**b**	$\lvert\hat{\lambda}_0 - b\rvert/\hat{\lambda}_0$
-0.00002	0.030881	0.019

Table 6.29: **Results of the fit and comparison with the direct solution of equation** (6.20) **for the test case *gs-lmgr*.** Values of the coefficients computed by fitting the experimental functional relation of Figure 6.23(b) and the relative error between the estimated coefficient and the eigenvalue computed by direct solution of equation (6.20).

This test case numerically demonstrates that the diffusion-like operator also works when a metric term is included in the formulation of the operator and when the the entropy functional explicitly depends on the coordinates of the domain. During the simulation, the energy functional is preserved and the entropy relaxes toward a constrained minimum.

6.3.4 Test case II: *gs-imgr*

Here we present the same test case described in Section 6.3.3, evolved with the collision-like operator of Section 4.2.

The setup for this test case is summarized in Table 6.30.

Variable	Value
Operator	collision-like, equation (4.42)
Entropy	Herrnegger-Maschke, $S(u) = \frac{1}{2}\int_\Omega \frac{u^2}{CR^2+D}\frac{dRdz}{R}$, equation (6.18)
Initial condition	Gaussian, equation (A.6), with $\sigma_R^2 = 0.5$, $\sigma_z^2 = 3.2$
Domain	rectangular $\Omega = [1,7]\times[-9.5,9.5]$
Boundary condition	Homogeneous Dirichlet
Resolution	64×64
GMRES tolerance	atol $= 10^{-15}$, rtol $= 10^{-13}$
Newton tolerance	atol $= 10^{-14}$, rtol $= 10^{-13}$
Picard tolerance	tol $= 10^{-12}$
Δt update, cf. Algorithm 1	$N_{\min} = 6$, $N_{\max} = 10$, $\Delta t_{\max} = 1$, $f_{\text{update}} = 2$

Table 6.30: **Setup of the *gs-imgr* test case.**

In Table 6.31 we report the runtime information for the test case. By comparing this with Table 6.28 for the diffusion-like operator, we observe that the simulation converges in 126× less number of time steps. However, each step has a greater computational cost because of the evaluation of the diffusion and friction coefficients. Note that, because of the choice of the entropy functional, the system we solve at each Picard step is linear.

Time steps	Picard	Newton	GMRES	dt_i	dt_f
1055	5.06	1.0	111.85	0.01	1.28

Table 6.31: **Runtime information for the *gs-imgr* test case.** We show the total number of time steps, the average number of Picard iterations per time step, the average number of Newton iterations per Picard step and the average number of GMRES iterations per Newton step. Also reported are the initial (dt_i) and final (dt_f) values of the time step, which is changed automatically according to the number of Picard iterations per time step, as discussed in Section 6.1.

In Figure 6.24 we see the relative energy error (with respect to the initial value) (a) and the entropy (b). The same remarks formulated in Section 6.3.3 for the test case evolved with the diffusion-like operator apply. In Figure 6.25 we see the relaxed state: panel (a) shows the color plot, while (b) the scatter plot. We notice that the functional relation at the final state, represented by the red circles, overlaps with the linear relation (green crosses) predicted by the variational principle, cf. the discussion at the end of Section 6.3.3. We can compute the prediction of the variational principle (6.17) and compare the eigenvalue $\hat{\lambda}_0$, which has the same value as in Section 6.3.3, with the result of a fit of the scatter plot in Figure 6.25(b), as discussed in Section 6.3.3 for the *gs-lmgr* test case. We show these results in Table 6.32. Finally, we notice that the relative error with respect to the solution of equation (6.20) is three orders of magnitude less than the case of the diffusion-like operator, cf. Table 6.29.

a	b	$\|\hat{\lambda}_0 - b\|/\hat{\lambda}_0$
1.334733e-08	0.030302	1e-5

Table 6.32: **Results of the fit and comparison with the direct solution of equation** (6.20) **for the test case *gs-imgr*.** The same as in Table 6.29, but for the collision-like operator. The fit is applied to the functional relation represented by the red circles of Figure 6.25(b).

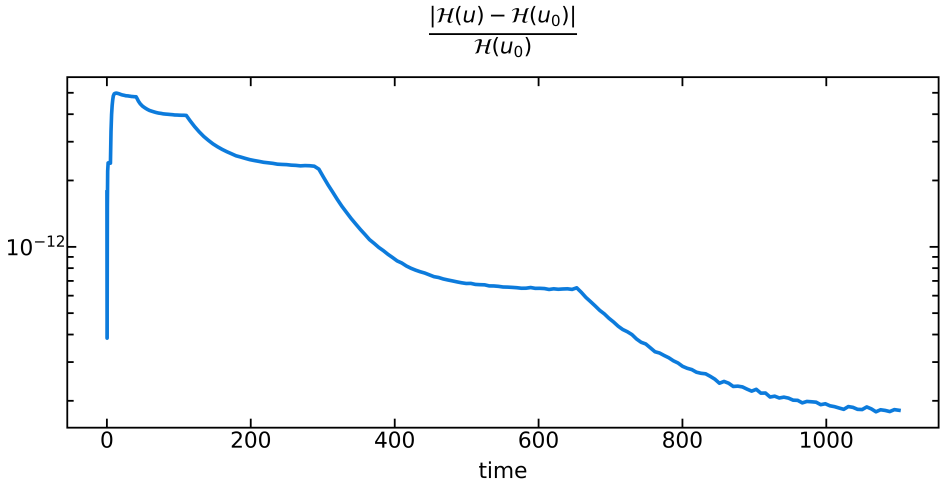

(a) Temporal evolution of the relative energy error.

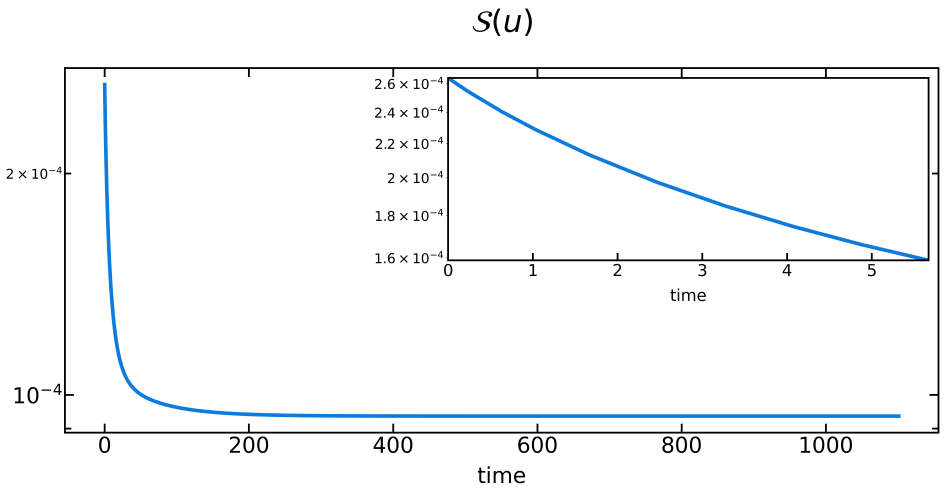

(b) Temporal evolution of the entropy.

Figure 6.24: **Evolution of the test case *gs-imgr*.** The same as in Figure 6.22, but for the collision-like operator. In (a) the maximum error on the energy conservation is 10^{-11}.

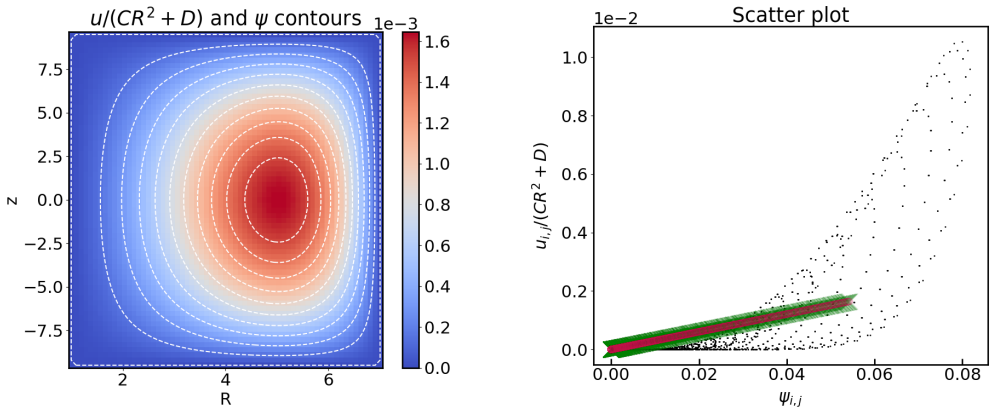

(a) **Color plot.** (b) **Scatter plot.**

Figure 6.25: **Relaxed state for the *gs-imgr* test case.** The same as in Figure 6.23, but for the collision-like operator. We note from (b) that the agreement of the relaxed state and the prediction of the variational principle is better than that obtained with the diffusion-like operator, shown in Figure 6.23(b).

6.3.5 Test case III: *gs-lmgc*

In addition to the features of the test case *gs-lmgr*, discussed in Section 6.3.3, we introduce here the additional complexity of a mapped domain.

The test case *gs-lmgc* is essentially the same as the one presented in Section 6.3.3, but for the choice of the domain, which is constructed via the Czarny mapping as discussed in Appendix A.4.2. In Table 6.33 we summarize the setup for this test case.

Variable	Value
Operator	diffusion-like, equation (4.65) with (4.67)
Entropy	Herrnegger-Maschke, $S(u) = \frac{1}{2}\int_\Omega \frac{u^2}{CR^2+D}\frac{dRdz}{R}$, equation (6.18)
Initial condition	Gaussian, equation (A.6), with $\sigma_R^2 = 0.6$, $\sigma_z^2 = 6.0$
Domain	Czarny, discussed in A.4.2.
Boundary condition	Homogeneous Dirichlet
Resolution	64×64
GMRES tolerance	atol $= 10^{-15}$, rtol $= 10^{-13}$
Newton tolerance	atol $= 10^{-14}$, rtol $= 10^{-13}$
Δt update, cf. Algorithm 1	$N_{\min} = 3$, $N_{\max} = 6$, $\Delta t_{\max} = 50000$, $f_{\text{update}} = 2$

Table 6.33: **Setup of the *gs-lmgc* test case.**

In Table 6.34 we report the runtime information for this test case. We notice that the number of time steps is the same order of magnitude as for the rectangular domain, cf. Table 6.28. However, the average number of GMRES iterations per Newton step is five times larger.

Time steps	Newton	GMRES	dt_i	dt_f
101350	1.1	145.18	0.01	83886.08

Table 6.34: **Runtime information for the *gs-lmgc* test case.** The same as in Table 6.28, but for the case of the Czarny domain discussed in Section A.4.2.

In Figure 6.26 we show the evolution of the relative energy error (with respect to the initial value) (a) and the entropy (b). In Figure 6.27 we show the relaxed state. In (a) we show the color plot of the solution, while in (b) the scatter plot. We notice that the final functional relation (red circles) almost overlaps the prediction of the variational principle (green crosses) with a numerical estimate of the eigenvalue λ, i.e. the iterative method [1, pp. 22-23, equations 2.111 and 2.112]. As in Section 6.3.3, we compute numerically the solution of the variational principle, obtaining the eigenvalue $\hat{\lambda}_0 = 0.002599$ in 28 iterations. This is compared with the fit of the relaxed state in Figure 6.27(b). In Table 6.35 we report the estimated values of the coefficients and the relative error with the numerically estimated eigenvalue.

a	**b**	$\|\hat{\lambda}_0 - b\|/\hat{\lambda}_0$
-0.000005	0.00268	0.031

Table 6.35: **Results of the fit and comparison with the direct solution of equation** (6.20) **for the test case *gs-lmgc*.** The same as in Table 6.29, but for a mapped domain.

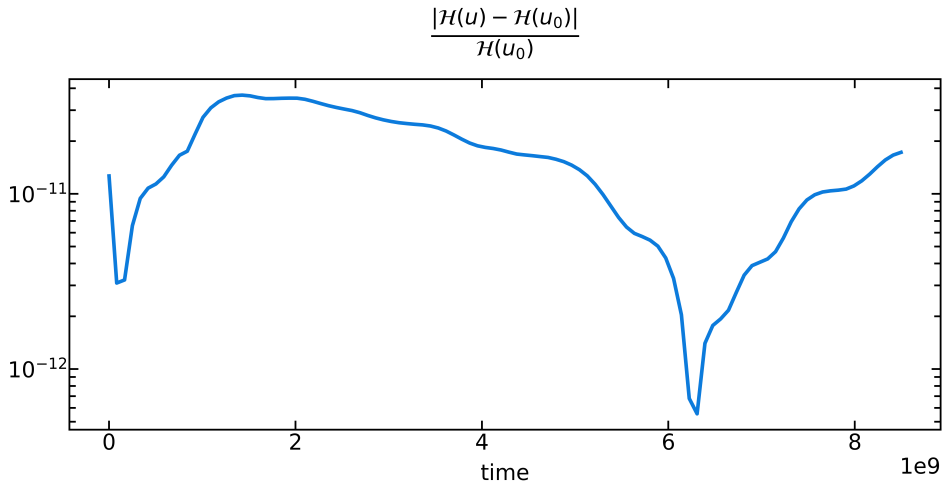

(a) Temporal evolution of the relative energy error.

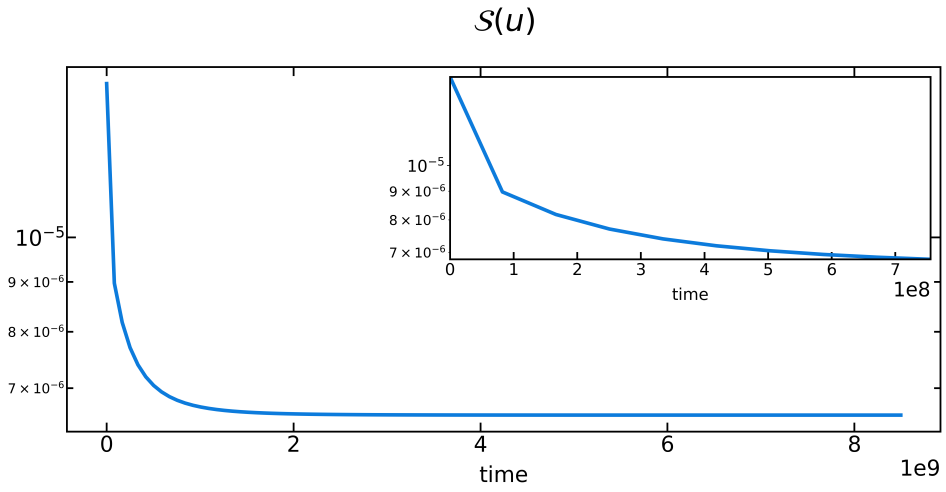

(b) Temporal evolution of the entropy.

Figure 6.26: **Evolution of the test case *gs-lmgc*.** The same as in Figure 6.22, but for the case of the Czarny domain discussed in Section A.4.2.

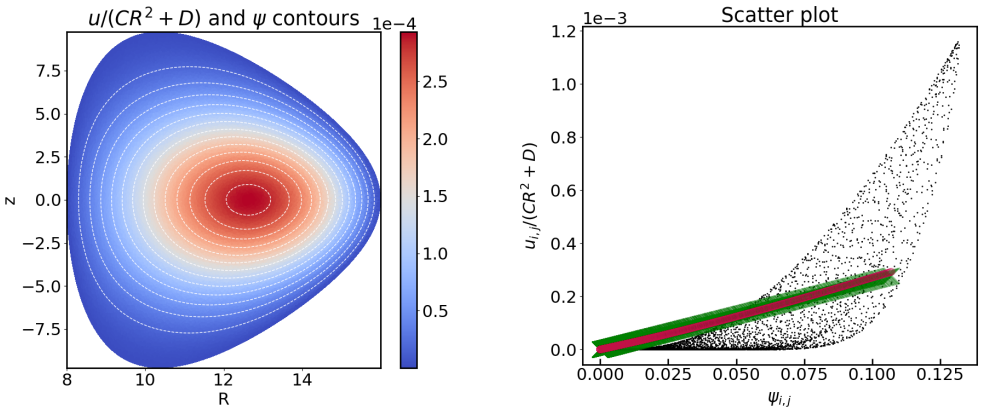

(a) Color plot. (b) Scatter plot.

Figure 6.27: **Relaxed state for the *gs-lmgc* test case.** The same as in Figure 6.23, but for the case of the Czarny domain discussed in Section A.4.2.

6.3.6 Test case IV: *gs-imgc*

As a last case, we test the collision-like operator on a mapped domain. In Table 6.36 we report the setup of the test case.

Variable	Value
Operator	collision-like, equation (4.42)
Entropy	Herrnegger-Maschke, $S(u) = \frac{1}{2}\int_\Omega \frac{u^2}{CR^2+\mathrm{D}} \frac{dRdz}{R}$, equation (6.18)
Initial condition	Gaussian, equation (A.6), with $\sigma_R^2 = 0.6$, $\sigma_z^2 = 6.0$
Domain	Czarny, discussed in A.4.2.
Boundary condition	Homogeneous Dirichlet
Resolution	64×64
GMRES tolerance	atol $= 10^{-15}$, rtol $= 10^{-13}$
Newton tolerance	atol $= 10^{-14}$, rtol $= 10^{-13}$
Picard tolerance	tol $= 10^{-12}$
Δt update, cf. Algorithm 1	$N_{\min} = 4$, $N_{\max} = 6$, $\Delta t_{\max} = 1$, $f_{\text{update}} = 2$

Table 6.36: **Setup of the *gs-imgc* test case.**

In Table 6.37 we report the runtime information for this test case. We observe that both the number of time steps and total number of GMRES iterations per time step are comparable with those required by the collision-like operator in the rectangular domain, cf. Table 6.31. Also note that for each Picard iteration we solve a linear system.

Time steps	Picard	Newton	GMRES	dt_i	dt_f
1563	2.99	1.0	142.88	0.01	1.28

Table 6.37: **Runtime information for the *gs-imgc* test case.** The same as in Table 6.28, but for the collision-like operator and the case of the Czarny domain discussed in Section A.4.2.

Figure 6.28 shows the relative energy error (a) and entropy (b). In Figure 6.29 we see the color plot (a) and the scatter plot (b). With respect to the test case *gs-lmgc* with the diffusion-like operator, here the red circles representing the final functional relation are in better agreement with the prediction of the variational principle in equation (6.17), drawn with the green crosses. As in the previous Section, we compare the fitted eigenvalue of the relaxed state with that predicted by the variational principle which is the same as in Section 6.3.5. We report the results of the fit and the comparison in Table 6.38. Notice that with respect to Table 6.35 the error is three orders of magnitude smaller.

a	**b**	$\lVert\ \lvert\hat{\lambda}_0 - b\rvert / \hat{\lambda}_0$
-5.911027e-09	0.002599	8e-05

Table 6.38: **Results of the fit and comparison with the direct solution of equation** (6.20) **for the test case *gs-imgc*.** The same as in Table 6.35, but for the collision-like operator.

The collision-like operator shows the expected properties and relaxes to the equilibrium condition predicted by the variational principle, in the mapped domain defined by the Czarny mapping. Moreover, the final equilibrium state computed with the collision-like operator achieves a smaller error with respect to the eigenvalue computed from the direct numerical solution of the variational principle.

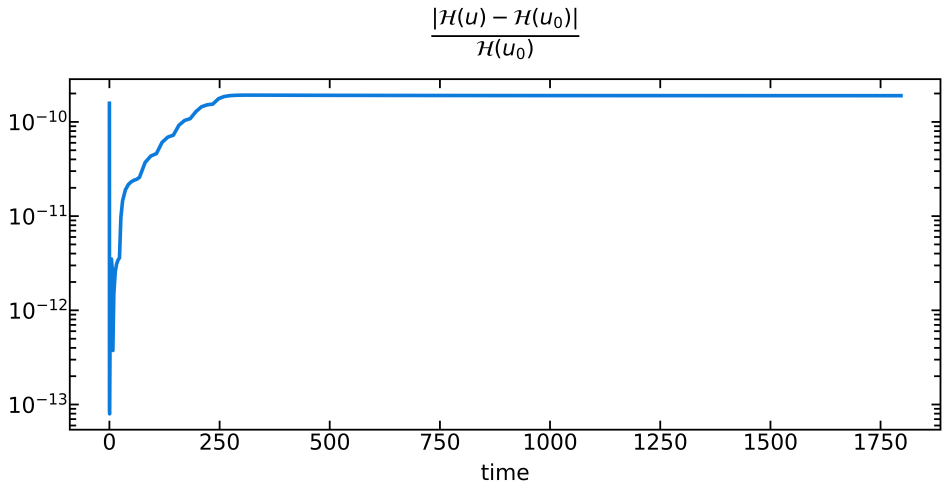

(a) Temporal evolution of the relative energy error.

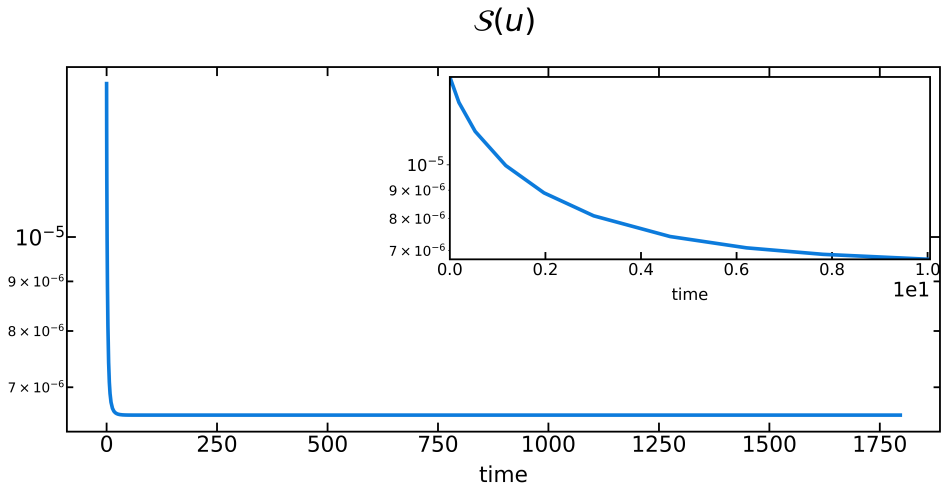

(b) Temporal evolution of the entropy.

Figure 6.28: **Evolution of the test case *gs-imgc*.** The same as in Figure 6.22, but for the collision-like operator and for the case of the Czarny domain discussed in Section A.4.2.

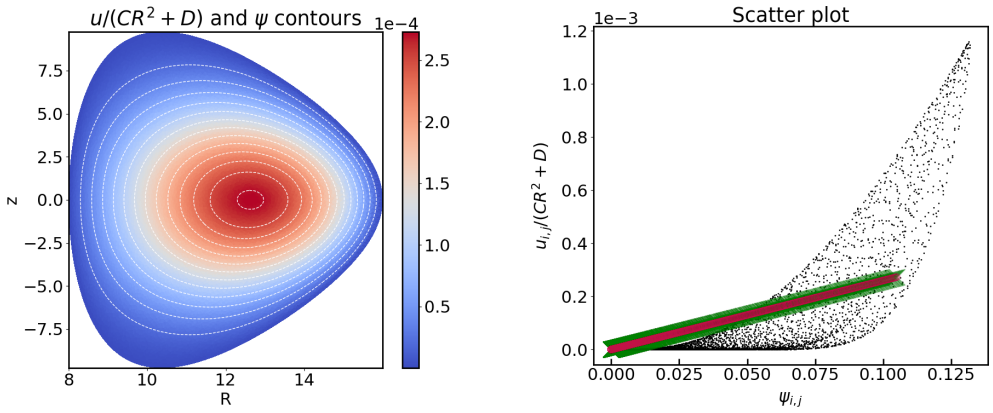

(a) **Color plot.** (b) **Scatter plot.**

Figure 6.29: **Relaxed state for the *gs-imgc* test case.** The same as in Figure 6.23, but for the collision-like operator and the case of the Czarny domain discussed in Section A.4.2. With respect to Figure 6.27(b) for the diffusion-like operator, we see from (b) that the agreement between the relaxed state and the prediction of the variational principle is better.

Chapter 7

Discretization: curl-curl brackets

In this Chapter we discuss the structure-preserving discretization in the framework of finite element exterior calculus of the relaxation method with the diffusion-like operator for force-free fields. Although the relaxation method obtained from this bracket amounts to the same method known as magnetic relaxation [22, 13, 23], its structure-preserving discretization, to the best of the author's knowledge, appears to be a novel contribution.

In Section 7.1, we introduce the notation used in this chapter, while in Section 7.2 and 7.3 we discuss the continuous system and the corresponding numerical scheme. We conclude with remarks about computational aspects and implementation in Section 7.4 and 7.5, respectively.

7.1 Notation

We follow the setup and ideas proposed by Hu *et. al.* [24] for incompressible ideal MHD. Let $\Omega \subset \mathbb{R}^3$ be a polyhedral domain and let $\partial\Omega$ denote its boundary. We discretize Ω via finite elements with a shape regular and uniform triangulation, denoted as $\mathbb{T}_h$.

With $\mathrm{grad} = \nabla$, curl and div viewed as unbounded operators from $L^2(\Omega) \to L^2(\Omega)^3$, $L^2(\Omega)^3 \to L^2(\Omega)^3$, and $L^2(\Omega)^3 \to L^2(\Omega)$, respectively, we define the linear sub-spaces

$$\begin{aligned} H(\mathrm{grad},\Omega) &:= \{v \in L^2(\Omega) :\ \nabla v \in L^2(\Omega)^3\} \subset L^2(\Omega), \\ H(\mathrm{curl},\Omega) &:= \{w \in L^2(\Omega)^3 :\ \nabla \times w \in L^2(\Omega)^3\} \subset L^2(\Omega)^3, \\ H(\mathrm{div},\Omega) &:= \{w \in L^2(\Omega)^3 :\ \nabla \cdot w \in L^2(\Omega)\} \subset L^2(\Omega)^3. \end{aligned}$$

These are the domains of the respective operators, and are Banach spaces with respect to the graph norm of the operator.

The operations, defined for $v \in C^\infty(\overline{\Omega})$, $w \in C^\infty(\overline{\Omega}, \mathbb{R}^3)$,

$$t_{\mathrm{grad}} v = v_{|\partial\Omega}, \qquad t_{\mathrm{curl}} w = w \times n_{|\partial\Omega}, \qquad t_{\mathrm{div}} w = w \cdot n_{|\partial\Omega},$$

where n is the unit outward normal to $\partial\Omega$, can be extended to continuous linear operators on $H(\mathrm{grad},\Omega)$, $H(\mathrm{curl},\Omega)$, and $H(\mathrm{div},\Omega)$, respectively. Then,

$$\begin{aligned} H_0(\mathrm{grad},\Omega) &:= \{v \in H(\mathrm{grad},\Omega) : t_{\mathrm{grad}} v = 0\}, \\ H_0(\mathrm{curl},\Omega) &:= \{w \in H(\mathrm{curl},\Omega) : t_{\mathrm{curl}} w = 0\}, \\ H_0(\mathrm{div},\Omega) &:= \{w \in H(\mathrm{div},\Omega) : t_{\mathrm{div}} w = 0\}. \end{aligned}$$

We shall look for an approximation of the solution in the following conforming finite element

spaces,

$$V_h^0 \subset H_0(\mathrm{grad},\Omega) := H_0^1(\Omega), \quad V_h^1 \subset H_0(\mathrm{curl},\Omega), \quad V_h^2 \subset H_0(\mathrm{div},\Omega), \quad V_h^3 \subset L^2(\Omega), \tag{7.1}$$

where the parameter $h > 0$ represents the size of an element in $\mathbb{T}_h$.

We shall consider a contractible domain Ω and choose the spaces V_h^i, $i \in \{0,\dots,3\}$, such that the sequence

$$V_h^0 \xrightarrow{\ \nabla\ } V_h^1 \xrightarrow{\ \nabla\times\ } V_h^2 \xrightarrow{\ \nabla\cdot\ } V_h^3, \tag{7.2}$$

is exact [92], that is,

$$N(curl) = R(grad), \qquad N(div) = R(curl), \tag{7.3}$$

where N denotes the kernel (null space) and R the range of the operator.

We also need to define:

1. the discrete weak curl operator:

$$\nabla_h\times : V_h^2 \to V_h^1, \quad s.t. \quad (\nabla_h \times u_h, v_h) = (u_h, \nabla\times v_h), \qquad \forall\, v_h \in V_h^1; \tag{7.4}$$

2. the discrete divergence operator:

$$\nabla_h\,\cdot\, : V_h^1 \to V_h^0, \quad s.t. \quad (\nabla_h\,\cdot\, u_h, v_h) = -(u_h, \nabla v_h), \qquad \forall\, v_h \in V_h^0; \tag{7.5}$$

3. the L^2-orthogonal projectors:

$$\mathbb{P}_i : [L^2(\Omega)]^3 \to V_h^i, \quad s.t. \quad (\mathbb{P}_i u_h, v_h) = (u_h, v_h), \qquad \forall\, v_h \in V_h^i, \quad i = 0,\cdots,3. \tag{7.6}$$

Let us define the discrete numerical approximation of the variable u as the sequence

$$u_h = (u_h^n)_n,$$

where $u_h^n \approx u(t_n)$ is the numerical approximation of u evaluated at time t_n, where $0 = t_0 < t_1 < \dots t_N$ are discrete points in time, $n = 0,1,\dots,N$.

With the idea of applying the Crank-Nicolson scheme for the discretization in time we define, cf. Section 5.1,

$$\delta(u_h)^{n+1} = \frac{1}{\Delta t_n}(u_h^{n+1} - u_h^n), \qquad u_h^{n+1/2} = \frac{1}{2}(u_h^{n+1} + u_h^n), \tag{7.7}$$

with $\Delta t_n = t_{n+1} - t_n$.

7.2 Formulation of the continuous problem

Equation (2.63) with the diffusion-like bracket specialized to the case of force-free fields, cf. equation (4.69), yields the magnetic relaxation equation (4.71), which can be formulated as

$$\big(\partial_t B, \alpha\big) + (\nabla\times E, \alpha) = 0, \qquad \forall\, \alpha = \alpha(x), \tag{7.8a}$$

$$(\mathrm{H}, \beta) - (B, \beta) = 0, \qquad \forall\, \beta = \beta(x), \tag{7.8b}$$

$$(J, \gamma) - (B, \nabla\times\gamma) = 0, \qquad \forall\, \gamma = \gamma(x), \tag{7.8c}$$

$$(E, \eta) - (\mathrm{H}\times J, \mathrm{H}\times\eta) = 0, \qquad \forall\, \eta = \eta(x), \tag{7.8d}$$

$$B\cdot n = 0, \qquad E\times n = 0, \qquad \mathrm{H}\times n = 0, \qquad J\times n = 0 \qquad \text{on } \partial\Omega, \tag{7.8e}$$

where n is the outward unit normal vector of the domain Ω and we set the boundary conditions for B and E such that the normal and tangential traces are zero, respectively.

The system (7.8) is to be complemented with initial conditions for B. In system (7.8) we introduced the auxiliary variables H, J, and E, which can be interpreted as an effective magnetic field, current density, and electric field, respectively.

Equation (4.71), and thus system (7.8), have been derived using as entropy and Hamiltonian the functionals

$$S(B) = \frac{1}{2}\int_\Omega |B|^2\, dx = 4\pi W(b) \qquad \text{and} \quad H(B) = \frac{1}{2}\int_\Omega A\cdot B\, dx = \frac{1}{2}\mathscr{H}(B),$$

respectively, with $\nabla\times A = B$, $\nabla\cdot A = 0$. Then S is proportional to the magnetic energy $W(B) = \|B\|_{L^2}^2/8\pi$, and H is proportional to the magnetic helicity $\mathscr{H} = (A,B)$.

7.3 The numerical scheme

Our numerical scheme is adapted from the one suggested by Hu and co-authors [24] for incompressible visco-resistive MHD. We look for an approximation of the solution of the system (7.8) in the sequence of spaces defined in equation (7.1).

We introduce the following auxiliary variables, which represent the numerical approximations of the auxiliary fields at the mid-point in time:

$$\begin{aligned} \mathrm{H}(t_n + \Delta t/2) &\approx H_h^{n+1/2} \in V_h^1, \\ J(t_n + \Delta t/2) &\approx J_h^{n+1/2} \in V_h^1, \\ E(t_n + \Delta t/2) &\approx E_h^{n+1/2} \in V_h^1. \end{aligned} \tag{7.9}$$

The discrete initial condition is $B_h^0 \in V_h^2$. The numerical approximation of the solution at any subsequent point in time is given by:

Find $(B_h^{n+1}, H_h^{n+1/2}, J_h^{n+1/2}, E_h^{n+1/2}) \in V_h^2 \times (V_h^1)^3$, such that

$$(\delta(B_h)^{n+1}, \alpha_h) + (\nabla\times E_h^{n+1/2}, \alpha_h) = 0, \qquad \forall\, \alpha_h \in V_h^2, \tag{7.10a}$$

$$(H_h^{n+1/2}, \beta_h) - (B_h^{n+1/2}, \beta_h) = 0, \qquad \forall\, \beta_h \in V_h^1, \tag{7.10b}$$

$$(J_h^{n+1/2}, \gamma_h) - (B_h^{n+1/2}, \nabla\times\gamma_h) = 0, \qquad \forall\, \gamma_h \in V_h^1, \tag{7.10c}$$

$$(E_h^{n+1/2}, \eta_h) - (H_h^{n+1/2}\times J_h^{n+1/2}, H_h^{n+1/2}\times\eta_h) = 0, \qquad \forall\, \eta_h \in V_h^1. \tag{7.10d}$$

The last three equations can also be written as

$$H_h^{n+1/2} = \mathbb{P}_1 B_h^{n+1/2}, \tag{7.11a}$$

$$J_h^{n+1/2} = \nabla_h \times B_h^{n+1/2}, \tag{7.11b}$$

$$E_h^{n+1/2} = -\mathbb{P}_1[H_h^{n+1/2}\times(H_h^{n+1/2}\times J_h^{n+1/2})], \tag{7.11c}$$

with the projectors defined in equation (7.6) and weak curl operator defined in equation (7.4).

7.3.1 Properties of the numerical scheme

In the following, we prove that the numerical scheme introduced in equation (7.10) preserves the properties of the diffusion-like bracket discussed in Section 5.4.2. The argument is similar to that for incompressible MHD [24].

Proposition 7.3.1 (The magnetic field is solenoidal)**.** For any solution of (7.10) with $\nabla\cdot B_h^0 = 0$, B_h^n is divergence-free, $\nabla\cdot B_h^n = 0\ \forall\, n \geq 0$.

Proof. Equation (7.10a) can be written as, cf. equation (7.7),

$$B_h^{n+1} - B_h^n + \Delta t_n \nabla\times E_h^{n+1/2} = 0 \ \in\ V_h^2.$$

Applying the divergence operator yields

$$\nabla \cdot B_h^{n+1} = \nabla \cdot B_h^n,$$

where we used the fact that $\nabla \cdot (\nabla \times E_h^{n+1/2}) = 0$. It follows that if $\nabla \cdot B_h^0 = 0$, then $\nabla \cdot B_h^n = 0$ for any $n \geq 0$. □

Remark 7.3.1. Given an initial analytical condition B^0, such that $\nabla \cdot B^0 = 0$, the projection

$$B_h^0 = \mathbb{P}_2 B^0 \tag{7.12}$$

may not be divergence-free. For B_h^0 to be divergence-free as well, the following should hold,

$$\mathbb{P}_3 \nabla \cdot B = \nabla \cdot \mathbb{P}_2 B \qquad \forall B \in H_0(\mathrm{div}, \Omega),$$

but the L^2 projectors may not have this property. For this reason, instead of prescribing the initial condition as equation (7.12), we can initialize B^0 as the curl of a vector potential $A^0 \in H_0(\mathrm{curl}, \Omega)$, such that $B^0 = \nabla \times A^0$, and then B_h^0 and A_h^0 are, respectively,

$$A_h^0 = \mathbb{P}_1 A^0, \qquad B_h^0 = \nabla \times A_h^0, \tag{7.13}$$

which finally represents an exact divergence-free approximation of the initial analytical condition B^0.

Proposition 7.3.2 (Dissipation of the discrete entropy)**.** For any solution of the system (7.10), the discrete entropy is monotonically non increasing,

$$S(B_h^{n+1}) \leq S(B_h^n) \quad \forall\, n \geq 0.$$

Proof. In equation of (7.10a) we can choose the test function $\alpha_h = B_h^{n+1/2} \in V_h^2$. The first term reads, cf. equation (7.7),

$$(\delta(B_h)^{n+1}, B_h^{n+1/2}) = \frac{1}{2\Delta t_n}(B_h^{n+1} - B_h^n,\, B_h^{n+1} + B_h^n) = \frac{1}{\Delta t_n}\left[S(B_h^{n+1}) - S(B_h^n)\right]. \tag{7.14}$$

On the other hand, with $\alpha_h = B_h^{n+1/2}$, equation (7.10a) reads

$$\begin{aligned}(\delta(B_h)^{n+1}, B_h^{n+1/2}) &= -(\nabla \times E_h^{n+1/2},\, B_h^{n+1/2}) \\ &= -(E_h^{n+1/2},\, J_h^{n+1/2}) \\ &= -\|H_h^{n+1/2} \times J_h^{n+1/2}\|^2 \leq 0,\end{aligned} \tag{7.15}$$

where the first identity comes from equation (7.10c) with $\gamma_h = E_h^{n+1/2} \in V_h^1$ and the last from (7.10d) with $\eta_h = J_h^{n+1/2} \in V_h^1$. Equations (7.14) and (7.15) then give

$$S(B_h^{n+1}) - S(B_h^n) = -\Delta t_n \|H_h^{n+1/2} \times J_h^{n+1/2}\|^2 \leq 0.$$

□

Finally, we need to prove the conservation of the Hamiltonian, or equivalently of magnetic helicity. For this purpose, given $B_h^n \in V_h^2$ such that $\nabla \cdot B_h^n = 0$ we introduce the discrete vector potential $A_h^n \in V_h^1$

$$\nabla \times A_h^n = B_h^n \in V_h^2, \qquad \nabla_h \cdot A_h^n = 0, \qquad A_h^n \times n_{|\partial\Omega} = 0, \tag{7.16}$$

n being the outward normal on $\partial\Omega$.

Existence and uniqueness of the solution of this problem is discussed in Section 7.3.2 below. Then the helicity of the field B_h^n is defined by

$$\mathscr{H}(B_h^n) = (A_h^n, B_h^n).$$

Apart from a factor $1/2$ this is also the Hamiltonian of the metric bracket.

Proposition 7.3.3 (Conservation of the discrete magnetic helicity)**.** For any solution of the system (7.10) with $\nabla \cdot B_h^0 = 0$, helicity $\mathscr{H}(B_h^n) = (A_h^n, B_h^n)$ is defined for all $n \in \{0,\dots,N\}$ and

$$\mathscr{H}(B_h^n) = \mathscr{H}(B_h^0) \qquad \forall\, n \in \{0,\dots,N\}.$$

Proof. Since $\nabla \cdot B_h^0 = 0$, Proposition 7.3.1 gives $\nabla \cdot B_h^n = 0\ \forall n \in \{0,\dots,N\}$. Therefore B_h^n is in the domain of the helicity function $\mathscr{H}$ and $\mathscr{H}(B_h^n) = (B_h^n, A_h^n)$ where A_h^n is computed from B_h^n by solving problem (7.16). We observe that

$$(A_h^{n+1}, B_h^n) = (A_h^n, B_h^{n+1}), \tag{7.17}$$

which follows from

$$\begin{aligned}(A_h^{n+1}, B_h^n) &= (A_h^{n+1}, \nabla \times A_h^n) \\ &= (\nabla \times A_h^{n+1}, A_h^n) + \int_{\partial\Omega} A_h^n \cdot (A_h^{n+1} \times n) d\sigma,\end{aligned}$$

where n is the outward unit normal vector of the domain Ω and $d\sigma$ the surface element on the boundary $\partial\Omega$. In the first identity we used the definition of the discrete magnetic vector potential in equation (7.16), while in the second we integrated by parts. The boundary term is zero, cf. equation (7.16).

If A_h^n is obtained from (7.16), then the linear combination $A_h^{n+1/2}$ satisfies

$$\nabla \times A_h^{n+1/2} = B_h^{n+1/2}, \tag{7.18}$$

and we compute,

$$\begin{aligned}\mathscr{H}(B_n^{n+1}) - \mathscr{H}(B_h^n) &= (A_h^{n+1} + A_h^n, B_h^{n+1} - B_h^n) + (A_h^{n+1}, B_h^n) - (A_h^n, B_h^{n+1}) \\ &= 2\Delta t_n (A_h^{n+1/2}, \delta(B_h)^{n+1}),\end{aligned}$$

where equation (7.7) has been accounted for.

Because $\delta(B_h)^{n+1} = -\nabla \times E_h^{n+1/2}$, we have

$$\begin{aligned}(A_h^{n+1/2}, \delta(B_h)^{n+1}) &= -(A_h^{n+1/2}, \nabla \times E_h^{n+1/2}) \\ &= -(B_h^{n+1/2},\, E_h^{n+1/2}) \\ &= -(B_h^{n+1/2},\, \mathbb{P}_1 E_h^{n+1/2}),\end{aligned}$$

where in the second identity we integrated by parts and we used equation (7.16). In the third and last identity we applied the orthogonal projector $\mathbb{P}_1$, since by definition $E_h^{n+1/2} = \mathbb{P}_1 E_h^{n+1/2} \in V_h^1 = R(\mathbb{P}_1)$

Finally, upon using the symmetry of the orthogonal projector $\mathbb{P}_1$ and equation (7.11a) we have

$$-(B_h^{n+1/2},\, \mathbb{P}_1 E_h^{n+1/2}) = -(H_h^{n+1/2},\, E_h^{n+1/2}) = (H_h^{n+1/2} \times J_h^{n+1/2},\, H_h^{n+1/2} \times H_h^{n+1/2}) = 0,$$

where for the last identity we chose the test function in equation (7.10d) as $\eta_h = H_h^{n+1/2} \in V_h^1$. Therefore

$$\mathscr{H}(B_h^{n+1}) - \mathscr{H}(B_h^n) = 2\Delta t_n (A_n^{n+1/2}, \delta(B_h)^{n+1}) = 0.$$

□

Proposition 7.3.4 (Lower bound on the relaxation)**.** For any $B_h^n \in V_h^2$ such that $\nabla \cdot B_h^n = 0$, there exists a constant $C > 0$ such that

$$2CS(B_h^n) \geq |\mathscr{H}(B_h^n)|.$$

Remark 7.3.2. We note that this property is independent from the equation of motion.

Proof. We follow a standard argument [105, pp. 122]. We have that

$$|\mathscr{H}(B_h^n)| = |(B_h^n, A_h^n)| \leq \|A_h^n\| \|B_h^n\|, \tag{7.19}$$

where in the last step we applied the Schwarz inequality. Because we can choose $A_h^n \in V_h^1$ such that $\nabla_h \cdot A_h^n = 0$, the Poicaré inequality also holds [106, 107]

$$\|A_h^n\| \leq C \|\nabla \times A_h^n\|.$$

Therefore equation (7.19) leads to

$$|\mathscr{H}(B_h^n)| \leq 2CS(B_h^n).$$

□

Therefore the solution B_h^n of the system (7.10) dissipates the entropy at most up to a lower bound set by $\mathscr{H}(B_h^0)/(2\,C)$. We also see that if the initial magnetic helicity is zero, then entropy can be dissipated to zero and the relaxed state is trivial.

7.3.2 Computation of the vector potential

For contractible domains Ω and assuming that the spaces V_h^i form an exact sequence, a magnetic vector potential $A_h \in V_h^1$ satisfying equation (7.16) exists for every $B_h \in V_h^2$ such that $\nabla \cdot B_h = 0$. In fact, for an exact sequence of spaces, the curl operator in V_h^1 is surjective onto the kernel of the divergence operator in V_h^2.

In order to compute the magnetic vector potential A_h, we consider the following problem: given B_h with $\nabla \cdot B_h = 0$, find $(q_h, A_h) \in V_h^0 \times V_h^1$ such that

$$\begin{aligned} (\nabla \times A_h, \nabla \times \phi_h) + (\nabla q_h, \phi_h) &= (B_h, \nabla \times \phi_h), \qquad \forall\, \phi_h \in V_h^1, \\ (A_h, \nabla \psi_h) &= 0, \qquad \forall\, \psi_h \in V_h^0. \end{aligned} \tag{7.20}$$

We notice that equation (7.20) is a saddle point problem of the form

$$\begin{aligned} a(\phi_h, A_h) + b(\phi_h, q_h) &= \langle \phi_h, B_h \rangle, \qquad \forall\, \phi_h \in V_h^1, \\ b(\psi_h, A_h) &= 0, \qquad \forall\, \psi_h \in V_h^0, \end{aligned} \tag{7.21}$$

where $a(u,v) = (\nabla \times u, \nabla \times v)$ is a continuous bilinear form on $H_0(\mathrm{curl}, \Omega)$ and $b(u, \phi) = (u, \nabla \phi)$ is a continuous bilinear form on $H_0(\mathrm{curl}, \Omega) \times H_0^1(\Omega)$.

We can use general results for saddle point problems in equation (7.20) to prove that there exists a solution A_h of equation (7.20), such that $\nabla \times A_h = B_h$ and $q_h = 0$, for every $B_h \in V_h^2$ with $\nabla \cdot B_h = 0$. For simply connected domains and an exact sequence of finite element spaces, we can use the results of existence and uniqueness given by Brezzi [108].

7.4 Computational aspects

The simplest stable choice for the sequence of conforming finite element spaces in (7.1) is represented by linear Lagrange Elements [93], linear Nedelec elements of the first kind [109], linear Raviart-Thomas elements [109] and discontinuous Lagrange elements of order zero [95, and references therein]. The same sequence of conforming finite element spaces is used for the solution of the linear system of the vector potential A, cf. Section 7.3.2.

We solve the linear system in equation (7.20) with the GMRES method. The solution of the nonlinear system (7.10) can be found by applying the Newton method, which leads to the solution of successive non-symmetric linear problems. A standard GMRES method can

be applied to solve each linear problem. However, this becomes computationally intractable as the time step Δt_n and the mesh resolution (number of elements) increase. The number of GMRES iterations required to solve the linear system increases prohibitively.

We show that it is possible to solve the system by a Picard iteration scheme which is energy stable. Additionally, we show that the linear problem at each Picard iteration can be reduced to a symmetric, positive semi-definite system. The linear system obtained in such manner is well conditioned.

First, let us write the numerical scheme in (7.10) to be solved for the magnetic field at half time step, i.e. $B_h^{n+1/2} = (B_h^{n+1} + B_h^n)/2$. Then the time derivative $\delta(B_h)^{n+1}$ reads

$$\delta(B_h)^{n+1} = \frac{B_h^{n+1} - B_h^n}{\Delta t_n} = \frac{2}{\Delta t_n}(B_h^{n+1/2} - B_h^n),$$

and problem (7.10) becomes: find $(B_h^{n+1/2}, H_h^{n+1/2}, J_h^{n+1/2}, E_h^{n+1/2}) \in V_h^2 \times (V_h^1)^3$ such that

$$(B_h^{n+1/2}, \alpha_h) + \frac{\Delta t_n}{2}(\nabla \times E_h^{n+1/2}, \alpha_h) = (B_h^n, \alpha_h), \qquad \forall\, \alpha_h \in V_h^2, \tag{7.22a}$$

$$(H_h^{n+1/2},\, \beta_h) - (B_h^{n+1/2}, \beta_h) = 0, \qquad \forall\, \beta_h \in V_h^1, \tag{7.22b}$$

$$(J_h^{n+1/2}, \gamma_h) - (B_h^{n+1/2}, \nabla \times \gamma_h) = 0, \qquad \forall\, \gamma_h \in V_h^1, \tag{7.22c}$$

$$(E_h^{n+1/2}, \eta_h) - (H_h^{n+1/2} \times J_h^{n+1/2}, H_h^{n+1/2} \times \eta_h) = 0, \qquad \forall\, \eta_h \in V_h^1. \tag{7.22d}$$

From the solution $B_h^{n+1/2}$ of the system (7.22), the update of the magnetic field is

$$B_h^{n+1} = 2B_h^{n+1/2} - B_h^n.$$

Because the only non-linearity is given by the term $H_h^{n+1/2} \times J_h^{n+1/2}$ in equation (7.22d), we can envisage the following scheme. Let us denote each variable in the Picard loop by a hat symbol and let the index p label the Picard iterations. Then we initialize $\hat{B}_h^p$ as B_h^n for $p = 0$. The Picard iteration scheme is:

- solve for the auxiliary variable $\hat{H}_h^p \in V_h^1$,

$$(\hat{H}_h^p,\, \beta_h) = (\hat{B}_h^p,\, \beta_h), \qquad \forall\, \beta_h \in V_h^1; \tag{7.23}$$

- solve for $(\hat{B}_h^{p+1}, \hat{E}_h^{p+1}, \hat{J}_h^{p+1}) \in V_h^2 \times V_h^1 \times V_h^1$ the linear system,

$$(\hat{B}_h^{p+1}, \alpha_h) + \frac{\Delta t_n}{2}(\nabla \times \hat{E}_h^{p+1}, \alpha_h) = (B_h^n, \alpha_h), \qquad \forall\, \alpha_h \in V_h^2, \tag{7.24a}$$

$$(\hat{E}_h^{p+1}, \eta_h) - (\hat{H}_h^p \times \hat{J}_h^{p+1}, \hat{H}_h^p \times \eta_h) = 0, \qquad \forall\, \eta_h \in V_h^1, \tag{7.24b}$$

$$(\hat{J}_h^{p+1}, \gamma_h) - (\hat{B}_h^{p+1\cdot}, \nabla \times \gamma_h) = 0, \qquad \forall\, \gamma_h \in V_h^1; \tag{7.24c}$$

- verify that the residual ε_p of the Picard iteration is below a given threshold. The residual is computed as

$$\varepsilon_p = \|\hat{B}_h^{p+1} - \hat{B}_h^p\|_{L^\infty}; \tag{7.25}$$

At the end of each Picard loop, we update the time step according to the number of Picard iterations. The procedure of updating the time step is the same as the one described in Algorithm 1, cf. Section 3.3.5.

The solution $(\hat{B}_h^{p+1}, \hat{H}_h^{p+1}, \hat{E}_h^{p+1}, \hat{J}_h^{p+1})$ solves the nonlinear system (7.22) within the tolerances.

We can now prove that the Picard time stepping scheme introduced in equation (7.23) and (7.24) is energy stable, which we do in Section 7.4.1, and that the linear system in (7.24) can also be written as a symmetric and positive semi-definite system, in Section 7.4.2.

7.4.1 Boundedness of the Picard iterations

Proposition 7.4.1 (Boundness of the Picard iterations)**.** Let us consider $B_h^n \in V_h^2$ and let us initialize the Picard iteration of equations (7.23) and (7.24) with $\hat{B}_h^0 = B_h^n$. Then at each Picard iteration we have

$$\|\hat{H}_h^p\| \leq \|\hat{B}_h^p\| \leq \|B_h^n\| \qquad \forall\, p \geq 0.$$

Proof. The first step in the Picard iteration scheme is a projection, which reduces the L^2 norm by definition. In fact, upon choosing $\beta_h = \hat{H}_h^p$ we have

$$(\hat{H}_h^p, \hat{H}_h^p) = \|\hat{H}_h^p\|^2 = (\hat{B}_h^p,\, \hat{H}_h^p) \leq \|\hat{B}_h^p\| \cdot \|\hat{H}_h^p\|,$$

where, in the last step, we applied the Schwarz inequality. Therefore $\|\hat{H}_h^p\| \leq \|\hat{B}_h^p\|$.

Then we consider the system (7.24). If $\alpha_h = \hat{B}_h^{p+1}$ in equation (7.24a),

$$\|\hat{B}_h^{p+1}\|^2 + \frac{\Delta t_n}{2}(\hat{E}_h^{p+1}, \nabla_h \times \hat{B}_h^{p+1}) = (\hat{B}_h^n,\, \hat{B}_h^{p+1}) \leq \|\hat{B}_h^n\| \cdot \|\hat{B}_h^{p+1}\|, \tag{7.26}$$

which follows from the definition of the weak curl in equation (7.4) and again from the Schwarz inequality.

In equation (7.24b) we can choose the test function η_h as $\nabla_h \times \hat{B}_h^{p+1}$, which corresponds to $\hat{J}_h^{p+1}$. Then we have

$$(\hat{E}_h^{p+1}, \nabla_h \times \hat{B}_h^{p+1}) = \|\hat{H}_h^{p+1} \times \hat{J}_h^{p+1}\|^2. \tag{7.27}$$

Substituting equation (7.27) in equation (7.26) we finally have

$$\|\hat{B}_h^{p+1}\|^2 \leq \|\hat{B}_h^{p+1}\|^2 + \frac{\Delta t_n}{2}\|\hat{H}_h^{p+1} \times \hat{J}_h^{p+1}\|^2 \leq \|\hat{B}_h^n\| \cdot \|\hat{B}_h^{p+1}\|.$$

Therefore $\|\hat{B}_h^{p+1}\| \leq \|\hat{B}_h^n\|$. □

7.4.2 The linear system of a Picard iteration

Let us write the system (7.24) in terms of the degrees of freedom. Let $\{\Lambda_l^1\}_l$ and $\{\Lambda_i^2\}_i$, $l \in \{1,\dots,N_1\}$, $i \in \{1,\dots,N_2\}$, be bases for the discrete spaces V_h^1 and V_h^2, respectively. Here, N_1 and N_2 are integers corresponding to the dimension of the discrete spaces V_h^1 and V_h^2, respectively. Then the discrete variables can be expanded over these basis functions, that is

$$\hat{B}_h^{p+1} = \sum_i \mathtt{b}_i \Lambda_i^2, \qquad \hat{E}_h^{p+1} = \sum_l \mathtt{e}_l \Lambda_l^1, \qquad \hat{J}_h^{p+1} = \sum_l \mathtt{j}_l \Lambda_l^1$$

where $\mathtt{b} \in \mathbb{R}^{N_2}$ and $\mathtt{e}$, $\mathtt{j} \in \mathbb{R}^{N_1}$ are the vectors of the degrees of freedom.

We define the following matrices element-wise

- the mass matrices $\mathtt{M}_1$ and $\mathtt{M}_2$,

$$\mathtt{M}_{1,ll'} = (\Lambda_l^1, \Lambda_{l'}^1), \qquad \mathtt{M}_{2,ii'} = (\Lambda_i^2, \Lambda_{i'}^2)$$

- the rectangular matrix $\mathtt{C}$ representing the curl operator,

$$\nabla \times \Lambda_l^1 = \sum_i \mathtt{C}_{il} \Lambda_i^2, \qquad \text{such that} \qquad \nabla \times \hat{E}_h^{p+1} = \sum_i (\mathtt{Ce})_i \Lambda_i^2 \tag{7.28}$$

- the matrix $\mathtt{Q} = \mathtt{Q}(\hat{H}_h^p)$ with elements

$$\mathtt{Q}(\hat{H}_h^p)_{ll'} = (\hat{H}_h^p \times \Lambda_l^1, \hat{H}_h^p \times \Lambda_{l'}^1). \tag{7.29}$$

The magnetic field at the previous time step can also be expanded over the same basis function of the discrete space V_h^2,

$$B_h^n = \sum_i \mathtt{b}_i^n \Lambda_i^2.$$

In terms of these matrices and degree of freedom, the system of equations (7.24) reads

$$\begin{pmatrix} \mathtt{M}_2 & \frac{\Delta t_n}{2}\mathtt{M}_2\mathtt{C} & 0 \\ 0 & \mathtt{M}_1 & -\mathtt{Q}(\hat{H}_h^p) \\ -\mathtt{C}^T\mathtt{M}_2 & 0 & \mathtt{M}_1 \end{pmatrix} \begin{pmatrix} \mathtt{b} \\ \mathtt{e} \\ \mathtt{j} \end{pmatrix} = \begin{pmatrix} \mathtt{M}_2\mathtt{b}^n \\ 0 \\ 0 \end{pmatrix}, \tag{7.30}$$

where $\mathtt{C}^T$ is the transpose of the curl matrix $\mathtt{C}$, and $\Delta t = \Delta t_n$ is the local time step.

Proposition 7.4.2. The linear system in (7.24) or equivalently in (7.30) has a unique solution for any $B_h^n \in V_h^2$, $\hat{H}_h^p \in V_h^1$ and $\Delta t_n \geq 0$.

Proof. The mass matrices are strictly positive definite and therefore non-singular. System (7.30) is then equivalent to

$$\begin{aligned} \mathtt{M}_2\mathtt{b} + \frac{\Delta t_n}{2}\mathtt{M}_2\mathtt{C}\mathtt{e} &= \mathtt{M}_2\mathtt{b}^n \\ \mathtt{e} &= \mathtt{M}_1^{-1}\mathtt{Q}(\hat{H}_h^p)\mathtt{j} \\ \mathtt{j} &= \mathtt{M}_1^{-1}\mathtt{C}^T\mathtt{M}_2\mathtt{b}. \end{aligned}$$

We can back-substitute $\mathtt{j}$ in the equation for $\mathtt{e}$,

$$\mathtt{e} = \mathtt{M}_1^{-1}\mathtt{Q}(\hat{H}_h^p)\mathtt{M}_1^{-1}\mathtt{C}^T\mathtt{M}_2\mathtt{b},$$

and then $\mathtt{e}$ in the equation for $\mathtt{b}$,

$$\left(\mathtt{M}_2 + \frac{\Delta t_n}{2}\mathtt{A}\right)\mathtt{b} = \mathtt{M}_2\mathtt{b}^n, \qquad \text{with } \mathtt{A} = \mathtt{M}_2\mathtt{C}\mathtt{M}_1^{-1}\mathtt{Q}(\hat{H}_h^p)\mathtt{M}_1^{-1}\mathtt{C}^T\mathtt{M}_2. \tag{7.31}$$

The matrix $\mathtt{A}$ is by construction symmetric and positive semi-definite since $\mathtt{Q}(\hat{H}_h^p)$ is. Then $\mathtt{M}_2 + \frac{\Delta t_n}{2}\mathtt{A}$ is strictly positive definite and non-degenerate for any $\Delta t_n \geq 0$. Given $\mathtt{b}$, the solutions for $\mathtt{e}$ and $\mathtt{j}$ can be computed explicitly. □

The solution of equation (7.31) for B_h is found with a matrix-free GMRES method, choosing the mass matrix $\mathtt{M}_2$ as a natural left preconditioner. See Section 7.5 for implementation details. We summarize the entire time-stepping scheme with Picard iterations in Algorithm 5.

Algorithm 5 Time stepping scheme with Picard iterations

N_T, total number of time steps
$B_h^n \in V_h^2$, magnetic field at the full time step
$\hat{B}_h^p \in V_h^2$, magnetic field at the previous Picard iteration
$(\hat{B}_h^{p+1}, \hat{H}_h^{p+1}, \hat{E}_h^{p+1}, \hat{J}_h^{p+1}) \in V_h^2 \times (V_h^1)^3$, fields at the current Picard iteration
ε_p, residual of Picard iteration
$\text{tol}_{\varepsilon_p}$, tolerance over the residual of Picard iteration
N_p, number of Picard iterations
$\max_{N_p}$, maximum number of Picard iterations
Initialize $B_h^n = B_h^0 = \nabla \times A_h^0 \in V_h^1$ at $n = 0$, cf. Remark 7.3.1
while $t \leq N_T$ **do** ▷ time stepping loop
  Initialize the Picard loop with $\hat{B}_h^p = B_h^n$ at $p = 0$
  while $\varepsilon_p \geq \text{tol}_p$ **and** $N_p \leq \max_{N_p}$ **do** ▷ Picard loop
    Solve for $\hat{H}_h^p \in V_h^1$ equation (7.23) with GMRES
    Update the $\mathtt{Q}$ matrix via equation (7.29)
    Solve for $\hat{B}_h^{p+1} \in V_h^2$ with GMRES, with $\mathtt{M}_2$ as left preconditioner

$$(\mathtt{M}_2 + \frac{\Delta t}{2}\mathtt{A})\mathtt{b} = \mathtt{M}_2\mathtt{b}^n, \qquad \text{with} \quad \mathtt{A} = \mathtt{M}_2\mathtt{C}\mathtt{M}_1^{-1}\mathtt{Q}\mathtt{M}_1^{-1}\mathtt{C}^T\mathtt{M}_2$$

    Compute the residual of the Picard iteration ε_p according to equation (7.25)
    Update $\hat{B}_h^p \leftarrow \hat{B}_h^{p+1}$
    Update the current Picard iteration index, $p \leftarrow p + 1$
  end while
  Compute explicitly $\hat{J}_h^{p+1} \in V_h^1$ with

$$\mathtt{j} = \mathtt{M}_1^{-1}\mathtt{C}^T\mathtt{M}_2\mathtt{b}$$

  Compute explicitly $\hat{E}_h^{p+1} \in V_h^1$ with

$$\mathtt{e} = \mathtt{M}_1^{-1}\mathtt{Q}\mathtt{j}$$

  Update:

$$\begin{aligned} B_h^{n+1} &\leftarrow 2\hat{B}_h^{p+1} - \hat{B}_h^n \\ E_h^{n+1/2} &\leftarrow \hat{E}_h^{p+1} \\ J_h^{n+1/2} &\leftarrow \hat{J}_h^{p+1} \\ H_h^{n+1/2} &\leftarrow \hat{H}_h^{p+1} \end{aligned}$$

  Update $\hat{B}_h^n \leftarrow \hat{B}_h^{n+1}$
  Update the current time step $t \leftarrow t + \Delta t$
  Update the time step according to the procedure described in Algorithm 1
end while

7.5 Implementation

We implemented the time stepping scheme summarized in Algorithm 5 within the `PyMCO` code, cf. Section 5.6.

The finite elements spaces in `FEniCS` are denoted by $\mathtt{P}_1$, $\mathtt{N1}_1^e$, $\mathtt{N1}_1^f$ for the linear Lagrange, linear Nedelec of the first kind, and linear Raviart-Thomas. For visualization purposes, we always use linear Lagrange elements $\mathtt{P}_1$.

The implementation of the Picard iteration scheme is standard except for the matrix-free iterative solver that we use to solve the system (7.30) by back-substitution. In the following, we outline the main implementation steps.

We refer to Section 5.6.1 for the definition of the `FEniCS` objects `dx`, `grad`, `assemble`, `inner`. Additionally, we introduce the operations:

- `cross`: cross product between two vector-valued expressions;
- `curl`: curl operator.

First, we build the matrices of the degrees of freedom, `M1`$= \mathtt{M}_1$, `M2`$= \mathtt{M}_2$ and the product `M2_C`$= \mathtt{M}_2\mathtt{C}$. These can be assembled once at the beginning of the code execution. Given the `Trial` and `TestFunction` on $\mathtt{N1}_1^e$, `t_curl` and `v_curl`, and on $\mathtt{N1}_1^f$, `t_div` and `v_div`, we have

```
M1 = assemble(inner(t_curl, v_curl) * dx)
M2 = assemble(inner(t_div, v_div) * dx)
M2_C = assemble(inner(curl(t_curl), v_div) * dx)
```

where the last matrix is the product between `M2` and `C`, cf. definition (7.28).

For simplicity, we also define upfront `Ct_M2`, the transpose of `M2_C`. This is equivalent to

```
Ct_M2 = assemble(inner(t_div, curl(v_curl)) * dx, keep_diagonal=False).
```

The matrix `Q` is updated at each Picard iteration, since it depends on $\hat{H}_h^p$ at the previous Picard iteration, i.e. `Hk`:

```
Q = assemble(inner(cross(Hk, t_curl), cross(Hk, v_curl)) * dx).
```

Finally we define the matrix-free solver by inheriting from the class `df.LinearOperator` and overloading the method `mult(x, y)` of the class, which defines the action of the matrix on the vector `x` as `y=Ax`. Our implementation of `mult` is

```
def mult(self, x, y):
    y.zero()
    X2 = Ct_M2 * x
    X3 = _invert_m1(X2, M1) # Solves the system M1 X3 = X2
    X4 = Q * X3.vector()
    X5 = _invert_m1(X4, M1) # Solves the system M1 X5 = X4
    X6 = M2_C * X5.vector()
    X8 = M2 * x + X6 * dt / 2.
    y.axpy(1., X8) # Assigns X8 to y
    bcs_Hdiv.apply(y)
```

where we used the operation `_invert_m1`, which solves the relevant linear system with GMRES. The only important remark when solving this linear system is that suitable boundary conditions need to be applied, i.e. tangential traces of the output vector need to be set to zero. Notice that we also apply boundary conditions at the end of the `mult` method. Here, the operation `bcs_Hdiv.apply(y)` sets the normal traces of the output field to zero.

The solution for the magnetic field can be computed with the GMRES method by applying the matrix-vector operation defined in the `mult` method. We use the mass matrix `M2` as a natural left preconditioner of the system.

Finally, we compute the solution for the electric field and current density explicitly, i.e.

```
X2 = Ct_M2 * B.vector()
J = _invert_m1(X2, M1) # Solves the system M1 J = X2
bcs_Hcurl.apply(J.vector())
```

where `B` is the solution of the linear system (7.30) via back-substitution and the tangential traces of the output field are set to zero.

The electric field is similarly given by

```
X2 = Ct_M2 * B.vector()
X3 = _invert_m1(X2, M1)
X4 = Q * X3.vector()
E = _invert_m1(X4, M1) # Solves the system M1 E = X4
bcs_Hcurl.apply(E.vector())
```

where `B` and the boundary conditions are as in the computation of `J`.

Chapter 8

Numerical Experiments: curl-curl brackets

In this chapter we present the numerical experiment performed with the diffusion-like bracket discussed in Section 4.2, applied to the problem of finding force-free MHD equilibria, cf. Section 2.1.3. As already mentioned, the same test case with the collision-like operator is computationally intractable in the framework selected for the implementation of these operators. For this, an optimized parallel algorithm, on the line of those developed for the Landau collision operator [101, 102, 103], appears essential, but it is beyond the scope of this work.

We recall in Section 8.1 the setup of the test case. In Section 8.2 and 8.3 we discuss the computational aspects and the diagnostics used to analyze the results. In Section 8.4 we present the initial condition and in 8.5 we discuss the numerical experiment *beltrami-lltb*. We refer to the Appendix A.2 for the explanation of the assigned experiment tag.

8.1 Experiment's setup

We consider the domain $\Omega = [0,1]^3$. The Hamiltonian and entropy functionals, proportional to magnetic helicity and energy, respectively, are

$$H(B) = \frac{1}{2}\int_\Omega A \cdot B dx, \qquad S(B) = \frac{1}{2}\int_\Omega |B|^2 dx, \tag{8.1}$$

where the dynamical variable is the magnetic field $B = (B_1, B_2, B_3)$, with $\nabla \cdot B = 0$, and $A = (A_1, A_2, A_3)$ is the vector potential determined as the solution of

$$\begin{aligned} \nabla \times A &= B, && \text{in } \Omega, \\ \nabla \cdot A &= 0, && \text{in } \Omega, \\ A \times n &= 0, && \text{on } \partial\Omega. \end{aligned} \tag{8.2}$$

The functional derivatives of the Hamiltonian and entropy functionals in equation (8.1), with respect to the dynamical variable B, amount to

$$\frac{\delta H}{\delta B} = A, \qquad \frac{\delta S}{\delta B} = B. \tag{8.3}$$

Using equation (8.3), the necessary condition for solutions of the variational principle, cf. equation (2.26), becomes

$$B + \lambda A = 0, \tag{8.4}$$

which, upon using equation (8.2) and given that λ is a constant, reads

$$\nabla \times B = \lambda B. \tag{8.5}$$

8.2 Diagnostics

We identified several diagnostics to analyze the numerical results:

(i) temporal evolution of the relative Hamiltonian error;
(ii) temporal evolution of entropy;
(iii) temporal evolution of the L^2 norm of the strong divergence of the magnetic field;
(iv) the cross product between the magnetic field and the current density;
(v) the Poicaré plot [110, Section 1.6].

The temporal evolution of the relative error of the Hamiltonian (i) is shown to assess the conservation property of the numerical scheme, cf. Proposition 7.3.3. Because the magnetic vector potential A does not explicitly enter the formulation, it is computed "off-line" from the results of the simulation for this specific diagnostics, cf. Section 8.3.

The evolution of entropy (ii) is related to the relaxation process. This quantity is predicted to be monotonically non-increasing with the selected metric operator, and the numerical scheme we envisaged is expected to preserve this property, as we proved in Proposition 7.3.2. If it converges, the system has reached an equilibrium. Magnetic helicity provides a lower bound to the relaxation of the magnetic energy, cf. Proposition 7.3.4. To avoid a trivial solution, the helicity of the initial condition needs to be different from zero, cf. Proposition 7.3.4.

We compute the L^2 norm of the strong divergence of the magnetic field (iii) to ensure that it remains solenoidal during the evolution. This is another property of the numerical scheme, cf. Proposition 7.3.1.

Together with the entropy, we can also compute the cross product between the magnetic field and the current density (iv), which also reveals whether the system has reached an equilibrium. This quantity reads

$$||H \times J||_{L^2}, \tag{8.6}$$

where H and J are the magnetic and current density fields, cf. Section 7.3. Because of equation (7.10d), when $H \times J = 0$, then $E = 0$, and thus it corresponds to equilibrium points of the dynamics.

Finally, the Poicaré plot (v) is used for the visualization of the field and to identify possibly interesting topological features. For these structures, we also compute and visualize the streamlines, aided by the Poicaré plot in the selection of the initial conditions. In particular, we identified magnetic islands and we will plot their streamlines.

8.3 Computational aspects

We choose a domain $\Omega = [0,1]^3$ discretized with a uniform grid of 32^3 nodes, which `FEniCS` further divides in tetrahedra.

We recall that we solve the nonlinear system (7.10) with Picard iterations and the linear system at each Picard iteration is solved with GMRES, cf. Section 7.4. For the computation of the vector potential A we solve the linear system in equation (7.20) also with GMRES. We report the values chosen for the tolerances of these methods in Table 8.1.

	`atol`	`rtol`	`N_max`
`GMRES`	10^{-12}	10^{-12}	2000
`Picard`	10^{-13}	-	100
`GMRES` for A	10^{-16}	10^{-12}	1000

Table 8.1: **Setup of the Picard and GMRES method.** The last row refers to the GMRES parameters for the computation of the vector potential A. The parameters `atol`, `rtol` and `N_max` are the absolute and relative tolerance, and the maximum number of iterations, respectively.

The time step during the evolution is updated according to Algorithm 1, cf. Section 3.3.5. The values selected for the minimum and maximum number of iterations $N_{\min}$ and $N_{\max}$, and for the time step relative increment and maximum allowed time step, f_{update} and $\Delta t_{\max}$ respectively, are reported in the setup of the test case, cf. Table 8.2.

For the computation of the streamlines, as discussed in Section 8.2, we use the open source `scipy` library for scientific and technical computing [111] with the `dopri5` integrator [112, 113], an explicit runge-kutta method of order (4)5. The absolute and relative tolerances of the integrator have both been set to 10^{-13}, while the maximum number of sub-steps during one time step is 1000. Default values were used for the other parameters.

8.4 Initial condition with tunable helicity

We want to construct an initial condition on $\Omega = [0,1]^3$ such that the magnetic field is divergence-free, all of its components vanish at the boundary of the domain, and the magnetic helicity is non zero and can be set by appropriate choice of parameters.

To achieve this, we start from a linear periodic Beltrami field on the unit cube, and we localize it to the interior of the domain.

Let $\Omega = [0,1]^3$, with Cartesian coordinates $x = (x_1, x_2, x_3)$.

The linear periodic Beltrami field is

$$u(x) = A_0 \begin{bmatrix} \left(n/\sqrt{m^2+n^2}\right)\sin(\pi m x_1)\cos(\pi n x_2) \\ -\left(m/\sqrt{m^2+n^2}\right)\cos(\pi m x_1)\sin(\pi n x_2) \\ \sin(\pi m x_1)\sin(\pi n x_2) \end{bmatrix}, \tag{8.7}$$

where m, $n \in \mathbb{N}$ are positive integers and $A_0 \in \mathbb{R}$ is a constant. These parameters determine the value of the magnetic helicity.

We can verify that the vector field u defined in equation (8.7) satisfies

$$\nabla \times u = \mu u, \quad \mu = \pi\sqrt{m^2+n^2}, \qquad \nabla \cdot u = 0, \tag{8.8}$$

where μ is the eigenvalue. Equation (8.8) is the definition of a linear periodic Beltrami field.

The localization function is used to construct an initial condition that satisfies the required boundary conditions. This function needs to vanish on the boundary with sufficiently high order. As an example, we choose

$$\eta(x) = h(x_1)\, h(x_2)\, h(x_3), \qquad \text{with} \quad h(z) = z^2(1-z)^2. \tag{8.9}$$

Both the function $\eta(x)$ and its first order derivative $\nabla\eta(x)$ vanish at the boundary, by construction. In fact, the function h and its derivative h' vanish for $z = 0$ and $z = 1$.

We define the magnetic vector potential A by multiplying the localization function η in equation (8.9) by the vector field u in equation (8.7),

$$A = \eta u. \tag{8.10}$$

The magnetic field B is the curl of the vector potential of equation (8.10), or equivalently

$$B = \nabla\eta \times u + \mu\eta u, \tag{8.11}$$

which follows from a vector calculus identity and the fact that u is a Beltrami field. We can verify that the magnetic field in equation (8.11) satisfies the required properties:

- it is divergence-free by definition, as it is constructed as the curl of the vector potential A in equation (8.10);
- it satisfies the homogeneous Dirichlet boundary conditions. In fact, both η and $\nabla\eta$ vanish at the boundary, and u is smooth and bounded in Ω;

- it has non-zero magnetic helicity $\mathscr{H}(B)$, depending on the choice of the parameters n, m and A_0, i.e.

$$\mathscr{H}(B) = \int_\Omega A \cdot B \, dx = \int_\Omega \mu \eta^2 u^2 \, dx.$$

In particular, we choose $n = m = 1$ and $A_0 = 10^4$, which gives $\mathscr{H}(B) = 1.437$.

In Figure 8.1 we present the Poicaré plot of the initial condition on the plane $y = 1/2$. Notice the rich fieldline topology and the presence of multiple chains of islands.

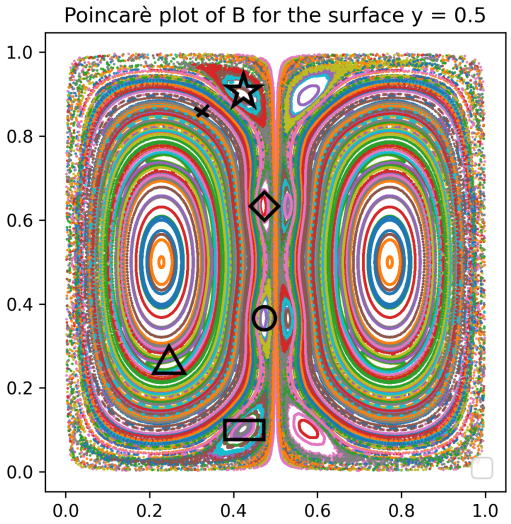

Figure 8.1: **Poincaré plot on the plane y = 1/2 of field** (8.11)**.** Each fieldline is assigned a different color. We use selected markers (a star, a diamond, a circle and a rectangle) to mark the four islands of period 2. A triangle identifies an island of period 10, while a small island of period 18 is marked by a cross.

In the Poincaré plot of Figure 8.1 we can clearly identify four different islands of period 2 (the number of intersections with the Poincaré surface). They are the big islands that are marked with a black star, a diamond, a circle and a rectangle, respectively. We can manually select the initial conditions from Figure 8.1 to compute the streamlines corresponding to these magnetic islands. We show the streamlines and Poincaré plot of the islands of period 2 in Figure 8.2. We can also recognize an island of higher periodicity, equal to 10, marked with a black triangle in Figure 8.1. Its streamlines and Poincaré plot are shown in Figure 8.3. By zooming in Figure 8.1 we can also see chains of islands of very high periodicity, up to 60. We show an example of an island with period 18 in Figure 8.4. It is marked by a black cross in Figure 8.1, although it is hardly visible without zooming. It is useful in this case to isolate the intersection of the island with the Poincaré surface, as done in Figure 8.4(c).

The same topological structures can be identified if, instead of the Poincaré section of the analytical field, we plot the projection of the initial condition onto the finite element space denoted in `FEniCS` as $\mathtt{P}_1$. Comparing the Poincaré plot of the test case *beltrami-lltb* at the first point in time with the one of the analytical condition in Figure 8.1, we observe that the discretization has the effect of destroying the islands of higher periodicity, which are still visible in Figure 8.1. For this reason we are unable to follow their evolution.

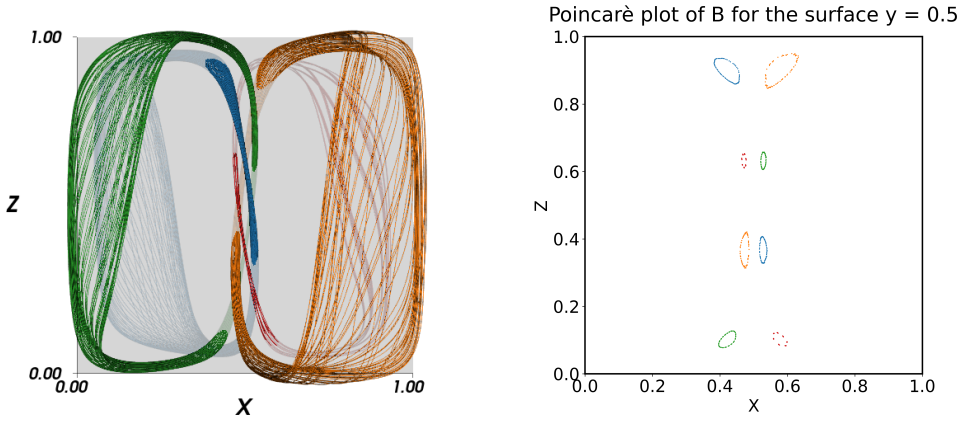

(a) Streamlines. (b) Poincaré plot.

Figure 8.2: **Streamlines (a) and Poincaré plot on the plane $y = 1/2$ (b) of the four magnetic islands with periodicity 2**. In (a) we see a visualization of the streamlines of the four magnetic islands with period 2. The gray plane corresponds to the surface $y = 1/2$. In (b) we see the Poincaré plot on the plane $y = 1/2$ of the same islands. Note that the colors match those used in (a) for the streamlines. This plot allows us to easily infer the periodicity and appreciate the linking of the islands.

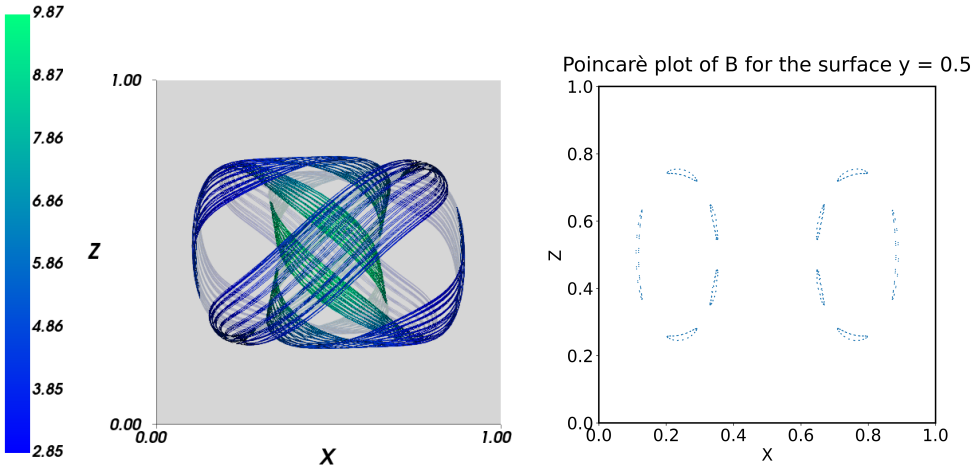

(b) Streamline. (c) Poincaré plot.

Figure 8.3: **Streamline (b) and Poincaré plot on the plane $y = 1/2$ (c) of the magnetic island with periodicity 10**. In (b) the gray plane corresponds to the surface $y = 1/2$. On the left we see the colorbar showing the intensity of the field along the streamline. This island is marked by the black triangular shape in Figure 8.1.

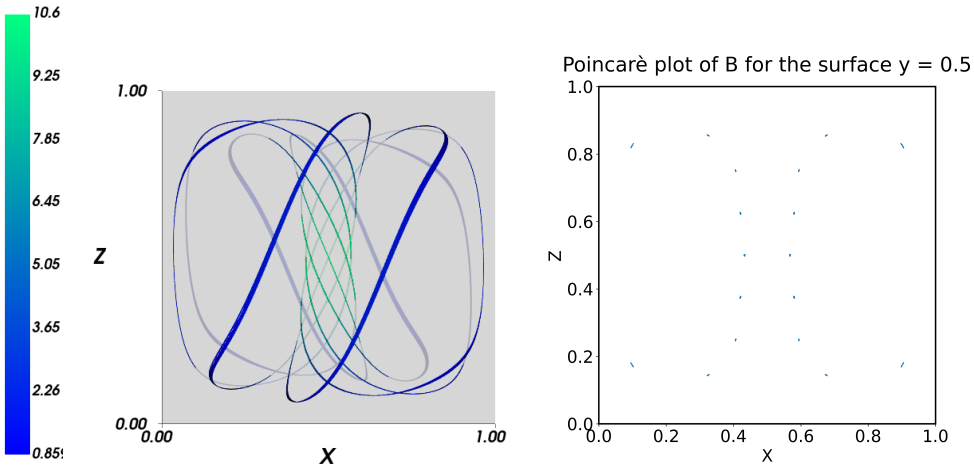

(b) Streamline. (c) Poincaré plot.

Figure 8.4: **Streamline (b) and Poincaré plot on the plane $y = 1/2$ (c) of the magnetic island with periodicity 18**. The same as in Figure 8.3, but for an island with periodicity equal to 18. This island is hardly visible in Figure 8.1, where it is marked by a black cross.

8.5 Test case: beltrami-lltb

This test case aims at understanding whether the diffusion-like operator relaxes the initial condition to a nonlinear Beltrami field, as expected from the continuous problem, rather than to a solution of the variational principle, cf. (8.4). We also want to verify the properties of the numerical scheme discussed in Section 7.3.1.

In Table 8.2 we summarize the setup of this test case, while in Table 8.3 we present the runtime information.

Variable	Value
Operator	diffusion-like, equation (4.69)
Entropy	quadratic, $S(B) = \frac{1}{2}\int_\Omega \|B\|^2 dx$, equation (8.1)
Initial condition	Localized periodic Beltrami field, equation (8.11)
Domain	cubic $\Omega = [0,1]^3$
Boundary condition	Homogeneous Dirichlet
Resolution	$32 \times 32 \times 32$
GMRES tolerance	atol $= 10^{-12}$, rtol $= 10^{-12}$
Picard tolerance	tol $= 10^{-13}$
Δt update, cf. Algorithm 1	$N_{\min} = 5$, $N_{\max} = 40$, $\Delta t_{\max} = 10^{-3}$, $f_{\text{update}} = 1.5$

Table 8.2: **Setup of the *beltrami-lltb* test case.**

One can notice the very small values of the initial and also final time step, which can be attributed to the high-order nonlinearity of the problem. Also it is worth noticing the small number of GMRES iterations per Picard step. This is thanks to the method we used to solve the numerical scheme of equation (7.10), which leads to a well conditioned, positive semi-definite system, cf. Section 7.4. Using back-substitution to solve the final linear system also provides with a natural preconditioner, which further reduces the number of required GMRES iterations.

In Figure 8.5 we show the evolution in time of the relative Hamiltonian error (a) and entropy (b). The chosen numerical scheme preserves the Hamiltonian with a maximum

Time steps	Picard	GMRES	dt_i	dt_f
25002	5.55	21.73	1.5e-08	0.000001

Table 8.3: **Runtime information for the *beltrami-lltb* test case.** We report the total number of time steps, the average number of Picard iterations per time step and the average number of GMRES iterations per Picard step. We also report the initial (dt_i) and final (dt_f) values of the time step, which is adapted according to the number of Picard iterations as discussed in Section 8.3.

relative error of 10^{-10}. The entropy is instead dissipated as predicted by theory.

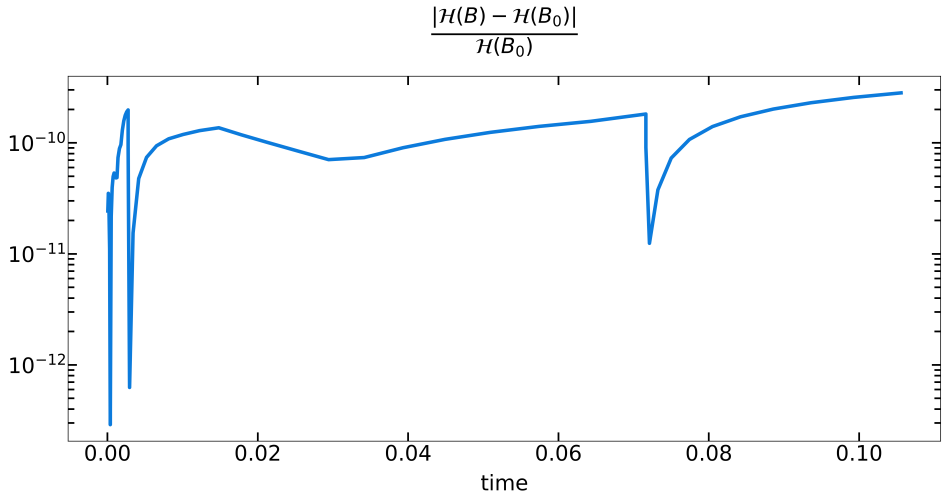

(a) Temporal evolution of the relative Hamiltonian error.

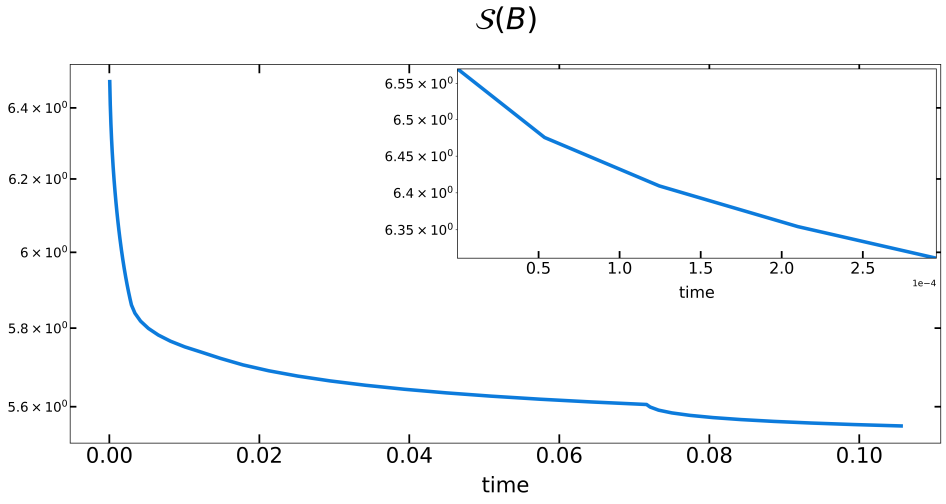

(b) Temporal evolution of the entropy.

Figure 8.5: **Evolution of the test case *beltrami-lltb*.** In (a) we see the temporal evolution of the relative Hamiltonian error in a semi-logarithmic scale. The maximum error saturates at 10^{-10}. In (b) we see the evolution of the entropy, while the inset shows the same quantity during an early phase of the simulation. The jumps and corner in (a) and (b) respectively are due to a restart of the test case with larger time step.

In Figure 8.6 we show the temporal evolution of two other relevant quantities, the L^2 norm of the strong divergence of the field (a) and the L^2 norm of the force-free condition

(b), cf. equation (8.6). The value of the L^2 norm of the strong divergence in Figure 8.6(a) is due to round-off errors. In fact, if we normalize it by the number of time steps and degrees of freedom the value is of the order of machine-precision.

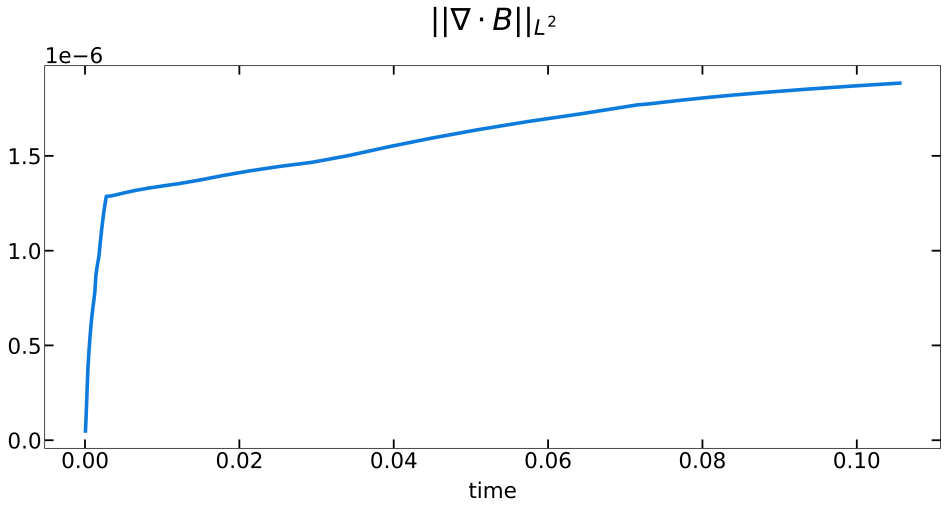

(a) Temporal evolution of the L^2 norm of the strong divergence of the magnetic field.

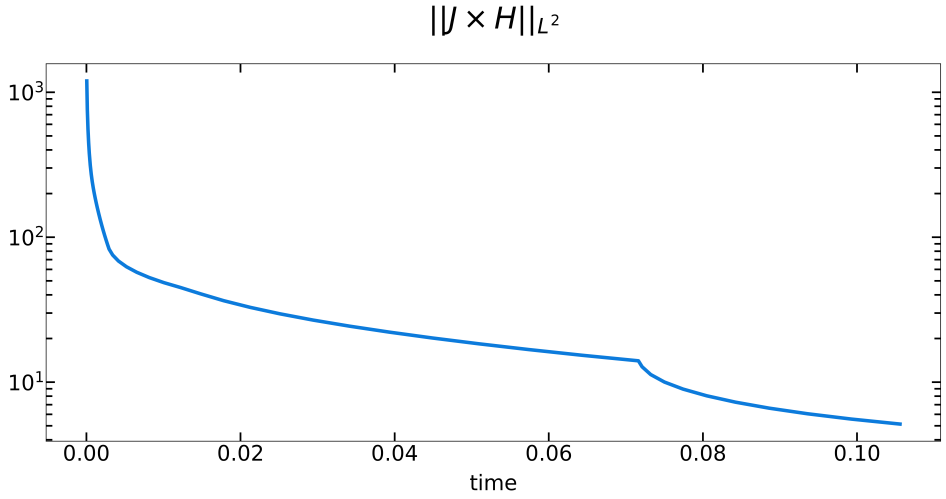

(b) Temporal evolution of the equilibrium condition of Section 8.2

Figure 8.6: **Evolution of the test case *beltrami-lltb*.** The temporal evolution of the L^2 norm of the strong divergence of the magnetic field is shown in (a). The order of magnitude of this quantity is 10^{-6}. In (b) we see in a semi-logarithmic scale the diagnostics of the equilibrium condition, cf. Section 8.2. The corners in both plots are due to a restart with a larger time step.

We show in Figure 8.7 the Poincaré plot on the plane $y = 1/2$ at the last point in time. Figure 8.7 can be compared with the Poincaré plot of the initial condition in Figure 8.1. We could not draw quantitative conclusions about the evolution of the islands of Figure 8.1. However, we can identify some of the larger ones in Figure 8.7 and compare them with those appearing in the initial condition.

As an example, the four islands of period 2 in Figure 8.7 can be traced back to the ones we identified in the initial condition, cf. Figure 8.2. They are marked in Figure 8.7 with the same symbols (a star, a diamond, a circle and a rectangle) used in Figure 8.1. In Figure 8.8 we see their streamlines and Poincaré plot. We use the same colors of Figure 8.2 for a

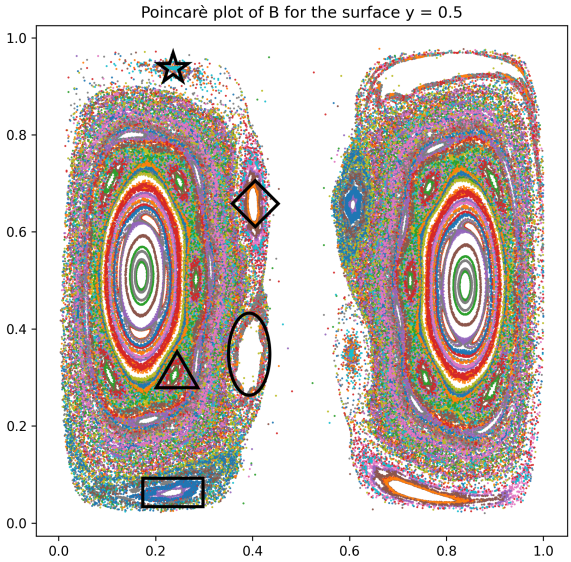

Figure 8.7: **Poincaré plot at the equilibrium state of the test case *beltrami-lltb*.** The same as in Figure 8.1, but for the last point in time of the test case *beltrami-lltb*. We use the same island markers as in Figure 8.1.

better comparison. We see that their linking has not changed.

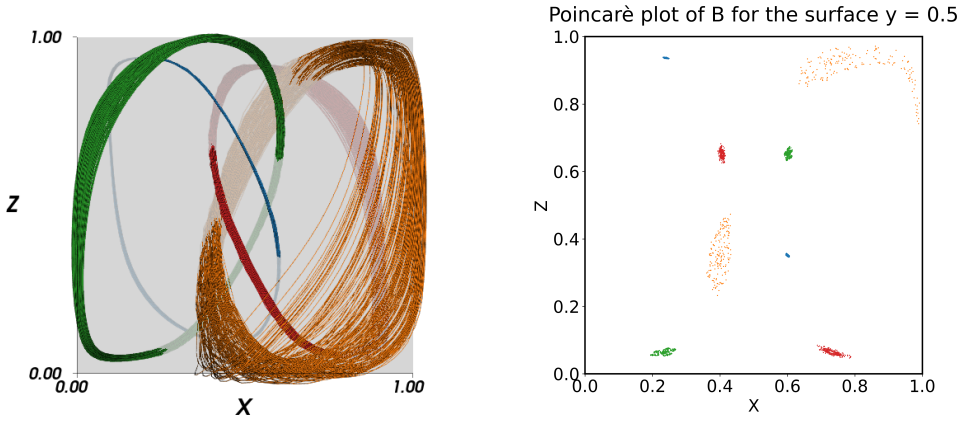

(a) Streamline. (b) Poincaré plot.

Figure 8.8: **Streamlines (a) and Poincaré plot on the plane $y = 1/2$ (b) of the four magnetic islands with periodicity 2 at the last point in time of the test case *beltrami-lltb*.** The same as in Figure 8.2, but for the last point in time of the test case *beltrami-lltb*. These islands can be traced back to the ones with period 2 of the analytical initial condition, which we showed in Figure 8.2. To make the comparison clearer, we used the same colors to identify each island. The Poincaré plot in (b) allows us to easily identify these islands in Figure 8.7.

In Figure 8.9 we show a magnetic island of period 10. This corresponds to the island marked with a triangle in Figure 8.7 and can be traced back to the island of Figure 8.3 of the analytical initial condition, marked with the same symbol. Also in this case we can see that the topology of the island is the same.

It is not possible to draw similar conclusions for smaller islands with higher periodicity because of the limited resolution.

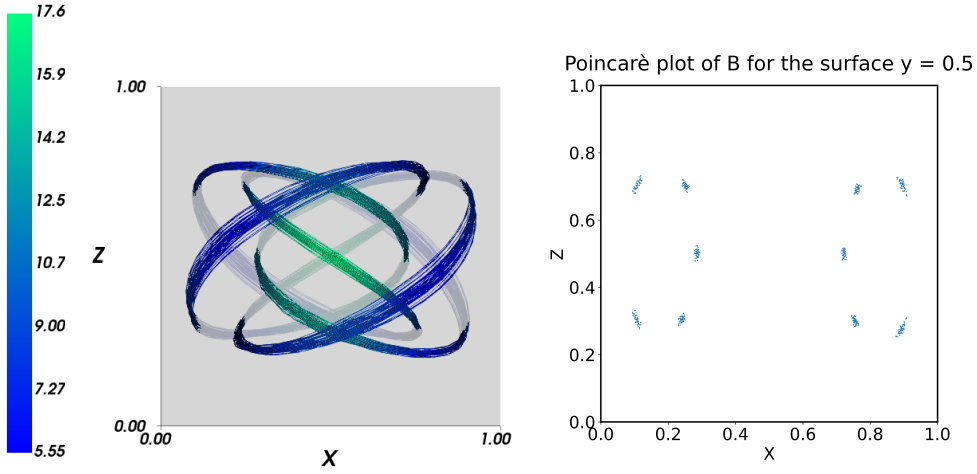

(b) Streamline. (c) Poincaré plot.

Figure 8.9: **Streamline (b) and Poincaré plot on the plane $y = 1/2$ (c) of the magnetic island with periodicity 10 at the last point in time of the test case *beltrami-lltb*.** The same as in Figure 8.3, but for the last point in time of the test case *beltrami-lltb*. This island is marked in Figure 8.7 with a black triangle, and can be qualitatively traced back to the one we showed in Figure 8.3 of the analytical condition. Note that the topology of this particular island appears to be preserved after the evolution.

These plots show that the topology of the big magnetic islands, those with higher magnetic energy, is preserved. However, there is no theoretical guarantee that fieldline topology is preserved at the discrete level. This is a property of the continuous system (7.8), which is in fact equivalent to the Lie-dragging of $\boldsymbol{B}$ along an effective flow, but the numerical scheme guarantees conservation of the global magnetic helicity only, cf. Figure 8.5(a).

The frozen-in law of the continuous system poses nonetheless a strong constraint on the relaxation process. For this reason and because of the complexity of the relaxed state we observe in Figure 8.7, we conclude that the system has not completely relaxed to a constrained entropy minimum and that the final state is in fact a non-linear Beltrami field, and not a Woltjer-Taylor state as predicted by the variational principle of equation (8.4). This behavior is expected and consistent with the theory of the method. The relaxed states computed by the diffusion-like operator are valid force-free equilibrium points. As we discussed in Section 9.2, this has interesting applications.

Chapter 9

Conclusions

We summarise the main conclusions of this work in Section 9.1, while we present some directions for future work in Section 9.2.

9.1 Conclusions

In this work, we proposed a relaxation method for the solution of equilibrium problems by means of a new metric bracket, the collision-like bracket. For computational reasons, we also introduced a different version, called diffusion-like bracket, designed to mitigate the computational cost of the original bracket. They are discussed in Section 4.2 and 4.3, respectively.

We developed a code for the implementation of these new classes of brackets and their applications to three selected physical examples: Euler's equations and the Grad-Shafranov equation in two dimensions, and force-free MHD equilibria in three dimensions. These experiments are discussed in Chapter 6 and Chapter 8, respectively for the two and three dimensional cases. Among all possible equilibria, we have singled out those that satisfy a variational principle, that is, entropy extrema at constant energy. These are still physical equilibria, but the fact they they satisfy a variational principle can be useful in certain specific applications. For instance, satisfying the variational principle is important for applications to Grad-Shafranov equilibria (cf. Section 6.3) and for linear Beltrami fields. For nonlinear Beltrami fields (i.e. generic force-free equilibria) one might not need to relax the entropy completely to a constrained minimum. By an appropriate choice of the entropy function the variational principle selects those equilibria compatible with additional physical constraints (encoded in the chosen entropy). Possibilities for other applications of this method are discussed below in Section 9.2.

Finally, the numerical schemes are of key importance for such relaxation simulations. We proposed a structure preserving discretization of the relaxation method with the diffusion-like operator for force-free fields within the framework of FEM, as discussed in Chapter 7.

9.2 Future work

The relaxation method we propose for the calculation of equilibria of force-free fields could be extended to full MHD and combined with existing variational methods, such as the ones implemented in the VMEC [4], DESC [8], or GVEC [7] codes. An initial condition could be appropriately prepared to have a certain topology by including a magnetic-island seed into a VMEC or GVEC equilibrium. With magnetic-island seed we refer to the process of injecting an island in a magnetic field configuration which is characterised by a foliation of space into a family of nested toroidal flux surfaces. This is achieved by selecting a resonant

surface and adding to the original initial condition an appropriate perturbation.

Then the relaxation method proposed in this work could be used to evolve this initial condition toward an equilibrium with islands. We note that this approach requires some a priori knowledge of the expected equilibrium condition, that is, the island seed.

Throughout this work, the entropy density has been selected such that its derivative is a monotonic function. This constraint can be relaxed, upon introducing *phantom fields* in the formulation of the equations of motion, following Yoshida and Morrison [114]. In [114], phantom fields are used to systematically embed a Hamiltonian system in a larger phase space: they represent a topological constraint that is conserved in the extended system, but not integrable in the embedded one. This construction is adopted to explain bifurcations and instabilities in some Hamiltonian systems [114]. The application of this approach in the current work is currently under investigation. By writing the equations of motion for the extended system, including the phantom field, we can show that the constraint on the monotonicity of the derivative of the entropy density can be relaxed. The possibility of computing nonmonotonic equilibrium states is important to simulate those profiles that exhibit a region of negative current density near the axis, which is usually referred to as current hole [115]. This has been studied from a theoretical and numerical perspective, e.g. by [116, 117].

Appendix A

Diagnostics and initial conditions for the numerical experiments

In this Appendix we introduce the common setup for the numerical experiments we performed throughout this work. In Appendix A.1 we discuss the diagnostics that have been used to study each test case and in A.2 the common notation used to label the experiments. In Appendix A.3 and A.4 we present the initial conditions we considered for Euler's equation in the vorticity form and the Grad-Shafranov equation, cf. Section 2.1.1 and 2.1.2.

A.1 Diagnostics

The diagnostics used to evaluate the numerical results of our test cases are

- the temporal evolution of the entropy functional;
- the temporal evolution of the energy error;
- the scatter plot.

The time evolution of the entropy functional provides useful information about the relaxation process. We expect this quantity to be dissipated under the action of the selected metric operator. If there is no significant variation in the evolution of the entropy functional, it indicates that the system has reached or it is close to an equilibrium.

The time evolution of the energy error is shown to prove the conservation properties of the numerical scheme.

Finally, the scatter plot diagnostic is constructed by plotting the dynamical variable evaluated at every grid node (i, j) with respect to its corresponding scalar potential evaluated at the same points, e.g. $\omega_{i,j}$ versus $\phi_{i,j}$. These discrete values will show no particular correlation on the Cartesian plane when the system is far from the equilibrium condition. On the contrary, when the equilibrium condition is met, they will arrange themselves to form a functional relation $\omega_{i,j} = f(\phi_{i,j})$, which in turn can be compared with the theoretical relation given by the variational principle.

A.2 Experiment tags

For experiment reproducibility, we assign a unique experiment tag to each of the test cases, which also corresponds to the filenames used for the input scripts and the folders to save the experiments results.

The experiment tag is composed by two parts, separated by an hyphen: the first part refers to the physical model, while the second is a four-letter string composed from the type

of:

- the metric operator, which is either collision-like or diffusion-like. We use the character i (integral) for collision-like and l (local) for diffusion-like. For the single test case run with the metric double bracket, we use the character d (double).
- the entropy type, which is either quadratic, logarithmic or of Herrnegger-Maschke type. We use the character l for quadratic, h for logarithmic and m for Herrnegger-Maschke;
- the initial condition, that is either the centered anisotropic Gaussian discussed in Section A.3.1 or the perturbed eigenfunction of the Laplacian discussed in Section A.3.2. For the 3D test cases, we consider a localized periodic Beltrami field with tunable helicity, cf. Section 8.4. We use the character g for Gaussian, e for eigenfunction with perturbation or t for the condition with tunable helicity;
- the domain, which is either rectangular, that is $\Omega = [0,1]^2$, or the image of a given mapping. We consider a unit cube, $\Omega = [0,1]^3$, for the 3D test cases. We use the character r for rectangular, a special character for each mapping and b for the cubic domain.

The variables used to construct these experiment tags are summarized in Table A.1.

Variable	Values	Character Identifier
Operator	collision-like, diffusion-like, metric double	i, l, d
Entropy	quadratic, logarithmic, Herrnegger-Maschke	l, h, m
Initial condition	Gaussian, perturbed eigenfunction, tunable helicity	g, e, t
Domain	rectangular, mapped, cubic	r, c, b

Table A.1: **Construction of labels for the test cases.** Variable name, possible values and corresponding character identifiers of the relevant variables varied across the test cases. The character identifiers are used to build a unique experiment tag.

A.3 Initial conditions for Euler

We select two initial conditions for the numerical experiments for Euler's equations: a centered anisotropic Gaussian and an analytical solution of the Laplace equation with a Gaussian perturbation term. We discuss them in Appendix A.3.1 and Appendix A.3.2 respectively.

A.3.1 Centered Anisotropic Gaussian

We define an anisotropic Gaussian centered in the domain. Given the domain $\Omega = [0,1]^2$ with Cartesian coordinates $x = (x_1, x_2)$, the vorticity variable ω reads

$$\omega_G = A \exp\left(-(x_1 - x_{1,0})^2/\sigma_{x_1}^2 - (x_2 - x_{2,0})^2/\sigma_{x_2}^2\right) + \mathsf{C}, \tag{A.1}$$

where $x_0 = (x_{1,0}, x_{2,0})$ is the coordinate of the centre of the domain, A is the amplitude of the Gaussian and C an offset, whereas $\sigma_{x_1}^2, \sigma_{x_2}^2$ are the variances of the Gaussian in the x_1 and x_2 directions respectively. If not stated otherwise, A is equal to 1.0. The boundary conditions determine the constant C. If not specified, we choose homogeneous Dirichlet boundary conditions and we set $\mathsf{C} = 0$.

The variances of the Gaussian are chosen to be

$$\sigma_{x_1}^2 = 0.01, \qquad \sigma_{x_2}^2 = 0.07, \tag{A.2}$$

so that the field is negligible near the boundaries and consistent with the choice of the homogeneous Dirichlet boundary conditions.

The scalar potential ϕ is computed through the Poisson equation (6.2).

Figure A.1 shows the vorticity defined by equation (A.1) in the rectangular domain Ω. The resolution N is equal to 64 in both directions. In Figure A.1(a) we see the color plot of the dynamical variable ω and the contours of the scalar potential of ϕ (white dashed curves), computed by solving equation (6.2).

In Figure A.1(b) we see with the scatter plot diagnostics introduced in Appendix A.1 that there is no functional relation between the two dynamical variables, because the discrete values of the two dynamical variables are scattered over the plane. The initial condition is in fact constructed to be far from an equilibrium.

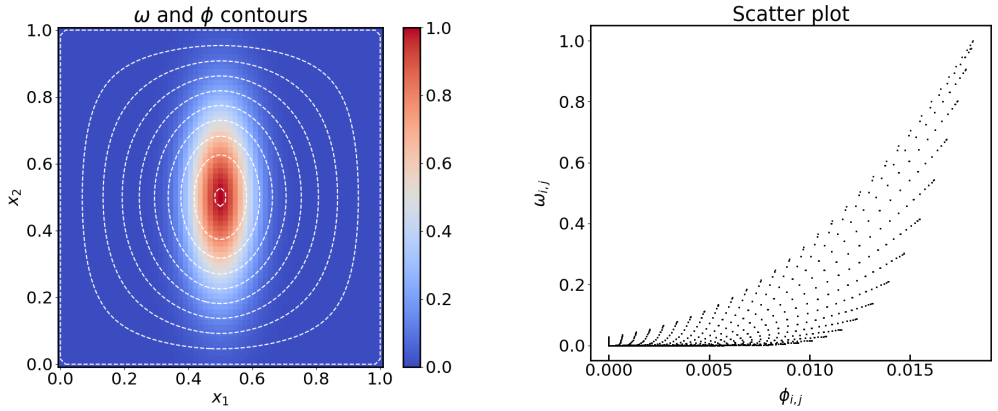

(a) Color plot. (b) Scatter plot.

Figure A.1: **A centered anisotropic gaussian.** In (a) we show the color plot of ω and contours (in white dashed curves) of ϕ in the rectangular domain $\Omega = [0,1]^2$. The color bar on the right shows the intensity of the vorticity field. In (b) we present the scatter plot between ω and ϕ at the initial condition (represented by black dots). See Section A.1 for more details about this diagnostic. We see that there is no distinguishable functional relation between the two variables, i.e. we are far from an equilibrium condition.

A.3.2 Analytical eigenfunction with perturbation

The second selected initial condition is an eigenfunction of the Laplace equation with a Gaussian perturbation.

For a summary of the eigenfunctions of the Laplace operator, see Appendix B. Given the domain $\Omega = [0,1]^2$ and homogeneous Dirichlet boundary conditions, the eigenfunctions of the Laplace operator can be written as, cf. equation (B.4) with $a = b = 1$,

$$f_{N,M}(x) = A_0 \sin(\pi N x_1) \cdot \sin(\pi M x_1) \tag{A.3}$$

where $N \geq 1$, $M \geq 1$ are positive integer numbers and the amplitude $A_0 = 1$. The eigenfunction corresponding to the minimum eigenvalue is given by $N = M = 1$. We consider the eigenstate of the Laplace operator given by $N = 6$ and $M = 4$ for which the energy $||\nabla f_{N,M}||^2$ is larger.

A centered anisotropic Gaussian perturbation, of the form of equation (A.1), is added to the eigenfunction (A.3) so that the initial vorticity then reads

$$\omega = f_{N,M}(x) + \omega_G(x), \qquad \text{with } N = 6,\ M = 4, \tag{A.4}$$

where ω_G is given in equations (A.1) and (A.2) and the values for the amplitude A are increased from $A = 0.01$, $A = 0.1$, up to $A = 1.0$. The initial potential ϕ is computed from ω by solving the Poisson problem (6.2).

Plots of the initial condition (A.4) for $A = 0.01$, $A = 0.1$ and $A = 1.0$ are shown in Figure A.3, A.4 and A.5, respectively. As a comparison, we also show the case for $A = 0$ in Figure A.2, which is an unperturbed eigenfunction of the Laplace operator.

We see from Figure A.3(a) to A.5(a) the increasing impact of the Gaussian perturbation. The scatter plot in Figure A.2(b) shows an equilibrium, and from Figure A.3(b) to Figure A.5(b) we see how the initial condition deviates from the equilibrium as A increases.

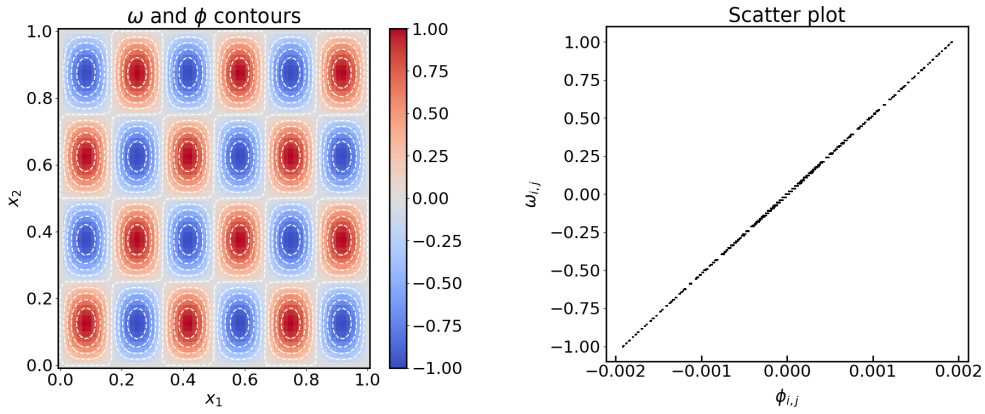

(a) Color plot. (b) Scatter plot.

Figure A.2: **Perturbed eigenfunction of the Laplacian by initial condition** (A.4) **with A = 0.** In (a) we present the color plot of the dynamical variable ω and the contours of its scalar potential ϕ (white dashed lines). The color bar on the right shows the intensity of the vorticity field. In (b) we show the functional relation between the two dynamical variables at the initial condition, visualized by means of the scatter plot discussed in Section A.1. We can distinguish a linear functional relation between the dynamical variables. In fact, this is by construction an equilibrium.

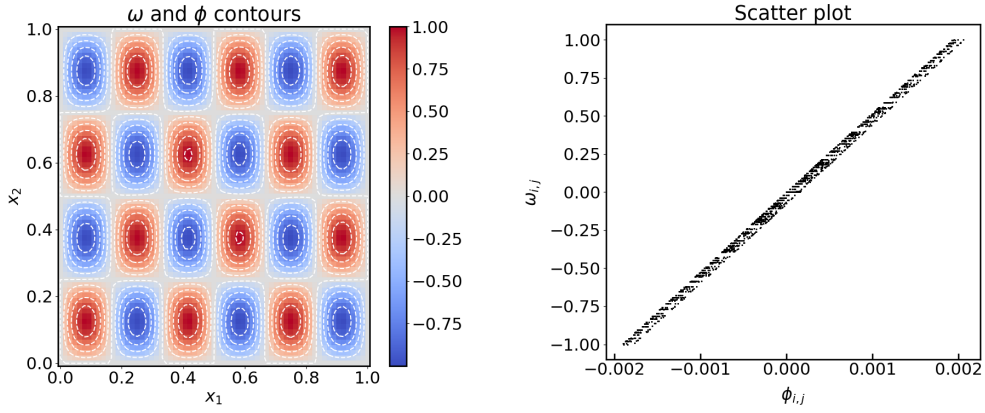

(a) Color plot. (b) Scatter plot.

Figure A.3: **Perturbed eigenfunction of the Laplacian by initial condition** (A.4) **with A = 0.01.** Same as in Figure A.2, but for $A = 0.01$. The initial condition is by construction close to an equilibrium.

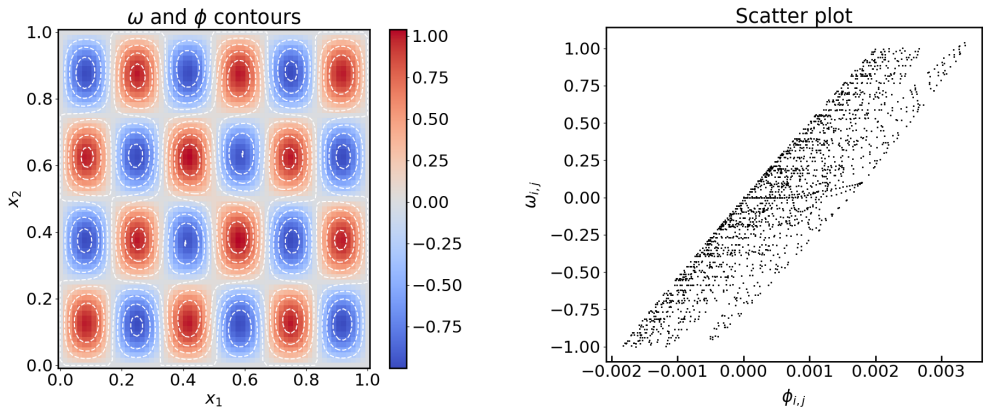

(a) Color plot. (b) Scatter plot.

Figure A.4: **Perturbed eigenfunction of the Laplacian (A = 0.1).** Same as in Figure A.3, but for $A = 0.1$. We notice that this initial condition is further away from equilibrium.

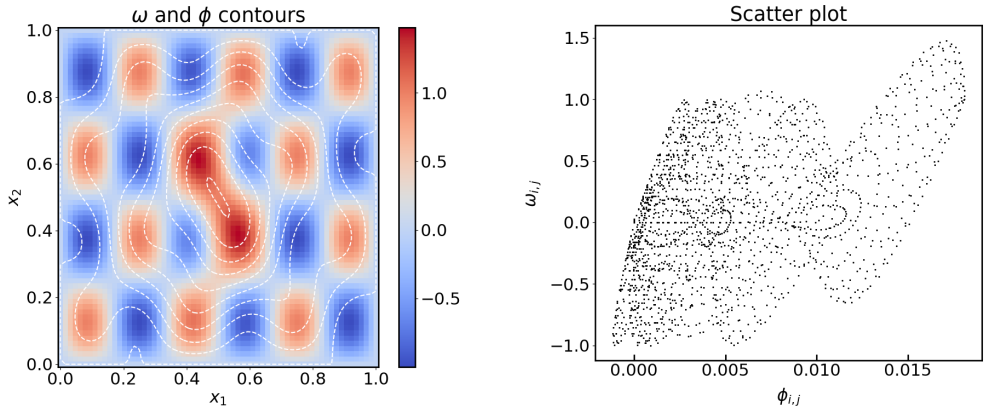

(a) Color plot. (b) Scatter plot.

Figure A.5: **Perturbed eigenfunction eigenstate of the Laplacian (A = 1.0).** Same as in Figure A.3 but for $A = 1.0$. This initial condition is further away from an equilibrium.

A.4 Initial conditions for Grad-Shafranov

For the case of the Grad-Shafranov equation, we consider two domains. In addition to a standard rectangular domain, we also consider a mapped domain obtained via the Czarny mapping [115].

A.4.1 Rectangular domain

The rectangular domain is

$$\Omega = [1.0, 7.0] \times [-9.5, 9.5],$$

and it is discretized by a uniform grid of 64×64 points which is further divided in triangles by `FEniCS`.

A.4.2 Czarny domain

The mapped domain is constructed from a unit disk mapped by a mapping inspired by the Czarny mapping [115]. We refer to this domain as Czarny domain for simplicity.

Let us denote by $(s,\theta) \in (0,1] \times [0,2\pi]$ the polar coordinates on the disk and by $x = (R,z)$ the coordinates on the physical domain Ω. The mapping is defined as [115, 118]

$$\begin{aligned} R(s,\theta) &= a\Big(b + \frac{1}{\varepsilon}\Big[1 - \sqrt{1+\varepsilon(\varepsilon+2s)}\Big]\Big), \\ z(s,\theta) &= c\,\frac{e\xi s\,\theta}{2 - \sqrt{1+\varepsilon(\varepsilon+2s)}}, \\ \xi &= 1/\sqrt{1-\frac{\varepsilon^2}{4}}, \end{aligned} \tag{A.5}$$

where ε and e are referred to as the inverse aspect ratio and the ellipticity, respectively, while a, b and c are rescaling constants. The value assigned to these parameters is shown in Table A.2.

ee	ε	a	b	c
1.4	0.3	4.	3	6.3

Table A.2: **Parameters of the mapping of equation** (A.5)**.**

We notice that the mapping defined in equation (A.5) has a singularity at $s = 0$ where $(R(0,\theta),z(0,\theta)) = a(b + (1-\sqrt{1+\varepsilon^2}/\varepsilon),0)$.

This mapped domain Ω is discretized by an unstructured triangular mesh with 8270 points.

A.4.3 Centered Anisotropic Gaussian in a rectangular domain

We can now discuss the choice of an anisotropic Gaussian initial condition in the rectangular domain discussed in Appendix A.4.1.

The dynamical variable u is initialized as

$$\begin{aligned} &u(R,z) = \exp(-(R-R_0)^2/\sigma_R^2 - (z-z_0)^2/\sigma_z^2), \\ &\sigma_R^2 = 0.5, \qquad \sigma_z^2 = 3.2 \end{aligned} \tag{A.6}$$

where $(R,\ z)$ are the radial and axial coordinates of a cylindrical reference system, while σ_R^2 and σ_z^2 are the variances of the Gaussian in the radial and axial dimension. The associated scalar potential ψ is computed from u according to equation (6.14).

We show this initial condition in the rectangular domain $\Omega = [1.0,7.0] \times [-9.5,9.5]$ in Figure A.6. In (a) we show the color plot, and in (b) the corresponding scatter plot. Both plots show that the initial condition is far from an equilibrium. Note that in both cases we rescale u by the factor $(CR^2 + D)$ because this is the quantity expected to be in linear relation with ψ, cf. Section 6.3.1.

A.4.4 Centered Anisotropic Gaussian in a Czarny domain

The second initial condition we consider is a centered anisotropic Gaussian in a Czarny domain, defined in Appendix A.4.2. We refer to equation (A.6) for the definition of the Gaussian in the domain. We only choose the variances of the Gaussian differently in both directions, i.e.

$$\sigma_R^2 = 0.6, \qquad \sigma_z^2 = 6.0. \tag{A.7}$$

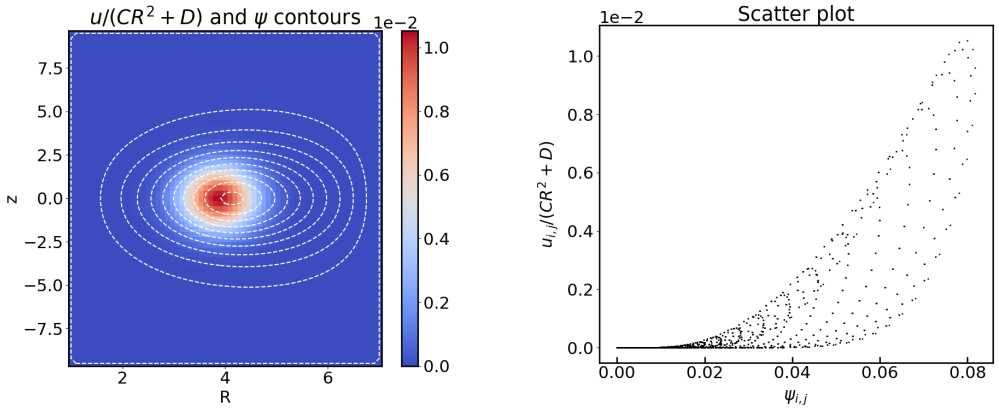

(a) Color plot. (b) Scatter plot.

Figure A.6: **A centered anisotropic Gaussian in the rectangular domain.** The dynamical variable u is a centered anisotropic Gaussian in the rectangular domain $\Omega = [1.0, 7.0] \times [-9.5, 9.5]$ with cylindrical coordinates (R, z). In (a) we present the color plot of the variable $u/(CR^2 + D)$ and the contours of its scalar potential ψ. The color bar on the right shows the intensity of $u/(CR^2 + D)$. In (b) we present with black dots the functional relationship between the two variables with the scatter plot diagnostic, discussed in Section A.1. This Figure shows a functional relation far from an equilibrium.

This initial condition is presented in Figure A.7: we see the color plot in (a) and the scatter plot in (b). We notice the elongated shape of the domain mapped via the Czarny mapping. As we can see from the plot, the initial condition is constructed to be far from an equilibrium. The same remark on the rescaling factor $(CR^2 + D)$ of Section A.4.3 applies.

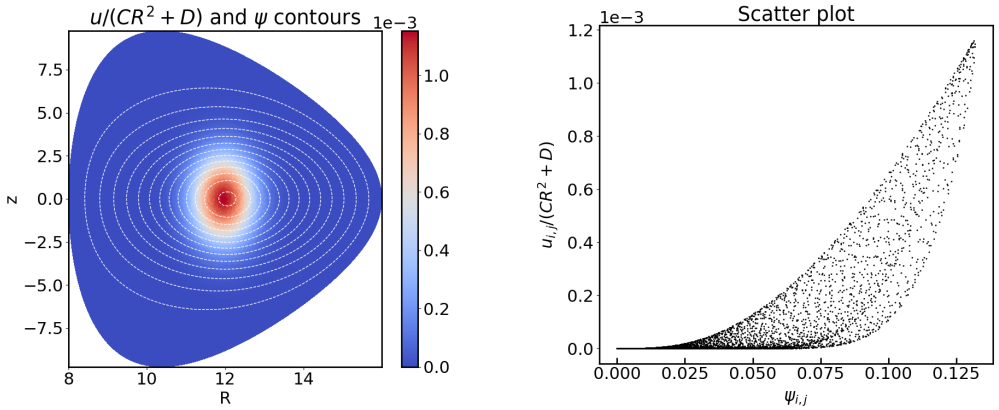

(a) Color plot. (b) Scatter plot.

Figure A.7: **A centered anisotropic Gaussian in the domain constructed via a Czarny mapping.** The same as in Figure A.6, but for the domain Ω discussed in Section A.4.2.

Appendix B

The eigenvalue problem for the Laplacian

In this Appendix we briefly recall some known results about the eigenvalue problem for the Laplacian on the domain

$$\Omega = [0,a] \times [0,b], \tag{B.1}$$

with a and b being two positive real numbers.

The eigenvalue problem of the Laplacian Δ for the pair (λ, u), with $\lambda \in \mathbb{R}$, $u : \Omega \to \mathbb{R}$, reads

$$\begin{aligned} -\Delta u &= \lambda u, \qquad \text{in } \Omega, \\ u &= 0, \qquad \text{on } \partial\Omega, \end{aligned} \tag{B.2}$$

and a solution pair (λ, u) is referred to as the eigenvalue and eigenvector pair.

Equation (B.2) can be solved analytically. The eigenvalues λ are

$$\lambda_{n,m} = \pi^2 \Big(\Big(\frac{n}{a}\Big)^2 + \Big(\frac{m}{b}\Big)^2 \Big), \quad n, m \geq 1, \tag{B.3}$$

where n and m are integer numbers.

The corresponding eigenfunctions u are

$$u_{n,m}(x_1, x_2) = A \, \sin\Big(\frac{\pi n}{a} x_1\Big) \cdot \sin\Big(\frac{\pi m}{b} x_2\Big) \quad n, m \geq 1, \tag{B.4}$$

where the normalization constant A can be fixed by prescribing a norm of u. The eigenpair with minimum eigenvalue and energy $||\nabla u||^2$ is found by choosing $n = m = 1$ in both equation (B.3) and (B.4):

$$\begin{aligned} u_{1,1}(x_1, x_2) &= A \, \sin\Big(\frac{\pi}{a} x_1\Big) \cdot \sin\Big(\frac{\pi}{b} x_2\Big), \\ \lambda_{1,1} &= \pi^2 \Big(\Big(\frac{1}{a}\Big)^2 + \Big(\frac{1}{b}\Big)^2 \Big). \end{aligned} \tag{B.5}$$

Particularly, for $a = b = 1$ equation (B.5) reads

$$\begin{aligned} u_{1,1}(x_1, x_2) &= A \, \sin(\pi x_1) \cdot \sin(\pi x_2) \\ \lambda_{1,1} &= 2\pi^2 \approx 19.73921. \end{aligned} \tag{B.6}$$

We fix $A = 1$.

List of publications

1. N. Bouzat, C. Bressan, V. Grandgirard, G. Latu, and M. Mehrenberger (2017). Targeting Realistic Geometry in Tokamak Code Gysela. ESAIM: Proceedings and Surveys. 63. 10.1051/proc/201863179.
2. C. Bressan, M. Kraus, P. J. Morrison, and O. Maj. (2018). Relaxation to magnetohydrodynamics equilibria via collision brackets. Journal of Physics: Conference Series. 1125. 012002. 10.1088/1742-6596/1125/1/012002.

Bibliography

[1] T. Takeda and S. Tokuda. Computation of MHD Equilibrium of Tokamak Plasma. *Journal of Computational Physics*, 93:1–107, 1991.

[2] F. Bauer, O. Betancourt and P. Garabedian. *A computational method in plasma physics*, volume 14. Springer, New York, 1978.

[3] O. Betancourt. BETAS, a Spectral Code for Three-Dimensional Magnetohydrodynamic Equilibrium and Nonlinear Stability Calculations. *Communications on Pure and Applied Mathematics*, 41:551, 1988.

[4] S. P. Hirshman and J. C. Whitson. Steepest-descent Moment Method for Three-dimensional Magnetohydrodynamic Equilibria. *Physics of Fluids*, 26(12):3553–3568, 1983.

[5] M. Taylor. A High Performance Spectral Code for Nonlinear MHD Stability. *Journal of Computational Physics*, 110(2):407–418, 1994.

[6] S. R. Hudson, R. L. Dewar, G. Dennis, M. J. Hole, M. McGann, G. von Nessi, and S. Lazerson. Computation of multi-region relaxed magnetohydrodynamic equilibria. *Physics of Plasmas*, 19(11):112502, 2012.

[7] F. Hindenlang and O. Maj. GVEC (Galerkin Variational Equilibrium Code), 2019.

[8] D. W. Dudt and E. Kolemen. DESC: A stellarator equilibrium solver. *Physics of Plasmas*, 27(10):102513, 2020.

[9] A. Reiman and H. Greenside. Calculation of Three-dimensional MHD Equilibria With Islands And Stochastic Regions. *Computer Physics Communications*, 43:157–167, 1986.

[10] S. P. Hirshman, R. Sanchez and C. R. Cook. SIESTA: A Scalable Iterative Equilibrium Solver for Toroidal Applications. *Physics of Plasmas*, 18:062504, 2011.

[11] K. Harafuji, T. Hayashi, and T. Sato. Computational Study of Three-dimensional Magnetohydrodynamic Equilibria in Toroidal Helical Systems. *Journal of Computational Physics*, 81:169–192, 1989.

[12] R. Chodura and A. Schlüter. A 3D code for MHD equilibrium and stability. *Journal of Computational Physics*, 41(1):68–88, 1981.

[13] H. K. Moffatt. Magnetostatic equilibria and analogous Euler flows of arbitrarily complex topology. Part 1. Fundamentals. *Journal of Fluid Mechanics*, 159:359–378, 1985.

[14] H. K. Moffatt. Magnetostatic equilibria and analogous Euler flows of arbitrarily complex topology. Part 2. Stability considerations. *Journal of Fluid Mechanics*, 166:359–378, 1986.

[15] P. J. Morrison. Bracket formulation for irreversible classical fields. *Physics Letters A*, 100(8):423–427, 1984.

[16] P. J. Morrison. Some Observations regarding Brackets and Dissipation. Technical report, University of California, Berkeley, 1984.

[17] P. J. Morrison. A paradigm for joined Hamiltonian and dissipative systems. *Physica D: Nonlinear Phenomena*, 18(1):410–419, 1986.

[18] P. J. Morrison. Hamiltonian description of the ideal fluid. *Review of Modern Physics*, 70(2):467–521, 04 1998.

[19] L. D. Landau. *Physikalische Zeitschrift der Sowjetunion*, 10(154):34–38, 1936.

[20] A. Lenard. On Bogoliubov's kinetic equation for a spatially homogeneous plasma. *Annals of Physics*, 10(3):390–400, 1960.

[21] R. Balescu. Irreversible Processes in Ionized Gases. *Physics of Fluids*, 3(1):52–63, 1 1960.

[22] T. Wiegelmann, and T. Sakurai. Solar Force-free Magnetic Fields. *Living Reviews in Solar Physics*, 9, 08 2012.

[23] S. Candelaresi, and D. I. Pontin, and G. Hornig. Magnetic field relaxation and current sheets in an ideal plasma. *The Astrophysical Journal*, 808(2):134, jul 2015.

[24] K. Hu, Y.-J. Lee and J. Xu. Helicity-conservative finite element discretization for incompressible MHD systems. *Journal of Computational Physics*, 436:110284, 2021.

[25] M. S. Alnæs, J. Blechta, J. Hake, A. Johansson, B. Kehlet, A. Logg, C. Richardson, J. Ring, M. E. Rognes, and G. N. Wells. The FEniCS Project Version 1.5. *Archive of Numerical Software*, 3(100), 2015.

[26] A. Logg, K.-A. Mardal, G. N. Wells, *et al. Automated Solution of Differential Equations by the Finite Element Method*. 2012.

[27] F. Gay-Balmaz and D. D. Holm. Selective decay by Casimir dissipation in inviscid fluids. *Nonlinearity*, 26:495, 01 2013.

[28] A. J. Chorin and J. E. Marsden. *A mathematical introduction to fluid mechanics*, volume 4. Springer-Verlag, 1993.

[29] R. Abraham, J. E. Marsden and T. Ratiu. *Manifolds, Tensor Analysis and Applications*. Springer, 2007.

[30] A. Palha and M. Gerritsma. A mass, energy, enstrophy and vorticity conserving (MEEVC) mimetic spectral element discretization for the 2D incompressible Navier–Stokes equations. *Journal of Computational Physics*, 328:200–220, 2017.

[31] M. E. Taylor. *Partial differential equations*. Springer, 2011.

[32] J. P. Freidberg. *Ideal MHD*. Cambridge University Press, 2014.

[33] H. Berestycki and H. Brezis. On a free boundary problem arising in plasma physics. *Nonlinear Analysis: Theory, Methods and Applications*, 4(3):415–436, 1980.

[34] A. Ambrosetti and G. Mancini. A free boundary problem and a related semilinear equation. *Nonlinear Analysis: Theory, Methods and Applications*, 4(5):909–915, 1980.

[35] L. Woltjer. A Theorem on Force-Free Magnetic Fields. *Proceedings of the National Academy of Sciences*, 44(6):489–491, 1958.

[36] J. B. Taylor. Relaxation of Toroidal Plasma and Generation of Reverse Magnetic Fields. *Physical Review Letters*, 33(19):1139–1141, 1974.

[37] J. B. Taylor. Relaxation and magnetic Reconnection in Plasmas. *Reviews of Modern Physics*, 58(3):741–763, 1986.

[38] H. Qin, W. Liu, H. Li, and J. Squire. Woltjer-Taylor State without Taylor's Conjecture: Plasma Relaxation at all Wavelengths. *Physical Review Letters*, 109(23), 2012.

[39] Z. Yoshida, and Y. Giga. Remarks on Spectra of Operator Rot. *Mathematische Zeitschrift*, 204:235–245, 1990.

[40] S. R. Hudson, M. J. Hole, and R. L. Dewar. Eigenvalue problems for Beltrami fields arising in a three-dimensional toroidal magnetohydrodynamic equilibrium problem. *Physics of Plasmas*, 14(5):052505, 2007.

[41] D. Lortz, W. Lotz, J. Nuehrenberg, and F. Cap. Three-dimensional Analytical Force-free MHD Equilibria. *Zeitschrift Fur Naturforschung Section A-a Journal of Physical Sciences - Z NATURFORSCH SECT A*, 36:144–149, 02 1981.

[42] N. Sato, and M. Yamada. Local representation and construction of Beltrami fields. *Physica D: Nonlinear Phenomena*, 391:8–16, 2019.

[43] M. O'Neil, and A. J. Cerfon. An integral equation-based numerical solver for Taylor states in toroidal geometries. *Journal of Computational Physics*, 359:263–282, 2018.

[44] D. Malhotra, A. Cerfon, L. M. Imbert-Gérard, and M. O'Neil. Taylor states in stellarators: A fast high-order boundary integral solver. *Journal of Computational Physics*, 397:108791, nov 2019.

[45] S. Candelaresi, D. Pontin, and G. Hornig. Mimetic Methods for Lagrangian Relaxation of Magnetic Fields. *SIAM Journal on Scientific Computing*, 36, 05 2014.

[46] H. Grad and H. Rubin. Hydromagnetic Equilibria and Force Free Fields. In *Proceedings of the 2nd United Nations International Conference on the Peaceful Uses of Atomic Energy (United Nations, Geneva), 31*, pages 190–197, 1958.

[47] T. Amari, C. Boulbe, and T. Z. Boulmezaoud. Computing Beltrami Fields. *SIAM Journal on Scientific Computing*, 31(5):pp. 3217–3254, August 2009.

[48] V. I. Arnold. Sur la Geometrie Differentielle des Groupes de Lie de Dimension Infinie at ses Applications a l'Hydrodynamique des Fluids Parfaits. *Annales de l'Institut Fourier*, 16(1):319–361, 1966.

[49] V. I. Arnold. On a Priori Estimate In the Theory of Hydrodynamical Stability. *American Mathematical Society Translations*, 79:267–269, 1966.

[50] V. I. Arnold. Hamiltonian Character of the Euler Equations of the Dynamics of Solids and of an Ideal Fluid. *Uspekhi Matematicheskikh Nauk*, 24:225–226, 1969.

[51] Z. Yoshida and S. M. Mahajan. Variational Principles and Self-Organization in Two-Fluid Plasmas. *Physical Review Letters*, 88:095001, Feb 2002.

[52] J. Liouville. Sur l'équation aux différences partielles $\frac{d^2 \log \lambda}{dudv} \pm \frac{\lambda}{2a^2} = 0$. *Journal de Mathématiques Pures et Appliquées*, pages 71–72, 1853.

[53] G. Bratu. Sur les équations intégrales non linéaires. *Bulletin de la Société Mathématique de France*, 42:113–142, 1914.

[54] I. M. Gel'fand. Some problems in the theory of quasilinear equations. volume 29, pages 295–381, 1963.

[55] H. Grad. Some New Variational Properties of Hydromagnetic Equilibria. *Physics of Fluids*, 7(8):1283–1292, August 1964.

[56] L. L. Lao, S. P. Hirshman, and R. M. Wieland. Variational moment solutions to the Grad–Shafranov equation. *The Physics of Fluids*, 24(8):1431–1440, 1981.

[57] F. Herrnegger. On the equilibrium and stability of the belt pinch. volume 1, page 26. European Physical Society, 1972.

[58] E. K. Maschke. Exact solutions of the MHD equilibrium equation for a toroidal plasma. *Plasma Physics*, 15(6):535–541, jun 1973.

[59] P. R. Chernoff and J. E. Marsden. *Properties of Infinite Dimensional Hamiltonian Systems*. Springer, 1974.

[60] D. Mendelson, A. R. Nahmod, N. Pavlović, M. Rosenzweig and G. Staffilani. A Rigorous Derivation of the Hamiltonian Structure for the Nonlinear Schrödinger Equation. *Advances in Mathematics*, 365:81, 05 2020.

[61] B. Kolev. Poisson brackets in Hydrodynamics. *Discrete & Continuous Dynamical Systems - A*, 19(3):555–574, 2007.

[62] R. Salmon. Hamiltonian Fluid Mechanics. *Annual Review of Fluid Mechanics*, 20:225–256, 1988.

[63] R. Salmon. *Lectures on Geophysical Fluid Dynamics*. Oxford University Press, 1998.

[64] A. N. Kaufman and P. J. Morrison. Algebraic Structure of the Plasma Quasilinear Equations. *Physics Letters A*, 88(8):405–406, 1982.

[65] A. N. Kaufman. Dissipative Hamiltonian Systems: a Unifying Principle. *Physics Letters A*, 100(8):419–422, 1984.

[66] M. Grmela. Bracket formulation of dissipative fluid mechanics equations. *Physics Letters A*, 102(8):355–358, 1984.

[67] M. Materassi and P. J. Morrison. Metriplectic Torque For Rotation Control of a Rigid Body. *Cybernetics and Physics*, 7(2):78–86, 2018.

[68] C. Eldred and F. Gay-Balmaz. Single and Double Generator Bracket Formulations of Geophysical Fluids with Irreversible Processes. pages 1–37, 2018.

[69] B. J. Edwards and A. N. Beris. Non-canonical Poisson bracket for nonlinear elasticity with extensions to viscoelasticity. *Journal of Physics A: Mathematical and General*, 24(11):2461–2480, 1991.

[70] M. Materassi and E. Tassi. Metriplectic Framework for Dissipative Magneto-Hydrodynamics. *Physica D*, 241(6), 2012.

[71] B. Coquinot and P. J. Morrison. A general metriplectic framework with application to dissipative extended magnetohydrodynamics. *Journal of Plasma Physics*, 86(3):835860302, 2020.

[72] M. Mittnenzweig and A. Mielke. An Entropic Gradient Structure for Lindblad Equations and Couplings of Quantum Systems to Macroscopic Models. *Journal of Statistical Physics*, 167:205–233, 2017.

[73] P. J. Morrison. Thoughts on Brackets and Dissipation: Old and New. *Journal of Physics: Conference Series*, 169, 2009.

[74] M. Grmela and H. C. Oettinger. Dynamics and Thermodynamics of Complex Fluids: Development of a General Formalism. *Physical Review E*, 56(6):6620–6633, 1997.

[75] A. Mielke. Formulation of Thermoelastic Dissipative Material Behavious Using GENERIC. *Continuum Mechanics and Thermodynamics*, 23:233–256, 2011.

[76] H. C. Oettinger. *Beyond Equilibrium Thermodynamics*. Wiley-Interscience, New York, 2005.

[77] R. W. Brockett. Dynamical systems that sort lists, diagonalize matrices and solve linear programming problems. *Proceedings of the IEEE Conference on Decision and Control*, 10010:799–803, 1991.

[78] G. K. Vallis, G. F. Carnevale, and W. R. Young. Extremal energy properties and construction of stable solutions of the Euler equations. *Journal of Fluid Mechanics*, 207:133–152, 1989.

[79] G. F. Carnevale and G. K. Vallis. Pseudo-advective relaxation to stable states of inviscid two-dimensional fluids. *Journal of Fluid Mechanics*, 213:549–571, 1990.

[80] A. Bloch, P. S. Krishnaprasad, J. E. Marsden, and T. S. Ratiu. The Euler-Poincaré Equations and Double Bracket Dissipation. *Communications In Mathematical Physics*, 175:1–42, 1996.

[81] A. M. Bloch. Steepest Descent, Linear Programming and Hamiltonian Flows. *Contemporary Mathematics AMS*, 114:77–88, 1990.

[82] T. G. Shepherd. A general method for finding extremal states of Hamiltonian dynamical systems, with applications to perfect fluids. *Journal of Fluid Mechanics*, 213(5):573–587, 1990.

[83] G. R. Flierl and P. J. Morrison. Hamiltonian–Dirac simulated annealing: Application to the calculation of vortex states. *Physica D: Nonlinear Phenomena*, 240(2):212–232, 2011. "Nonlinear Excursions" Symposium and Volume in Physica D to honor Louis N. Howard's scientific career.

[84] D. D. Holm, V. Putkaradze, and C. Tronci. Geometric gradient-flow dynamics with singular solutions. *Physica D: Nonlinear Phenomena*, 237(22):2952–2965, 2008.

[85] D. C. Brody, D. C. P. Ellis, and D. D. Holm. Hamiltonian statistical mechanics. *Journal of Physics A: Mathematical and Theoretical*, 41(50), 2008.

[86] Y. Chikasue and M. Furukawa. Simulated annealing applied to two-dimensional low-beta reduced magnetohydrodynamics. *Physics of Plasmas*, 22(02251(2015)), 2015.

[87] Y. Chikasue and M. Furukawa. Adjustement of vorticity fields with specified values of Casimir invariants as initial condition for simulated annealing of an incompressible, ideal neutral fluid and its MHD in two dimensions. *Journal of Fluid Mechanics*, 774, 2015.

[88] M. Furukawa and P. J. Morrison. Simulated annealing for three-dimensional low-beta reduced MHD equilibria in cylindrical geometry. *Plasma Physics and Controlled Fusion*, 59(5), 2017.

[89] M. Furukawa, T. Watanabe, P. J. Morrison, and K. Ichiguchi. Calculation of large-aspect-ratio tokamak and toroidally-averaged stellarator equilibria of high-beta reduced magnetohydrodynamics via simulated annealing. *Physics of Plasmas*, 25(8), 2018.

[90] A. Bloch, P. J. Morrison, and T. Ratiu. Gradient Flows in the Normal and Kähler Metrics and Triple Bracket Generated Metriplectic Systems. *Springer Proceedings in Mathematics and Statistics*, 35:371–415, 01 2013.

[91] Y. Nambu. Generalized Hamiltonian Dynamics. *Physical Review D*, 7:2405–2412, Apr 1973.

[92] D. N. Arnold, R. S. Falk, and R. Winther. Finite element exterior calculus: From hodge theory to numerical stability. *Bulletin of the American Mathematical Society*, 47:281–354, 2010.

[93] R. Courant. Variational methods for the solution of problems of equilibrium and vibrations. *Bulletin of the American Mathematical Society*, 49(1):1–23, 1943.

[94] P. A. Raviart and J. M. Thomas. A mixed finite element method for 2-nd order elliptic problems. In Galligani, Ilio and Magenes, Enrico, editor, *Mathematical Aspects of Finite Element Methods*, pages 292–315, Berlin, Heidelberg, 1977. Springer Berlin Heidelberg.

[95] A. Logg, G. N. Wells and J. Hake. DOLFIN: a C++/Python finite element library. In K.-A. Mardal A. Logg and G. N. Wells, editors, *Automated Solution of Differential Equations by the Finite Element Method*, volume 84 of *Lecture Notes in Computational Science and Engineering*, chapter 10. Springer, 2012.

[96] S. Balay, S. Abhyankar, M. F. Adams, S. Benson, *et al.* PETSc Web page. `https://petsc.org/`, 2022.

[97] S. Balay, S. Abhyankar, M. F. Adams, S. Benson, *et al.* PETSc/TAO Users Manual. Technical Report ANL-21/39 - Revision 3.17, Argonne National Laboratory, 2022.

[98] S. Balay, W. D. Gropp, L. C. McInnes, and B. F. Smith. Efficient Management of Parallelism in Object Oriented Numerical Software Libraries. In E. Arge, A. M. Bruaset, and H. P. Langtangen, editors, *Modern Software Tools in Scientific Computing*, pages 163–202. Birkhäuser Press, 1997.

[99] Forum, Message P. MPI: A Message-Passing Interface Standard. Technical report, USA, 1994.

[100] J. Crank and P. Nicolson. A practical method for numerical evaluation of solutions of partial differential equations of the heat-conduction type. *Mathematical Proceedings of the Cambridge Philosophical Society*, 43(1):50–67, 1947.

[101] M. Kraus and E. Hirvijoki. Metriplectic integrators for the Landau collision operator. *Physics of Plasmas*, 24(10):102311, 2017.

[102] M. F. Adams, E. Hirvijoki, M. G. Knepley, J. Brown, T. Isaac, and R. Mills. Landau Collision Integral Solver with Adaptive Mesh Refinement on Emerging Architectures. *SIAM Journal on Scientific Computing*, 39(6):C452–C465, 2017.

[103] E. Hirvijoki and M. F. Adams. Conservative discretization of the Landau collision integral. *Physics of Plasmas*, 24(3):032121, 2017.

[104] Y. Saad and M. H. Schultz. GMRES: A Generalized Minimal Residual Algorithm for Solving Nonsymmetric Linear Systems. *SIAM Journal on Scientific and Statistical Computing*, 7(3):856–869, 1986.

[105] V. Arnold and B. Khesin. Topological Methods in Hydrodynamics. *Annual Review of Fluid Mechanics*, 24:145–166, 11 2003.

[106] H. Poincaré. Sur les Equations aux Dérivées Partielles de la Physique Mathématique. *American Journal of Mathematics*, 12(3):211–294, 1890.

[107] D. N. Arnold, R. S. Falk, and R. Winther. Finite element exterior calculus, homological techniques, and applications. *Acta Numerica*, 15:1–155, 2006.

[108] F. Brezzi. On the existence, uniqueness and approximation of saddle-point problems arising from lagrangian multipliers. *ESAIM: Mathematical Modelling and Numerical Analysis - Modélisation Mathématique et Analyse Numérique*, 8(R2):129–151, 1974.

[109] J. C. Nedelec. Mixed Finite Elements in IR3 . *Numerische Mathematik*, 35:315–342, 1980.

[110] G. Teschl. *Ordinary Differential Equations and Dynamical Systems*, volume 140. Amer.

Math. Soc., 2012.

[111] P. Virtanen, R. Gommers, T. E. Oliphant, M. Haberland, *et al.* SciPy 1.0: Fundamental Algorithms for Scientific Computing in Python. *Nature Methods*, 17:261–272, 2020.

[112] J. R. Dormand and P. J. Prince. A family of embedded Runge-Kutta formulae. *Journal of Computational and Applied Mathematics*, 6(1):19–26, 1980.

[113] E. Hairer, S.P. Norsett, and G. Wanner. *Solving Ordinary Differential Equations i. Nonstiff Problems*. Springer-Verlag, 2 edition, 1993.

[114] Z. Yoshida and P. J. Morrison. Hierarchical structure of noncanonical Hamiltonian systems. *Physica Scripta*, 91(2):24001, 2016.

[115] O. Czarny and G. Huijsmans. Bézier surfaces and finite elements for MHD simulations. *Journal of Computational Physics*, 227:7423–7445, 08 2008.

[116] T. Fujita. Tokamak equilibria with nearly zero central current: the current hole. *Nuclear Fusion*, 50(11):113001, nov 2010.

[117] E. Deriaz, B. Després, G. Faccanoni, K. P. Gostaf, L. M. Imbert-Gérard, G. Sadaka, and R. Sart. The grad-shafranov equation & the current hole. 2011.

[118] E. Zoni and Y. Güçlü. Solving Hyperbolic-Elliptic Problems on Singular Mapped Disk-like Domains with the Method of Characteristics and Spline Finite Elements. *Journal of Computational Physics*, 398(C), dec 2019.